

**IDENTIFICATION OF PRECLINICAL IMPLICATIONS FOR
NOVEL INDOLE-BENZIMIDAZOLES AND
PHENOTHIAZINES
USING IN VITRO CANCER CELL LINE AND
IN VIVO ZEBRAFISH MODELS**

A DISSERTATION SUBMITTED TO
THE GRADUATE SCHOOL OF ENGINEERING AND SCIENCE
OF BILKENT UNIVERSITY
IN PARTIAL FULFILLMENT OF THE REQUIREMENTS
FOR THE DEGREE OF
DOCTOR OF PHILOSOPHY
IN NEUROSCIENCE

By

MURAT YAMAN

SEPTEMBER 2020

IDENTIFICATION OF PRECLINICAL IMPLICATIONS FOR NOVEL INDOLE-BENZIMIDAZOLES AND PHENOTHIAZINES USING IN VITRO CANCER CELL LINE AND IN VIVO ZEBRAFISH MODELS

By Murat Yaman

September 2020

We certify that we have read this thesis and that in our opinion it is fully adequate, in scope and in quality, as a thesis for the degree of Doctor of Philosophy.

Özlen Konu Karakayalı (Advisor)

Michelle M. Adams

Ali Osmay Güre

Tunca Doğan

Zeynep Alagöz

Approved for the Graduate School of Engineering and Science:

Ezhan Karaşan

Director of the Graduate School

ABSTRACT

IDENTIFICATION OF PRECLINICAL IMPLICATIONS FOR NOVEL INDOLE-BENZIMIDAZOLES AND PHENOTHIAZINES USING IN VITRO CANCER CELL LINE AND IN VIVO ZEBRAFISH MODELS

Murat Yaman

PhD in Neuroscience

Supervisor: Özlen Konu Karakayalı

September 2020

Breast cancer (BC) and hepatocellular carcinoma (HCC) are two major health problems with significant mortality rates. Although drug therapies are available, therapeutic success remains limited. Because of low bioavailability, high toxicity and recurring drug resistance, novel therapeutic options are essential. In the present thesis, a multitude of *in vitro*, *in silico* and *in vivo* approaches were executed to test anti-cancer effects and preclinical potentials of novel indole-benzimidazoles and phenothiazines in BC and HCC, respectively. In the first component of the thesis, I evaluated BC cell line toxicity and estrogen receptor (ER) relationship of novel indole-benzimidazole derivatives using *in vitro* cancer lines, *in vivo* zebrafish embryos/larvae, and *in silico* comparative transcriptomics analyses. In the second part, antipsychotic compounds phenothiazines (PTZ) were repurposed for HCC therapy. Therefore, generic PTZ derivatives alone or in combination with sorafenib (SFB) were tested using *in vitro* cancer lines followed by zebrafish developmental assays and embryonic stage xenografts. In addition, RNAseq analyses were performed on trifluoperazine (TFP), SFB, and TFP+SFB combination treated Hep3B cells to understand synergistic/antagonistic effects of the drugs at gene expression level. Lastly, anti-HCC potential of novel PTZ derivatives were explored by *in vitro* and *in vivo* screenings. Moreover, effects of the novel and generic derivatives on neural pathways were evaluated by cholinesterase assays and motor response measurements. The findings of the dissertation present potential leads for conducting further preclinical studies tailored towards novel BC and HCC therapies.

Keywords: Breast cancer, Hepatocellular carcinoma, Indole-benzimidazoles, Phenothiazines, Sorafenib synergism, Drug repurposing, Preclinical drug discovery, *In vitro* / *in vivo* toxicity profiling, Behavioral assays, Acetylcholinesterase, Comparative transcriptomics

ÖZET

İN VİTRO KANSER HÜCRE HATLARI VE İN VİVO ZEBRABALIĞI MODELLERİ KULLANILARAK YENİ İNDOL-BENZİMİDAZOLLER VE FENOTİYAZİNLER İÇİN PREKLİNİK ETKİLERİN TANIMLANMASI

Murat Yaman

Nörobilim Doktora Programı

Tez Danışmanı: Özlen Konu Karakayalı

Eylül 2020

Meme kanseri (BC) ve hepatosellüler karsinom (HCC), kayda değer ölüm oranlarına sahip iki önemli sağlık sorunudur. İlaç tedavileri mevcut olmasına rağmen, terapötik başarı sınırlıdır. Düşük biyoyararlanım, yüksek toksisite ve tekrarlayan ilaç direnci nedeniyle yeni tedavi seçenekleri gereklidir. Bu tezde, BC ve HCC'de, sırası ile, yeni indol-benzimidazol ve fenotiyazinlerin anti-kanser etkilerini ve klinik öncesi potansiyellerini test etmek için farklı *in vitro*, *in siliko* ve *in vivo* yaklaşımlar uygulandı. Tezin ilk bölümünde, *in vitro* kanser hatları, *in vivo* zebabalığı embriyo ve larvaları ve *in siliko* karşılaştırmalı transkriptomik analizler kullanarak yeni indol-benzimidazol türevlerinin BC hücre hattı toksisitelerini ve östrojen reseptörü (ER) ile ilişkilerini değerlendirdim. İkinci bölümde ise antipsikotik bileşikler olan fenotiyazinler (PTZ), HCC tedavisi için yeniden konumlandırıldılar. Bu nedenle, tek başına veya sorafenib (SFB) ile kombinasyon halinde jenerik PTZ türevleri, *in vitro* kanser hatları, ardından zebabalığı gelişim testleri ve embriyonik aşama zenografları kullanılarak test edildiler. Ek olarak, RNAseq analizleri, ilaçların gen ekspresyon düzeyindeki sinerjistik/antagonistik etkilerini anlamak üzere trifluoperazin (TFP), SFB ve TFP + SFB kombinasyonu ile muamele edilen Hep3B hücreleri üzerinde gerçekleştirildi. Son olarak, yeni PTZ türevlerinin anti-HCC potansiyelleri, *in vitro* ve *in vivo* taramalarla araştırıldı. Ayrıca, yeni ve jenerik türevlerin nöral yolaklar üzerindeki etkileri, kolinesteraz testleri ve motor tepki ölçümleri ile değerlendirildi. Tezin bulguları, özgün BC ve HCC tedavilerine istinaden ileri klinik öncesi çalışmaların yürütülmesine potansiyel yol gösterici niteliktedir.

Anahtar kelimeler: Meme kanseri, Hepatoselüler karsinom, İndol-benzimidazoller, Fenotiyazinler, Sorafenib sinerjizmi, İlaçların yeniden konumlandırılmaları, Klinik öncesi ilaç

keşfi, *İn vitro/in vivo* toksisite profillemesi, Davranış testleri, Asetilkolinesteraz,
Karşılaştırmalı transkriptomik disiplinler

For my honorable family,

ACKNOWLEDGEMENTS

Bringing me up till this moment of PhD, I am grateful to my supervisor, Assoc. Prof. Özlen Konu; for her enduring support, being always accessible, her quality in initiating collaborative work, and - most importantly - being an irreplaceable model for me as a future manager. With Özlen Hoca's remarkable guidance, I had the chance to meet and to know many scholars and colleagues that deserve full of appreciation.

Initially, Prof. Dr. Zeynep Ateş-Alagöz has been an excellent person with her character, and I am deeply thankful for her collaboration. Moreover, her students Fikriye Zengin Karadayı and Mehmet Murat Kışla had gained respect, and I sincerely wish the best for them. They have synthesized and purified the novel derivatives in this thesis. Due to their ways of supplying the novel derivatives, they have further deserved the applause with some gentle and blue gloves.

Secondly, Dr. Ravindra Peravali and his students (especially Amrish Kumar) have shown great qualities in their works and achievements as scholars and individuals. During my stay in Karlsruhe, they have provided valuable support for me in pursuing the zebrafish experiments; developmental toxicity assays, locomotor assays and PMR setups. Importantly, their works, pace and accomplishments in the facilities have been an eye-opening experience that I shall acknowledge. I hope they will pursue even more.

My jury and committee members Prof. Dr. Michelle M. Adams and Assoc. Prof. Ali Osmay Güre have been immensely insightful for my studies and apprenticeship in Bilkent University. I am genuinely thankful for their supports and understandings that they have shown whenever I needed the most. In addition, I would like to express my sincere gratitude to Assist. Prof. Tunca Doğan for his participation in my defense and for his suggestions on improving this thesis.

My presence, as a Konu Lab member, has also been fruitful because of my colleagues who are kind in heart and competent with their works. In addition to their supports with the experiments, I am truly thankful to getting to know you all past and present Konu Lab members: Ahmet Hincer (locomotor assay analyses), Ayse Gokce Keskus (preprocessing transcriptomic data and her insightful leads for statistical analyses), Busra Korkmaz (xenograft injections and advanced hatching rate analyses), Cem Bugra Kaboglu (locomotor

assay analyses), Damla Gunes, Ilknur Safak Demirel, Kubra Calisir (preprocessing the RNAseq data), Omer Bayazeid (data retrieval from SwissTargetPrediction and support for MTT assays), Ronaldo Leka (preprocessing the RNAseq data), Said Tiryaki, Seniye Targen, Tuna Baydin and many others. In addition, I am grateful to Zebrafish Lab technician, Tülay Arayici, for her valuable support in zebrafish experiments in Bilkent University. It is for sure that each one of you will advance and reach high. I wish you the best for your future careers.

I would like to thank Bilkent University for the scholarships and the facilities which were provided. Lastly, I am grateful to TUBITAK (The Scientific and Technological Research Council of Turkey) because of the research grants (213S037 (PI: Zeynep Ates-Alagoz), the indole-benzimidazole study; and 116Z388 (PI: Ozlen Konu), the phenothiazine study, and COST CA17112 (PI: Ozlen Konu)) that allowed me to pursue the experiments for my PhD studies.

Most important of all, I am grateful to life for bringing me into my family; İbrahim, Ayten and Merve Gül Yaman. They made me who I am and showed me how a human should be - in the ways living his life and treating the others as equals. Whatever good things I come to do, they are the main reasons in the first place. Thus, I fully dedicate my family every bit of work that I have done.

I have been lucky as my path was crossed with many good people. Starting with my undergraduate years, my friends have been there for me. They brought joy and good examples with their invaluable characters that I should never forget: ABBAS Güven Akçay, Ali “Carlito” Castellan, Arzu Oğçin-Selim Kıdal, “Aslan Şampiyon” Aimane, Berhan Akgür, Can Telkenar, Cem Küncü, Constanza Kurman Petrozelli, Derya Karaarslan, Elif Erdoğan, F. Seyhun Üstün, Hakan İyisoğlu, İbrahim Kiremitçi, Jason Nasarovsky, Kay Kyungyong Chang, Lord Tobi Max Grosse, M. İ. Barış Dubalı, Martin Hrouda, Metin Yazar, Osman Ali Çiftçi, Pınar Berksun, Sedat Yalçınkaya, Seniye Targen, T. Kerem Uzel, V. H. İbrahim Miraloğlu, Waqas Akbar, YEFE ... You are a bless, you deserve the best, I am happy to encounter you all.

TABLE OF CONTENTS

ABSTRACT	iii
ÖZET.....	v
ACKNOWLEDGEMENTS	viii
TABLE OF CONTENTS	x
ABBREVIATIONS.....	xv
CHAPTER 1: INTRODUCTION	1
1.1 Drug discovery and preclinical drug assessments for cancer therapeutics.....	1
1.2 Additional considerations and prominent strategies on initiation of preclinical drug evaluations.....	3
1.2.1 Structure-activity relationship (SAR).....	3
1.2.2 Drug repurposing.....	4
1.2.3 Combination therapies.....	6
1.2.4 Zebrafish as an <i>in vivo</i> model.....	7
1.3 Breast cancer (BC) and estrogen (E2) signaling	10
1.3.1 Molecular classification of breast cancers	10
1.3.2 Estrogen signaling and selective estrogen receptor modulators (SERMs).....	11
1.4 Primary liver cancers	13
1.4.1 Hepatocellular carcinoma (HCC) molecular subtypes.....	13
1.4.2 Drug therapies in HCC	15
1.4.3 Repurposing antipsychotics and phenothiazine derivatives for treatment of HCC	16
CHAPTER 2: OBJECTIVES AND RATIONALE	19
CHAPTER 3: MATERIALS AND METHODS.....	21
3.1 Materials	21
3.1.1 Screened novel and known molecules	21
3.1.2 Cell culture reagents.....	22
3.1.3 Zebrafish culture materials, equipment and reagents.....	22
3.1.4 Equipment	23
3.1.5 Kits and supplements	23
3.1.6 qPCR primers	24
3.2 Methods	26
3.2.1 Cell culture methods.....	26
3.2.2 Zebrafish culture methods.....	27

3.2.3	MTT cytotoxicity assay and toxicity measurements on the cell lines.....	29
3.2.4	Embryonic toxicity assessments in zebrafish.....	30
3.2.5	mRNA isolation and cDNA synthesis.....	31
3.2.6	qPCR experiments and relative gene quantity measurements.....	32
3.2.7	Protein collection and measurements.....	33
3.2.8	Cholinesterase activity evaluations.....	33
3.2.9	AB genotype zebrafish behavioral analyses.....	34
3.2.10	<i>In silico</i> target screenings for the derivatives.....	35
3.2.11	Microarray analyses.....	35
3.2.12	RNAseq analyses.....	37
CHAPTER 4: RESULTS.....		38
4.1	Indole-benzimidazole study.....	38
4.1.1	<i>In vitro</i> toxicity analyses of indole-benzimidazoles.....	38
4.1.2	<i>In vivo</i> toxicities of the novel indole-benzimidazoles used as leads.....	42
4.1.3	Transcriptome level analyses on indole-benzimidazole exposures.....	43
4.2	Repurposing and novel derivative screening of phenothiazines for treatment of HCC 53	
4.2.1	<i>In vitro</i> toxicities of the derivatives.....	53
4.2.2	<i>In vivo</i> toxicities of the derivatives.....	64
4.2.3	Xenograft potencies of the derivatives.....	70
4.2.4	<i>In silico</i> target screenings for the derivatives.....	71
4.2.5	Effects of the derivatives on cholinesterase levels.....	72
4.2.6	<i>In vivo</i> behavioral analyses of the derivatives on AB strain zebrafish embryos	74
4.2.7	RNAseq analyses of TFP-SFB combinations on Hep3B cell line.....	82
CHAPTER 5: CONCLUSIONS AND DISCUSSION.....		93
5.1	Anti-BC and antiestrogenic potentials of novel indole-benzimidazole derivatives ..	97
5.2	Repurposing generic phenothiazines in combination with SFB for HCC therapies	100
5.3	Preclinical evaluation of novel and synthesized derivatives.....	104
5.4	Future Perspectives.....	105
REFERENCES.....		108
APPENDIX A.....		140
APPENDIX B.....		149
COPYRIGHTS AND PERMISSIONS.....		171

LIST OF FIGURES

Figure 1.1 Drug development stages representing the expenses and amounts of screened compounds on each stage.	2
Figure 1.2 Molecular classes and related histological and clinical features of HCCs.	14
Figure 4.1 GRcalculator analyses based on $\log_{10}IC_{50}$ values (μM) derived from the viability percentiles after the exposures on MCF-7 cell line.	40
Figure 4.2 PCA of the candidate indole-benzimidazole derivatives.	41
Figure 4.3 PCA of 72 hpf embryonic morphometric measurements.	43
Figure 4.4 Preliminary microarray analyses for the novel indole-benzimidazoles.	44
Figure 4.5 Heatmaps for qPCR results.	46
Figure 4.6 qPCR results for E2 signaling genes.	47
Figure 4.7 <i>In vivo</i> qPCR results for the R ₁ : p-fluorobenzyl members.	48
Figure 4.8 Expression profile contrasts between the compound 51, (A) E2, (B) Dioxin and (C) AA (-).	49
Figure 4.9 Correlation heatmap of SERMs, AA (-), Dioxin and indole-benzimidazole derivatives.	50
Figure 4.10 Generic PTZ derivative screenings on multiple cell lines (24 h).	54
Figure 4.11 (A) eGFP status and (B) time-dependency evaluations on the responses of Hep3B and SkHep1 towards generic derivatives.	55
Figure 4.12 Non-generic PTZ derivative screenings <i>in vitro</i>	56
Figure 4.13 Dependence of the novel derivatives' toxicity profiles on (A) eGFP status and (B) exposure time.	57
Figure 4.14 Preliminary SFB synergism evaluations of PCP and TFP.	58
Figure 4.15 Synergy maps and dose-response curve shifts for the TFP-SFB combination exposures (24 hour) across the liver cancer lines.	60
Figure 4.16 Synergy maps and dose-response curve shifts for the TFP-SFB combination exposures (48 hour) across the liver cancer lines.	62
Figure 4.17 SFB-PD-5 synergism evaluations on Hep3B.	63
Figure 4.18 Hatching (%) of zebrafish embryos within the timeframe of 30 hpf - 72 hpf.	65
Figure 4.19 Hatching (%) of zebrafish embryos within the timeframe of 30 hpf - 72 hpf.	67
Figure 4.20 <i>In vivo</i> synergy maps for the SFB combinations of the generic derivatives.	68
Figure 4.21 <i>In vivo</i> synergy maps for the SFB combinations of the generic derivatives.	69
Figure 4.22 SkHep ^{eGFP} xenograft tumor CTCF comparisons for PCP (10 μM and 20 μM) and TFP (10 μM) exposures.	70
Figure 4.23 SkHep ^{eGFP} xenograft tumor CTCF comparisons for PD-3 (20 μM), PD-5 (10 μM), PD-9 (5 μM), PD-11 (5 μM) and PD-29 (20 μM).	71
Figure 4.24 Ward distance based heatmap derived from SwissTarget prediction scores.	72
Figure 4.25 Cholinesterase activity measurements across (A) SkHep1, (B) Hep3B and (C) zebrafish embryos.	73
Figure 4.26 Cholinesterase activity changes after 48 hour exposures of TFP and SFB combinations on Hep3B.	74
Figure 4.27 PCP (20 μM) PMR results.	75

Figure 4.28 TFP (20 μ M) PMR results.	76
Figure 4. 29 SFB (2 μ M) PMR results.	76
Figure 4.30 PCP (20 μ M) - SFB (2 μ M) PMR results.	77
Figure 4.31 TFP (20 μ M) - SFB (2 μ M) PMR results.	78
Figure 4.32 PD-9 (10 μ M) PMR results.	79
Figure 4.33 PD-11 (10 μ M) PMR results.	79
Figure 4.34 Locomotion distance analyses across single derivative and SFB combination exposures.	81
Figure 4.35 (A) PCA and (B) heatmap clusters of RNAseq data.	83
Figure 4.36 mRNA level changes after TFP-SFB combination exposures.	92

LIST OF SCHEMES

Scheme 2.1 Workflow of the thesis studies	19
---	----

LIST OF TABLES

Table 1.1 Molecular subtypes of BC and status of each molecular marker	11
Table 3.1 Codes and R ₁ and R ₂ designations of novel indole-benzimidazole structures	21
Table 3.2 Codes and R ₁ , R ₂ and R ₃ designations of generic phenothiazines	22
Table 3.3 Cell culture reagents used in the studies	22
Table 3.4 Equipment used in the studies	23
Table 3.5 Kits and supplements used in the studies	23
Table 3.6 List of primer pairs used throughout the qPCR studies	24
Table 3.7 qPCR parameter used for reaction cycles	32
Table 4.1 GRcalculator derived IC ₅₀ values (μ M) of the indole-benzimidazoles after 24-hour exposures in MCF-7	39
Table 4.2 IC ₅₀ values (μ M) for the candidate derivatives across the cell lines	41
Table 4.3 48 hpf hatching and abnormality status of indole-benzimidazole exposed embryos	42
Table 4.4 Top LINCS Query matches for the compound 51	52
Table 4.5 Synergy scores of TFP-SFB combinations from Figure 4.15 and Figure 4.16	61
Table 4.6 EC ₅₀ values for 72 hpf and 120 hpf zebrafish after the generic molecules	64
Table 4.7 EC ₅₀ values for 72 hpf and 120 hpf zebrafish after the non-generic derivatives	66
Table 4.8 Top 10 KEGG annotations (adj.p-value < 0.05)	84
Table 4.9 SFB 1 μ M and SFB 2 μ M gene expression comparisons	85
Table 4.10 SFB 1 μ M and TFP 12 μ M-SFB 1 μ M gene expression comparisons	86
Table 4.11 SFB 2 μ M and TFP 12 μ M-SFB 2 μ M gene expression comparisons	88
Table 4.12 TFP 12 μ M-SFB 1 μ M and TFP 12 μ M-SFB 2 μ M gene expression comparisons	89
Table 4.13 TFP 12 μ M and TFP 12 μ M-SFB 1 μ M gene expression comparisons	90

APPENDIX A

Figure Appendix A1 Pearson's correlations between GraphPad Prism and GRcalculator derived IC ₅₀ values.	140
Figure Appendix A2 Viability percentile-based cell line effect comparisons across varying concentrations of the candidate indole-benzimidazoles.	141
Figure Appendix A3 Representation of cell line based log ₁₀ (IC ₅₀) values (μM) (GRcalculator).	142
Table Appendix A4 List of Reactome Pathways as represented on Figure 4.4 (C).	143
Table Appendix A5 Compound 51 KEGG pathway annotations	145
Table Appendix A6 Compounds 50-51-53 KEGG pathway annotations	146
Table Appendix A7 KEGG pathways-based contingency table	147
Table Appendix A 8 Molecular docking scores of the derivatives and ligands.	148

APPENDIX B

Figure Appendix B1 Non-generic PTZ derivative log ₁₀ IC ₅₀ response t-test comparisons between Hep3B and SkHep1 cell lines.	149
Figure Appendix B2 Cell line-based comparisons for the PTZ derivatives.	149
Table Appendix B3 Zebrafish images after exposures to individual derivatives.	150
Table Appendix B4 Representative images for xenograft experiments.	158
Figure Appendix B5 Validation experiment on the direction of AChE/BChE activities on Hep3B.	159
Figure Appendix B6 PCP (20 μM) versus PCP (20 μM) - SFB (2 μM) PMR results.	159
Figure Appendix B7 TFP (20 μM) versus TFP (20 μM) - SFB (2 μM) PMR results.	160
Table Appendix B8 n-way ANOVA results for the effects of treatment, concentration, combination and their interactions on the raw distance data.	160
Table Appendix B9 n-way ANOVA results for the effects of treatment, concentration, combination and their interactions on the raw speed data. (p-value: * < 0.05)	160
Figure Appendix B10 Locomotion speed analyses across single derivative and SFB combination exposures.	161
Figure Appendix B11 Percentiles of each principal component generated by the PCA approach at Figure 4.35.	162
Table Appendix B12 SFB 1 μM and TFP 12 μM-SFB 1 μM gene expression comparisons	163
Table Appendix B13 SFB 2 μM and TFP 12 μM-SFB 2 μM gene expression comparisons	165
Table Appendix B14 TFP 12 μM-SFB 1 μM and TFP 12 μM-SFB 2 μM gene expression comparisons.	167
Table Appendix B15 TFP 12 μM and TFP 12 μM-SFB 1 μM gene expression comparisons.	169

ABBREVIATIONS

AA (-)	Amino acid depletion
AChE	Acetylcholinesterase
AhR	Aryl hydrocarbon receptor
BC	Breast cancer
BChE	Butyrylcholinesterase
CPM	Count per million
CPT	Camptothecin
CSS	Combination sensitivity score
dpf	Days post-fertilization
DMSO	Dimethyl sulfoxide
DV	Dorsoventral
E2	Estrogen
EC ₅₀	Half maximal effective concentration
eGFP	Enhanced green fluorescent protein
ER	Estrogen receptor
FC	Fold change
GPER1	G Protein-Coupled Estrogen Receptor
HCC	Hepatocellular carcinoma
hpf	Hours post-fertilization
IC ₅₀	Half maximal inhibitory concentration
LC ₅₀	Half maximal lethal concentration
MoA	Mechanism of action
MTT	3-(4,5-dimethylthiazol-2-yl)-2,5-diphenyltetrazolium bromide
NOAEL	No-observed-adverse-effect levels
PCA	Principal component analysis
PCP	Prochlorperazine
PK/PD	Pharmacokinetic/pharmacodynamic
PMR	Photomotor response
PPH	Perphenazine
PTZ	Phenothiazine

qPCR	Quantitative Polymerase Chain Reaction
RNAseq	RNA sequencing
RC	Rostrocaudal
RQ	Relative quantity
SAR	Structure-activity relationships
SERM	Selective estrogen receptor modulator
SFB	Sorafenib
SMILES	Simplified Molecular Input Line Entry System
TNBC	Triple negative breast cancer
TFP	Trifluoperazine

CHAPTER 1: INTRODUCTION

1.1 Drug discovery and preclinical drug assessments for cancer therapeutics

Cancer is the second major health problem and current therapies remain limited [1, 2]. Drug therapy is one of the prominent choices in clinic; however, low bioavailability, high toxicity and recurring drug resistance circumvent its success [3]. Therefore, there is an essential need for new therapeutic options and discovering new drug candidates [4]. Nevertheless, a drug-like compound demands high workload over long periods of time before becoming accessible for the patients [5].

A drug can be defined as: “a substance intended for use in the diagnosis, cure, mitigation, treatment, or prevention of disease” [6]. Thereby, one can follow a therapeutic regime, so the condition at hand can be managed. Accordingly, Ehrlich’s “magic bullet hypothesis” has been the driving force of the modern drug discovery processes [7]. In its essence, the idea comprises that a pathology of interest can be dealt with specific factors, so-called *magic bullets*. For years, it has become an inspiration for researchers to identify such compounds as remedies.

Thorough investigations and multidisciplinary collaborations are crucial in finding an applicable therapeutic, which is both efficient and safe. Starting from thousands of possible structures only one or two therapeutics can make it to the market, by the end of a study. Proposed by preliminary research and libraries of compounds, novel therapeutics undergo multiple steps of analyses and validations, during a period of more than ten years with an overall success rate lower than 4% (**Figure 1.1**) [8, 9]. On each step, numbers of candidate molecules are filtered based on their efficacies and safety profiles for the management of the healthcare condition. Here, the fields of medicinal chemistry, pharmacology and toxicology, medicine, biology and statistics show major contribution in the discovery and screening processes by producing large sums of data. Although in-depth knowledge on mechanism of action (MoA) is not obligatory, it is desirable in obtaining the best-in-class applications [10].

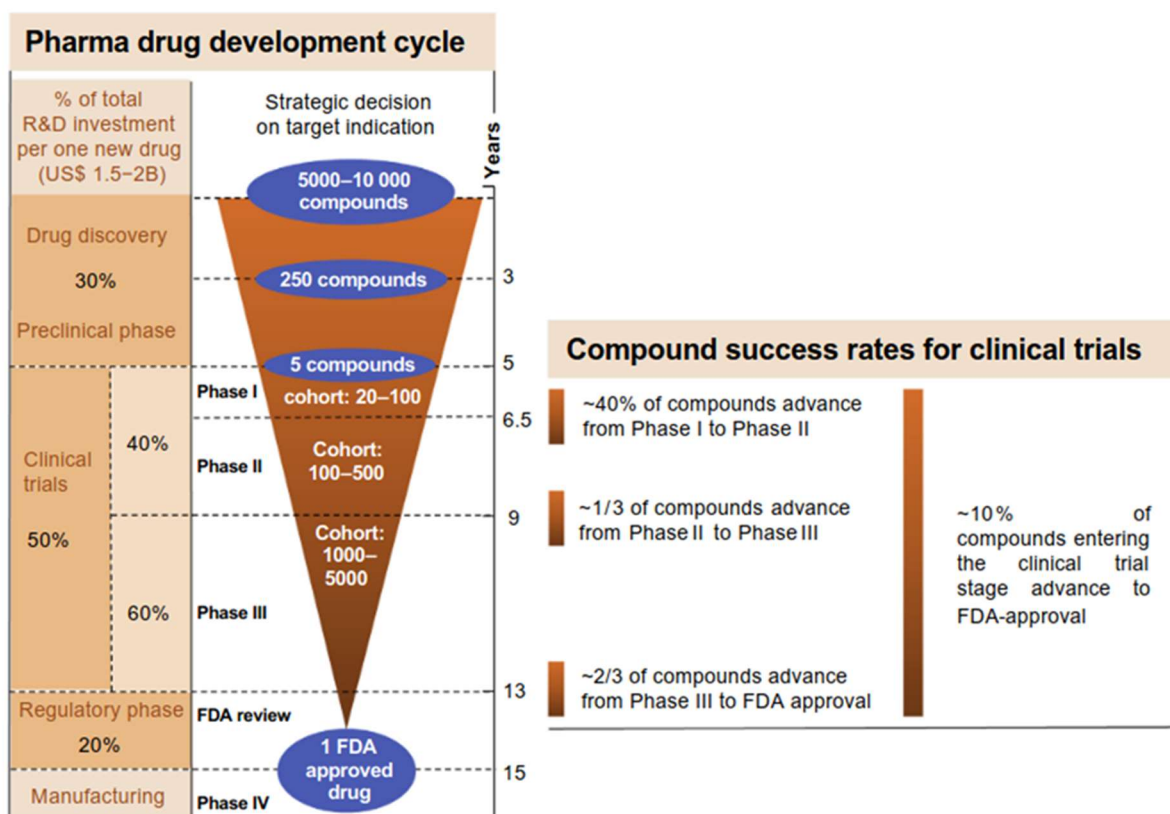


Figure 1.1 Drug development stages representing the expenses and amounts of screened compounds on each stage. Adapted from Harrer S. et al., 2019. Trends in Pharmacological Sciences [8] (Licensed by CC BY NC ND)

Preclinical stages serve as the major bottlenecks for eliminating a massive number of therapeutic candidates from the pipeline under the main criteria that are efficacy and safety in non-human conditions [5]. This is done by identifying the most convenient lead and drug-like compounds from basic research and large-scale screening libraries. In this regard, *in vitro* and *in vivo* conditions are utilized to evaluate the capabilities of the candidates to target predetermined molecular mechanisms or the phenotypes of interest. For that, good laboratory practices and multiple lines of research activities become crucial in providing the pharmacokinetic/pharmacodynamic (PK/PD) qualities and toxicity profiles [11]. Some of the major activities are lead identifications, *in vitro* and *in vivo* toxicity assays, genomic and protein biomarker assays [12]. Detailed list of initial screening methodologies can be accessed in Hughes JP. et al. (2019) [13]. Therefore, many of the candidates, that do not exert a significant effect or that are toxic, fail to be included in future analyses. This leaves a limited number of candidates to examine in clinical conditions, as preclinical findings do not fully ensure success in patients.

1.2 Additional considerations and prominent strategies on initiation of preclinical drug evaluations

Tedious with years and lines of multidisciplinary preclinical works, effective and safe therapeutic options can then be subjected to clinical trials. These options remain a handful in numbers concluded by more than three years of effort with high expenses, exceeding 300 million dollars [8, 14]. Considering that much endeavor and budget spent may not be favorable due to the likelihood of high number of failed candidates, there is still an urge to bring about more cost-and-time-effective strategies for the earlier stages of preclinical work. In this regard, (i) structure-activity relationship studies, (ii) drug repurposing and (iii) combination approaches and (iv) *in vivo* animal models (e.g. zebrafish) provide marked improvements on initiating and executing the preclinical assessments.

1.2.1 Structure-activity relationship (SAR)

SAR studies focus on how substructures of a compound can influence a chemical or biological activity [15]. Either qualitative or quantitative, the approach can categorize the candidate structures as well as side-chain modifications if they relate, not relate, or how much relate with the activity [16, 17]. In this sense, they underlie hit-lead-drug discovery paradigms [18]. Ideally, the hit compounds pose sub-micromolar activity levels (lower than $< 10 \mu\text{M}$) and optimizable chemical structures [13]. Following that, medicinal chemistry approaches can take place to validate and apply structural alterations on the hit compound series into lead molecules to improve the potencies to the nanomolar scale [19, 20]. In addition, lead molecules can be further derived and optimized by side-chain alterations [21]. This allows enhancements on the activity, selectivity and safety profiles, respectively. For that, level of understanding on the SAR becomes essential element on the success by considering *in vitro/in vivo* toxicity levels and *in silico* model findings.

In vitro and *in vivo* environments allow initial evaluations on the efficiencies and PK/PD properties of the candidates. By doing so, clinical relevance of the hit-lead compounds and the influence of side-chain modifications can be confirmed in high-resolution. The findings by Ni L. et.al and Al-Refai M. et.al supported that each side chain alteration can be categorized based on the concentrations that inhibit the cell growths by 50% (IC_{50}), and on multiple cell lines [22, 23]. So, they were able anticipate which derivative versions to pursue with. Interestingly, their SAR studies demonstrated that different positions on the main scaffold can synergize in the resulting toxicity profiles. Structural synergism has been a long-standing phenomenon where subunits of the same structure can interact, hence impacting the final

action of the compounds [24, 25]. Therefore, structural synergism further suggests additional considerations on SAR pipelines. Moreover, SARs can be further extended into classifying *in vivo* toxicity data. Accordingly, Hao and colleagues presented that zebrafish developmental abnormality and toxicity scores can be utilized in SAR of dorsomorphin analog side chains [26].

In silico environments pose as cost and time effective alternatives by allowing SAR predictions in a single atomic resolution [27, 28]. By doing so, PK/PD, toxicity properties and target dockings can be addressed for each side modifications before doing the actual *in vitro* work [15]. Considering the spectrum of possible therapeutics and modifications, *in silico* environments can further limit the time by forecasting the most likely candidates to go with. Therefore, candidate improvements by side chain alterations can be pursued in advance, limiting the cost by refraining from unlikely candidates. Yet, these computational findings hold suggestive values which demand further *in vitro* validations. Accordingly, *in silico* SAR likelihood estimations yield relatively more effective scenarios on starting the preclinical stages.

Lastly, SAR studies demand additional considerations on privileged compounds whose structures are naturally active and show predisposition to interact with multiple biotargets [15, 29]. For example, indoles, benzimidazoles and phenothiazines possess privileged chemistry [30-32]. Although they provide good starting points for lead generations, their multi-target affinities can bring about challenges on interpreting SARs [33]. Neves and colleagues showed that a large selectivity profile can lead to activity on multiple targets which can obscure conclusions by single target-oriented SAR studies [34].

Therefore, SAR findings on *in vitro/in vivo* toxicity data and *in silico* models are crucially informative and can save time.

1.2.2 Drug repurposing

Drug repurposing, also known as drug repositioning, is a pharmaceutical process where the benchmark compounds are functionalized for alternative purposes [35]. Contrasting with Ehrlich's magic-bullet concept, the approach is based on the idea that one drug can also be useful in treating different pathologies. For example, Chou and Huang promoted antipsychotic derivatives for repurposing approaches due to anti-cancer effects that they exert [36, 37]. As pharmacokinetic and pharmacodynamic properties of such compounds are already well-documented, candidate compounds can minimize the time and work for standard preclinical

practices [38]. Various studies suggested high success rates for repurposing approaches (30-70%) [39, 40].

Modern repurposing studies utilize computational environments and experimental approaches in finding suitable candidates [41]. Duan and colleagues provided a massive and relatively simplified gene signature matching algorithm to compare queries with 100000 perturbagens with mostly known molecular targets, across multiple cell lines [42]. So-called LINCS L1000 data is ready and free to use with embedded tools. This allows users to relate targets and mechanisms with the queries, which are also suggestive for further repurposing approaches. Although the data originally represents the gene signatures for almost 1000 genes only, the tool provides enormous support for hypothesis-driven preclinical practices. For instance, Li and colleagues were able to utilize this tool in repurposing the antipsychotic compound pimozide as an anti-cancer agent *in vitro* [43]. Not only gene signatures, but also chemical structures can also serve as models for repurposing studies. Gfeller and colleagues have built the SwissTargetPrediction algorithm where the users can anticipate the targets of their compounds based on 2D and 3D similarities with known ligands [44]. As *in silico* studies are inadequate to fully represent the actual *in vitro* affinities with possible targets, validations can be proceeded by binding assays [45, 46]. Retrospective clinical data analyses also provide immense amount of information for repurposing studies. For instance, originally proposed as an osteoporosis agent raloxifene was later indicated for breast cancer by Ely Lilly, as thalidomide was later subjected to multiple myeloma cases [47, 48]. In addition, DRUGSURV tool was able gather patient-derived survival data for clinical compounds where they proposed the antipsychotic thioridazine for anti-cancer therapies [49]. Accordingly, phenotypic screenings were able to show its selective toxicity on cancer stem cells, and the drug was further taken in clinical trials. Although partially successive in suppressing the progress of acute myeloid leukemia (AML), prolonged toxicity levels halted further evaluations, demanding structural improvements [50]. Therefore, there is no guarantee that a repurposed drug can remake it to the market for alternative pathologies, though preclinical studies can be supportive.

As a result, drug repurposing holds high potential for early preclinical testing and demand computational as well as experimental approaches to validate the compounds for clinical settings.

1.2.3 Combination therapies

Combination therapies can improve the efficacies of candidate remedies [51, 52]. Efficacy of a single compound can be limited against the complex nature of specific cancer types [53]. Involvement of multiple oncogenic elements further complicate the therapeutic indices which may not be improved by increasing the dosages due to high toxicities and adverse effects [54, 55]. As development for newer compounds also require more time and costs, there becomes a need for additional revisions on the therapeutic regimes [52]. In this regard, combination therapies have been one of the major strategies that provide improvements in treating cancer [56]. Yet, advance preclinical trials are needed to confirm likelihood for synergism. For that, PK/PD properties as well as toxicology profiles require a thorough understanding of the effective combination concentrations and, if possible, MoA [53, 54, 57, 58].

Synergy calculations supplement valuable information on applicable doses. IC_{50} values or viability scores can be obtained after exposures to a series of drug concentrations and their combinations [59]. Then, they can be subjected to evaluating the degree of synergism between the combination compounds. Despite the presence of a vast numbers of combination assessment algorithms, each approach assumes distinct strategies in modeling the combination parameters, leaving a debate for the choice of model to utilize [60, 61]. This complication was further eased by Ianevski and colleagues who developed SynergyFinder web-interface. The tool allows users to explore multiple algorithms and provides interactive graphical representations for combination topologies [62]. It was further implemented by DECREASE algorithm to scale-up the assessments for high-throughput screenings [63].

Nonetheless, combination sensitivity, efficacy and respectively side-effect estimations are needed for better interpretations on the concentrations. SynToxProfiler and combination sensitivity score (CSS) have been deployed to address clinical relevance where users can compare sample-type dependencies [64, 65]. Interestingly, combination assessment models can be also employed *in vivo*, providing valuable information on no-observed-adverse-effect levels (NOAEL) [66]. Accordingly, the doses that cause developmental failures and organ toxicities can be presented by multiple lines of studies via synergistic effect assessments [67-69]. Therefore, finding the right concentration intervals for clinical settings demands a better understanding of sensitivity, efficacy and *in vivo* toxicity profiles.

Conventional approach to understand the mechanism of synergy relies on two main hypotheses, as described by Pritchard and colleagues [70]. Firstly, one of the compounds can stimulate the effect of another, suggesting overlapping directions on the expression profiles.

Weber and colleagues further supported this hypothesis by using tumor sensitizing agent 17-AAG which was able to promote the effects of taxol on both cellular and molecular levels [71]. Secondly, the combination can result in acquiring a relatively distinctive profile from the individual treatments. Cilengitide and Gemcitabine combination therapy can represent this scenario. For example, vascular promotion is acquired by Cilengitide which indirectly improves the uptake of apoptotic agent Gemcitabine, resulting with a decrease of *in vivo* tumor size and metastasis [72]. Moreover, the success of combination was also dependent on dosing and time, implying a need for in-depth understanding of possible synergistic combinations and their mechanisms [53, 68].

To sum up, a consensus between large-scale concentration assessments, both *in vitro* and *in vivo*, can provide the most suitable combinations and concentrations to advance in a preclinical setting.

1.2.4 Zebrafish as an *in vivo* model

In vivo works are essential to translate preclinical data into clinical settings [17, 73]. Organ toxicity, mutagenicity, survival and abnormality rates, type of dosing (acute, chronic, sub-acute) as well as behavioral affects are some of the major concerns to address before the clinical trials [11]. Although use of murine models has been the golden standard, zebrafish models emerge as tremendously beneficial and more productive alternatives for the early stages of preclinical assessments [74]. As they represent similarities with human at both physiological and molecular levels (by 70%), the zebrafish models become advantageous in preclinic [75-78]. However, major profits of zebrafish come from their high fecundity rates, *ex utero* developments, short life spans, ease of maintenance and compliant drug exposures procedures [79, 80]. Therefore, zebrafish allow large scale assessments in a relatively short amount of time, with low costs and with high numbers of biological replicates. Especially for initial preclinical evaluations, zebrafish can outperform on high-throughput toxicity assays and xenograft studies leading to prospects of the study to be foreseen earlier [81, 82].

1.2.4.1 High-throughput toxicity studies

High throughput toxicity assays in zebrafish are performed during the early preclinic stages to refrain from focusing on potentially harmful compounds further. In general, assays are done in embryos ranging from 0-5 days post-fertilization (dpf) [83]. Transparency of each single embryo and advancing screening technologies allow qualitative and quantitative assessments

on drug toxicities [84]. Therefore, developmental defects/lethality and organ toxicities of the applied doses can be evaluated in advance.

Developmental defects and lethality paradigms can be investigated accurately in zebrafish embryos [85]. Survival ratios and morphometric parameters can be considered in the evaluations. In this regard, half maximal lethal and effective concentrations (LC_{50} and EC_{50} , respectively) can be incorporated with morphologic changes of the embryos after the exposures, as done by Selderslaghs and colleagues [86]. Besides the teratogenicity estimations with LC_{50} and EC_{50} scores, effects of the hit compounds can be classified by examining multiple morphometric measurement sets via principal component analyses (PCA) and alike methodologies [87]. Accordingly, yolk size, eye size, body axes, hatching rates after 48 hours post fertilization (hpf) can be informative on the levels of toxicity. Therefore, morphometric changes and effective dose estimations can provide valuable insights for developmental toxicities of the screened candidates.

Adverse effect profiles can be further anticipated via organ toxicity experiments allowing estimations on the lowest observed effective concentration (LOEC) levels. As cardiotoxicity assessments were done by Gao and colleagues, heartbeats, circulation, edema and thrombosis parameters can be evaluated on individual embryos after 48 hpf [88]. Moreover, drug-induced liver injury is a crucial factor in clinical applications, which can be further evaluated via liver-tagged transgenic lines between 3 dpf - 5 dpf, as demonstrated by Zhang and colleagues [89]. However, morphologic hepatotoxicity measurements may require additional considerations. Because abnormal effects on heart can also influence the size of the swelling of liver after the exposure. This controversial feature can be addressed by integrated organ toxicity evaluations [90]. For example, ZeGlobalTox study allowed recordings on cardio, neuro and hepatotoxicity of each individual embryo in a time series (100 hpf, 120 hpf and 128 hpf, respectively), supporting the ease for better assessment of adverse profiles.

Moreover, screening of neurotoxicity is widely applied during preclinical studies, as they also hold functional implementations [91]. For example, Cousin and colleagues were able to repurpose compounds and combinations for treatment of tobacco dependence [92]. In their study, they were able to profile dose dependent adverse toxicities, besides electing candidate remedies for clinical settings. Moreover, type of locomotion and exposure intervals are important factors to consider during preclinical trials [93-95]. As an example, a study done by Jordi and colleagues, showed distinctive functions by the candidates that correlate with different locomotor response types they exhibited in the phenotype [96]. These concentration,

function and compound-wise correlations are observable by photomotor response assays which is a fast, robust and statistically meaningful behavioral assay in zebrafish [97]. The photo-stimulated approach consists of multiple phases where activity signatures across the phases can predict MoA of neuroactive compounds, i.e., adrenergic, dopaminergic and serotonergic [98].

In summary, zebrafish increases the pace and scale of toxicity evaluations for early preclinical candidates where predictions on function can be moderately inferred.

1.2.4.2 Xenograft studies

Xenograft studies in embryonic stage are representative for human cancer, as model cell lines (patient derived or generic *in vitro* lines) for the clinical subtypes improve the reliability of the screening results [99-102]. In addition, they allow visualizing the transplants clearly in high-throughput settings with large biological replicate sizes [103]. Thus, toxicity and adverse effects can be reliably assessed at the same time [104]. For example, Lin and colleagues were able to configure novel liver cancer drug from a xenograft platform [105]. In their study, the candidate compound 419S1 has demonstrated improved therapeutic index and lower hepatotoxicity levels, hence better drug efficacy and toxicity. Interestingly, other closely related derivatives and the standard liver cancer drug sorafenib (SFB) underperformed. Furthermore, large sample sizes become helpful in these assessments as therapeutic indices for preclinical candidates can be generated fast and reliably. For example, Tseng and colleagues have developed a novel anti-HCC agent. In their study, they were able to show its potential via robust xenograft assays showing the dose-dependency with no lethal profiles, strongly indicative for further preclinical assessments [106]. Moreover, xenografts are suitable for combination evaluations. As shown by Zhu and colleagues, 5-Fluorouracil and Furanodiene can synergize together and exert anti-cancer effects on liver and breast cancer models [107]. In the same study, they have further represented therapeutic efficacies of the generic anti-cancer compounds on various xenograft models. Their findings were supportive of the potential of zebrafish xenografts for preclinical cancer drug pipelines, as therapeutic windows can be investigated in xenograft platforms [108, 109]. In addition, imaging of the xenografts can be improved by utilizing stably expressed fluorescent tags in the *in vitro* lines, allowing to monitor the tumor growth with fluorescence signals [110]. A novel peptide screening on zebrafish xenografts has utilized 20 samples per group where time and cell type dependencies were computable across two different time points and in GFP tagged MCF-7

and MDA-MB-231 cell lines [111]. However, drug response profiles between the clones and the neutral lines can also vary suggesting extra care on the studies [112, 113].

As a result, high similarities with human cases and ability to work fast in high numbers can speed up the early preclinical works.

1.3 Breast cancer (BC) and estrogen (E2) signaling

According to 2019 reports in US, BC has the second highest incidence and mortality rates in women [114]. Cellular origins can be pinned down to the ducts and lobules of the mammary gland [115]. They give rise to invasive or *in situ* type cancers where the invasive ductal carcinoma accounts for almost 80% of the cases [116]. Moreover, each BC histological subtypes represent diverse profiles and heterogeneous therapeutic responses [117]. Therefore, there has been an immense need for better subtyping methods and therapies for BC [118].

1.3.1 Molecular classification of breast cancers

Molecular classification methods robustly supplement conventional histopathological measures [117]. Perou and colleagues have showed that patient-derived BC samples can be classified into major molecular classes that are in line with hormone signaling [119]. Moreover, consideration of the molecular subtypes improved the conventional histopathological prognostics. Several lines of follow-up studies supported the idea for better predictive and survival outcomes based on the molecular subtyping of BC [120, 121]. Therefore, hormone receptor status for estrogen receptor alpha (ER α), progesterone receptor (PgR) and human epidermal growth factor receptor 2 (HER2) as well as amount of proliferation marker gene (Ki67) have come to light [122]. In this regard, luminal A, luminal B, HER2+ and triple negative breast cancer (TNBC or basal-like) were annotated for the names of the four molecular subtypes (**Table 1.1**) [123]. Subsequent experiments implemented more subtypes into these categories [124]. For example, levels of claudin protein can be utilized in sub-categorizing the TNBCs, as preferential relapse areas can be indicative for normal-like subtypes [125, 126]. Moreover, transcriptomic signatures can increase the spectrum of classes [121, 127]. As in PAM50 approach, expression signatures of selected fifty genes could improve the prognostic value [128]. Yet, these molecular classifications still pose some limitations, especially on the predictive abilities towards better survival outcomes [129, 130]. Since more biomarkers can be incorporated in the classification settings, multi-modal approaches and multi-component analyses may improve the predictive abilities on therapy efficacies [131, 132].

Preclinical evaluations demand representative *in vitro* models. Besides that, early stages of preclinical vastly utilize generic cell lines, due to well-established *in vitro* and xenograft protocols as well as high clinical relevancies by the biomarker levels [133, 134]. For example, a hormone responsive (ER α and PgR positive) MCF-7 cell line have been widely and robustly used in preclinical settings as a subject for luminal A cancer therapeutics [135, 136]. Similarly, MDA-MB-231 has been the model for aggressive cell line for TNBC-claudin low subtype BC oriented drug screenings [137, 138]. Interestingly, both cell lines have also been used as controls for one another due to their distinctive molecular profiles, especially in development of novel estrogen receptor modulators [138-140].

Table 1.1 Molecular subtypes of BC and status of each molecular marker

Molecular subtypes	Estrogen receptor α (ERα)	Progesterone receptor (PgR)	Human epidermal growth factor receptor 2 (HER2)	Ki67
Luminal A	+	+/-	-	<14%
Luminal B	+	+/-	+/-	\geq 14%
HER2+	-	-	+	\geq 14%
TNBC	-	-	-	\geq 14%

Adapted from He L. et al., 2019. Cancer Management and Research [123]. (Licensed by CC BY-NC 3.0)

1.3.2 Estrogen signaling and selective estrogen receptor modulators (SERMs)

Estrogens belong to steroid hormone family, and they exert carcinogenic potentials in various tissues including breast and liver [141, 142]. The physiological and cancer related actions propagate through binding to their targets, the estrogen receptors (ER α , ER β and G Protein-Coupled Estrogen Receptor (GPER1)) [143, 144]. In the case of ER α and ER β , estrogen-ER complex attaches to estrogen receptor elements on the DNA, then regulates expression of cell proliferation and survival genes [145]. Ligand binding profiles and activities of these two nuclear receptors can alternate, bringing additional considerations into estrogen signaling and cancer mechanisms [125, 146]. On the other hand, binding with GPER1 can induce signal transduction and secondary messengers for transcription machineries. Ion channel modulations, EGFR, Ras-MAPK and PLC/PKC pathways can be accounted for the most

prominent effects transduced by GPER1 [147-150]. Moreover, antioxidant properties of estrogens were acclaimed in the literature as an ER independent action of estrogens [151]. Interestingly, ER β and GPER1 can show activity levels in TNBC as in the *in vitro* model MDA-MB-231 [152-155]. Moreover, these ER subtypes were also evident in an HCC line HepG2 where they did not exert pro-proliferative effects as observed in breast cancer [142, 156, 157]. Accordingly, estrogen signaling presents multifaceted levels of cancer related events where presence and activities of each ER types can vary across and within different cancers [146].

Due to actions of estrogens in breast cancer, ample amount of efforts has been given to modulate the ERs. More specifically, ER α signaling has been the major target of investigations due to profound prevalence exceeding 50% in breast cancer cases and its significance as a subtype marker [158, 159]. In this regard, development of selective estrogen receptor modulators (SERMs), such as tamoxifene, raloxifene, bazedoxifene and losofoxifene have represented improvements in clinics [143, 160, 161]. Yet, side-effect and adverse effect profiles in long-term require progress for toxicity ranges and tissue specificities [162]. In this regard, SERM development strategies shall also consider binding affinities towards abundant ERs across multiple tissues [163-165].

To address selectivity and effectivity issues, indole, benzimidazole and benzene sulphonyl privileged pharmacophores have given promising indications for early phases of preclinical studies. Indole scaffolds in bazedoxifene and ER α /ER β -selective ligands melatonin and KB9520, have shown SERM-like properties [146, 166]. In addition, phenyl indole moieties were implemented to serve as ER ligands [167, 168]. Beside indole moieties, benzimidazole scaffolds were also found to interact with ER. For example, methyl and naphthyl derivations on benzimidazole-based sulfonamides by single positions have revealed alternative binding profiles towards ER α and ER β [169]. In this study, differential cytotoxicity profiles on MCF-7 and MDA-MB-231 were also observable. Similarly, phenyl benzimidazole moieties were able to exert cell type dependent toxicities between MCF-7 and MDA-MB-231 [170]. However, antitumor activities were also observable between HepG2 and MCF-7 for the benzimidazole substitutions by the second position, indicating a lack of tissue specificity [171]. A recent study for indole-benzimidazole hybrid structures have revealed binding affinities towards ER α in nanomolar scale [172]. Relatively active substitutions were observed to contain benzylations by indole, and bromine by benzimidazole scaffolds. Furthermore, breast cancer subtype and tumor type specificities of benzene sulphonyl

pharmacophores were implemented in some studies [173, 174]. Nevertheless, privileged structures can also allow indoles and benzimidazoles to interact with aryl hydrocarbon receptor (AhR), tubulin and microtubule structures, inquiring additional considerations on ER oriented SAR studies [175-180]. Therefore, indole, benzimidazole and benzene sulfonyl moieties emerge as attractive candidates for preclinical drug development strategies in breast cancer.

1.4 Primary liver cancers

The liver tissue is structured into lobules that comprise of mainly hepatocytes, bile ducts, sinusoids (Kupffer cells and endothelium), veins, arteries and connective tissue [181]. Primary liver cancers originate from the liver and top six incidence and mortality rates in cancer belong to primary liver cases, with more predisposition in men that can reach up to 5-folds in comparison with women [181].

Liver cancers and the subtypes are highly heterogeneous and represent malignant profiles [182]. Accordingly, 5-year relative statistics indicate relatively poor (18%) survival and leading to a great demand for better therapeutic options [183]. More than 70% of these cases belong to HCC with high malignancy which arise from hepatocytes originally. Moreover, intrahepatic cholangiocarcinoma (ICC) accounts for 12% of the incidences as they derive from cholangiocytes by the bile ducts [183]. Remaining primary liver cancers are relatively rare cases; angiosarcoma, hemangiosarcoma and hepatoblastoma [184]. Although some histological phenotypes are detectable, Calderaro and multiple lines of studies suggested better prognostic means with molecular signatures [185-188].

1.4.1 Hepatocellular carcinoma (HCC) molecular subtypes

According to EACL, molecular subtypes of HCC strongly influenced the disease management [189]. Initial steps by Hoshida and colleagues have provided two major categories of proliferative (aggressive) and non-proliferative (hepatocyte-like) classes based on the gene set enrichments on molecular pathways and clinical backgrounds [190]. The approach was further supplemented with sub-categories by mutation and epigenetic profiles, as finely curated by Rossi and colleagues (**Figure 1.2**) [191, 192]. Therefore, molecular subtypes and phenotypic signatures of HCC provide an established standpoint for targeted therapies [189, 193, 194].

	PROLIFERATION CLASS		NON-PROLIFERATION CLASS
CELL LINEAGE FEATURES	Progenitor-like	Hepatocyte-like	Hepatocyte-like
PROGNOSTIC GENE SIGNATURES	EpCAM S2 Hepatoblastoma-C2 Hepatoblast-like Cluster A Vascular invasion signature G1-3 / 5-gene signature	Late TGF- β S1	S3 Cluster B WNT / CTNNB1 Poly 7 Immune related G5-6
DNA SOMATIC ALTERATIONS	Chr 11q13 amplif. (FGF19 / CCND1)		CTNNB1 mut. DNA ampl. Chr7
SIGNALING PATHWAY ACTIVATION	NOTCH IGF2 RAS / MAPK MET AKT / MTOR	TGF β Liver-WNT	Classical WNT
EPIGENETIC-BASED SUBTYPES	36 CpG DNA methylation signature miRNA Class C3	miRNA Class C2 (C19MC)	miRNA Class B
CLINICAL FEATURES			

Figure 1.2 Molecular classes and related histological and clinical features of HCCs. *Adapted from Zucman-Rossi J. et al., 2015. Gastroenterology [191]. (License Number 4901951483383 for free copyright permission, title of my thesis is needed)*

Preclinical investigations on HCC should be able to represent actual HCC cases in clinic. Chen and colleagues have shown that almost half of the HCC lines from Cancer Cell Line Encyclopedia (CCLE) do not align with The Cancer Genome Atlas HCC tumor data [195]. HLE, HLF, SNU-449 and JHH-6 lines for example failed to represent the clinical cases. Yet, frequently used and well-differentiated cell lines Hep3B, HepG2 and Huh7 significantly correlated with the tumor data. Therefore, choice of cell lines should be carefully made. Moreover, inclusion of multiple cell lines with known background and genetic alterations can improve the clinical relevance of the preclinical settings [196, 197]. In this regard, Hep3B,

HepG2 and Huh7 have been utilized in preclinical drug screenings often [198-201]. Their differences in gene mutation patterns such as TP53, and in cellular pathways like drug metabolism and TGF β , can be representative for clinical variabilities [197, 198, 202-205]. Moreover, multiple lines of studies have also included SkHep1 cell lines which was presumed to be HCC [206-209]. However, this adenocarcinoma cell line has been precluded from HCC due to endothelial origins [210-212]. Yet, it is still accounted as a primary liver cancer model, hence able to represent the mosaic nature of liver cancers that are responsive to sorafenib and related molecular events [206, 213-215].

1.4.2 Drug therapies in HCC

Targeted therapies hold strong promises for HCC treatment, as molecular profiles can be additionally informative [216]. In this regard, modulation of several targets such as tyrosine kinases, VEGFR, FGFR, PDGFR, RET, KIT, human death receptor 5, Wnt signaling and STAT3, can improve the outcomes [189, 217]. However, strong chemo-resistant profile of HCC leaves out a handful of drug regimes. Even for the advanced cases, first systemic drug, was prescribed only after 2007. This drug was a tyrosine kinase inhibitor compound, sorafenib (SFB) [218]. Another first-line treatment and a multi-kinase inhibitor Lenvatinib and its combination with sorafenib were also found to be successful. Second-line therapies are also in progress, with the applications of another multi-kinase inhibitor regorafenib [219]. However, toxicity profiles of the drugs and side-effects make it necessary to develop better therapeutic options [216, 220].

Heterogeneous nature of HCC can complicate the targeted therapies by single compounds, inquiring a need for combination therapies [221]. Ligands with either mutual or distinctive targeting abilities with SFB were found to be hopeful attempts during clinical trials. Detailed clinical information can be found elsewhere [222-224]. In these regards, MEK/ERK modulators, antiangiogenic factors, PI3K/AKT/MTOR ligands, Wnt signaling agents and HDAC modulators are some of the agents that can be considered. In addition to multi-TKI properties of SFB, reactive oxygen species dependent-ferroptosis is also among the pathways that SFB induces, hence calling for attention [225, 226]. As multidrug resistance is an obstacle for the success of SFB, drug sensitizer regimes with SFB are also of importance [227, 228].

As a result, clinical success of current therapies including SFB has remained limited, due to the complex nature of HCC. Novel therapeutic choices and possible SFB combinations are in demand, as they also require well-informed mechanistic understandings.

1.4.3 Repurposing antipsychotics and phenothiazine derivatives for treatment of HCC

Interestingly, inverse associations between cancer incidence and schizophrenia as well as use of antipsychotic therapies have been noted across several clinical studies [229-233]. Even a phenothiazine derivative, chlorpromazine, has been recently filed for Phase II clinical trials in glioblastoma multiforme [234]. However, this association has remained controversial in the case of liver cancers and HCC since there are both cases that favor the antipsychotics for protective roles or discourage their uses in liver cancer due to hepatotoxicity [235-238]. Moreover, tobacco and alcohol dependence are also both confounding and major factors contributing the liver injury, which has been also annotated for antipsychotics [235-239]. Hence, clinical data need better estimations on scrutinizing the effects of antipsychotics and dependence on the confounding factors. Nonetheless, careful considerations are needed on repurposing these compounds for liver cancer and HCC, because history of tobacco/liver dependence and dosing regimens hold crucial information for the clinical settings [232, 236, 238].

By recent years, repurposing antipsychotic drugs for HCC gained attention for preclinical studies [240]. For example, pimozide has been found to modulate STAT3 and Wnt signaling pathways, resulting in anti-HCC effects in Hep3B, HepG2 and Huh7 cell lines and xenograft studies [241-243]. Another antipsychotic compound fluspirilene can target CDK2 and inhibit HepG2 and Huh7 growth by the G1 phase [244]. Moreover, valproic acid (both antipsychotic and HDAC inhibitor) can stimulate endocytosis of doxorubicin in HepG2, further leading to apoptosis unlike in the normal-like MIHA cells [245]. Furthermore, a cohort-study was also indicative for use of selective serotonin reuptake inhibitors and reduced likelihood of HCC occurrence [246].

1.4.3.1 Phenothiazine (PTZ)

PTZ derivatives are one of the major subjects in drug repurposing strategies for cancer, yet they were scarcely studied in HCC [247].

The derivatives have been originally prescribed for schizophrenia, bipolar disorder and psychiatric conditions via modulation of dopaminergic signaling [248]. The privileged PTZ structure has allowed the derivatives to interact with multiple targets: D2, D4, cholinergic

receptors, AChE, BChE, MRP1, HDAC, BCL-2, CBs, CaM and FOXO1 [249-257]. Therefore, varying levels of anti-cancer effects were also found to propagate through Wnt, MAPK, Akt, p38 and ERK pathways, followed-up with TP53 and p21 related cell-cycle and/or cell-death mechanisms [247, 258-262]. Moreover, oxidative stress, ferroptosis and lipid metabolism are among the recently inferred pathways modulated upon exposure to PTZ derivatives in various cancer lines [263-266]. Interestingly, actions of the derivatives were also found to relate with multiple drug resistance (MDR) where they can modulate the MDR activities by reducing the rate of drug efflux *in vitro* and *in vivo* [267-271]. Furthermore, combination of the derivatives with standard cancer drugs have suggested improvements on the anti-cancer effects in multiple cancer lines [260, 272-276]. Therefore, anti-cancer potentials of phenothiazines, combination therapies and detailed mechanistic understandings have been subjects for preclinical assessments.

Originally pharmacodynamic features of the derivatives have been annotated as antidopaminergic, antihistaminergic, antiserotonergic, antiadrenergic and anticholinergic, as they can also exert dose-dependent activity levels [269, 277-279]. Moreover, activation of the cholinergic receptors is known to strongly relate with oncogenic processes as suggested by several lines of studies [280-283]. In addition, isoforms of dopaminergic receptors and their activities have been related with cancers in a subtype and dose-dependent manner [281]. Interestingly, a dopamine receptor agonist fisetin was shown to counteract the liver tumor progress, but whether the effect was due to dopaminergic receptor activity or due to additional target modulations, remain to be addressed [284]. Besides varying degrees of mRNA level changes on dopaminergic receptors, the phenothiazine derivative thioridazine was able to reduce the tumorigenesis *in vivo* [285]. Yet, again causality of the dopaminergic regulation requires thorough examinations. Furthermore, cholinergic stimulus on the dopaminergic system also brings about additional considerations on the activities of phenothiazine derivatives [286, 287]. However, the crosstalk has been mainly accounted within the proximities of the central nervous system, suggesting involvement of alternative mechanisms for pathologies like liver cancer.

Intriguingly, acetylcholinesterase (AChE) activity levels have been found to strongly relate with chemosensitivity of HCC, as supplementary acetylcholine was able to trigger cancer cell proliferation [288]. In addition, levels of AChE have been good prognostic factors for SFB therapies in HCC cases, further implying functional roles for the cholinergic system in HCC

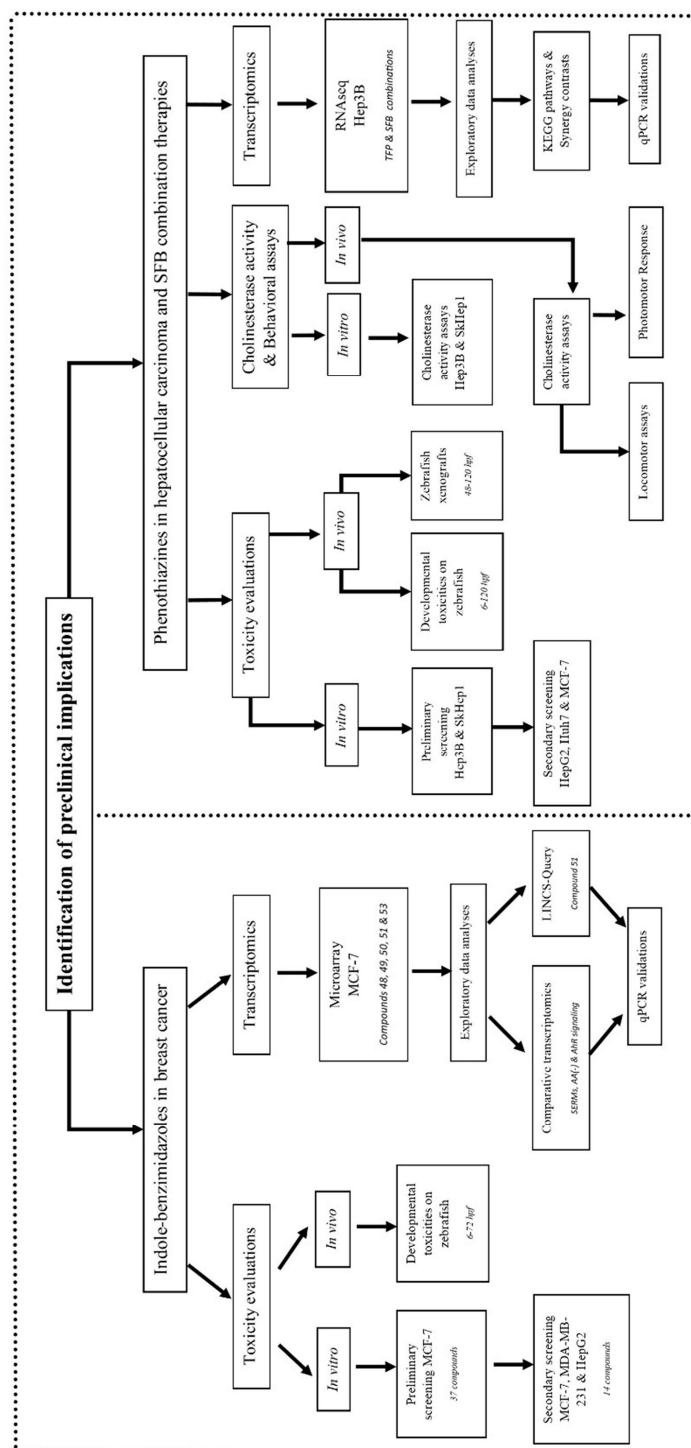
[289, 290]. Therefore, the phenothiazine derivatives with enhanced cholinergic system modulatory activities can become useful in HCC therapies.

Anti-HCC potential of the derivatives has been barely studied. Aptitudes of the derivatives for HCC were firmly interpreted by “Encyclopedia of Hepatocellular Carcinoma genes Online 2” platform. Hence, chlorpromazine (CPZ) and trifluoperazine (TFP) emerged as potential HCC compounds from a Connectivity Map (CMap) based analyses, as they were subsequently shown to obscure HCC tumor progress in HCC mouse xenografts [291]. Moreover, cytotoxic potentials of prochlorperazine (PCP) were also recorded on two HCC lines (HepG2 and Mahlavu) and non-HCC liver cancer line SkHep1 [292]. Another derivative thioridazine has supplemented these findings where cell cycle arrest, decreased levels of stemness genes and low tumor progress were observed in HCC xenografts [285]. Moreover, anti-cancer effects were also noted in Huh7 and HepG2 cell lines upon exposures to PTZ derivatives in a cell-type and compound dependent manner in separate studies [293-295]. Nevertheless, proliferative effects of low-doses of TFP in glioma cells have also suggested a need for better understanding on the dose-dependent effects of the derivatives [296].

To sum up, *in vitro* and *in vivo* studies on antipsychotics and phenothiazines have been strongly in favor of their repurposing towards multiple cancer types and HCC. Yet, clinical translation also is in demand for careful assessments on the history of the patients and to no-observed-adverse-effect-levels (NOAEL). Hence, there is a need for thorough understanding on the mechanisms, structure and dose-dependent activities across heterogeneous HCC profiles, which can be initially addressed via *in vitro* and *in vivo* studies [296, 297].

CHAPTER 2: OBJECTIVES AND RATIONALE

The workflow for the approaches followed during the thesis is provided in the **Scheme 2.1**.



Scheme 2.1 Workflow of the thesis studies

Preclinical studies of novel indole-benzimidazoles synthesized by Ankara University: *In vitro* and *in vivo* zebrafish models

- 1) To analyze the cell line, dose and drug dependent anti-cancer effects of novel indole-benzimidazoles using n-way ANOVAs and multivariate statistics both *in vitro* and *in vivo* as a complement to IC₅₀ measurements
- 2) Using GRcalculator and GRcalculator derived IC₅₀ values to firmly integrate the structural properties of novel derivatives together with their biological activities to obtain SARs and to have lead molecules
- 3) Perform *in vivo* studies using zebrafish embryonic toxicity model and develop a multivariate PCA based test for deciphering molecule effects
- 4) Perform and analyze microarray studies for the lead molecules and compare them with existing datasets to identify MoAs.

Repurposing generic phenothiazines in combination with SFB for HCC therapy

- 1) Screen generic phenothiazines at different doses for their anti-cancer activity in hepatoma cells, Hep3B, liver specific endothelial cancer cells SkHep1 and MCF-7 breast cancer cell line to identify IC₅₀ values.
- 2) Perform synergy screens with SFB, the most commonly used HCC drug, to increase anti-cancer activity in cell lines
- 3) Perform synergy screens with SFB in zebrafish embryonic toxicity model
- 4) Understand the pathways modulated by TFP, SFB and TFP+SFB combination in Hep3B cells in which SFB and TFP synergized using RNAseq and qPCR analyses
- 5) Analyze effects of generic molecules alone or in combination to motor responses as a mean of assessing toxicity
- 6) Test effects of the generic compounds on xenografts in zebrafish

Preclinical studies of novel phenothiazines synthesized by Ankara University

- 1) Screen novel phenothiazines for their anti-cancer activity in different HCC cell lines and calculate IC₅₀ values and test for cell line and time effects.
- 2) Perform high throughput toxicity assays and xenografts in zebrafish model for preclinical purposes
- 3) Perform synergy screens with SFB for selected lead molecule PD-5
- 4) Analyze effects of generic and novel derivative doses on AChE activity levels
- 5) Develop an analysis routine and software for larval movement

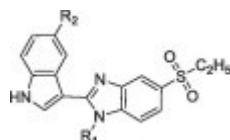
CHAPTER 3: MATERIALS AND METHODS

3.1 Materials

3.1.1 Screened novel and known molecules

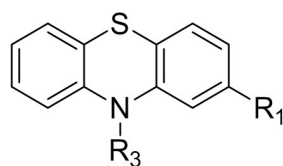
Indole-benzimidazole derivatives were synthesized by Ankara University as an action for TUBITAK 1001-213S037 project. List of derivatives are given in the **Table 3.1**.

Table 3.1 Codes and R₁ and R₂ designations of novel indole-benzimidazole structures



No	R ₁	R ₂	No	R ₁	R ₂	No	R ₁	R ₂
23	-H	-H	36	-C ₃ H ₇	-Br	49	-p-fluorobenzyl	-OCH ₃
24	-H	-Br	37	-C ₄ H ₉	-H	50	-p-fluorobenzyl	-Cl
25	-CH ₃	-H	38	-C ₄ H ₉	-Cl	51	-p-fluorobenzyl	-Br
26	-CH ₃	-OCH ₃	39	-C ₄ H ₉	-Br	52	-3,4-difluorobenzyl	-H
27	-CH ₃	-Cl	40	-cyclohexyl	-H	53	-3,4-difluorobenzyl	-OCH ₃
28	-CH ₃	-Br	41	-cyclohexyl	-OCH ₃	54	-3,4-difluorobenzyl	-Cl
29	-C ₂ H ₅	-H	42	-cyclohexyl	-Cl	55	-3,4-difluorobenzyl	-Br
30	-C ₂ H ₅	-OCH ₃	43	-cyclohexyl	-Br	56	-3,4-dichlorobenzyl	-H
31	-C ₂ H ₅	-Cl	44	-benzyl	-H	57	-3,4-dichlorobenzyl	-OCH ₃
32	-C ₂ H ₅	-Br	45	-benzyl	-OCH ₃	58	-3,4-dichlorobenzyl	-Cl
33	-C ₃ H ₇	-H	46	-benzyl	-Cl	59	-3,4-dichlorobenzyl	-Br
34	-C ₃ H ₇	-OCH ₃	47	-benzyl	-Br			
35	-C ₃ H ₇	-Cl	48	-p-fluorobenzyl	-H			

Phenothiazine (PTZ), perphenazine (PPH), prochlorperazine (PCP), trifluoperazine (TFP) were commercially obtained (**Table 3.2**). Remaining novel derivatives labeled PD-1 to PD-30 were synthesized by Ankara University as an action for TUBITAK 1001 – 116Z388 project and are proprietary and unpublished therefore no structure is provided herein.

Table 3.2 Codes and R₁, R₂ and R₃ designations of generic phenothiazines

	R₁	R₃
PTZ	-H	-H
PPH	-Cl	
PCP	-Cl	
TFP	-CF ₃	

3.1.2 Cell culture reagents

Reagents given in **Table 3.3** were utilized in cell culture experiments

Table 3.3 Cell culture reagents used in the studies

Dulbecco's Modified Eagle Medium (DMEM)	BE12-707F	Lonza
Dulbecco's Modified Eagle Medium (DMEM) w/o phenol red	11880028	GIBCO
Opti-MEM Reduced Serum Medium	31985070	GIBCO
PBS	BE17-516F	Lonza
FBS	S181G-500	Biowest
NEAA	BE13-114E	Lonza
Na Pyruvate	BE13-115E	Lonza
Penicillin - Streptomycin	DE17-602E	Lonza
L-glutamine	BE17-605E	Lonza
Trypsin-Versene	BE17-161E	Lonza

3.1.3 Zebrafish culture materials, equipment and reagents

E3 medium (60X): 17.2 gr NaCl (Sigma Aldrich 13423), 0.76 gr KCl (Sigma Aldrich 12636), 2.9 gr CaCl₂ (Carlo Erba 327607) and MgSO₄ (Sigma Aldrich M2773) in 1-liter milli-Q H₂O). Additional 1 ml of 0.01% methylene blue (Fluka Chemical 66720) in 1X and 1L of E3 medium in Bilkent University zebrafish facility conditions.

Tricaine stock (4 mg/ml, pH:7.5) was prepared by adding 400 mg tricaine, 2 ml Tris pH 9.0 into 98 ml dH₂O as pH was later adjusted to 7.5. For working solution of anesthesia 1:25 dilution ratio was applied in E3 medium.

3.1.4 Equipment

List of equipments used throughout the studies are provided in the **Table 3.4**

Table 3.4 Equipment used in the studies

LightCycler 480 Instrument	Roche (Switzerland)
μQuant Universal Microplate Spectrophotometer	BioTek (USA)
Thermal cycler TC-512	Techne (UK)
NanoDrop ND-1000	Thermo Scientific (USA)
MZ10F microscope	Leica (Germany)
DMi8 microscope	Leica (Germany)
Leica Application Suite v4.7	Leica (Germany)
Aixio Imager	Zeiss (Germany)
DPcontroller (v3.3.1.292)	Olympus (Japan)

3.1.5 Kits and supplements

Kits and supplements used throughout the studies in the studies are provided in the **Table 3.5**

Table 3.5 Kits and supplements used in the studies

Nuclease free H ₂ O	SH30538.01	HyClone (USA)
LightCycler® 480 SYBR Green I Master	4887352001	Roche (Switzerland)
LightCycler 480 Multiwell Plate 96, White	4729692001	Roche (Switzerland)
RNase-Free DNase Set (50)	79254	Qiagen (Germany)
RevertAid First Strand cDNA Synthesis Kit	K1622	Fermentas (Canada)
MTT	M6494	Invitrogen (USA)
RNeasy Mini Kit	74104	Qiagen (Germany)
SDS	71725	Sigma-Aldrich (Germany)
HCl	7102	Sigma-Aldrich (Germany)
HEPES	H-1016	Sigma-Aldrich (Germany)
Sodium chloride	31434	Sigma-Aldrich (Germany)
EGTA	A0878	AppliChem (Germany)
Glycerol	15524	Sigma-Aldrich (Germany)
Triton X100	T8787	Sigma-Aldrich (Germany)
Phosphatase inhibitor (Phosstop Easypack)	4906845001	Roche (Switzerland)
EDTA-free protease inhibitor (cOmplete)	11873580001	Roche (Switzerland)

Geneticin (G418) sulfate	sc-29065A	ChemCruz (The Netherlands)
Lipofectamine 2000	11668027	Invitrogen (USA)
QIAzol lysis reagent	79306	Qiagen (Germany)
EtOH	B2221	Sigma-Aldrich (Germany)
BCA Protein Assay kit	23227	Thermo Scientific (USA)
Chloroform	24216	Sigma-Aldrich (Germany)
Pierce BCA Protein Assay kit	23227	Thermo Scientific (USA)
Acetylcholinesterase Assay Kit (Colorimetric)	ab138871	ABCAM (UK)
2-propanol	24137	Sigma-Aldrich (Germany)
Dimethyl sulfoxide (DMSO)	A1584	Applichem (Germany)
mEGFP-N1	Plasmid #54767	Addgene (USA)
Sorafenib	Catalog No. S7397	Selleckchem (USA)
Phenothiazine	P14831-25G	Sigma-Aldrich (Germany)
Perphenazine	P6402-1G	Sigma-Aldrich (Germany)
Prochlorperazine	P9178-5G	Sigma-Aldrich (Germany)
Trifluoperazine	T8516-5G	Sigma-Aldrich (Germany)
Camptothecin	C9911	Sigma-Aldrich (Germany)
Tris hydrochloride	T3253	Sigma-Aldrich (Germany)

3.1.6 qPCR primers

List of primers are given in the **Table 3.6**.

Table 3.6 List of primer pairs used throughout the qPCR studies

Genes	Primer sequences	Amplicon size (bp)	Species	Associated KEGG pathways
TPT1	5'-GATCGCGGACGGGTTGT-3' 5'-TTCAGCGGAGGCATTTC-3'	100	<i>H. sapiens</i>	Microtubule stability (Housekeeping gene)
HMGCR	5'-TATCCGTTTCCAGTCCAGGT-3' 5'-GCTGGAATGACAGCTTCACA-3'	210	<i>H. sapiens</i>	Cholesterol metabolism
SQLE	5'-CGTGAATATCCTTGCTCAGGC-3' 5'-AGACAATACAGAAAGCAGCCCA-3'	145	<i>H. sapiens</i>	Cholesterol metabolism
SRSF7	5'-GGTCTAGATCACATTCTCG-3' 5'-CCAGACCTAGATCTTCTG-3'	154	<i>H. sapiens</i>	RNA processing & DNA replication
NOC3L	5'-ACCCAAAGGAAAAGCGACCA-3' 5'-CGCATGAACAGGCTCACTAGA-3'	170	<i>H. sapiens</i>	RNA processing & DNA replication
NIP7	5'-GGTGTACTATGTGAGTGAGAAGA-3' 5'-GCACCAGGCTTTATCCAAAC-3'	180	<i>H. sapiens</i>	RNA processing & DNA replication

Table 3.6 List of primer pairs used throughout the qPCR studies (<i>Cont'd</i>)				
Genes	Primer sequences	Amplicon size (bp)	Species	Associated KEGG pathways
LSS	5'-GGCGCTTAAGTATTTCCACAA-3' 5'-AACTCTAAGCCCTGCGTGAG-3'	81	<i>H. sapiens</i>	Cholesterol metabolism
CCNE1	5'-GCCAGCCTTGGGACAAT-3' 5'-CTTGACGTTGAGTTTGG-3'	104	<i>H. sapiens</i>	Cell cycle
CCNE2	5'-GTAGCTGGTCTGGCGAGGTTT-3' 5'-GGGCTGCTGCTTAGCTTGTA-3'	83	<i>H. sapiens</i>	Cell cycle
MKI67	5'-GTGTCAAGAGGTGTGCAGAA-3' 5'-GCCTTACTTACAGAATTCAC-3'	197	<i>H. sapiens</i>	Cell cycle & proliferation
CHEK1	5'-TGGTCACAGGAGAGAAGGCA-3' 5'-CAGATAAACCACCCCTGCCA-3'	151	<i>H. sapiens</i>	Cell cycle, DNA damage & apoptosis
ANLN	5'-TAAAGCAGGTGATTGTTCCGG-3' 5'-GTTCTTCATCAACACAGCAG-3'	180	<i>H. sapiens</i>	Cell cycle & Cytoskeleton
WDHD1	5'-AGCAGCCAAGGACGAGTAAA-3' 5'-CTTCGGCTTTGGAATCAGAG-3'	192	<i>H. sapiens</i>	Cell cycle
CDC6	5'-AGTCAGATGTCAAAAGCCAGACT-3' 5'-TTGGCTCAAGGTCATCCTGTTA-3'	146	<i>H. sapiens</i>	Cell cycle
CDKN1A	5'-GTCACTGTCTTGTACCCTTGTG-3' 5'-CGGCGTTTGGAGTGGTAGAA-3'	228	<i>H. sapiens</i>	Cell cycle, E2 signaling
RRM2	5'-TCCGGTTCTTTTGCATCGAT-3' 5'-TCCGATGGTTTGTGTACCAGG-3'	149	<i>H. sapiens</i>	Cell cycle, DNA repair, drug metabolism and amino acid metabolism
CCND1	5'-CTGCGAAGTGGAACCATCC-3' 5'-GCACTTCTGTTCCTCGCAGA-3'	199	<i>H. sapiens</i>	Cell cycle, E2 signaling, stress pathways
SLC7A11	5'-TCTTTGTTGCCCTCTCCTGC-3' 5'-GCTGGTAGAGGAGTGTGCTT-3'	142	<i>H. sapiens</i>	Ion channels, ferroptosis and stress pathways
DDIT3	5'-GTTAAAGATGAGCGGGTGGC-3' 5'-TGGATCAGTCTGGAAAAGCACA-3'	132	<i>H. sapiens</i>	DNA damage/repair and stress pathways
GADD45A	5'-TCTCGGCTGGAGAGCAGAAGAC-3' 5'-AGCTTGGCCGCTTCGTACAC-3'	121	<i>H. sapiens</i>	DNA damage/repair and stress pathways
HMOX1	5'-GCCAGCAACAAAGTGCAA-3' 5'-GAGTGTAAGGACCCATCGGA-3'	105	<i>H. sapiens</i>	Iron metabolism
MCM10	5'-GTGCGCCTATACCCACTTCA-3' 5'-CCGTCCCGTTCCATTTGTA-3'	180	<i>H. sapiens</i>	DNA damage/repair
CYP1B1	5'-AACGTACCGGCCACTATCAC-3' 5'-TCACCCATACAAGGCAGACG-3'	167	<i>H. sapiens</i>	Drug metabolism, amino acid metabolism
PGR	5'-GGAGGAGGAGGGAGGTATCA-3' 5'-CTGCTTGAAGACTCAGGGA-3'	210	<i>H. sapiens</i>	E2 signaling

Table 3.6 List of primer pairs used throughout the qPCR studies (<i>Cont'd</i>)				
Genes	Primer sequences	Amplicon size (bp)	Species	Associated KEGG pathways
TFF1	5'-CCATGGAGAACAAGGTGATCTGC-3' 5'-TTAGGATAGAAGCACCAGGGGAC-3'	208	<i>H. sapiens</i>	E2 signaling
AARS	5'-GAGTTGCTGGATGACCCCTC-3' 5'-GGCTTCTTCCGTCACGATCA-3'	120	<i>H. sapiens</i>	Amino acid metabolism
AQP3	5'-GGGACCCTCATCCTGGTG-3' 5'-GGTTGATGGTGAGGAAACCA-3'	91	<i>H. sapiens</i>	Ion channels
KCNS3	5'-GAGCGGAGCTAGCTGGATG-3' 5'-GGCCAAAAGAAGGGAAGAA-3'	108	<i>H. sapiens</i>	Ion channels
CLIC3	5'-ACCAAGCTCCAGCTGTTTGT-3' 5'-GAGGAGCAGGACCATGAAGA-3'	93	<i>H. sapiens</i>	Ion channels
SLC6A14	5'-TGGAGAGCTTGCTGGTTTGT-3' 5'-CCAGCCTAAAGCAACTCCCC-3'	129	<i>H. sapiens</i>	Ion channels
<i>aars</i>	5'-AGAGGAATGGGGGTCGATCT-3' 5'-TCATCTCCAGAGCCTTTGCC-3'	86	<i>D. rerio</i>	Amino acid metabolism
<i>rrm2</i>	5'-GATGAGGGTCTTCATTGCGAC-3' 5'-ATCAGGTCACAGTTCATGCCA-3'	167	<i>D. rerio</i>	Cell cycle, DNA repair, drug metabolism and amino acid metabolism
<i>b2m</i>	5'-TTCTTTGTCTGCTGTACACTG-3' 5'-TGCTTGGTGTCCGACATAAC-3'	184	<i>D. rerio</i>	Immune system (Housekeeping gene)

3.2 Methods

3.2.1 Cell culture methods

3.2.1.1 Maintaining and handling the cell lines

Breast cancer lines MCF-7 and MDA-MB-231 and hepatocellular carcinoma lines HepG2, Hep3B, SkHep1 and Huh-7 were used throughout the cell culture studies.

Cell lines were grown in complete DMEM/Low-Glucose containing 10% fetal bovine serum, 1% penicillin-streptomycin, 1% non-essential aminoacid, 2% l-glutamine and 1% Na-Pyruvate under the incubator conditions of 37 °C and 5% CO₂.

Passaging of the cell lines were performed as the cell culture reaches to 80%-90% confluency. For this purpose, the medium is removed, and the culture was washed with PBS (Lonza). Afterwards, the culture was exposed to Trypsin-Versene for 5 min at 37 °C. Following that, cells were mixed with complete DMEM thoroughly and seeded onto new culture plates to obtain new generations.

For long-term preservation of the cell lines, the cells were thawed at 1500 rpm for 5 minutes after the trypsinization and DMEM resuspension steps. Then, the supernatant was replaced with 2 ml freezing medium containing sterile FBS and DMSO. Following a brief pipetting the mixture was transferred to cryovials and consecutively kept at -20 °C (5 min), -80 °C (24 hours) and liquid nitrogen (for long term storage).

3.2.1.2 eGFP transfections in obtaining monoclonal Hep3B and SkHep1 lines

Initially cell lines were seeded into 24-well plates (20000 cells/well) with complete DMEM (w/o pen/strep). After 24 hours, transfection master mixes were prepared. For that, 0.5 µl of either lipofectamine or mEGFP-N1 constructs were kept in separate tubes each containing 50 µl of Opti-MEM for 5 min. Then the complex formation was proceeded for 20 min by mixing the lipofectamine and eGFP containing medium together. Afterwards, the complex was added onto the cells with freshly renewed medium (0.5 ml complete DMEM (w/o pen/strep)) and kept for 3 hours. Then, the media was renewed, and the cells were let to grow for 3 days without any antibiotics. As the cells grow by the third day, media was refreshed with appropriate concentrations of geneticin (Hep3B: 500 µg/ml; SkHep1: 900 µg/ml) to obtain polyclonal eGFP containing cells.

Relevant geneticin concentrations for each line were derived from kill curve assays on the naive cell lines. Here, briefly, Hep3B and SkHep1 were seeded onto 96-well plates (5000 cells/well) and exposed to varying active concentrations of geneticin (0-1000 µg/ml) for 3 days and 7 days to obtain optimal concentrations that kill the cells 100%.

Monoclonal eGFP bearing lines were further selected from polyclonal lines by applying serial dilutions of cells through 96-well plates as described by Ryan JA (2008) [298]. Single cell colonies were taken under careful examination daily by recording eGFP status on each well. eGFP positive colonies were further scaled up by passaging into larger surface areas (6-well plates and T75 flasks, respectively)

3.2.2 Zebrafish culture methods

Relevant methodologies were followed in compliance with Bilkent University Ethical Committee approvals (2015/15 & 2016/7) and Karlsruhe Institute of Technology institutional guidelines.

3.2.2.1 Breeding setups and maintenance of embryos

Adult fish were grown in 27.5 - 28.4 °C system water (pH: 7.4) with 14 hours of day and 10 hours of night periods. Wildtype AB (+/+) strain were utilized for breeding purposes. For that, parent fish 2 male and 2 females were settled in breeding tanks overnight. By the next morning, separator blocks from the opposite sexes were removed for allowing the reproduction. Embryos were then collected and maintained in 1X E3 medium at 28 °C. Embryos were euthanized on ice before 6 days post fertilization (6 dpf)

3.2.2.2 Generations of xenografts and tumor growth measurements

SkHep1^{eGFP} lines were collected by trypsinization of the cell culture (300 cells/embryo). After the collection, the cell pellet was obtained by centrifugation (1500 rpm for 3 min). Supernatant media was replaced with 500 µl PBS per 3x10⁶ cells, resuspended thoroughly and centrifuged for 1 min at 5000 rpm. Then, the supernatant was removed, the cells were mixed with 25 µl PBS by avoiding bubble formations and kept at 37 °C for 20 min. After centrifugation for 1 min at 5000 rpm the pellet was mixed with 500 µl FBS. Following that, the suspension was centrifuged for 1 min at 5000 rpm and washed with 500 µl PBS thrice. By the last centrifugation supernatant was replaced with 5 µl Phenol red + 95 µl PBS mixture.

Manually dechorionated embryos were anesthetized in E3 medium with tricaine (0.4 mg/ml) and 300 cells was microinjected to the yolk of each 48 hpf embryo. The medium was renewed without tricaine and injected embryos were kept at 32 °C further on. After 8 hours, eGFP positive embryos were maintained for experimental purposes. Fluorescence. Hence, tumor growth and status of the embryos were checked under Leica MZ10F microscope with GFP filter and imaged by using DPcontroller (v3.3.1.292) suite. Xenograft experiments concerning the compounds PD-3, PD-5, PD-28 and PD-29 were done together with Bilkent University MSc student Büşra Korkmaz where culturing and grafting of the embryos were performed on her behalf.

Tumor growth was further measured via ImageJ 1.50i by taking Corrected Total Cell Fluorescence (CTCF) levels into account as described by Jakic B. et al. (2017) [299]. Briefly, IntegratedDensity measures were subtracted from the multiplication of the selected area and background fluorescence levels, to calculate CTCF. Statistical meanings of the effects were evaluated by one-way ANOVA/Bonferroni tests in GraphPad Prism (v6.01).

3.2.3 MTT cytotoxicity assay and toxicity measurements on the cell lines

Toxicity of the compounds on the *in vitro* lines were assessed via MTT assay. After trypsinization the cells were seeded into 96-well plates (10000 cells/well and 5000 cells/well for 24 hour and 48-hour exposures, respectively) and kept for 24 hours before the treatments. After the exposures for given times the wells were washed with PBS and media were renewed with phenol free medium (100 μ l/well). Onto the medium 5 mg/ml MTT (3-(4,5-dimethylthiazol-2-yl)-2,5-diphenyltetrazolium bromide) in sterile PBS was added (10 μ l/well) and let for the formations of formazan crystals for 4 hours at 37 °C. Afterwards, 0.1 gr/ml SDS- (0.01 M) HCl solution was added on top of each well (100 μ l/well) and kept at 37 °C overnight. OD₅₇₀ readings for each well later collected via Microplate Spectrophotometer (μ Quant, Biotek). Relative cell viability ratios were calculated by initially correcting for blank values for each well and then by dividing with the corrected 0.1% DMSO control group OD₅₇₀ scores. Each MTT assay was executed with biological triplicates for each group where concentration of exposure contained fixed DMSO percentile (0.1%) and exposures were renewed daily.

Exposure to indole-benzimidazoles was initially carried out by applying four different concentration points (0.25 μ M, 2 μ M, 16 μ M and 40 μ M). Candidate compounds with relatively high toxicity levels were taken for secondary MTT assay screenings with MCF-7, MDA-MB-231 and HepG2 along with 8 concentration points (0.25 μ M, 2 μ M, 4 μ M, 8 μ M, 10 μ M, 12 μ M, 16 μ M and 40 μ M). CPT was used as positive control throughout the experiments and each exposure took place for only 24 hours.

Preliminary phenothiazine derivative exposures were performed with four concentration points (3.7 μ M, 11.1 μ M, 33.3 μ M and 100 μ M) on Hep3B and SkHep1 cell lines. In this setup for the two cell lines (and for their eGFP monoclonal), the MTT assays for the compounds PD-9, PD-10, PD-11, PD-12, PD-13, PD-14, PD-15, PD-16, PD-17, PD-18 and PD-19 were done by Clinical Pharmacist and Post-doctoral fellow Omer Bayazeid (Hacettepe University / Ankara). Promising candidates were then screened on HepG2, Huh7 and MCF-7 lines with the same concentration scale. SFB was used as the positive control (3.7 μ M and 11.1 μ M). Each screening was done for 24 hours of exposures. Additionally, PTZ, PPH, PCP, TFP, PD-3, PD-4, PD-5 and PD-6 were also screened for 48 hours with the same concentration scheme. Hep3B^{eGFP} monoclonal validations of these eight compounds (24 h) were also pursued in collaboration with Omer Bayazeid.

SFB combination exposures were also performed with the phenothiazine derivatives. For that, TFP, PCP and PD-5 were screened in combination with SFB on Hep3B, for 24 h and with 1:1 concentration dilution where maximum concentration for each compound is 50 μ M. In addition to that, a time series TFP-SFB combination experiments were performed on Hep3B, SkHep1, HepG2 and Huh7 lines with the same dilution scheme, yet 25 μ M as the maximum concentration for each compound. Synergism maps were further generated from viability percentiles for each concentration by using SynergyFinder tool (Bliss-LOESS parameters) [63].

In the case of indole-benzimidazoles, dose-response curves and IC_{50} values were obtained via GRcalculator tool by applying sigmoidal fits and capping GR values below 1, allowing group comparisons via one-sided Wilcoxon rank sum-test [300]. GRcalculator derived IC_{50} scores were additionally evaluated with the IC_{50} values previously obtained by GraphPad Prism (v6.01) – “log(inhibitor)-three parameters” (Fikriye Zengin, PhD Thesis, 2019). For the comparisons, Pearson’s correlations were calculated by using the $\log_{10}IC_{50}$ values from both tools as the IC_{50} ’s within the MTT assay concentration ranges were subjected to secondary Pearson’s correlation analyses. In contrast, phenothiazine derivative dose-responses and IC_{50} estimations were performed via GraphPad Prism (v.6.01) using “log(inhibitor)-four parameters” option. In case of inept IC_{50} interpolations, “log(inhibitor)-three parameters” option was referred. To assess the effects of treatments, cell line and possible interactions, \log_2 scaled viability scores from biological triplicates or the $\log IC_{50}$ scores were analyzed through n-way ANOVA. Additionally, t-tests were utilized in comparing two respective groups with each other. PCA was performed on comparing dose responses of cell lines for the exposures. Cell viability values for each concentration group and cell line were further analyzed with two-way ANOVA/Tukey in GraphPad Prism (v6.01). Moreover, dose-curve shifts upon combination treatments were proceeded with EC50 shift fitting option in GraphPad Prism environment. Accordingly, viability scores for each concentration were analyzed by two-way ANOVA/Dunnett and multiple t-tests/Holm-Sidak statistics.

3.2.4 Embryonic toxicity assessments in zebrafish

Developmental toxicities of the indole-benzimidazole derivatives 48, 49, 50 and 51 were performed on AB strain zebrafish embryos in Bilkent University. For that, 10-11 embryos per group were used with two biological replicate setups as the embryos were exposed to 20 μ M of compounds between 6 hpf and 72 hpf. Morphometric values: dorsoventral axis, rostro-caudal axis, yolk size and eye diameter, were measured and multivariate analyses were

applied via PCA in assessing developmental toxicities. In addition, hatching percentiles by 48 hpf were collected to supplement the toxicity data.

Time dependent embryonic toxicity experiments for PTZ derivatives were performed in Karlsruhe Institute of Technology (KIT) with AB line zebrafish for phenothiazine derivatives mainly. Media renewal was performed daily. For imaging and toxicity evaluations, ZEISS Axio Imager microscopes and ImageR applications were utilized in addition to authenticated softwares and automated platforms. Embryos were exposed to the derivatives, between 6 hpf and 120 hpf. On average 12 embryos/group was used for each concentration exposure between 0-40 μ M. Toxicity values were referred by calculating affected embryo ratios. For that purpose, counts for dead, abnormal or chorionated embryos were divided by initial counts of embryos at 6 hpf and then normalized to the non-affected embryo ratios of the 0.5% DMSO control groups. Obtained values were further used in deriving dose-response curves and EC₅₀ values via GraphPad Prism (v6.01). For the screening of TFP compound, 6 hpf-72 hpf data were used.

In assessing *in vivo* combination screenings with SFB, generic derivatives (PTZ, PPH, PCP, TFP) and in-house derivatives (PD-3, PD-5 and PD-9) were used, for 48 hpf-120 hpf exposures by calculating affected embryo ratios with respect to 0.5% DMSO control group. As the concentration scale for the derivatives was 0-20 μ M, whereas 0-4 μ M scale was used for SFB concentrations. 4 embryos/group were studied for the combination screenings. Synergistic and antagonistic nature of the combinations were examined via SynergyFinder tool (Bliss-LOESS parameters).

In the Bilkent University *in vivo* experiments, E3 medium was supplied with methylene blue

3.2.5 mRNA isolation and cDNA synthesis

RNeasy kit (QIAGEN) was used for RNA isolation from the *in vitro* samples with biological duplicates according to manufacturer's instructions. For the zebrafish samples, in-house mRNA isolation protocol was followed, and each step was carried out at 4 °C unless mentioned otherwise. Firstly, media was replaced with 700 μ l for each biological replicate group (11 embryo/group). Following that, each sample containing tube was homogenized on ice via syringes. Afterwards, 200 μ l chloroform was added onto samples. After 3 min, the mixture was centrifuged at 13000 rpm for 17 min. Supernatant from each tube was collected and briefly mixed with 200 μ l 2-propanol. After 10 min incubation at room temperature, samples were centrifuged at 13000 rpm for 12 min (4 °C). Then, the pellet was mixed with 1

ml 75% EtOH, centrifuged at 8000 rpm for 8 min. Moreover, the pellets were mixed with 1 ml 100% EtOH and centrifugation process was applied at 8000 rpm for 8 min. By the end, the pellet was air-dried and mixed with 20 μ l nuclease free water, hence the RNA samples were obtained.

RNA sample amounts were further obtained via NanoDrop ND-1000. 1 μ g RNA for each sample and oligo(dT)₁₈ primers were used in obtaining cDNAs by using RevertAid first strand cDNA synthesis kit (Fermentas) according to manufacturer's instructions.

3.2.6 qPCR experiments and relative gene quantity measurements

Firstly, qPCR reaction mix for each gene was prepared. For this purpose, 20 ng cDNA (1 μ l), 10 μ M gene specific forward and reverse primers (1 μ l each), 1 μ l nuclease free H₂O and 5 μ l LightCycler® 480 SYBR Green I Master mix was used in obtaining reaction mix (10 μ l/well). Then, the mixture was distributed along the LightCycler 480 Multiwell Plate 96 White. For each group technical duplicates were used in addition to TPT1 and b2m as the housekeeping genes for human and zebrafish lines, respectively. Afterwards, the plate was carefully enclosed with cover slips and centrifuged for 2 min at 1000 rpm.

Following these steps LightCycler® 480 Instrument and LightCycler® 480 software (1.5.1.62) were utilized in executing chain reaction cycles and the parameters are as given in **Table 3.7**.

Table 3.7 qPCR parameter used for reaction cycles

Cycles	Steps	Temperature (°C)	Duration	Acquisition mode	Ramp rate (°C/sec)
1	Pre-incubation	95	5 min	None	4.4
40-50	Denaturation	95	10 sec	None	4.4
	Annealing	57-61	20 sec	Single	2.2
	Extension	72	20 sec	None	4.4
1	Melt curve genotyping	95	5 sec	None	4.4
		55	1 min	None	2.2
		95	Nondetermined	Continuous (Acquisition per °C = 5)	0.11
1	Cooling	40	30	None	2.2

Ct values were later utilized in deriving relative quantity (RQ) amounts for each specific gene and exposure group. $\Delta\Delta$ Ct calculations were performed by Yuan JS et al. (2006) as in the Equation 1 and Equation 2. Later, the RQ values were represented on the log₂ scale [301].

3.2.7 Protein collection and measurements

Protein collection steps took place at 4 °C unless mentioned otherwise. Later, measurements on protein levels were followed with BCA protein assay by referring the manufacturer's instructions.

Collection of the cells in cold PBS were centrifuged for 1500 rpm for 5 min and the supernatant is removed. Then, the pellet was mixed with 200 µl lysis buffer (50 mM HEPES, 150 mM NaCl, 1 mM EGTA, 10% glycerol and 1% Triton X100) containing cOmplete protease inhibitor (1 drop/20 ml) and Phosstop protease inhibitor (1 drop/10 ml). By applying brief vortexing the mixture was kept at room temperature for 15 minutes. After centrifugation for 5 minutes at 1500 rpm, the supernatant that contains the protein load was collected.

In the case of zebrafish embryos, 250 µl Tris-HCl (50 mM, pH:8) was added onto the sample groups (15 embryos per each biological duplicate). After homogenizing by syringes, the samples were kept on ice for 30 minutes. Then, the centrifugation for 20 minutes at 13000 rpm and resuspension of the samples were followed in a sequence for four times. By the end, the supernatant parts mainly comprising the protein units were obtained.

3.2.8 Cholinesterase activity evaluations

Initially, the sample protein amounts were normalized to the sample with the minimum protein concentration to get equal levels of total proteins for each sample. Then, the manual provided by the Colorimetric Acetylcholinesterase Assay Kit (ABCAM (USA)) was followed. Additionally, cholinesterase amounts were derived from the standard sample exponential curves by using Windows Excel 2003. Afterwards, changes in cholinesterase activity levels were evaluated with respect to the DMSO control groups. For that purpose, activity count data were normalized to the control group average on log₂ scale. *In vitro* assessments on the activity were performed via one-way ANOVA/Tukey in comparing the samples together, whereas two-way ANOVA/Tukey and multiple t-test/Holm-Sidak were also followed in assessing the interactions of TFP and SFB with respect to their combinations. Two-way ANOVA/Tukey statistics were also applied on assessing the dose-effect on SkHep1. Additionally, one-way ANOVA/Holm-Sidak methodology was applied on *in vivo* cholinesterase data with multiple compounds and doses. Analyses were executed in GraphPad Prism environment by taking all the derivatives on the same experiment into account

3.2.9 AB genotype zebrafish behavioral analyses

Investigations were focused on the phenothiazine derivatives and performed in collaboration with Dr. Ravindra Peravali from Karlsruhe Institute of Technology (KIT) – Germany by using authenticated and automated platforms. AB genotype zebrafish were used throughout the studies where a total of 0.5% DMSO percentile was used for each exposure type.

3.2.9.1 Locomotor assays

On average 5 embryos per group were exposed to the compounds and to their SFB combinations between 48 hpf and 120 hpf. For this purpose, single compound exposures were performed on PTZ, PPH, PCP, TFP, PD-3, PD-4, PD-5 and PD-6 on the dose scale of 0, 1.25 μM , 2.5 μM , 5 μM , 10 μM and 20 μM). Similarly, but on a different concentration scale (0.15 μM , 0.31 μM , 0.63 μM , 1.25 μM , 2.5 μM and 5 μM), PD-9, PD-10, PD-11 and SFB were investigated for their effects on the locomotion. In addition to that, PTZ, PPH, PCP, TFP, PD-3, PD-4, PD-5 and PD-6 derivatives (2.5 μM and 5 μM each), besides PD-9 and PD-10 (0.63 μM and 1.25 μM) were studied concerning their effects on zebrafish motility in combination with SFB (0.15 μM).

By the end of the exposures, video recordings from the embryos were collected, 4 seconds each. In this template, embryos became adapted to the stable environment for two seconds. After that, they were stimulated with soundwaves shortly, and their activity responses were evaluated for the following 2 seconds. Therefore, through two phases of adaptation and stimulation, observations on locomotor responses could be made.

Obtained video files were then processed in the R environment (3.6.1). The image analyses were executed as a part of the senior projects of two undergraduate Bilkent University students: Cem Buğra Kaboğlu and Ahmet Hınçer. In this regard, each video was segmented into 200 static images and the objects, zebrafish, were identified on the background. Afterwards, motility distance was calculated based on replaced pixel value clusters along the coordinates of each segments. Collected distance values served as the raw data for further statistical analyses where multiple t-test/Holm-Sidak was used in comparing each compound with their SFB combinations. In addition to that, one-way ANOVA/Dunnett and two-way ANOVA/Sidak were also performed in evaluating the effects of doses, compounds and their SFB combinations separately.

3.2.9.2 Photomotor response (PMR)

Between 30 hpf and 34 hpf interval the embryos were exposed to 20 μ M PCP, 20 μ M TFP, 10 μ M PD-9, 10 μ M PD-11 and 2 μ M SFB. Additionally, combinations of PCP or TFP with SFB for the concentrations were also used in assessing the motor responses after photostimulations. During the approach 4 replicate/group and on average 13 embryos/replicate were used for each exposure. Video recordings, six seconds each, were obtained. For the first two seconds, basal movements of the embryos were recorded. Towards the end of this interval, the embryos become stimulated with a light source and their photomotor responses were recorded by the following last four seconds. The steps are as given below:

Basal phase (~2 sn)

Brief photo stimulation (latency) (~10 ms)

Motor response phase (E1, E2 and E3) (~2 sn)

Refractory phase (R1 and R2) (~2 sn)

Collected values were analyzed by using authenticated softwares of the KIT institute. Briefly, Q1 and Q3 quantile values as well as control groups (0.5% DMSO or the corresponding derivative for the combination) were referred in ANOVA based statistical tests. Information about PMR are provided in detail by Kokel D, et al. (2010) [98].

3.2.10 *In silico* target screenings for the derivatives

SMILES (Simplified Molecular Input Line Entry System) codes for the derivatives were generated and further implemented on the SwissProtPrediction tool by Omer Bayazeid (Hacettepe University/Turkey) to retrieve the probability of target binding, hence the target scores, of the derivatives [44]. Later, the scores were gathered and represented within the range of 0-1 where the likelihood for a target increases as the score reaches to one. After compiling the scores, the heatmap with ward distance was generated to elucidate the target profiles across the derivatives.

3.2.11 Microarray analyses

20 μ M of indole-benzimidazole derivatives 48, 49, 50, 51 and 53 were applied on MCF-7 cells for 24 hours. After mRNA collection, where 0.1% DMSO control and 51 exposure groups comprised biological duplicates, microarray methodology was pursued via Affymetrix

HuGene 2.0 ST platform provided by AY-KA Ltd. Şti. In the approach, data normalization was proceeded with Transcriptome Analysis Console Software (V3.0.0.466) with default parameters of Affymetrix analyses and with *rma* from the *affy* package [302]. Differential gene expression was performed via *limma* tool for the DMSO control and 51 samples [303]. In the case of genes with multiple probes, the probes that had the lowest adjust p-value were prioritized for subsequent analyses. Microarray data further represented on the heatmap by logFC values (adj.p-value<0.1 for the compound 51 (n=1116)). Correlations between the novel derivatives were performed by retrieving the gene lists that show more than 0.5 “log Fold Change” (logFC) differences after any exposures in comparison to control (n=3522). In addition, the retrieved gene list was also utilized while comparing the correlations between SERMs, AA (-), Dioxin and indole-benzimidazoles. Nonetheless, the length of the gene list remained relatively limited due to missing genes across the metaanalyzed groups (n=2113). Correlation’s were additionally represented via heatmaps by using ComplexHeatmap tool and ward distance options [304].

LINCS database was utilized in obtaining the list of perturbagens that yield comparable expression profiles with the compound 51 because of characteristic directions of the significantly up- or down-regulated genes. LogFC ranking for 150 upregulated genes and 150 downregulated genes were used for this purpose [305].

Additional *limma* analyses were executed in identifying gene expression differences between 48-49 and 50-51-53 exposures (adjusted p-value < 0.05). Pathway enrichment analyses were performed via STRING database for Reactome Pathways [306]. GSE35428 (SERM modulators), GSE7765 (Dioxin exposure) and GSE62673 (aminoacid depletion (AA (-))) public gene expression data were used for comparative transcriptomics.

Significantly changing expression levels between the compound 51 and external gene expression data was further investigated based on log₂ fold changes and p-values below 0.05. For 51 & E2 (N=2177), 51 & Dioxin (N = 111) and 51 & AA (N = 1480), significant KEGG pathways were found via STRING database.

Venn diagrams facilitated the means of representations between the datasets by showing the contrasts based on pathway mutuality (<http://bioinformatics.psb.ugent.be/webtools/Venn/>) [307]. Furthermore, diagrams for the pathway lists and contingency tables for the gene signatures were also generated helping the calculations on Fisher’s exact test in R.

0.5-fold (log₂ scale and for any of the indole-benzimidazole treatments) was selected as the cut-off for Pearson's correlation analyses where the coefficients between pairs were utilized in generating heatmaps with ward distances. Accordingly, analyses were performed in R environment and ComplexHeatmap library.

Microarray normalization, *limma* analyses of the microarray data and integration of external gene expression data were performed by Bilkent University PhD candidate Ayse Gokce Keskus.

3.2.12 RNAseq analyses

mRNAs were obtained from Hep3B lines which were exposed to DMSO (%0.1), SFB (1 μ M and 2 μ M), TFP (12 μ M) and TFP-SFB combinations for the relevant concentrations. RNAseq libraries were generated via NEBNext® Ultra™ RNA Library Prep Kit for Illumina® (NEB, USA). Clustering and sequencing processes were handled by utilizing HiSeq PE Cluster Kit cBot-HS (Illumina) device and cBot Cluster Generation System software. Afterwards, sequencing was performed on the Illumina Hiseq platform and 125 bp/150 bp paired-end readings were received. RNAseq experiments and raw data collection were done by BMLabosis BM Lab. Sist. Ltd. Şti. Raw reads were contained in fastq format and were aligned to human genome on BioJupies interface through Elysium “free alignment” tool where gene counts were also calculated via Kalisto algorithm (in collaboration with Kubra Calisir, MSc Student) [308]. Afterwards, logCPM normalized gene expression data was retrieved from the same tool and *limma* analyses were performed in evaluating the significances of each gene expression change upon exposures in comparison to 0.1% DMSO control group [303]. Functional deductions based on gene set enrichments were further proceed with minimum of 9 genes per gene sets. In this regard, 0.05 cut-off for *limma* adj.p-value was referred in (i) evaluating differences between hierarchical clusters and PCA; and (ii) top 10 most significantly enriched KEGG pathways were listed via EnrichR (p-value<0.1) [309, 310]. Gene or pathway-based contrasts were represented via Venn diagrams. Gene expression signatures for each exposure was further evaluated by using Fisher's exact test in R environment. For this purpose, significant genes that show expression change either on the same or opposite directions were utilized (*limma* adj.pval<0.05). Following that, mutual or differential gene lists were investigated by taking KEGG pathways into account in EnrichR interface, to understand the synergistic effects on gene-pathway levels.

CHAPTER 4: RESULTS

4.1 Indole-benzimidazole study

Lead-like properties of the compounds were evaluated via *in vitro* and *in vivo* toxicity assays and transcriptomic analyses with a focus on their potential ER modulatory roles.

4.1.1 *In vitro* toxicity analyses of indole-benzimidazoles

Cytotoxicity evaluations were addressed via MTT screenings. Accordingly, the assays were performed for novel ethylsulfonyl indole-benzimidazole derivatives that were synthesized and purified by Fikriye Zengin Karadayı (Ankara University/Turkey; PhD Thesis). Screening was conducted in two phases for 24 hours of exposures. First, responses of the ER α (+) MCF-7 breast cancer cell line against four different concentrations of the derivatives were investigated. In the second phase, cytotoxicity assays were employed for the selected compounds with eight different concentrations against MCF-7, MDA-MB-231 (an ER α (-) breast cancer line) and HepG2 (an ER α (+) HCC line). Moreover, IC₅₀ values for the respective assays were previously generated via GraphPad Prism environment and had been presented accordingly (Fikriye Zengin Karadayı, PhD thesis, 2019). Furthermore, I have carried on subsequent analyses and graphical representations by using GRcalculator tool and demonstrated them in our collaborative publication [311]. Comparative analyses between GRcalculator and GraphPad environments have shown high correlation rates for the IC₅₀ estimations of both tools, especially by the ranges below 40 μ M (**Figure Appendix A1**). Considering the maximal concentration applied on the MTT assays (40 μ M), IC₅₀ values of both tools were able to pinpoint relatively active derivatives, despite being less reliable beyond the experimental concentrations. Since GRcalculator has become tremendously helpful in relating structural differences with toxicity profiles, respective IC₅₀ are referred in the following section of the current thesis.

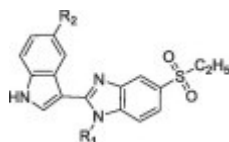
4.1.1.1 First phase MTT screening results

The derivatives were comprised of 10 different R₁ side chain alterations in addition to one of the 4 modifications on the R₂ position: -H, -OCH₃, -Cl or -Br (**Table 4.1**). These structural contrasts allowed further comparisons regarding the activity levels of the compound groups. According to the preliminary toxicity screenings, n-way ANOVA approaches revealed that both modifications on different side chains influence the cytotoxic activities (p-value < 2e-16) with R₁ as the most significant factor (p-value < 2e-16). Sole effect of R₂ alterations turned out to be milder (p-value=0.0885). Nevertheless, interaction between both side chains was

also eminent ($R_{1 \times 2}$ interaction p -value $< 2e-16$) implying that both positions can act together. Investigations on the GRcalculator tool has also presented that R_1 : -*p*-fluorobenzyl family (48, 49, 50 and 51) stood out from the rest of the R_1 modifications (p -value: 0.023) and other R_1 cyclic aromatic side chain moieties (p -value: 0.012) (**Figure 4.1**). Across the *p*-fluorobenzyl group members, compounds 50 and 51, with -Cl and -Br on the R_2 position respectively, posed relatively more potential activity levels on the first phase of MCF-7 screenings.

Besides the *p*-fluorobenzyl possessing derivatives, some compounds also showed strong activity levels. In contrast, rest of the members from their respective R_1 groups posed negligible anti-cancer toxicities. This brought additional considerations on possible synergisms with R_2 side chains. In this regard, some of the prominent compounds that can demand further considerations are: (i) 53 (R_1 : -3,4-difluorobenzyl x R_2 : -OCH₃), (ii) 27 (R_1 : -CH₃ x R_2 : -Cl), and (iii) 36 (R_1 : -C₃H₇ x R_2 : -Br).

Table 4.1 GRcalculator derived IC₅₀ values (μM) of the indole-benzimidazoles after 24-hour exposures in MCF-7



No	R ₁	R ₂	IC ₅₀	No	R ₁	R ₂	IC ₅₀	No	R ₁	R ₂	IC ₅₀
23	-H	-H	22.9	36	-C ₃ H ₇	-Br	13.4	49	- <i>p</i> -fluorobenzyl	-OCH ₃	41.3
24	-H	-Br	135	37	-C ₄ H ₉	-H	22.4	50	- <i>p</i> -fluorobenzyl	-Cl	13.2
25	-CH ₃	-H	206	38	-C ₄ H ₉	-Cl	ND	51	- <i>p</i> -fluorobenzyl	-Br	9.29
26	-CH ₃	-OCH ₃	ND	39	-C ₄ H ₉	-Br	53.6	52	-3,4-difluorobenzyl	-H	ND
27	-CH ₃	-Cl	6.99	40	-cyclohexyl	-H	34.4	53	-3,4-difluorobenzyl	-OCH ₃	11.9
28	-CH ₃	-Br	200	41	-cyclohexyl	-OCH ₃	84	54	-3,4-difluorobenzyl	-Cl	148
29	-C ₂ H ₅	-H	15.1	42	-cyclohexyl	-Cl	73.2	55	-3,4-difluorobenzyl	-Br	134
30	-C ₂ H ₅	-OCH ₃	ND	43	-cyclohexyl	-Br	378	56	-3,4-dichlorobenzyl	-H	ND
31	-C ₂ H ₅	-Cl	ND	44	-benzyl	-H	324	57	-3,4-dichlorobenzyl	-OCH ₃	ND
32	-C ₂ H ₅	-Br	ND	45	-benzyl	-OCH ₃	21.5	58	-3,4-dichlorobenzyl	-Cl	ND
33	-C ₃ H ₇	-H	51.1	46	-benzyl	-Cl	ND	59	-3,4-dichlorobenzyl	-Br	ND
34	-C ₃ H ₇	-OCH ₃	52.6	47	-benzyl	-Br	ND				
35	-C ₃ H ₇	-Cl	23.8	48	- <i>p</i> -fluorobenzyl	-H	47.9				

ND: No IC₅₀ detected

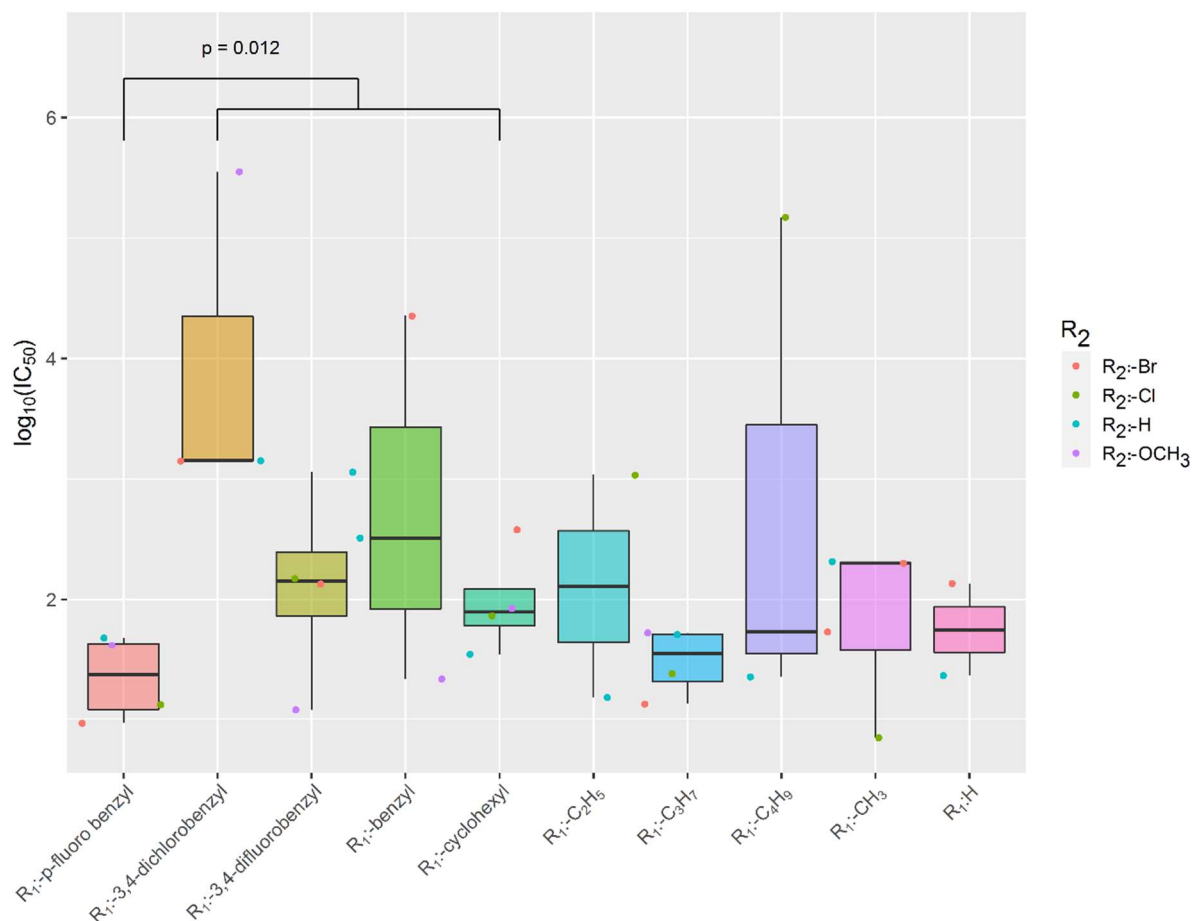


Figure 4.1 GRcalculator analyses based on $\log_{10}\text{IC}_{50}$ values (μM) derived from the viability percentiles after the exposures on MCF-7 cell line. Representations are given based on R₁ side chains modifications as the respective R₂ side chains are given by the colored points. One-sided Wilcoxon test statistics were followed in the tool to compare the scores from p-fluorobenzyl moieties to the R₁ aromatic side chains. Retrieved from Karadayi F.Z. & Yaman M. et al., 2020. *Bioorganic Chemistry* [311].

4.1.1.2 Large scale MTT screening results on multiple cell lines

In addition to ER α (+) MCF-7 line, an ER α (-) breast cancer line MDA-MB-231 and an ER α (+) HCC line HepG2 were exposed to 13 candidate compounds from the preliminary cytotoxicity assessments (**Table 4.2**). According to n-way ANOVA evaluations, the treatments significantly affected the viabilities ($p\text{-value} < 2e-16$) in a cell-type dependent manner ($p\text{-value}: 2.62e-08$). R₁ \times R₂ interaction, likely structural synergism, was observable ($p\text{-value} < 2e-16$), besides that R₁ and R₂ were able to influence the cell viabilities separately ($p\text{-value} < 2e-16$, for each position). Cell line dependencies were further confirmed by two-way ANOVA/Tukey comparisons (**Figure Appendix A2**). According to GRcalculator analyses,

MCF-7 has a trend to be a more sensitive line for the derivative concentrations with respect to the other cell lines screened (**Figure Appendix A3**).

Table 4.2 IC₅₀ values (μM) for the candidate derivatives across the cell lines

No	IC ₅₀ (μM)			No	IC ₅₀ (μM)		
	MCF-7	MDA-MB-231	HepG2		MCF-7	MDA-MB-231	HepG2
23	ND	64.7	ND	45	30	19.8	8.59
27	5.73	ND	ND	46	ND	10.5	97.5
29	ND	ND	ND	48	26.3	19.3	ND
35	282	ND	32.4	49	33.9	43.9	ND
36	15.1	ND	10.4	50	19.6	32.2	77.3
37	28.6	ND	29	51	33.3	31.7	16.9
40	51	63.6	291	53	19.1	ND	24.2

ND: No IC₅₀ detected

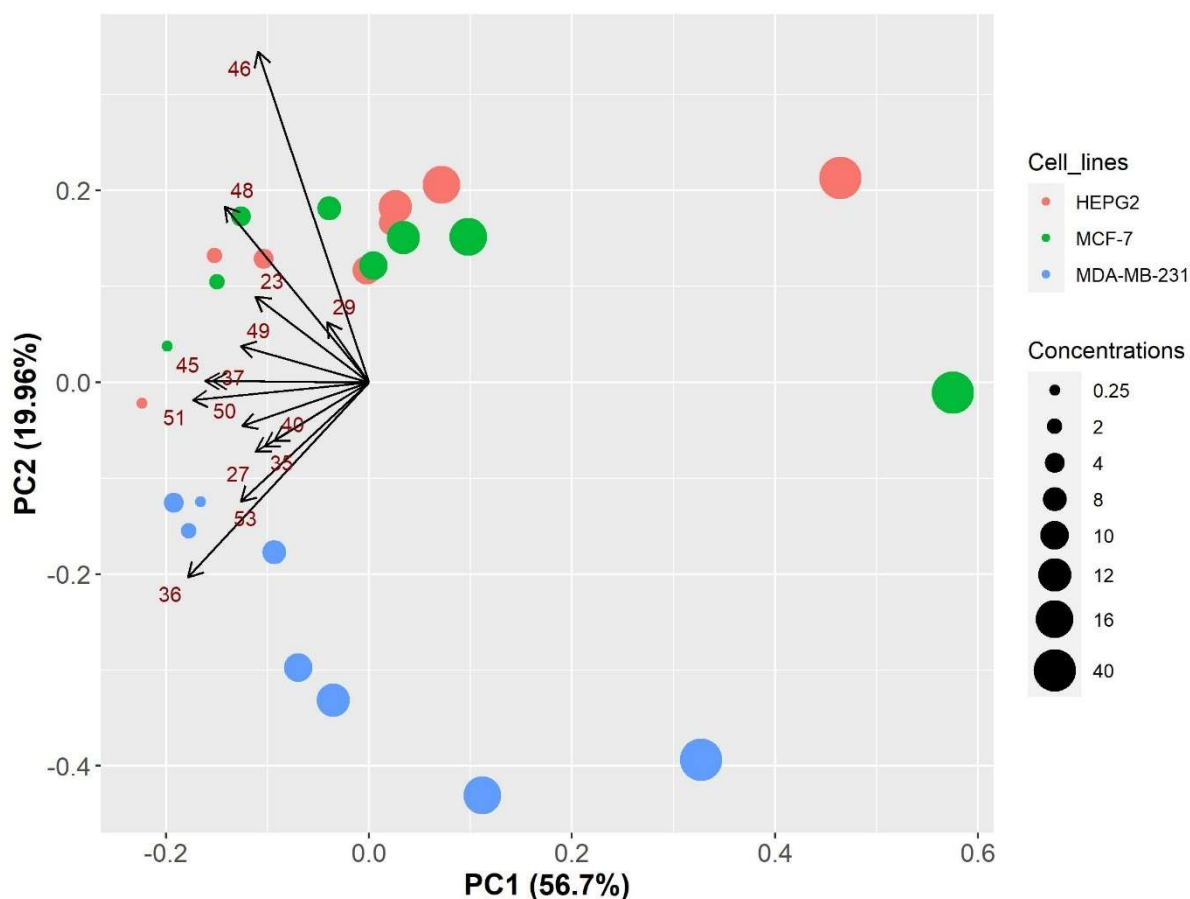


Figure 4.2 PCA of the candidate indole-benzimidazole derivatives. Log₂ scaled viability percentiles from the biological triplicates of each cell line were used for each concentration.

Viability scores were further employed in generating principal components enabling cell line and concentration-based comparisons (**Figure 4.2**). Accordingly, ER α (+) lines represented overlapping clusters in dose responses whereas the viabilities tend to deviate by the maximum

dose (40 μ M), further underlying dose-dependency. Moreover, principal directions of **50** and **53** aligned in a proximity along with **27** and **36**, whereas compounds **37**, **45**, **49** and **51** seemed to form another cluster.

GRcalculator-retrieved IC₅₀ values further eased the comparisons for the cell types and the treatments (**Table 4.2**). In contrast to the **Table 4.1**, the derivatives **23**, **27** and **51** unexpectedly yielded some shifts in the activity levels on MCF-7. Furthermore, some compounds posed more cytotoxic potencies towards the supplementary cell lines other than MCF-7, such as the compounds **45**, **46** and **51**. Surprisingly, the structures, enumerated between **45-51**, were able to affect the ER α (-) MDA-MB-231 line.

4.1.2 *In vivo* toxicities of the novel indole-benzimidazoles used as leads

AB strain zebrafish embryos were exposed to 20 μ M of the R₁: p-fluorobenzyl members between 6 hpf-72 hpf. Initial observations suggested high survival ratios (10-11 per group). Although fully hatched by 72 hpf, relatively low hatching rates of the embryos were also recorded by 48 hpf (**Table 4.3**). Especially the compounds **49** and **51** were indicative for a developmental delay by the exposures.

Table 4.3 48 hpf hatching and abnormality status of indole-benzimidazole exposed embryos

Replicates	Group A			Group B			Total
Status / Treatment	Hatched	Unhatched	Malformed	Hatched	Unhatched	Malformed	Hatching (%)
DMSO (0.5%)	10	1	0	10	1	0	90.91
48	9	2	0	5	6	0	63.64
49	9	2	0	0	10	0	42.86
50	7	3	0	8	3	0	71.43
51	2	9	0	4	7	0	27.27

Nevertheless, PCA was performed on 6 random 72 hpf samples from each exposure type by taking morphometric measurements into account (**Figure 4.3**). The analyses resulted in overlapping features between the groups, suggesting no clear distinction on the development with respect to the morphometric parameters. Accordingly, relative with the numeric value,

rostrocaudal (RC) axis length showed a separate direction from the remaining measurements that were in line with each other: dorsoventral (DV) axis, yolk length and eye width.

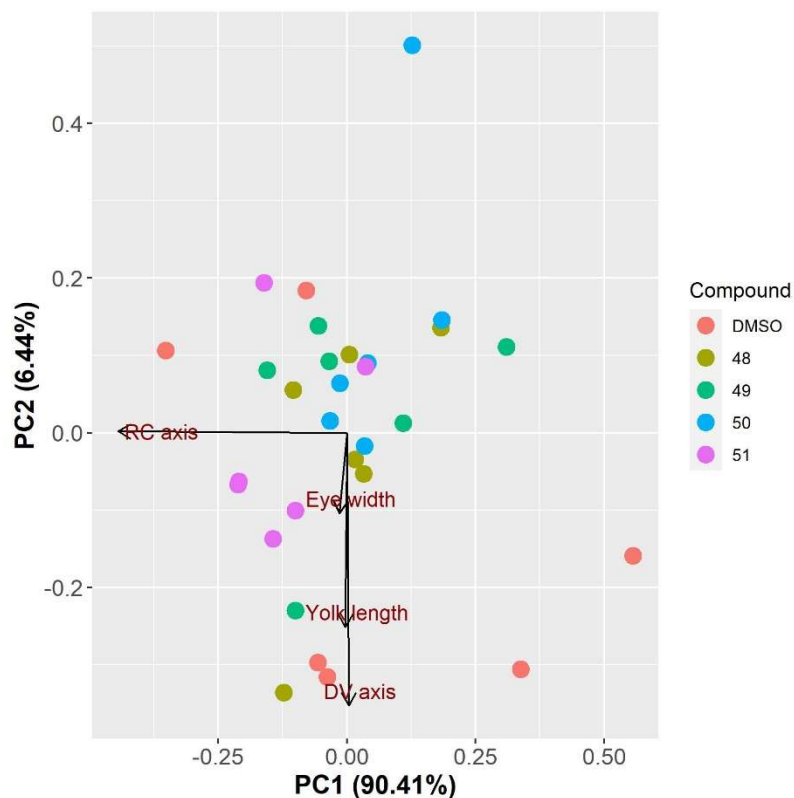


Figure 4.3 PCA of 72 hpf embryonic morphometric measurements. Lengths for dorsoventral (DV) and rostrocaudal (RC) axes, eye width and yolk were utilized in assessing the morphometric parameters after exposures to the derivatives.

4.1.3 Transcriptome level analyses on indole-benzimidazole exposures

Gene expression studies were initiated to understand the molecular networks relating with the indole-benzimidazoles. Based on the cytotoxicity profiles, candidate compounds were subjected to microarray analyses. For this purpose, R₁: -p-fluorobenzyl members (**48**, **49**, **50** and **51**) and compound **53** with a structural similarity by its R₂: -3,4-difluorobenzyl group were subjected to microarray analyses.

4.1.3.1 Gene expression profile correlations and dose-dependency evaluations

Initial explorations on the gene data posed to question whether the molecular signatures of each compound relate with each other. In line with the toxicity data, fold change differences in expression seemed milder in **48** and **49** than other R₁: -p-fluorobenzyl members and **53**,

indicative for dose-dependency on gene expression (**Figure 4.4 (A)**). Pearson correlation analyses have further supported the findings where **51** has yielded relatively higher correlation rates for more cytotoxic compounds on MCF-7 (**Figure 4.4 (B)**).

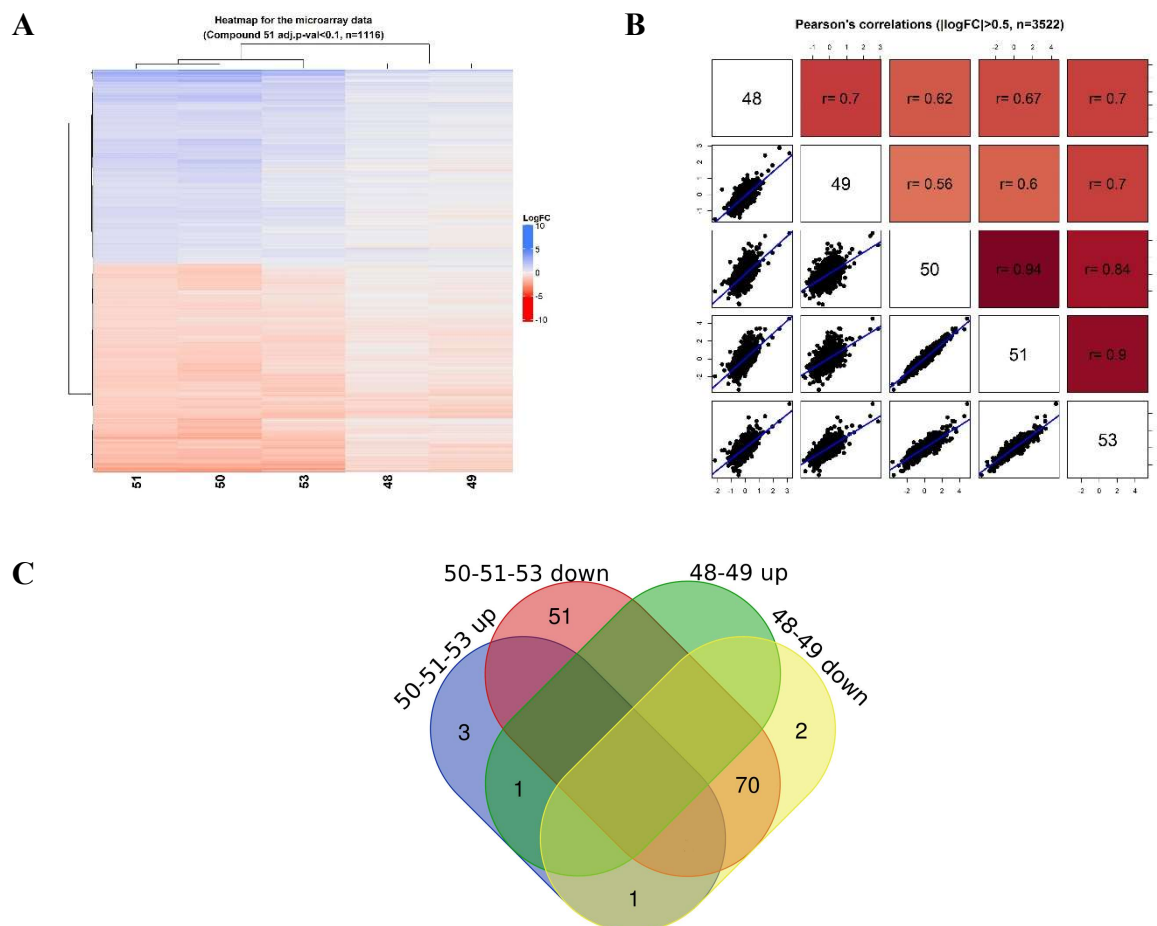


Figure 4.4 Preliminary microarray analyses for the novel indole-benzimidazoles. (A) Heatmap for microarray data. Ward distance is used and genes are filtered on the basis of adj.p-value<0.1 for the compound 51 (n=1116). (B) Pearson's correlation plots for the microarray data. LogFC data was used and the genes showing more than 0.5 logFC in either of the exposure was selected (n=3522). Compound names are provided on the diagonal line, scatter plots and blue regression lines on the bottom side and the Pearson's correlation scores on the top half of the diagonal axis. (C) *Limma* derived gene lists (adj.p-value < 0.05) for 49-50 and 50-51-53 groups were utilized in retrieving Reactome Pathways which were represented by the Venn diagram. List of the pathways are provided in the **Table Appendix A4** (Retrieved from Karadayi F.Z. & Yaman M. et al., 2020. *Bioorganic Chemistry* [311]).

Moreover, Reactome enrichment analyses were pursued in understanding possible gene level differences between **48-49** and **50-51-53** where 553 genes demonstrated differential expression levels between the groups (adj.p-value<0.05). In the contrasts for **50-51-53**,

comparisons presented a more pronounced influence on the numbers of genes that are relevant with cell cycle, ESR1, DNA damage and stress response pathways, further underlying dose-dependency on the cellular responses (**Figure 4.4 (C) & Table Appendix A4**). Therefore, microarray compounds revealed close relationships with each other on the gene expression. In addition, the relationships were also likely to rely on the substance concentrations along with the cytotoxicity profiles of the compounds. Furthermore, **51** emerged as a representative sample for the relatively active derivatives **50** and **53**.

4.1.3.2 Dose-dependent gene expression profile assessments

Gene expression confirmations and dose-dependency evaluations were further executed via qPCR (**Figure 4.5**). Here, mRNA levels under 40 μ M exposures on the MCF-7 were taken into analyses. Candidate genes were selected upon the top KEGG pathway annotations for the gene signatures from **51** and the compound series **50-51-53** (**Table Appendix A5 & Table Appendix A6**). The KEGG annotations were in line with aminoacyl-tRNA biosynthesis, p53 signaling and cellular stress related pathways.

Accordingly, structural similarities and differences were accountable for gene expression differences across multiple pathways. For instance, cell cycle genes (ANLN, WDHD1, CDC6, CDKN1A, RRM2 and CCND1) yielded overlapping profiles. However, the compounds **48**, **49** and **53** also showed slight differences for some genes such as CDKN1A, WDHD1 and RRM2. Moreover, overlapping profiles were eminent on the DNA damage and repair (DDIT3, GADD45A, MCM10 and RRM2) genes, as the compound **49** could not influence the gene GADD45A significantly. In the case of E2 signaling related genes, influence of TFF1 was remarkable, even though none of the derivatives could alter PGR levels by 40 μ M, surprisingly. In addition to that, drug metabolism, amino acid metabolism related genes (CYP1B1, AARS and RRM2) yielded remarkable fold changes as the AARS levels remained unaffected for each compound in contrast to 20 μ M microarray profiles. Levels of some ion channel genes (SLC7A11, SLC6A14, AQP3, KCNS3 and CLIC3) turned out to be affected by the exposures, but differential for AQP3 and KCNS3. As some of the genes additionally were related with ferroptosis or stress response pathways (CDKN1A, DDIT3, SLC7A11, GADD45A), fold changes were noteworthy with slight dependence on the compound. As a result, candidate genes from the microarray were mostly validated by the qPCR findings based on gene expression fold changes. Moreover, overlapping signatures and multiple mechanisms were prominent for the derivatives overall, yet there were also some contrasting features between them.

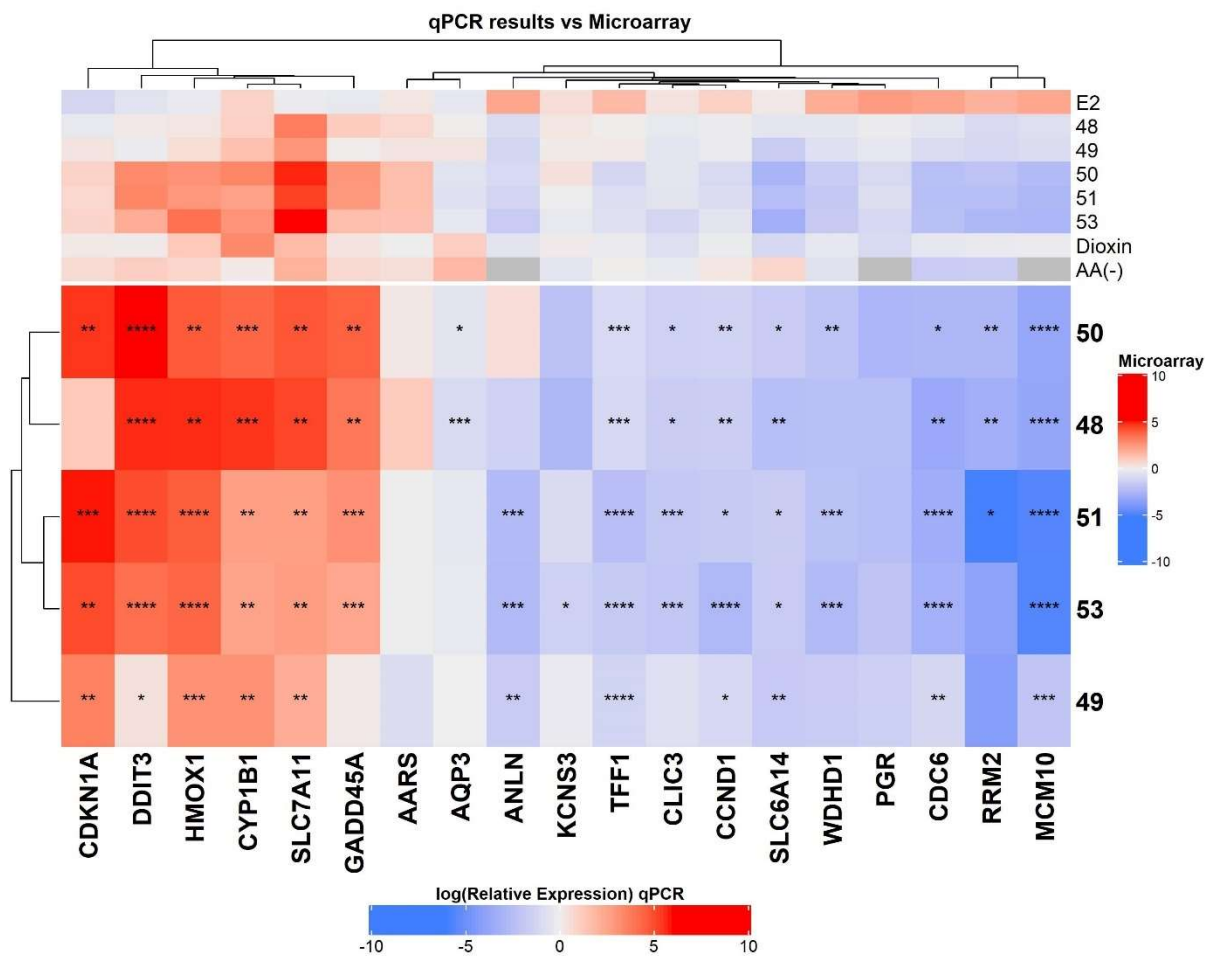


Figure 4.5 Heatmaps for qPCR results. The data is derived from the novel compounds exposed onto MCF-7 for 24 hours, and gene expression differences are presented on log₂ scaled relative quantity values (log₂RQ). Clusters are formed with average distances. Microarray data for the respective genes are additionally annotated on the top. Color scales are given from blue-to-red within the -10 and 10 boundaries. One-way ANOVA/Tukey p-value statistics for the qPCR results are provided on the heatmap. *: p<0.05, **: p<0.01, ***: p<0.001 and ****: p<0.0001. Adapted from Karadayi F.Z. & Yaman M. et al., 2020. *Bioorganic Chemistry* [311]

Microarray and qPCR comparisons demonstrated dose-dependency. We have initially observed that microarray and qPCR studies yielded different clusters. Although the list of the most significantly affected genes were shared between two assays, gene expression signatures slightly deviated from each other, As **48-49** and **50-51-53** clusters were formerly evident in microarray, compound **48** presented a similar profile with **50-51-53** group on the qPCR validations. Enrichment of qPCR significance scores in the case of **48** and **49** additionally implemented a gain of functionality by the increasing dosages from 20 μ M to 40 μ M. Dose comparison analyses for E2 signaling related genes CCND1, TFF1 and PGR were pursued via qPCR (**Figure 4.6**). Accordingly, TFF1 gene presented a significant dose-dependency (p-

value: 0.0207). In the case of CCND1 (p-value: 0.6284) and PGR (p-value:0.4252) group comparisons between doses did not yield significant scores. However, significances for **48** and **49** were found to alternate between doses, as the profiles had overlapping features across the compounds by 40 μ M.

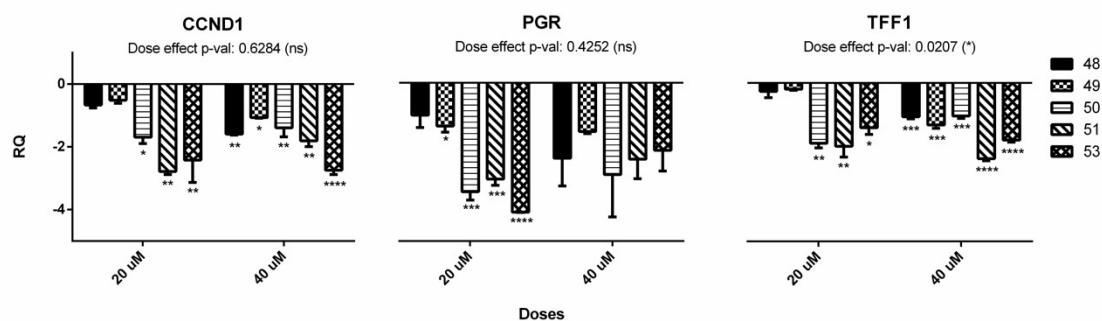


Figure 4.6 qPCR results for E2 signaling genes. Dose-dependency evaluations were performed on MCF-7 cells that were exposed to the compounds for 24 hours at 20 μ M and 40 μ M. Log₂ scaled relative quantity (RQ) amounts are provided on y-axis where the housekeeping gene TPT1 was referred. For each dose, one-way ANOVA and Dunnett multiple comparisons were done on against the respective DMSO control groups. Dose-dependency evaluations were performed via two-way ANOVA *: p<0.05, **: p<0.01, ***: p<0.001 and ****: p<0.0001. Retrieved from Karadayi F.Z. & Yaman M. et al., 2020. *Bioorganic Chemistry* [311]

4.1.3.3 qPCR studies *in vivo*

In vivo condition of the candidate genes *rrm2* and *aars* were evaluated on 72 hpf embryos that were exposed to 20 μ M of the compounds since the 6 hpf stage (**Figure 4.7**). Despite the insignificant scores by one-way ANOVA/Tukey comparisons, *rrm2* has shown a reducing trend by the derivatives, in line with *in vitro* microarray and qPCR findings. Interestingly, the trend for *aars* expression was on the opposite direction, suggesting involvement of cell-cycle and aminoacid metabolisms between *in vitro* cancer and *in vivo* embryonic developmental conditions, although somewhat differentially.

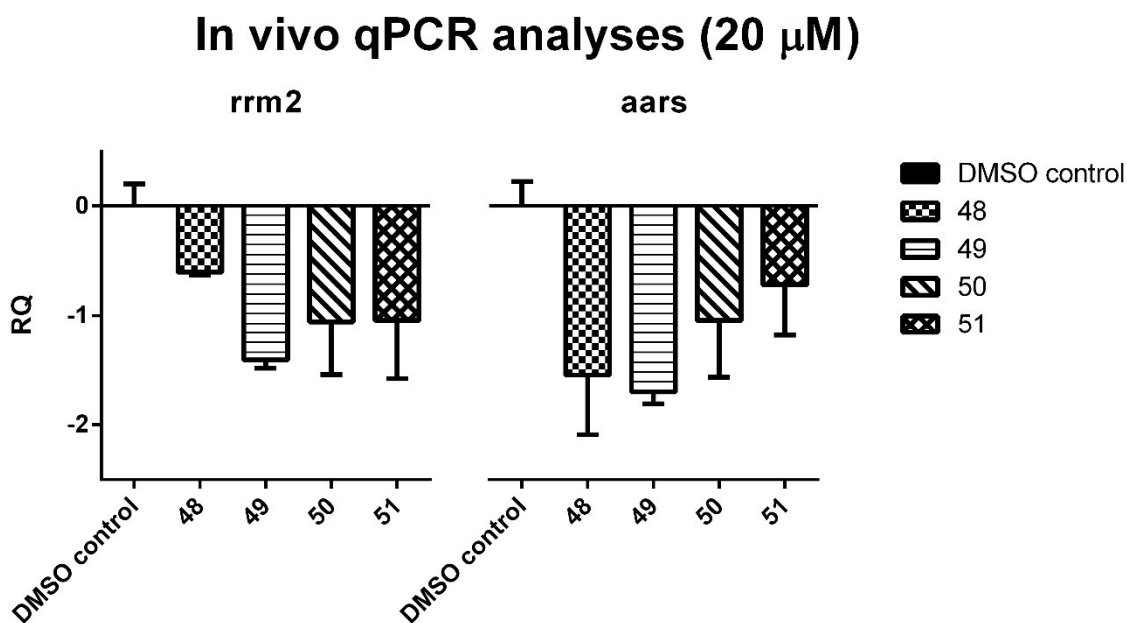


Figure 4.7 *In vivo* qPCR results for the R₁: p-fluorobenzyl members. The compounds were exposed onto zebrafish embryos between 6 hpf and 72 hpf, and gene level changes are provided by log₂RQ values. One-way ANOVA/Tukey p-value statistics for the qPCR results did not show significant differences with the DMSO control groups (0.5%)

4.1.3.4 Gene signature assessments across SERMs and multiple cellular networks

Annotations by the microarray level assessments yielded some possible correlations with multiple ontologies. For example, reverse profile of the E2 exposures suggested antiestrogenic characters of the derivatives, despite PGR levels remaining relatively unchanged by 40 μ M treatments, bringing alternative pathways into question. Accordingly, an E2 related pathway AhR (via dioxin exposures) and a stress response and amino acid metabolism related pathway via AA (-) were taken under investigations in line with preliminary **48-49-50-51-53** comparisons (**Figure 4.8**). For that purpose, DEG quantities across the exposures were evaluated and annotated by KEGG pathways. Compound **51** and E2 comparisons yielded significant associations between the groups. On one side of the inverse correlation there was TGF- β pathway and on the other side there were mismatch repair, cell cycle, DNA replication, spliceosome pathway, cysteine and methionine metabolism besides pyrimidine metabolism. List of genes on the same directions are given in **Table Appendix A7**. According to Fisher's exact tests, forward correlation between **51** and AA (-), as well as between **51** and dioxin were remarkable with a mutual enrichment of the "ferroptosis" term.

In addition, amino acid metabolism, E2 signaling pathway and steroid metabolism were mutually affected for **51** and dioxin exposures,

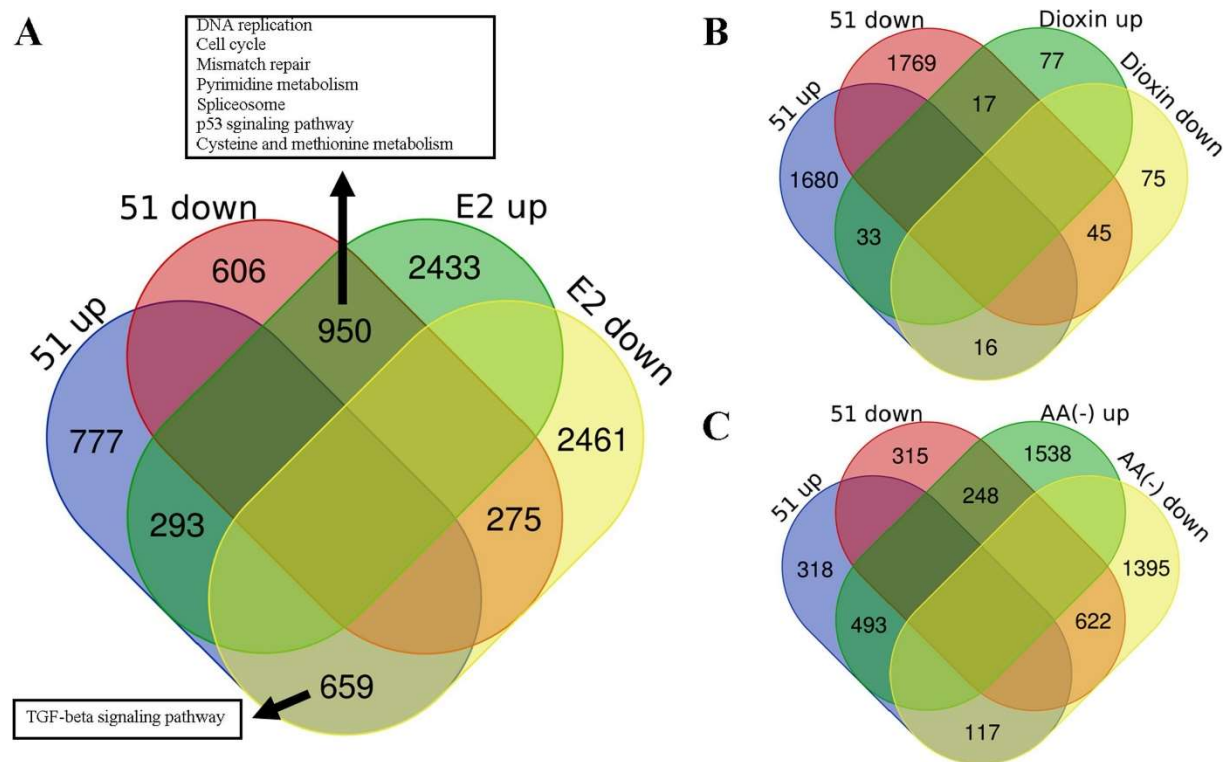


Figure 4.8 Expression profile contrasts between the compound **51**, (A) E2, (B) Dioxin and (C) AA (-). The gene sets were comprised of the lists of genes showing significant changes (p -value < 0.05) for each group. Retrieved from Karadayi F.Z. & Yaman M. et al., 2020. *Bioorganic Chemistry* [311]

Contrasts between the indole-benzimidazoles, E2, AhR and AA (-) were further supplemented by correlation maps (**Figure 4.9**). The list of genes that showed 0.5 logFC difference in any of the indole-benzimidazoles and available on the metaanalyzed list were utilized in forming the plots. Accordingly, large scale microarray profiles have shown that the novel compounds as well as dioxin and AA (-) can correlate with ER modulatory effects in expression. Although they have overlapping signatures with SERMs, they have also formed distinct clusters. Besides that, the expression profiles of the indole-benzimidazole group accordingly followed an inverse interrelationship with E2 exposures. Although estrogen modulatory roles can be annotated for the indole-benzimidazoles in this study, their selectivity towards the estrogen receptor remained as a doubtful case. Surprisingly, the signature of 5-hydroxytamoxifen (4-OHT) demonstrated vague SERM-likeness based on the reference gene list. Moreover, amino acid depletion AA (-) and partially AhR gene signatures correlated with the studied compounds and reference SERM molecules. The results strongly suggested

multifaceted nature of indole-benzimidazole actions and mutuality of E2-signaling events across various cellular paradigms.

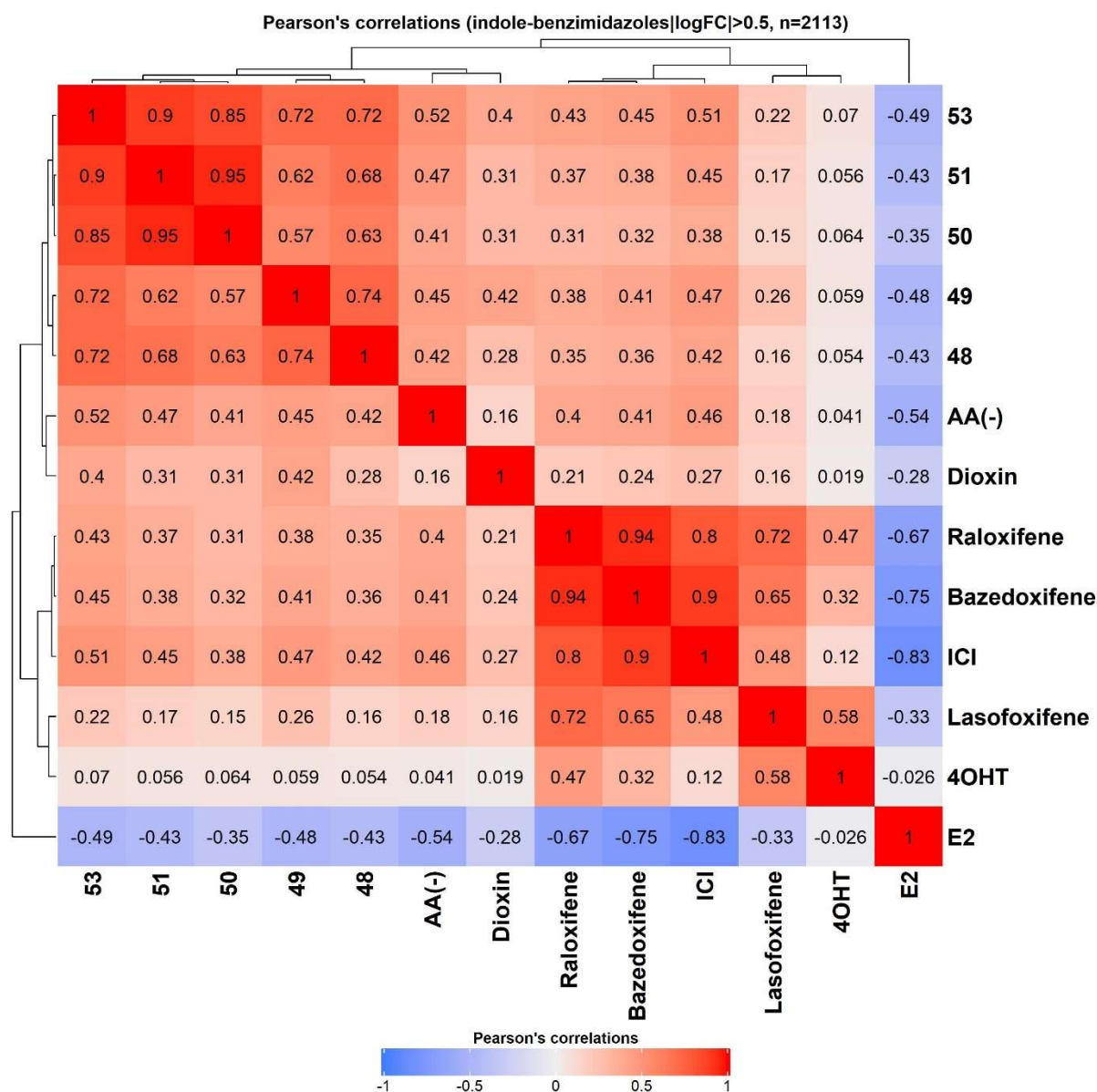


Figure 4.9 Correlation heatmap of SERMs, AA (-), Dioxin and indole-benzimidazole derivatives. Genes were selected by referring to the indole-benzimidazole signatures ($|\logFC|$ cut-off: 0.5, for any exposures) and further refrained by the gene lists available in the remaining datasets ($n=2113$). Clusters were formed via Ward distances as the Pearson's correlations were demonstrated in a color code of blue-white-red scale as provided on the legend.

4.1.3.5 Additional perturbagen type gene profile comparisons on LINCS-Query database

Upon confirmations on overlapping gene signatures, possible MoA hubs were investigated. Initial considerations on the pathway annotations have supported the involvement of anti-cancer related events regarding cell cycle, DNA damage as well as aminoacyl-tRNA biosynthesis (**Table Appendix A4, Table Appendix A5 & Table Appendix A6**). Findings were further supplemented by the overlapping features between the derivatives SERMs, amino acid depletion and dioxin. Yet, exact mechanisms on the upstream of events remained unresolved. To address that, LINCS database was utilized (**Table 4.4**). Specifically, the Query tool provides a wealth of gene level information upon perturbagen exposures to various cell lines. Therefore, a list of closely related perturbagens can be obtained fast with respect to gene level signatures, as primary events relating with the exposures can be enlightened. In this regard, analyses were performed for the compound **51** data deriving from biological duplicates. Meanwhile, the multiscale MCF-7 chemical perturbagen-gene expression data was considered. As doing so, tubulin and microtubule inhibitors, ER antagonists and known AhR ligands were gained additional considerations due to potential roles acclaimed for the indole and benzimidazole structures in the literature. Most similar agent was the VEGFR inhibitor oxindole-I and the calcium channel inhibitor nifedipine, which is also an activator for amino acid and integrated stress responses [312]. An ER antagonist ZK-164015 and reserpine (vesicular monoamine transporter inhibitor and an oxidative stress factor) were among the most related compounds which also pose indole moieties [313].

In line with literature suggestions on indoles and benzimidazoles, ER antagonists, microtubule inhibitors and tubulin inhibitors yielded high similarity scores, where structural similarities for these compounds were eminent (Score > 80). However, affinities of the derivatives towards some of these targets were milder than the standard ligands, according to docking studies performed in Ankara University, by M. Murat Kışla (**Table Appendix A 8**). Even for the compound **50** no successful binding model was generated. Although *in silico* docking studies usually demand *in vitro* validations, the work underlined that: (i) there can be multiple targets for the derivatives, and (ii) relatively moderate interactions with ER α , tubulin or VEGFR.

Table 4.4 Top LINCS Query matches for the compound **51**

	Score	Name	Description	Rings included in the structure
Top 10	99.98	oxindole-I	VEGFR inhibitor	indole
	99.98	niguldipine	Calcium channel blocker	none
	99.97	AG-592	Tyrosine kinase inhibitor	none
	99.96	AG-879	Angiogenesis inhibitor	none
	99.96	FCCP	Mitochondrial oxidative phosphorylation uncoupler	none
	99.96	ZK-164015	ER antagonist	indole
	99.96	reserpine	Vesicular monoamine transporter inhibitor	indole
	99.96	PD-198306	MAP kinase inhibitor	none
	99.96	CGK-733	ATR kinase inhibitor	none
	99.96	suloctidil	Adrenergic receptor antagonist	none
Literature supported groups	99.76	Vinblastine	Microtubule inhibitor	indole
	97.72	albendazole	Anthelmintic	benzimidazole
	97.2	SA-63133	Tubulin inhibitor	indole
	95.82	fenbendazole	Tubulin inhibitor	benzimidazole
	94.84	NPI-2358	Tubulin inhibitor	imidazole
	94.38	tamoxifen	ER antagonist	none
	94.34	mebendazole	Tubulin inhibitor	benzimidazole
	94.01	oxibendazole	Tubulin inhibitor	benzimidazole
	92.99	clomifene	ER antagonist	none
	92.51	vinorelbine	Tubulin inhibitor	indole
	89.22	SA-792574	Microtubule inhibitor	indole
	87.89	Y-134	ER antagonist	thiophene
	85.53	arctigenin	MEK inhibitor	none
	84.26	vindesine	Tubulin inhibitor	indole
80.22	nocodazole	Tubulin inhibitor	benzimidazole	

Adapted from Karadayi F.Z. & Yaman M. et al., 2020. Bioorganic Chemistry [311]

In the case of AhR binding agents in the LINCS Query, only arctigenin, a MEK inhibitor (85.53), has given a considerable similarity score. Rest of the AhR agonists, antagonists and ligands, including the indole itself, failed to meet the similarity criteria. Then, the derivations on the indole scaffold seemed to cause deviations in modulating its target AhR, which can be due to R₂ modifications and additions of benzimidazoles. However, gene level similarity with arctigenin was also noticeable.

4.2 Repurposing and novel derivative screening of phenothiazines for treatment of HCC

Repurposing potentials of phenothiazines on HCC and lead-like properties of novel compounds were initially assessed. Therefore, their cytotoxic effects alone or in combination with sorafenib (SFB) were evaluated via cytotoxicity assays, *in vivo* embryonic toxicity and behavioral assays. In addition, possible target mechanisms were investigated by *in silico* tools and RNAseq transcriptomic analyses.

4.2.1 *In vitro* toxicities of the derivatives

Anti-cancer potentials of the phenothiazine derivatives were primarily addressed via *in vitro* MTT assays on Hep3B, SkHep1, HepG2, Huh7 and MCF-7, besides the eGFP clones of Hep3B and SkHep1. For this purpose, generic compounds were obtained from SIGMA and screened on the cell lines to initiate repurposing assessments. In a parallel line novel and intermediary PTZ derivatives were synthesized and purified by Fikriye Zengin Karadayi and Mehmet Murat Kışla (Ankara University/Turkey). MTT assays were also performed for these compounds. At last, viability-based synergism evaluations were pursued with SFB combinations.

4.2.1.1 Individual generic compound exposures on the cell lines

4.2.1.1.1 Compound and cell type dependent changes on viability

Anti-cancer and anti-HCC potentials of the generic compounds were initially evaluated on multiple cell lines (**Figure 4.10 (A)**). Viability based n-way ANOVA have yielded significant effects on cellular viability in cell-type, compound and concentration dependent manners after 24 hours (p-values: 2.35e-07, 1.59e-08 and < 2e-16, respectively). Furthermore, we have observed significant interaction between cell line and treatments (p-value: 0.0069) suggesting differential effects of treatments on each cell type. Accordingly, generic compounds were found to influence the viability scores of the HCC and non-HCC lines (**Figure 4.10 (B)**). Interestingly, PTZ and PPH were less effective on Huh7 and MCF-7, unlike TFP and PCP which caused relatively more reduction on the IC₅₀ scores overall (**Figure 4.10 (C)**). As PTZ represents fewer toxic profiles than the remaining generic derivatives, responses of the HepG2 were observed to be more pronounced than the other naïve cell lines. Moreover, effect of PPH was also more profound on HepG2, indicative for selectivity towards HepG2 background. As a result, initial repurposing attempts pinpointed TFP and PCP for further studies, yet PPH is also suggestive for further studies.

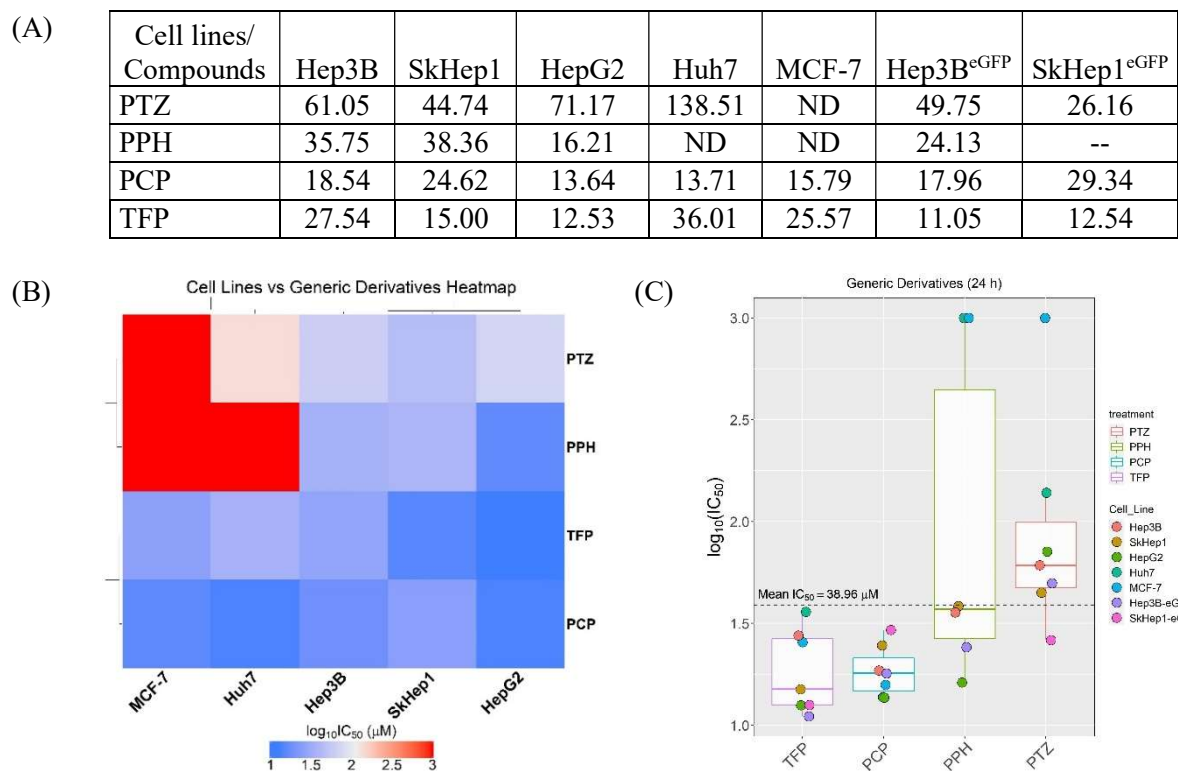


Figure 4.10 Generic PTZ derivative screenings on multiple cell lines (24 h). (A) IC₅₀ values (μM), (B) Heatmap representation for the compound responses across the cell lines, and (C) LogIC₅₀ distributions of the generic derivatives across multiple cell lines. ND: No IC₅₀ detected; --: No experiment

4.2.1.1.2 eGFP status on the toxicity profiles of generic compounds

As the eGFP clones of the cell lines are initially proposed for xenograft trials, comparability between the parent lines and eGFP monoclonal lines were questioned. Initial observations by IC₅₀ based t-test analyses have shown no significant differences between Hep3B-Hep3B^{eGFP} and SkHep1-SkHep1^{eGFP} pairs comparisons (p-values: 0.14 and 0.47, respectively) (**Figure 4.11** (A)). To comprehend the eGFP status effect, n-way ANOVA was performed with the log₂Viability percentiles. No remarkable differences by the status of the cell lines and their origins were recorded (p-values: 0.526 and 0.668, respectively), supplementing the comparability of the monoclonal lines and parent lines for the generic compounds. Significant effects by the treatment exposures further supported that each generic molecule behaved differently on the viability of the cell lines. No interaction between these factors were also observed. Thus, the clonal lines were found to be representative of the parent lines Hep3B and SkHep1.

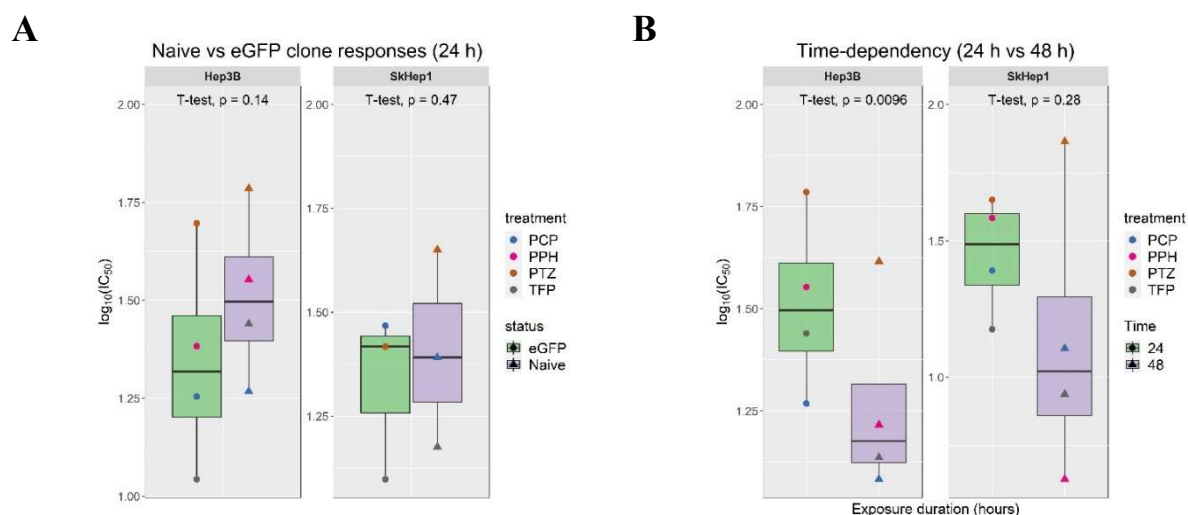


Figure 4.11 (A) eGFP status and (B) time-dependency evaluations on the responses of Hep3B and SkHep1 towards generic derivatives. T-tests were performed for initial comparisons.

4.2.1.1.3 Time-dependent changes on viability by 24 and 48 hours

IC₅₀ based 24-hour and 48-hour exposure comparisons have shown that time parameter can also be a significant factor for Hep3B, as SkHep1 also presented a trend for a more sensitive profile by 48 hours (p-values: 0.0096 and 0.28, respectively). To understand the time effect better, n-way ANOVA and log₂ Viability percentiles were utilized. Duration (p-value: 0.0166) and treatments (p-value: 3.36e-07) have caused significant differences. Nonetheless, no remarkable effects and interactions with exposure duration and treatments were observed by the cell lines, Hep3B and SkHep1, indicating that they behaved similarly during the exposures. Therefore, exposure time and treatments were found to be significant factors for the generic compounds tested.

4.2.1.2 *In vitro* toxicities of the novel derivatives

4.2.1.2.1 Compound and cell type dependent changes on viability

Novel derivatives and intermediary compounds, in total 30, were initially screened on Hep3B and SkHep1 where two-cell lines have shown significant differences, unlike the generic compounds (p-value: 0.0049) (**Figure Appendix B1**). Despite relatively high IC₅₀ values for most of the compounds, the intermediary derivatives PD-9 and PD-11 stood out from the rest of the molecules. Regarding the novel molecules, PD-3, PD-5, PD-6, PD-28, PD-29 and PD-30 yielded relatively promising results on viability (**Figure 4.12(A)**).

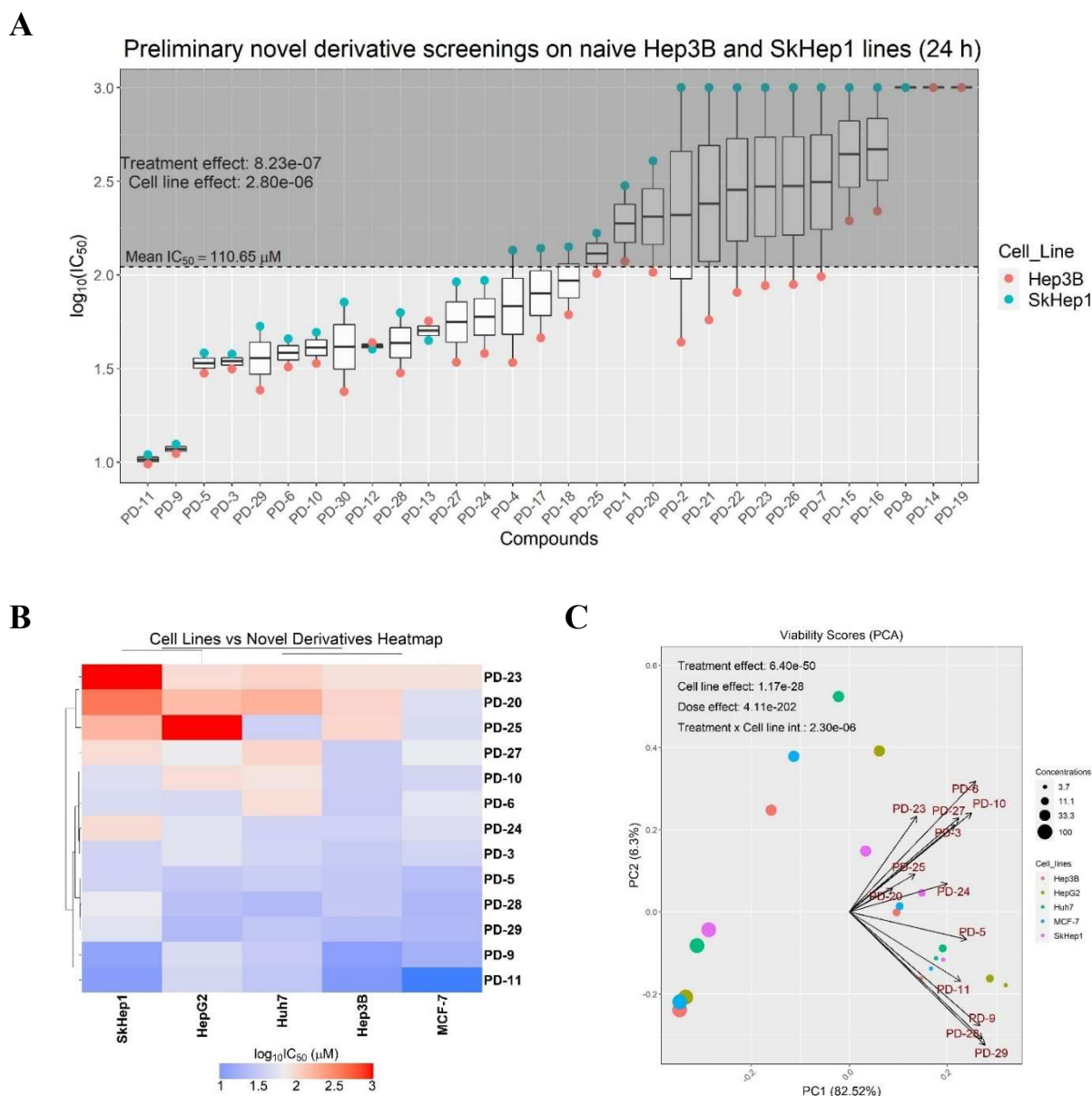


Figure 4.12 Non-generic PTZ derivative screenings in vitro. (A) Initial screenings across Hep3B and SkHep1 cell lines. (B) Heatmap clusters for the cell lines and logIC₅₀ values of each derivative. Blue-white-red scale indicate the amount of logIC₅₀. (C) PCA was generated by using the viability percentiles from the 24-hour exposures to the derivatives on multiple cell lines as n-way ANOVA statistics are provided.

Candidate compounds from the first screen were additionally tested on HepG2, Huh7 and MCF-7. The results have yielded overlapping profiles between MCF-7, SkHep1 and HCC lines, implying that the derivatives were also effective on non-HCC cell lines. In-depth comparisons were made easier with heatmap clusters where MCF-7 and Hep3B gave more similar results with each other, as SkHep1 and HepG2 bundled aside from the remaining cell

lines (**Figure 4.12(B)**). Furthermore, viability percentiles for each biological triplicate were utilized to investigate the effects of cell-types and concentrations of each treatment via n-way ANOVA (**Figure 4.12(C)**). We have observed separate clusters of concentrations, strongly supporting the dose-dependency (p-value: 4.11e-202) where the treatments affected the viability scores differently (p-value: 6.40e-50). Moreover, the cell lines in this study represented alternating profiles on the viabilities (p-value: 1.17e-28). Interaction between the treatment effects and the cell line factors were eminent for non-generic derivatives (p-value: 2.30e-06). Presence of the MCF-7 breast cancer control line was additionally questioned for the cell line effects. Therefore, non-parametric Kruskal-Wallis/Dunn's statistics were performed across the cell lines (**Figure Appendix B2**). Accordingly, the compounds were confirmed to be effective across the non-HCC and HCC lines. Besides that, the synthesized derivatives PD-5, PD-9, PD-11, PD-28 and PD-29 emerged as promising derivatives from the cytotoxicity assessments.

4.2.1.2.2 eGFP line comparisons and time-dependencies of the synthesized derivatives

eGFP status did not yield any significant results by t-tests for Hep3B and SkHep1 (p-values: 0.082 and 0.76)(**Figure 4.13(A)**). N-way ANOVA further complimented the irrelevance of eGFP status for the novel compounds, as the treatment effect (p-value < 2e-16) and Hep3B-SkHep1 cell type differences (p-value: 0.0082) were confirmed. Differential effects of the cell lines were recorded to be dependent on the type of compounds (p-value: 0.035).

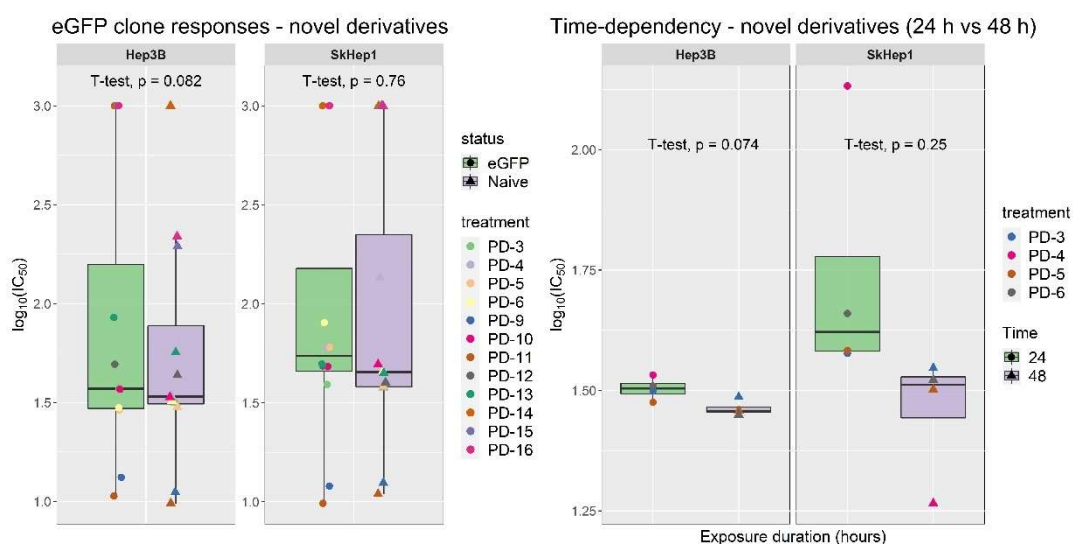


Figure 4.13 Dependence of the novel derivatives' toxicity profiles on (A) eGFP status and (B) exposure time. Hep3B and SkHep1 cell lines were used, as t-tests were performed for initial comparisons.

Initial t-test assessments were indicative for a time-dependency of the exposures (PD-3, PD-4, PD-5 and PD-6) on Hep3B and SkHep1 (**Figure 4.13(B)**). N-way ANOVA statistics by the viability scores further supported the effect of exposure time (p-value: 1.06e-05). The analyses also confirmed that Hep3B and SkHep1 responded differently to the exposures (p-value: 0.00388).

The findings supported the use of eGFP clones in representing the parent lines. Also, exposure duration is an important parameter for the responses of the derivatives, and novel compounds alike.

4.2.1.3 Cytotoxic effects of SFB combination exposures with the generic compounds

After exposures to a large scale of compound and combination concentrations, average viability percentiles were used in assessing the synergy scores via SynergyFinder tool. Initial evaluations were focused on PCP and TFP on Hep3B cell line for 24 hours of exposures. They showed that the derivatives can synergize with SFB where TFP caused a relatively higher synergistic potential (**Figure 4. 14**).

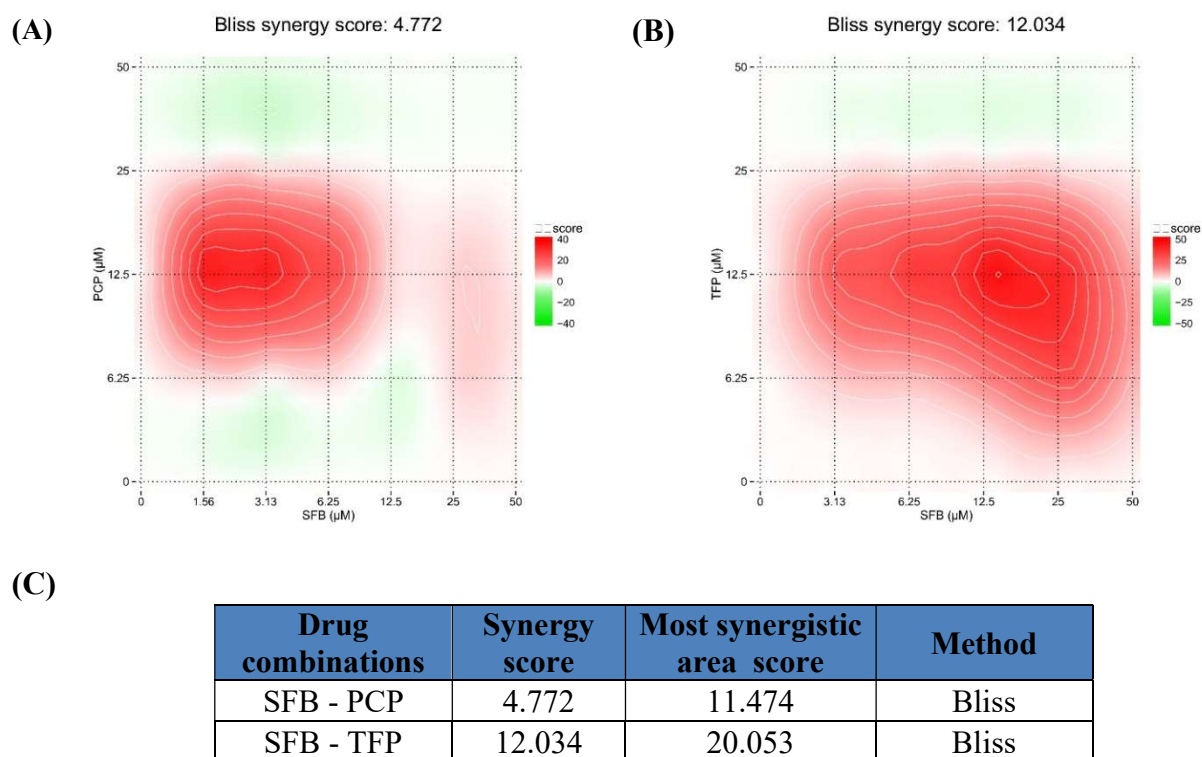


Figure 4. 14 Preliminary SFB synergism evaluations of PCP and TFP.(A) PCP-SFB synergy map, and (B) TFP-SFB synergy map, and (C) synergy scores, respectively. SynergyFinder with BLISS-LOESS parameters were utilized in deriving the synergy maps. Positive scores from this tool represent synergism where it becomes stronger as the score increases (provided on the red color scale). Oppositely, antagonistic levels are demonstrated by the scores below zero on the green color scale.

Next, we have investigated if the synergism is solely dependent on Hep3B and 24-hour exposures only. For that, TFP-SFB synergism was evaluated across the three HCC (Hep3B, HepG2 and Huh7) and one liver adenocarcinoma line (SkHep1) for 24 and 48 hours (**Figure 4.15** and **Figure 4.16**, respectively).

24-hour evaluations have prioritized the Hep3B line as relatively the most sensitive liver cell line to the synergism of TFP and SFB (**Figure 4.15 (A)**). Dose curve shifts (EC50 shifts) further supported this notion as the combination curve followed a sharp relocation from both TFP and SFB towards an improved cytotoxicity area. Furthermore, two-way ANOVA/Dunnett and multiple t-test/Holm-Sidak comparisons supplemented these findings where they revealed significant viability differences for each concentration point of combination against each single TFP and SFB treatment. Dose-by-dose differences were also observable for the other cell lines, yet their synergistic scores remained lower than Hep3B's. Surprisingly, SkHep1 represented a complete opposite trend where TFP and SFB pairs demonstrated strong antagonistic interactions (**Figure 4.15 (B)**). Based on the TFP 12.5 μM concentration curve shifts in SkHep1, the combination was able to increase the toxicity in comparison to TFP alone. However, the cytotoxic effects of SFB alone treatments were seemed to be diminished undoubtedly in the case of combination treatments on SkHep1 by 24 hours.

Interestingly, both synergistic and antagonistic dose areas were observable within and across the HCC lines and SkHep1. As the antagonistic areas were less visible for Hep3B and most eminent in SkHep1, synergistic/antagonistic effects followed a dual nature in HepG2 and Huh7 HCC lines (**Figure 4.15 (C, D)**). Although TFP-SFB synergism was effective by the low doses of exposures on HepG2, beyond 6.25 μM SFB antagonistic profiles came to light. Similar shifts were also noticeable in Huh7. Dose-by-dose effects were also comparable for both HepG2 and Huh7. Accordingly, presence of 12.5 μM TFP did not improve the effects posed by SFB alone, even it slightly diminished the cytotoxic effects in Huh7.

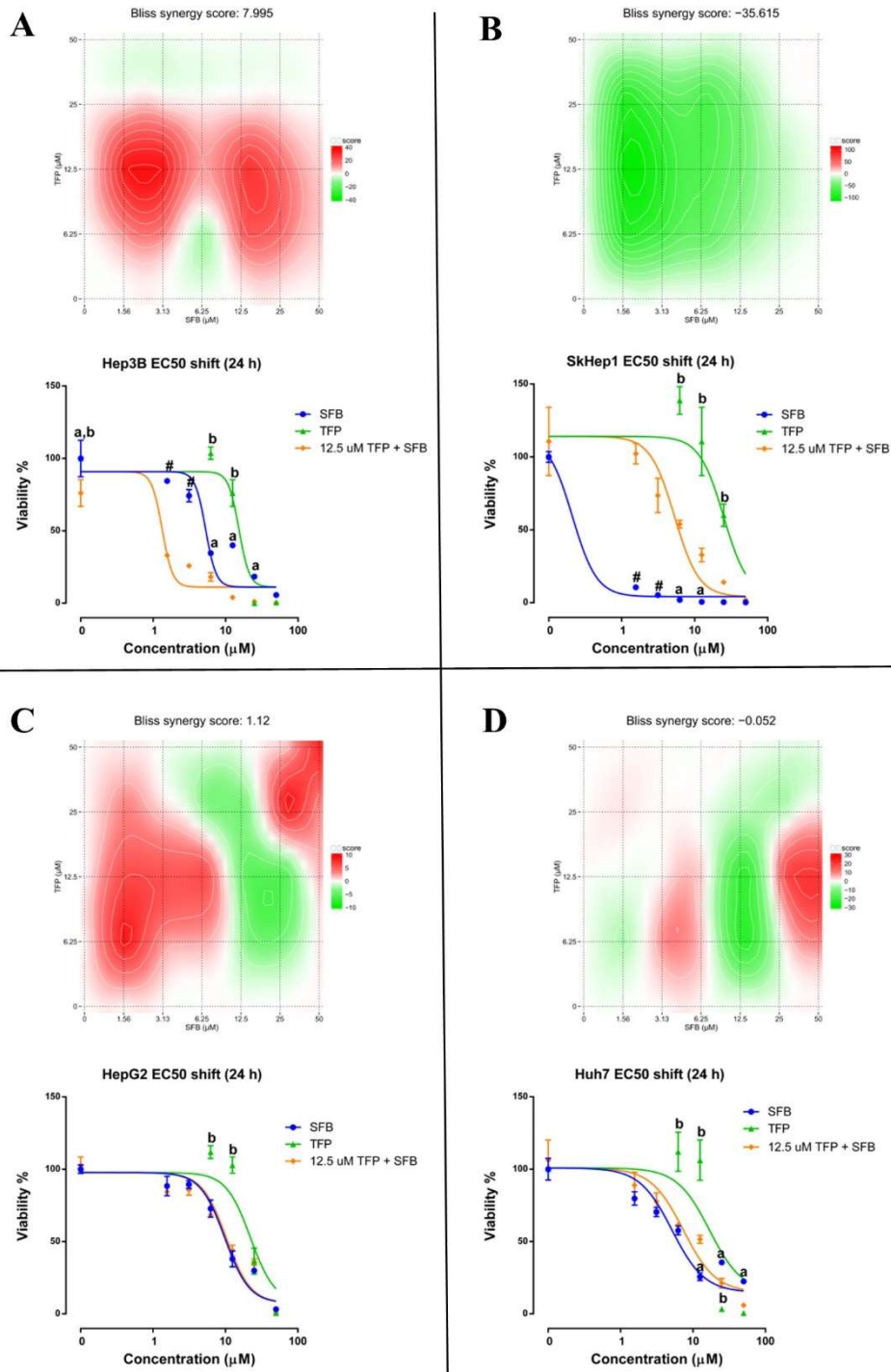


Figure 4.15 Synergy maps and dose-response curve shifts for the TFP-SFB combination exposures (24 hour) across the liver cancer lines: (A) Hep3B, (B) SkHep1, (C) HepG2 and (D) Huh7, respectively. p -values <0.05 ; a: SFB vs combination (two-way ANOVA/Dunnett), b: TFP vs combination (two-way ANOVA/Dunnett) and #: SFB vs combination (multiple t-test/Holm-Sidak)

48-hour exposures supported the previous synergy maps and concentration-curve shifts (**Figure 4.16**). Interestingly, synergy scores for Hep3B and SkHep1 became relatively closer to zero than what we observed at 24th hour (**Figure 4.16** (A, B)). Yet, synergistic effects of

TFP-SFB pair in Hep3B and antagonistic profiles of SkHep1 along the synergy maps and concentration curves were still remarkable. In the case of HepG2, dual synergistic/antagonistic events were discernible, although relatively synergistic effects were seeming to be constrained to the SFB concentrations lower than 2 μ M (**Figure 4.16 (C)**). Besides that, additions of TFP 6.25 μ M to the SFB solution did not seem to improve the potential of SFB, yet below this TFP concentration Huh7 was appeared to gain some synergistic profiles on viability (**Figure 4.16 (D)**).

As a result of the secondary SFB assessments across the primary liver cancer lines, we have seen that the cells can respond to the combination concentrations differently, as the effects might slightly differ by time (**Table 4.5**). Hep3B emerged as the cell line with relatively most synergistic effects of TFP-SFB, whereas non-HCC line SkHep1 with relatively most antagonistic profiles.

Table 4.5 Synergy scores of TFP-SFB combinations from **Figure 4.15** and **Figure 4.16**

Time (h)	Cell line	Synergy score	Most synergistic area score	Method
24	Hep3B	7.995	10.952	Bliss
	SkHep1	-35.615	-10.613	Bliss
	HepG2	1.12	3.551	Bliss
	Huh7	-0.052	1.04	Bliss
48	Hep3B	3.378	7.534	Bliss
	SkHep1	-15.586	-0.059	Bliss
	HepG2	-1.261	3.475	Bliss
	Huh7	1.886	6.111	Bliss

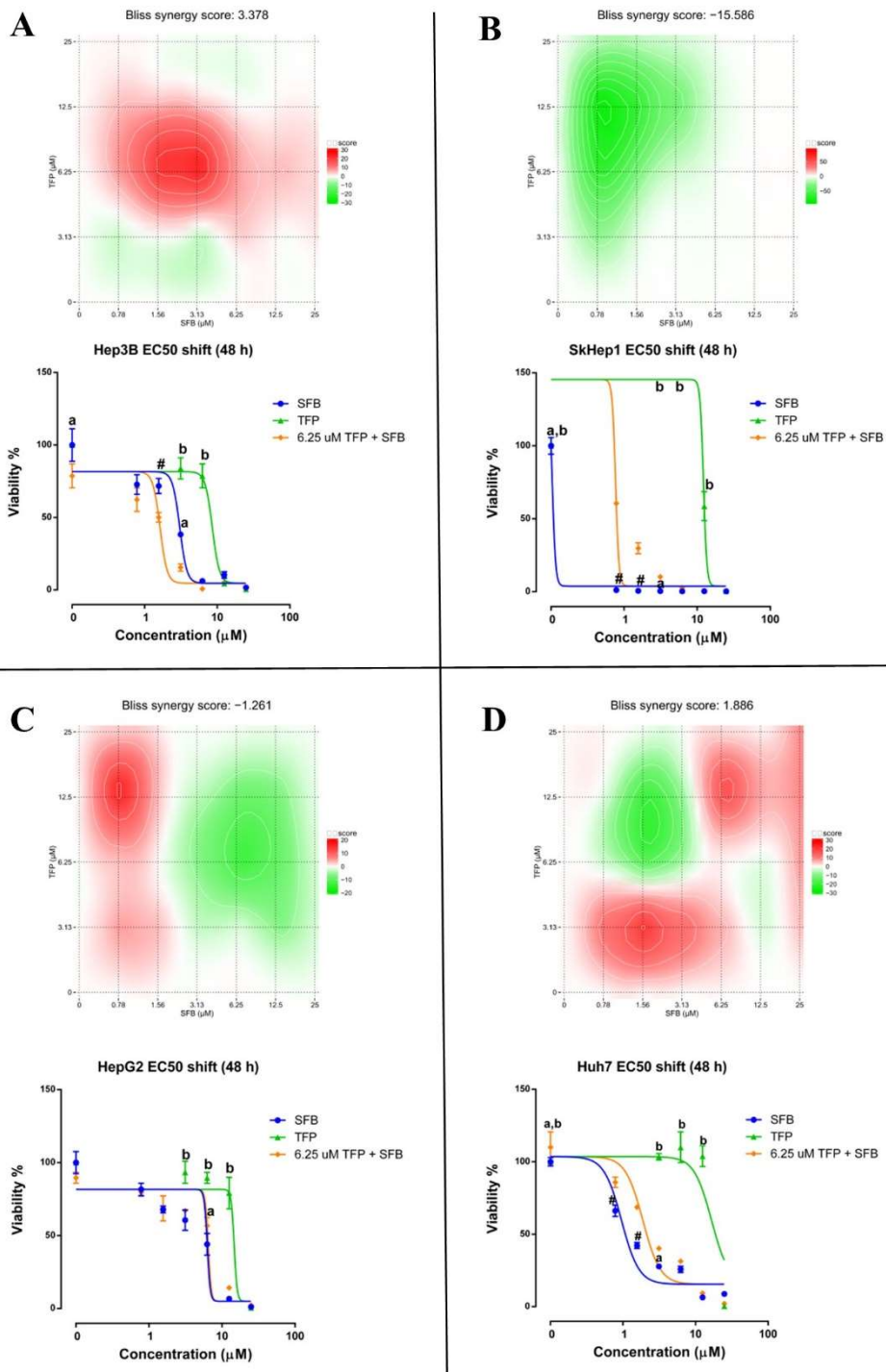


Figure 4.16 Synergy maps and dose-response curve shifts for the TFP-SFB combination exposures (48 hour) across the liver cancer lines: (A) Hep3B, (B) SkHep1, (C) HepG2 and (D) Huh7, respectively. p -values < 0.05 ; a: SFB vs combination (two-way ANOVA/Dunnett), b: TFP vs combination (two-way ANOVA/Dunnett) and #: SFB vs combination (multiple t -test/Holm-Sidak)

4.2.1.4 Synergistic effects of SFB-PD-5 combination on Hep3B cytotoxicity

SFB synergism was initiated on the novel derivatives. Then, the candidate compound PD-5 was taken into synergism evaluations on Hep3B for 24-hour exposures (**Figure 4.17**). Accordingly, PD-5 has yielded a high synergistic profile which was seemed to be comparable what we previously observed in TFP-SFB combinations. The synergistic area mainly fell between the PD-5 concentrations of 6.25 μM and 25 μM . Findings were suggestive for screening this compound and some candidates on multiple cell lines and for 48 hours, additionally.

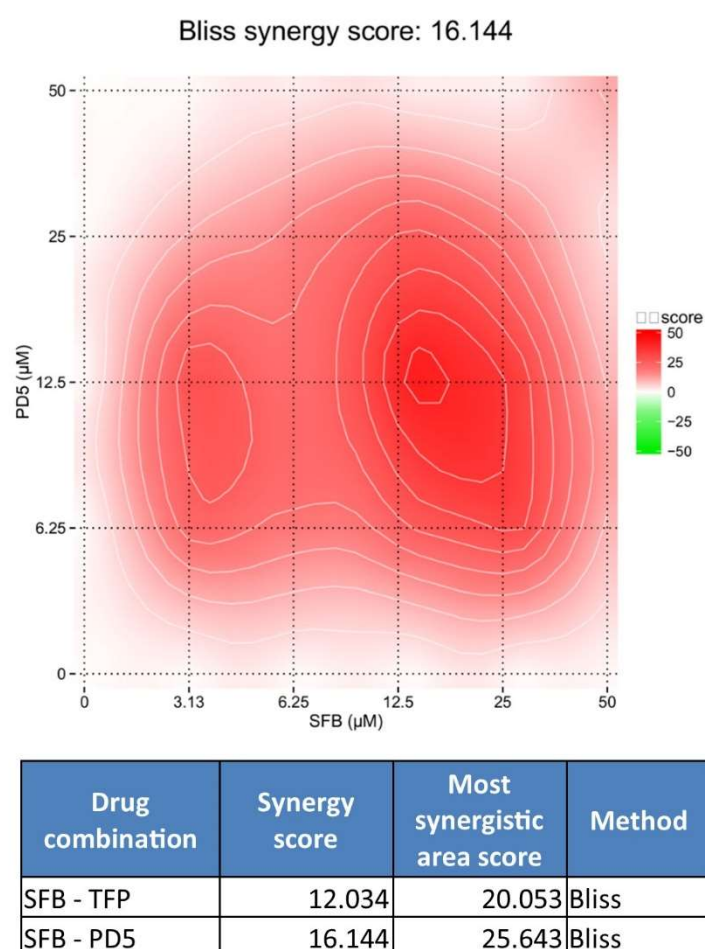


Figure 4.17 SFB-PD-5 synergism evaluations on Hep3B.(A) SFB-PD-5 synergy map, (B) SFB synergy scores for PD-5 and TFP, as TFP scores are referred for comparative purposes. SynergyFinder with BLISS-LOESS parameters were utilized in deriving the synergy maps. Positive scores from this tool represent synergism where it becomes stronger as the score increases (provided on the red color scale). Oppositely, antagonistic levels are demonstrated by the scores below zero on the green color scale.

4.2.2 In vivo toxicities of the derivatives

Toxicity and anti-cancer properties of the derivatives were also investigated *in vivo*. Initially, developmental effects of the compounds were assessed on zebrafish embryos. Secondly, the influence of SFB combinations for the candidate derivatives were explored based on the affected embryo percentiles. Lastly, xenograft potencies of the candidate derivative screenings were examined. As the first two steps were performed in Karlsruhe Institute of Technology (Germany), xenograft experiments were followed in the zebrafish facility of Bilkent University (Turkey).

4.2.2.1 Developmental toxicities of individual phenothiazines

Although cytotoxicity profiles can be promising, a drug candidate is also supposedly to be less harmful to developing embryos and normal-like surroundings. To address that, the potencies of the derivatives were evaluated on AB strain zebrafish embryos. The effects of the novel and synthesized compounds in embryonic development ranging from 6 hpf to 120 hpf were assessed. In this regard, dose responses of the embryos towards the chemicals were evaluated by means of affected embryo rates and hatching ratios.

4.2.2.1.1 Developmental effects of generic phenothiazines

Embryonic toxicity assays revealed that most of the generic derivatives also became toxic to the embryos by 72 hpf and 120 hpf, within the micromolar scale applied (**Table Appendix B3**). Despite the missing 120 hpf data for TFP, it emerged as the relatively fewer toxic compound from the generic molecules (**Table 4.6**). Yet, recordings by 120 hpf time-point is needed for more straight interpretations.

Table 4.6 EC₅₀ values for 72 hpf and 120 hpf zebrafish after the generic molecules

	EC ₅₀ (μM)	
	72 hpf	120 hpf
PTZ	14.27	14.32
PPH	5.80	5.33
PCP	11.74	9.69
TFP	38.5	NA
SFB	ND	3.81

ND: No EC₅₀ detected, NA: Not available

Images from the screening data further helped in evaluating the hatching percentiles. Calculations done in collaboration with Busra Korkmaz have shown reduction on hatching especially by 72 hpf, suggesting developmental delay by high doses (**Figure 4.18**). In this regard, applied concentrations of PPH and PCP have yielded toxic effects. However, overall toxicities of the compounds by the respective concentrations should be also considered. As a result of *in vivo*

developmental assays, TFP was found to be relatively less toxic within the ranges of doses applied, complementing its possible use for repurposing.

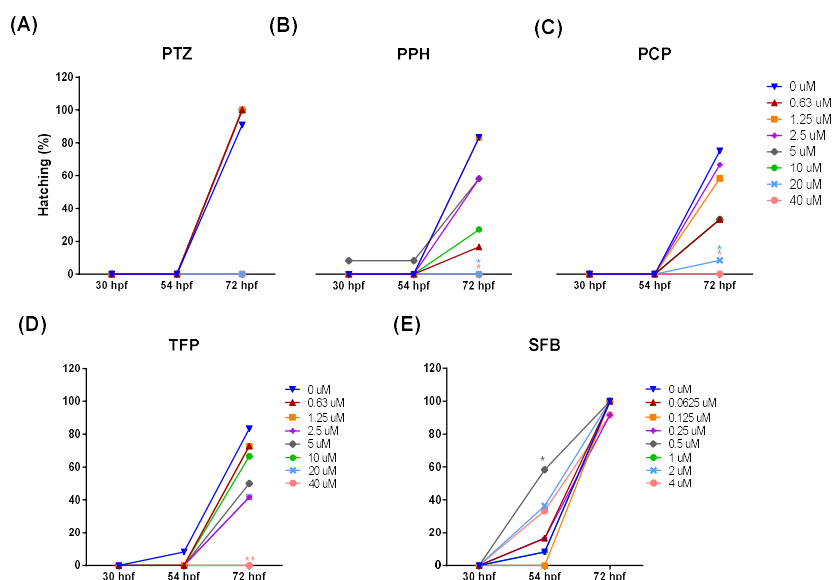


Figure 4.18 Hatching (%) of zebrafish embryos within the timeframe of 30 hpf - 72 hpf (A) PTZ, (B) PPH, (C) PCP (D) TFP and (E) SFB. Analyses were performed by Busra Korkmaz against 0 μM control group for each hpf. Two-way ANOVA/ Dunnett methodology was followed. (p-values: * ≤ 0.05 , ** ≤ 0.01 , *** ≤ 0.001)

4.2.2.1.2 Developmental effects of non-generic derivatives

Embryonic toxicities of the novel compounds were observed within the micromolar scale (Table Appendix B3). Relatively fewer toxic novel derivatives were PD-3, PD-5, PD-21 and PD-22, where PD-5 is strongly indicative for further analyses in line with the *in vitro* findings. Interestingly, the intermediary derivatives (PD-9, PD-10 and PD-11) that exerted relatively high toxicities *in vitro*, were also toxic *in vivo*. Since the candidate compounds PD-28 and PD-29 were not available by the time of screenings in Karlsruhe Institute of Technology, their embryonic toxicities were not evaluated thoroughly as for the compounds in the Table 4.7.

Table 4.7 EC₅₀ values for 72 hpf and 120 hpf zebrafish after the non-generic derivatives

	EC ₅₀ (μM)	
	72 hpf	120 hpf
PD-3	39.46045	28.47915
PD-4	15.36042	8.830335
PD-5	> 40	> 40
PD-6	12.8558	11.5349
PD-9	5.772856	5.065836
PD-10	4.437146	4.602024
PD-11	4.170947	6.032798
PD-21	> 40	> 40
PD-22	33.48097	20.84702
PD-23	17.38497	21.0482
PD-24	8.227576	8.537177

Hatching percentiles were additionally analyzed by Busra Korkmaz and revealed developmental delays by the derivatives: PD-3, PD-4, PD-6, PD-9, PD-10, PD-11, PD-23 and PD-24 (**Figure 4.19**). Overall toxicities by the respective concentrations should be also taken into account. In addition to TFP, in vivo developmental assays on novel derivatives indicated relatively fewer toxic profiles by PD-3, PD-5 and PD-21.

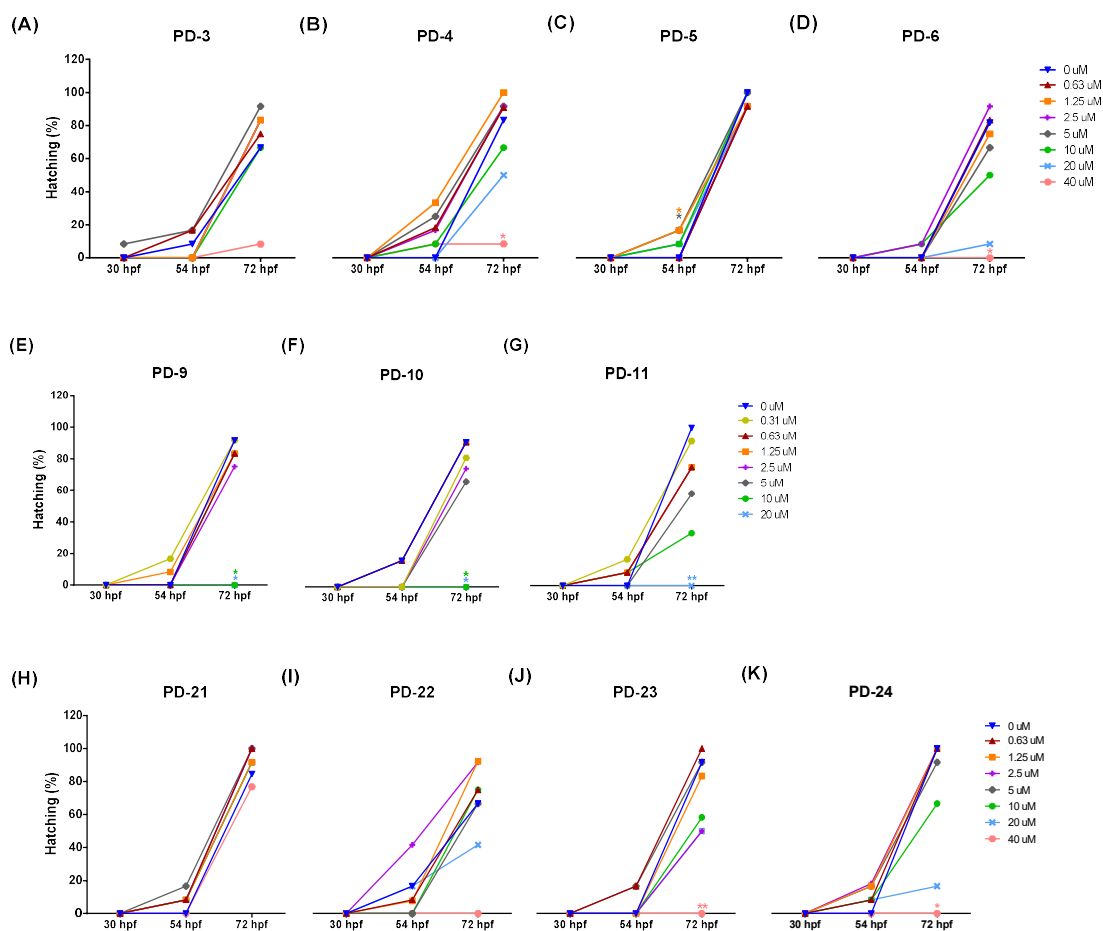


Figure 4.19 Hatching (%) of zebrafish embryos within the timeframe of 30 hpf - 72 hpf. (A) PD-3, (B) PD-4, (C) PD-5, (D) PD-6, (E) PD-9, (F) PD-10, (G) PD-11, (H) PD-21, (I) PD-22, (J) PD-23 and (K) PD-24. Analyses were performed by Busra Korkmaz against 0 μM control group for each hpf. Two-way ANOVA/ Dunnett methodology was followed. (p-values: * ≤ 0.05 , ** ≤ 0.01 , *** ≤ 0.001)

4.2.2.2 SFB combination effects on embryonic development

SFB synergisms were additionally investigated *in vivo* where the AB strain zebrafish embryos were exposed to varying concentrations of the derivatives and SFB between 48 hpf and 120 hpf

4.2.2.2.1 Generic phenothiazines

Antagonistic profiles were prominent after exposures, implying improved survival rates by the combinations with respect to their constituents alone, surprisingly (**Figure 4.20**). However, synergistic areas were also noticeable for most of the compounds. In the case of TFP-SFB pairs, the combinations were able to synergize and lead to more toxic profiles above the concentrations of SFB $2 \mu\text{M}$ and TFP $5 \mu\text{M}$ which were the most toxic areas. Although

relatively antagonistic topographies were observable below these concentrations, applicability of SFB and TFP in *in vivo* settings demanded additional considerations.

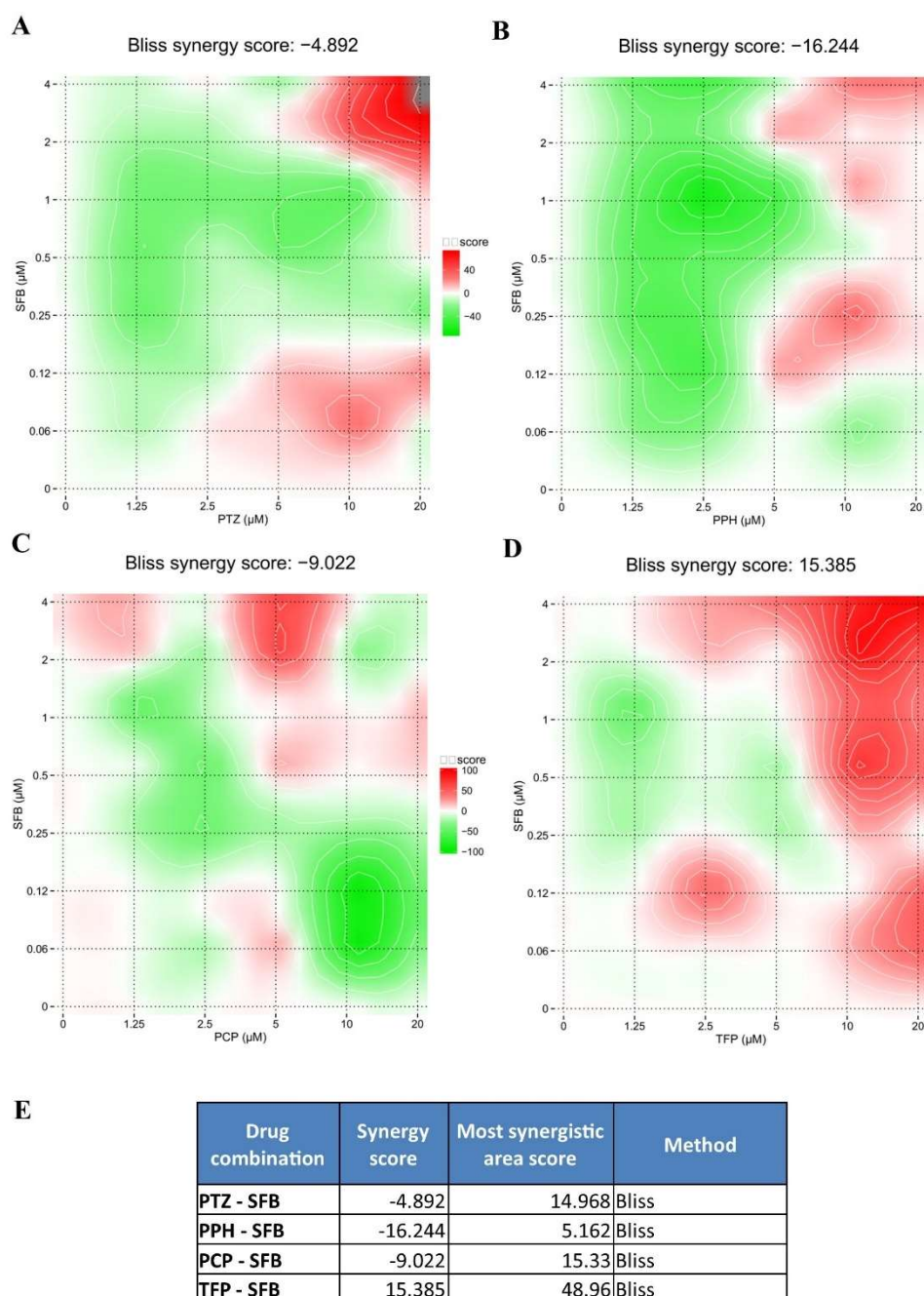


Figure 4.20 *In vivo* synergy maps for the SFB combinations of the generic derivatives.(A) PTZ, (B) PPH, (C) PCP, (D) TFP and (E) synergy scores. Green and red color scales represent antagonistic and synergistic dose intervals, respective. Gray color area indicates the topology masked by the SynergyFinder tool.

4.2.2.2 SFB combinations of PD-3, PD-5 and PD-9 *in vivo*

As in the generic derivatives, synthesized compounds also exerted both antagonistic and synergistic profiles (**Figure 4.21**). Synergistic areas were mainly observable by relatively high doses of SFB, implying that the combinations could not rescue survival rates as in the antagonistic ranges. SFB-PD-3 combinations have demonstrated relatively additive and synergistically neutral effects below PD-3 10 μM and SFB 2 μM ranges. Interestingly, SFB-PD-5 combinations clearly revealed antagonistic effects for the SFB concentrations between 0.125 μM and 2 μM , suggesting that the combination may counteract the toxic effects posed by the individual exposures. Moreover, developmentally toxic effects of PD-9 were further confirmed, although the concentration ranges below SFB 1 μM and above PD-9 1.25 μM were seemed to be more tolerable than the remaining concentrations. The results were in favor of PD-5 and SFB combinations from the novel derivatives, inquiring for further assessments.

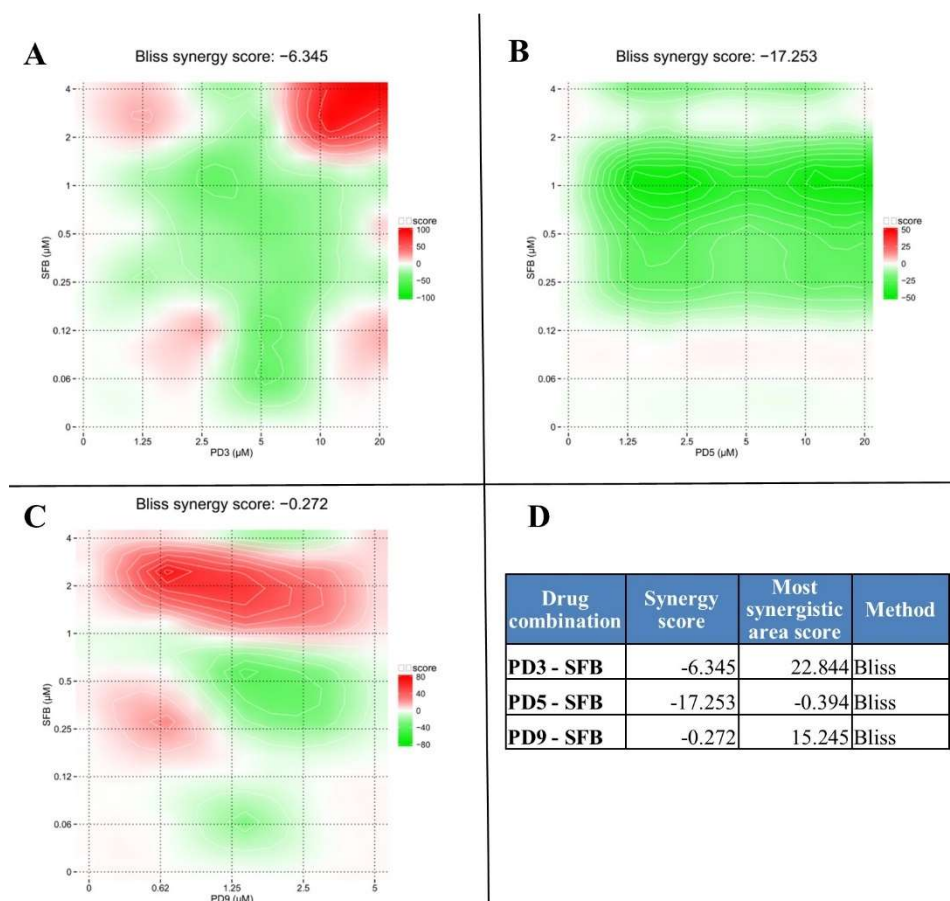


Figure 4.21 *In vivo* synergy maps for the SFB combinations of the generic derivatives. (A) PD-3, (B) PD-5, (C) PD-9, and (D) synergy scores. Green and red color scales represent antagonistic and synergistic dose intervals, respectively. Gray color area indicates the topology masked by the SynergyFinder tool.

4.2.3 Xenograft potencies of the derivatives

The derivatives TFP, PCP, PD-3, PD-5, PD-9, PD-11 and PD-29 were further evaluated for the tumor progression *in vivo*. For that purpose, SkHep1^{eGFP} cell lines were injected into the yolks of 48 hpf embryos and exposed to the relevant compounds until 120 hpf. Corrected total cell fluorescence (CTCF) amounts from the GFP signals were further utilized in calculating cancer cell proliferation. The table for representative images and survival/affected embryo ratios can be accessed in **Table Appendix B4**. As the Hep3B^{eGFP} lines did not recover after consecutive freeze-thaw procedures, we were not able to utilize them in xenograft settings.

4.2.3.1 Effects of TFP and PCP on tumor progress

Corrected total cell fluorescence (CTCF) amounts from the SkHep^{eGFP} cells showed significant reductions on the relative tumor sizes by TFP (10 μ M) exposures (**Figure 4.22**). Besides that, increasing doses of PCP also seemed to approach significance by 20 μ M. Therefore, role of TFP as an anti-cancer agent was further supported.

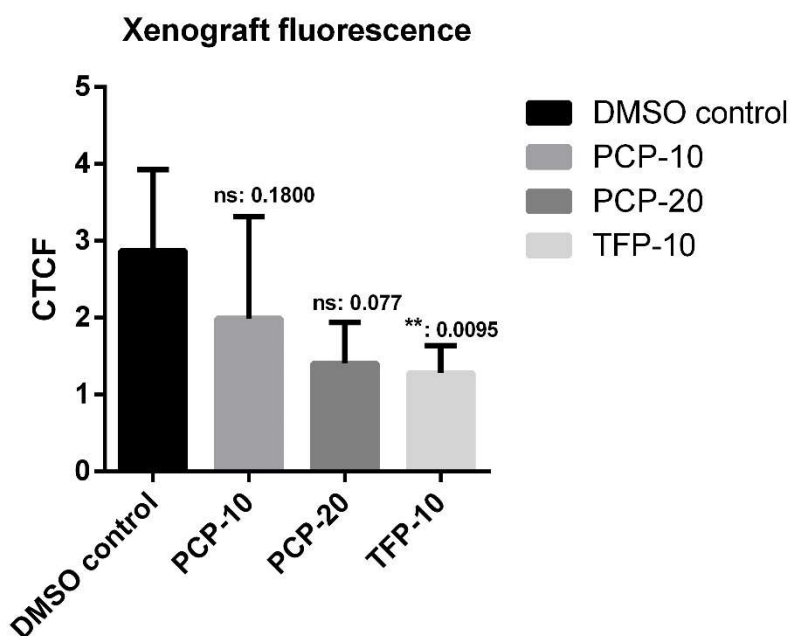


Figure 4.22 SkHep^{eGFP} xenograft tumor CTCF comparisons for PCP (10 μ M and 20 μ M) and TFP (10 μ M) exposures. One-way ANOVA/Bonferroni was performed for the comparisons against the DMSO control group (**: p-value<0.01, ns: not significant)

4.2.3.2 Effects of PD-3, PD-5, PD-9, PD-11 and PD-29 on tumor progress

CTCF amounts from the SkHep^{eGFP} cells demonstrated significant reductions on the relative tumor sizes by the compounds PD-3 (20 μ M), PD-5 (10 μ M), PD-9 (5 μ M), PD-11 (5 μ M) and PD-29 (20 μ M) (**Figure 4.23**). Although, findings supported the anti-tumor effects of PD-

3 and PD-29 by the applied doses, signals from the experiment comprising of DMSO (0.5%), PD-5, PD-9 and PD-11 were found to yield low CTCF overall, strongly demanding additional validations

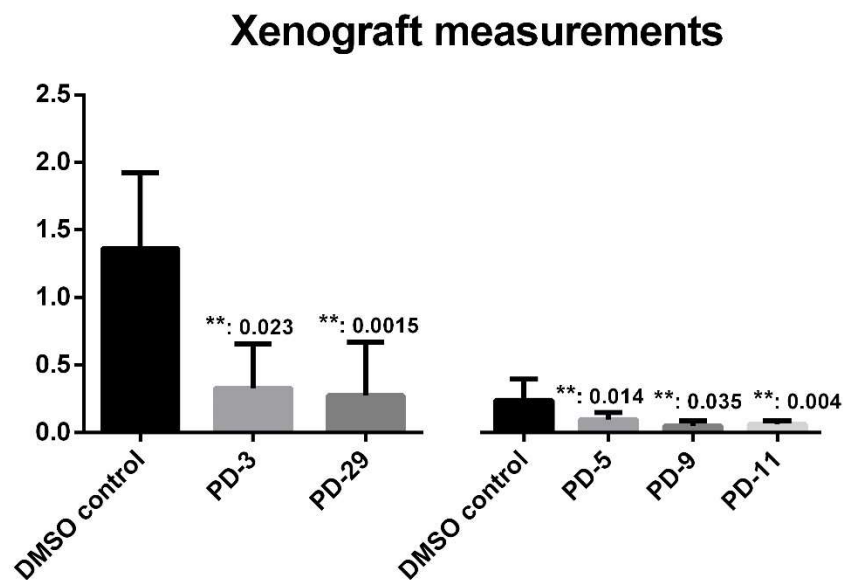


Figure 4.23 SkHep^{eGFP} xenograft tumor CTCF comparisons for PD-3 (20 μ M), PD-5 (10 μ M), PD-9 (5 μ M), PD-11 (5 μ M) and PD-29 (20 μ M). One-way ANOVA/Bonferroni was performed for the comparisons against the DMSO control group (**: p-value < 0.01, ns: not significant)

4.2.4 *In silico* target screenings for the derivatives

Initial line of work for PTZ derivative targets were followed by SwissTarget comparisons. The data retrieved by Omer Bayazeid (Hacettepe University/Turkey) was further investigated and later demonstrated by heatmap, suggesting multiple binding partners for the derivatives. (**Figure 4.24**). Accordingly, novel derivatives may follow distinctive profiles than the generic compounds. We have observed that cholinesterase affinity levels can be relatively higher in the non-generic derivatives which can also target ion dependent serotonergic, dopaminergic and aminoacid transporters. Moreover, the generics were seemed to be more related with acetylcholine receptors and adrenergic receptors. Conceivably, D2 and D4 dopaminergic receptors were found to be a mutual target for the derivatives. Therefore, preliminary *in silico* assessments have shown that generic and novel derivatives can have some targets in common, besides alternative mechanisms can also be influenced by the derivatives. Interestingly, prominent novel and intermediary derivatives PD-3, PD-5, PD-9 and PD-11 and generic derivative TFP were able to show possible interactions with muscleblind-like proteins.

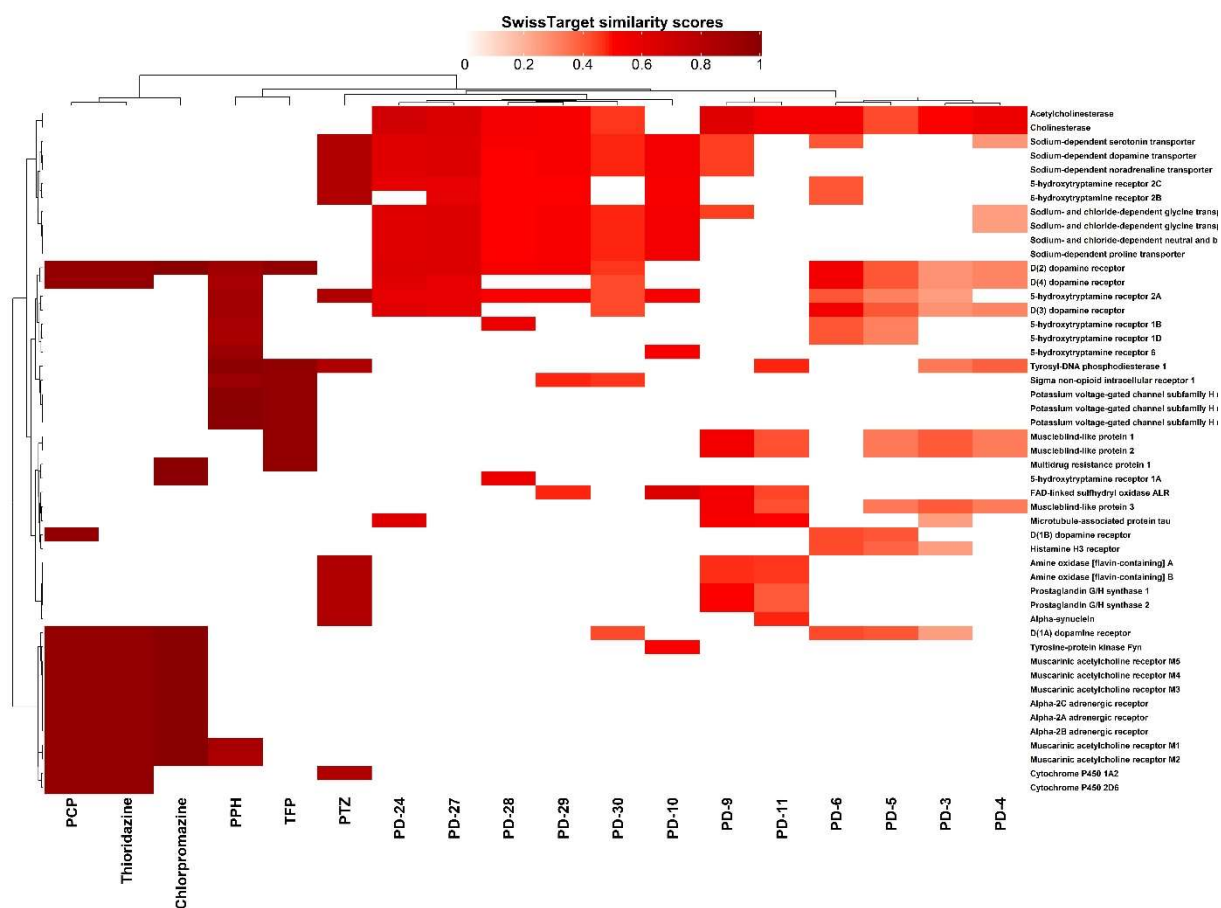


Figure 4.24 Ward distance based heatmap derived from SwissTarget prediction scores. Color scale indicates higher interaction rates from lighter to darker tones between the scale of 0-1.

4.2.5 Effects of the derivatives on cholinesterase levels

As AChE modulation can be a crucial element on the effects of the PTZ derivatives, functions of the exposures were initially evaluated through cholinesterase activity assays in both *in vitro* (Hep3B and SkHep1) and *in vivo* settings. Although *in vitro* work was non-specific towards AChE/BChE levels, lack of functional BChE in zebrafish embryos led to more AChE oriented results.

AChE/BChE activity levels were reduced in SkHep1 cell line where the effects were more noticeable by the novel derivatives (**Figure 4.25 (A)**). A significant dose effect was observed between 10 μ M and 20 μ M exposures via two-way ANOVA approach (p-value: 0.0138). In the case of Hep3B we have noticed an opposite trend on the cholinesterase activity levels where significant effects were more observable on the novel derivatives (**Figure 4.25 (B)**).

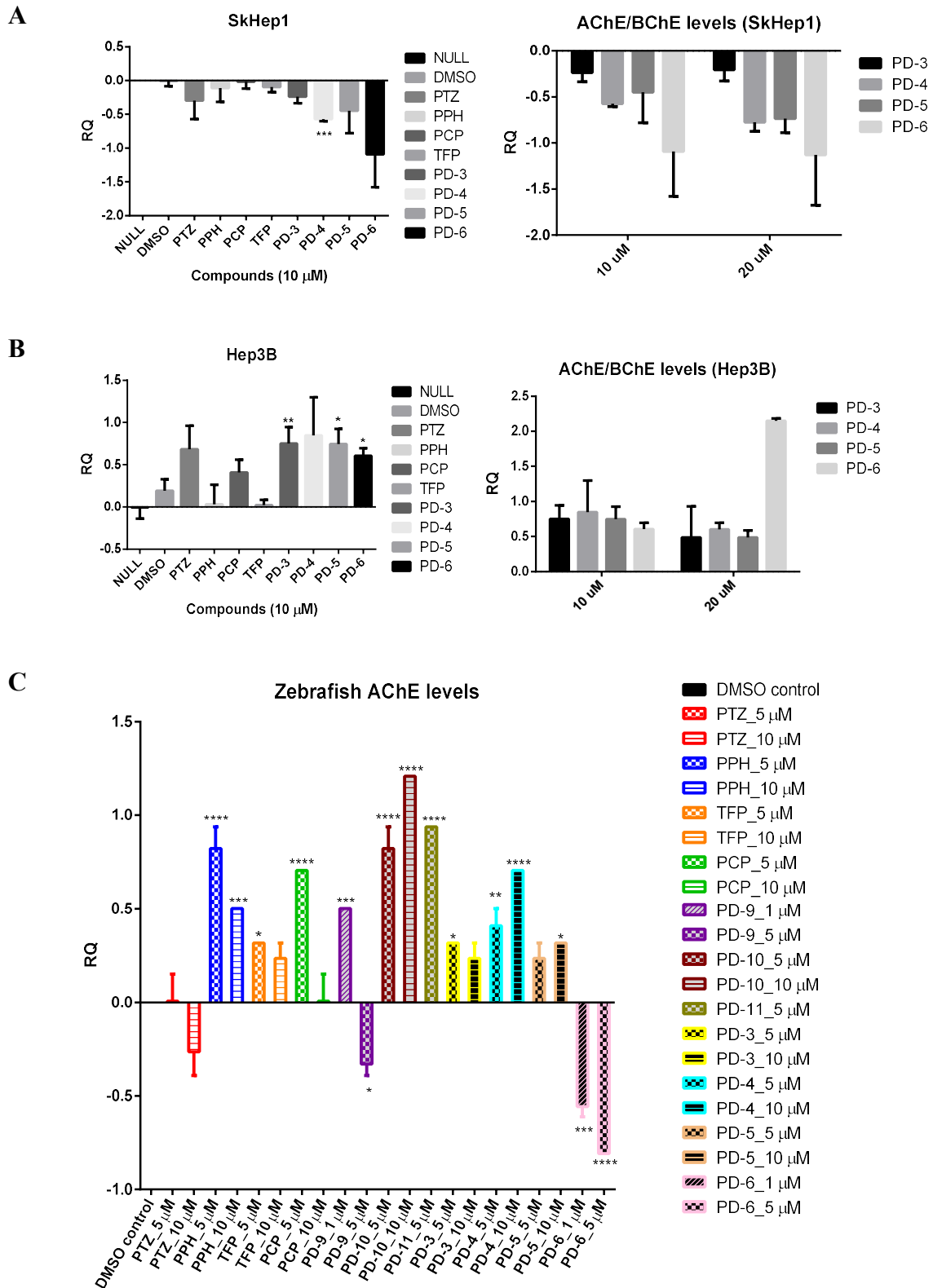


Figure 4.25 Cholinesterase activity measurements across (A) SkHep1, (B) Hep3B and (C) zebrafish embryos. Figures on the left-hand side indicate 10 μM exposures (A & B). (C) AChE activity screenings were obtained from various derivatives and concentration values applied based on the toxicity values. (*: $p < 0.05$, **: $p < 0.01$, an ***: $p < 0.001$)

Moreover, TFP-SFB combination effect on AChE/BChE activity was evaluated by 48 hours (Figure 4.26). SFB alone treatments were found to increase the levels (p-value: 0.0069). Interestingly, presence of TFP (12 μ M) seemed to reduce the AChE/BChE levels, most remarkably in combination with SFB 2 μ M (p-value: 0.005).

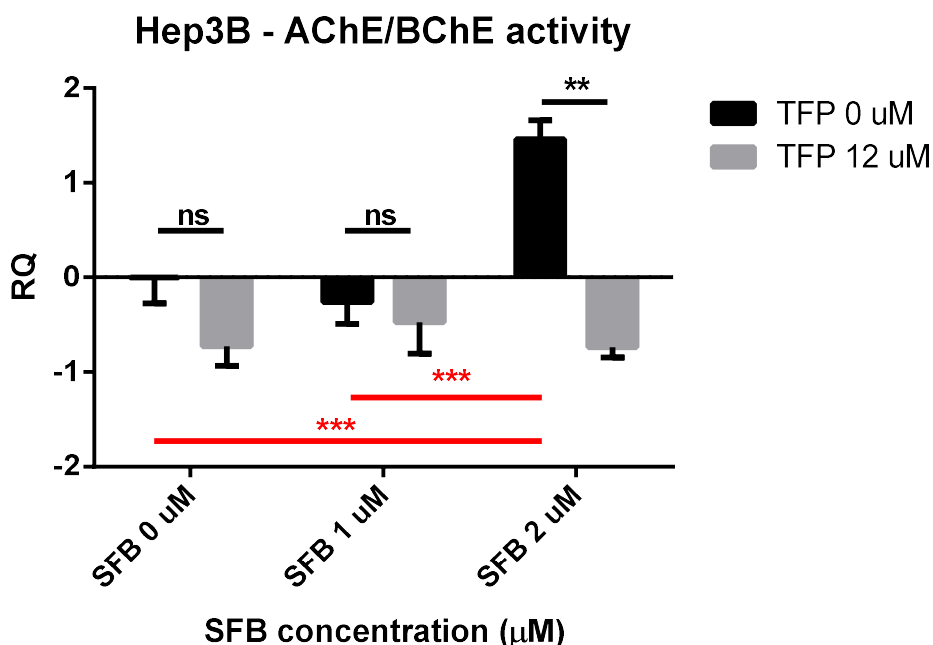


Figure 4.26 Cholinesterase activity changes after 48 hour exposures of TFP and SFB combinations on Hep3B. DMSO control (0.1%) (TFP 0 μ M – SFB 0 μ M) referred relative quantity values were provided in log₂ scale. TFP-SFB interactions were evaluated via two-way ANOVA/Tukey statistics (red color), as for each SFB concentration TFP effect was investigated via multiple t-test/Holm–Sidak approach (black color). *: p<0.05, **: p<0.01, ***: p<0.001. Two-way ANOVA p-values: TFP effect: 0.0002, SFB effect: 0.0069, TFP-SFB interaction: 0.0024 and multiple t-test by SFB 2 μ M: 0.005.

4.2.6 *In vivo* behavioral analyses of the derivatives on AB strain zebrafish embryos

As a follow-up to the findings on cholinesterase activity levels, we further explored the effects of the exposures *in vivo*. For that purpose, photomotor responses (PMR) after 30 hpf and locomotor responses by 5 dpf and were evaluated in AB strain zebrafish embryos.

4.3.1.1 PMR evaluations

Motor responses were additionally assessed on 30 hpf embryos by measuring their reactivities under light stimulus as the analyses were performed via Karlsruhe Institute of Technology authenticated softwares via ANOVA based approaches. For the assays, PCP, TFP, PD-9, PD-11 and SFB as well as combinations of SFB with PCP and TFP were evaluated.

4.3.1.1.1 PMR assessments for the generic compounds

Single PCP and TFP exposures revealed significant decreases in photomotor responses (PMR) by all three phases: basal, stimulus and refractory (**Figure 4.27** & **Figure 4.28**). Therefore, the compounds were observed to inhibit the motor abilities, irrespective of the light stimulus. The patterns were reminiscent of antipsychotic compounds: haloperidol and diazepam [98, 314].

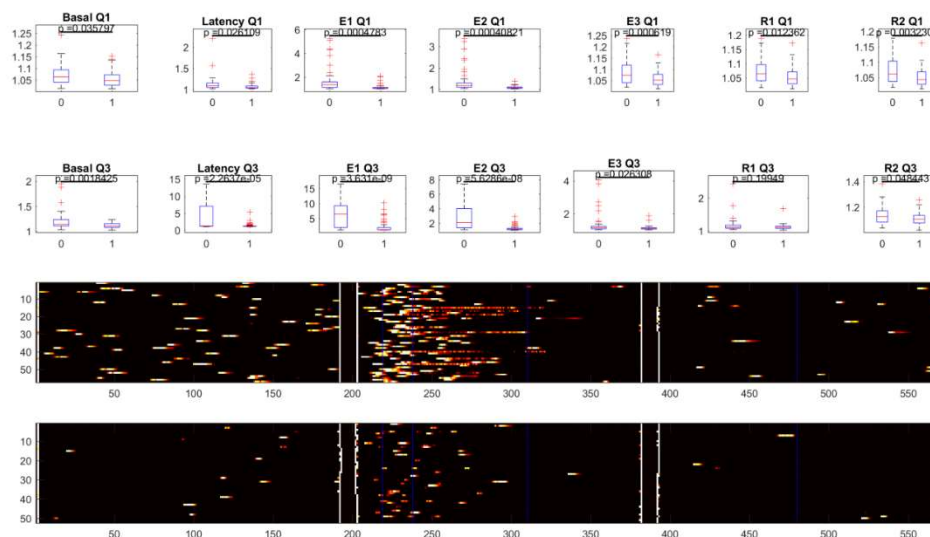


Figure 4.27 PCP (20 μ M) PMR results. Boxplots represent ANOVA statistics for each phase by contrasting with DMSO control. Heatmaps represent PMR intensities along the 6 seconds measurements where red indicates the highest, yellow modest and black no response. Upper panel heatmaps belong to the DMSO control group as the lower panel to the PCP group.

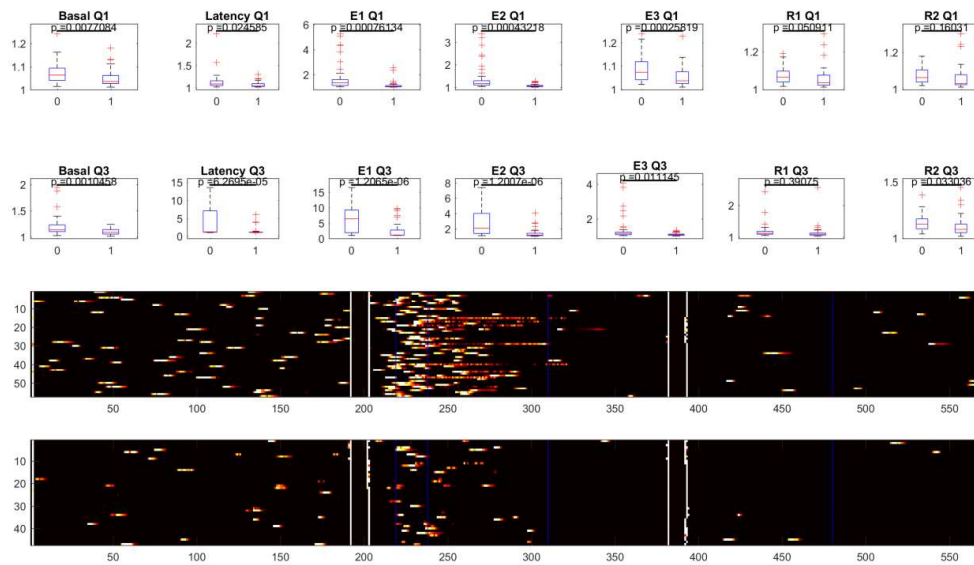


Figure 4.28 TFP (20 μM) PMR results.Boxplots represent ANOVA statistics for each phase by contrasting with DMSO control. Heatmaps represent PMR intensities along the 6 seconds measurements where red indicates the highest, yellow modest and black no response. Upper panel heatmaps belong to the DMSO control group as the lower panel to the TFP group.

SFB 2 μM exposure did not cause any significant differences in none of the phases. The photomotor responses of the embryos between the DMSO control group and SFB 2 μM have yielded overlapping activity patterns across the basal, stimulus and resting periods (**Figure 4.29**) Therefore, SFB with the applied concentration was found to not relate with motor activity.

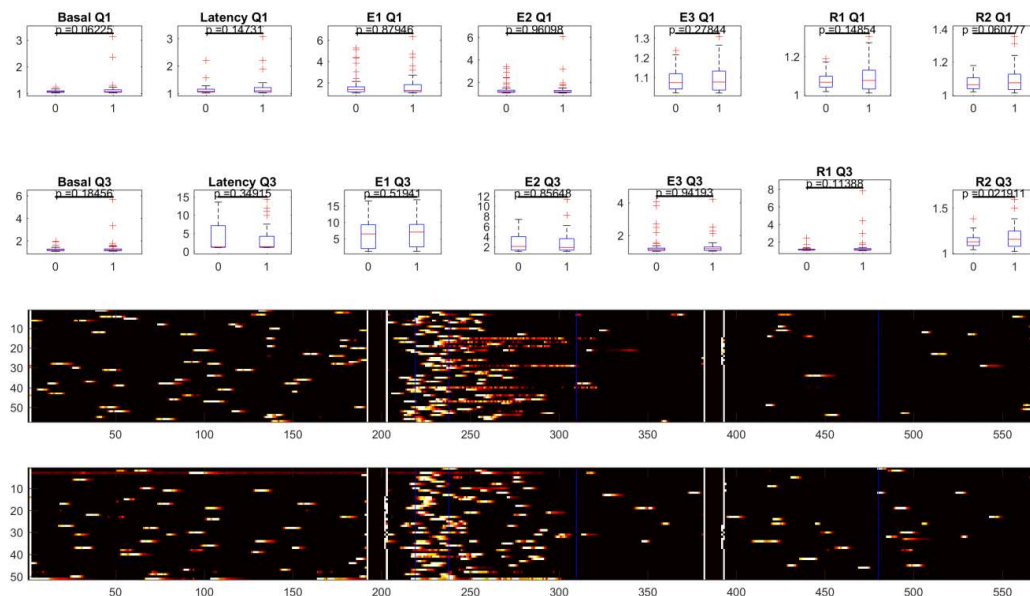


Figure 4. 29 SFB (2 μM) PMR results.Boxplots represent ANOVA statistics for each phase by contrasting with DMSO control. Heatmaps represent PMR intensities along the 6 seconds measurements where red indicates the highest, yellow modest and black no response. Upper panel heatmaps belong to the DMSO control group as the lower panel to the SFB group.

As in the case of individual PCP and TFP, embryos under the combination of SFB 2 μ M with PCP or TFP have remained relatively inert with respect to DMSO control group in all phases (**Figure 4.30 & Figure 4.31**). Thus, significant changes by the basal, stimulus and refractory phases were noticeable.

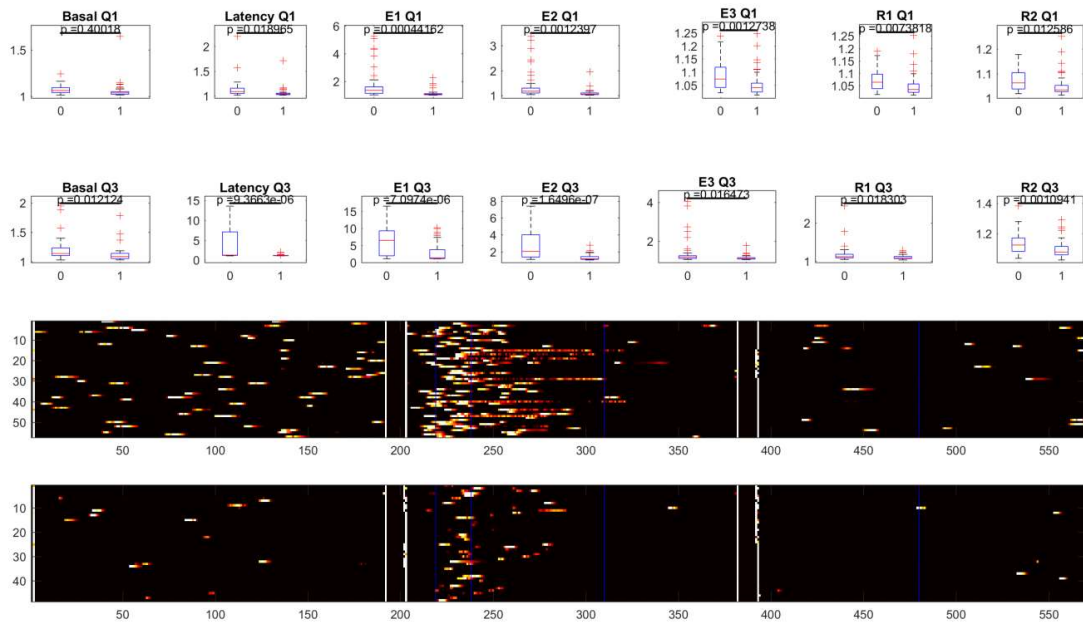


Figure 4.30 PCP (20 μ M) - SFB (2 μ M) PMR results. Boxplots represent ANOVA statistics for each phase by contrasting with DMSO control. Heatmaps represent PMR intensities along the 6 seconds measurements where red indicates the highest, yellow modest and black no response. Upper panel heatmaps belong to the DMSO control group as the lower panel to the PCP (20 μ M) - SFB (2 μ M) group.

Additional analyses confirmed the previous findings indicative for insufficient effect of SFB presence on the motor responses. For that purpose, the combination results were compared with their respective derivative concentration. Accordingly, we have not observed any significant changes in any of the phases, further supporting limited effects of SFB 2 μ M on motor responses overall (**Figure Appendix B6 & Figure Appendix B6**).

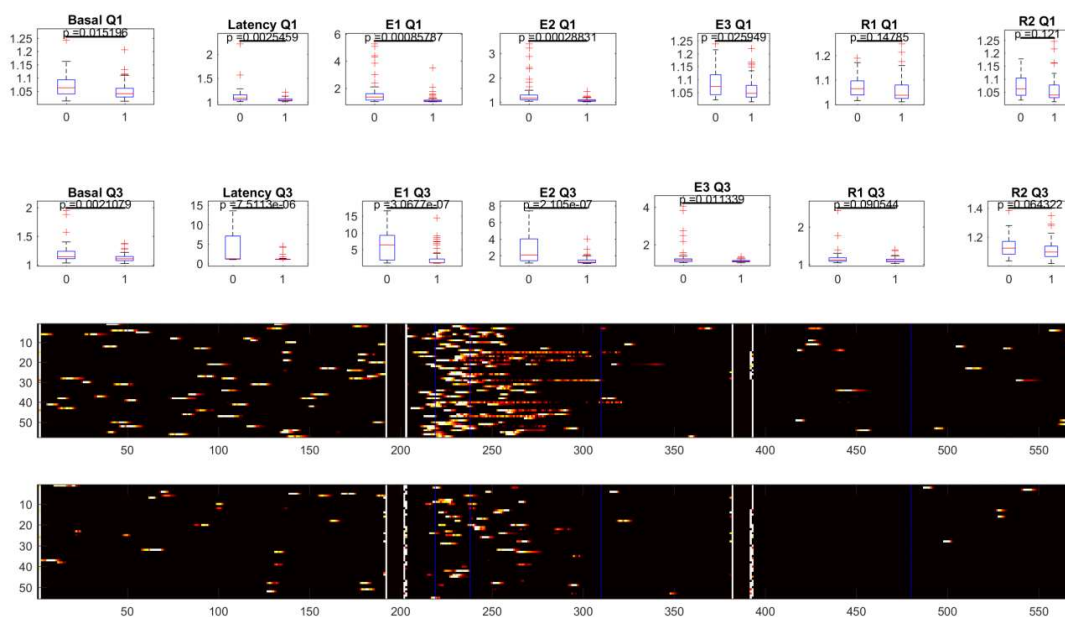


Figure 4.31 TFP (20 μM) - SFB (2 μM) PMR results. Boxplots represent ANOVA statistics for each phase by contrasting with DMSO control. Heatmaps represent PMR intensities along the 6 seconds measurements where red indicates the highest, yellow modest and black no response. Upper panel heatmaps belong to the DMSO control group as the lower panel to the TFP (20 μM) - SFB (2 μM) group.

4.3.1.1.2 PMR assessments for PD-9 and PD-11

Effects of PD-9 and PD-11 were limited to the excitation phases where PD-9 treatments have shown increase on the PMR levels (**Figure 4.32 & Figure 4.33**). Since the basal and resting phase activity levels do not show noticeable changes by these intermediary compounds, alternations on the activity levels were seemed to be more dependent on the initial light stimulus. Differential profiles were represented with respect to generic derivatives, suggesting an alternative MoA. Hence, large behavior-based compound libraries are in demand [98]. However, due to toxicity levels, the intermediary molecules were used in relatively lower concentrations bringing possible dose-dependent effects by 30 hpf exposures.

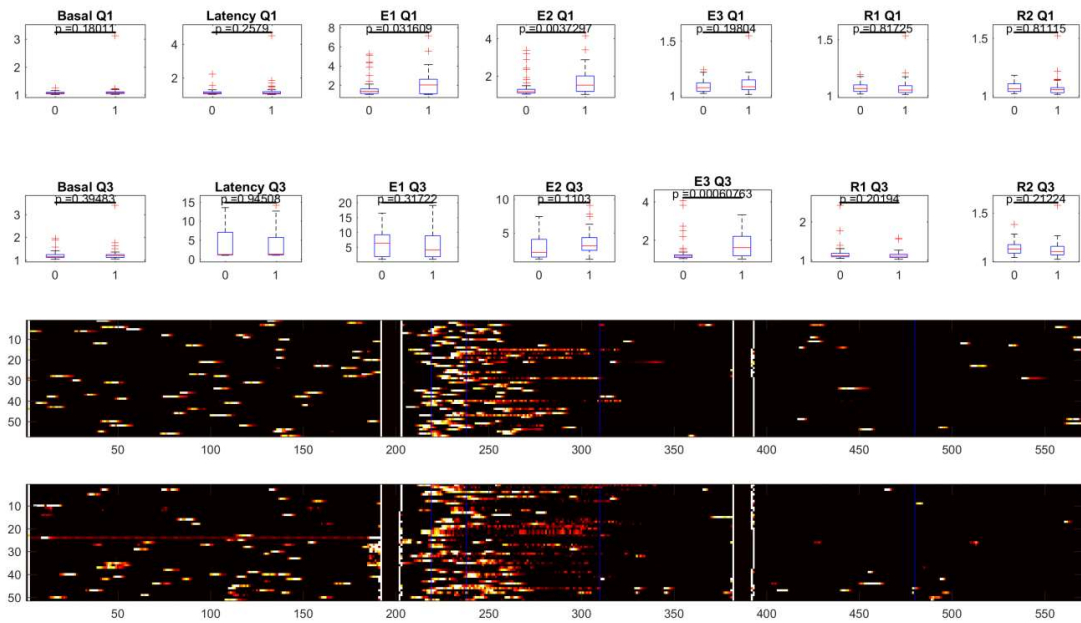


Figure 4.32 PD-9 (10 μ M) PMR results. Boxplots represent ANOVA statistics for each phase by contrasting with DMSO control. Heatmaps represent PMR intensities along the 6 seconds measurements where red indicates the highest, yellow modest and black no response. Upper panel heatmaps belong to the DMSO control group as the lower panel to the PD-9 group.

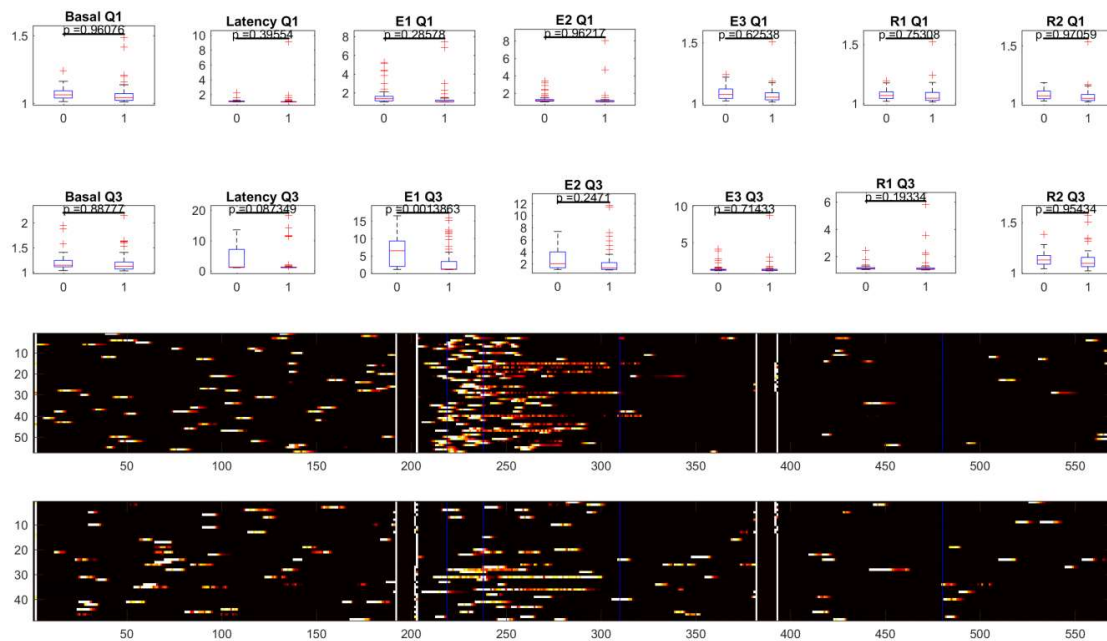


Figure 4.33 PD-11 (10 μ M) PMR results. Boxplots represent ANOVA statistics for each phase by contrasting with DMSO control. Heatmaps represent PMR intensities along the 6 seconds measurements where red indicates the highest, yellow modest and black no response. Upper panel heatmaps belong to the DMSO control group as the lower panel to the PD-11 group.

4.3.1.2 Preliminary analyses on locomotor responses of generic and novel derivatives

Locomotor response measurements were pursued with a large scale of exposure types. In this line of work, the embryos were exposed to single derivative or SFB combinations between 48 hpf-120 hpf. Then, their locomotor responses to the vibration stimulus were recorded and the distances or speed measures were obtained from these records. Initial n-way ANOVA analyses on the total distance parameters did not yield out significant scores on the comparison between the effects of treatment, concentration, combination and their interactions together (**Table Appendix B8**). Moreover, graphical representations of the preliminary data supported the statistics. Increased distance rate by PD-3 (10 μ M) has shown otherwise, suggesting processing of the data and in-depth analyses (**Figure 4.34**).

Interestingly, speed-wise comparisons for the preliminary findings have pointed-out that there can be an influence of combination on the effects of treatments (**Table Appendix B9**). Besides that, PD-3 (5 μ M) also implied decrease on the speed, relative to the DMSO control group (**Figure Appendix B10**). Although the results implemented concentration and combination related effects on the speed, toxicity of the compounds also should be considered. In addition, follow-up analyses can take separate phases and swimming patterns into account.

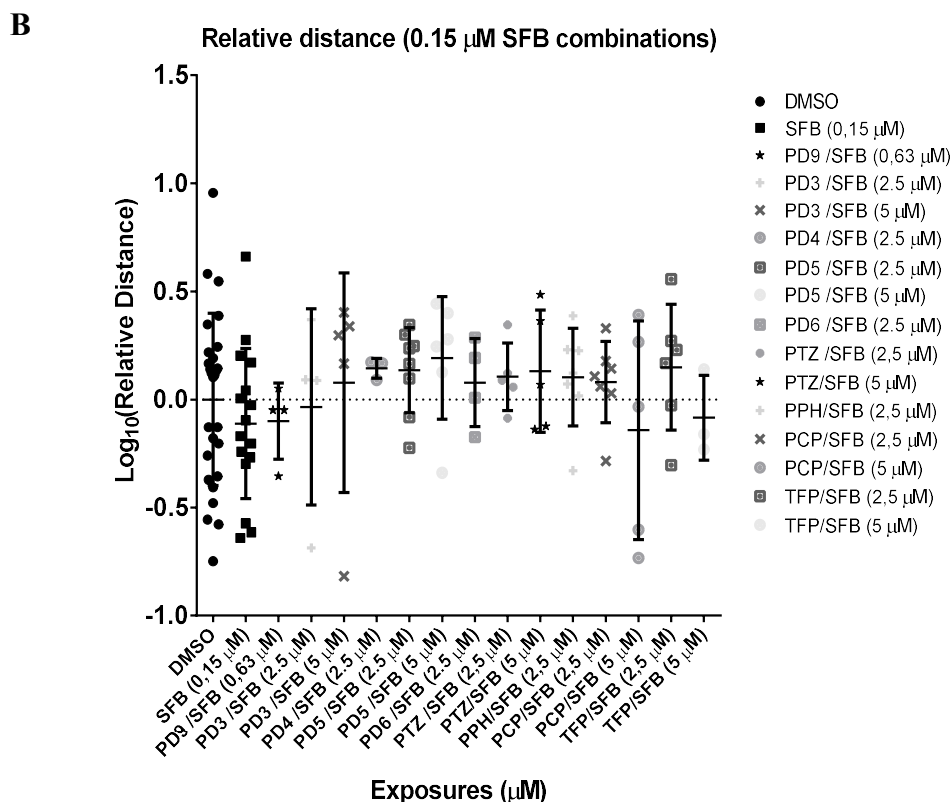
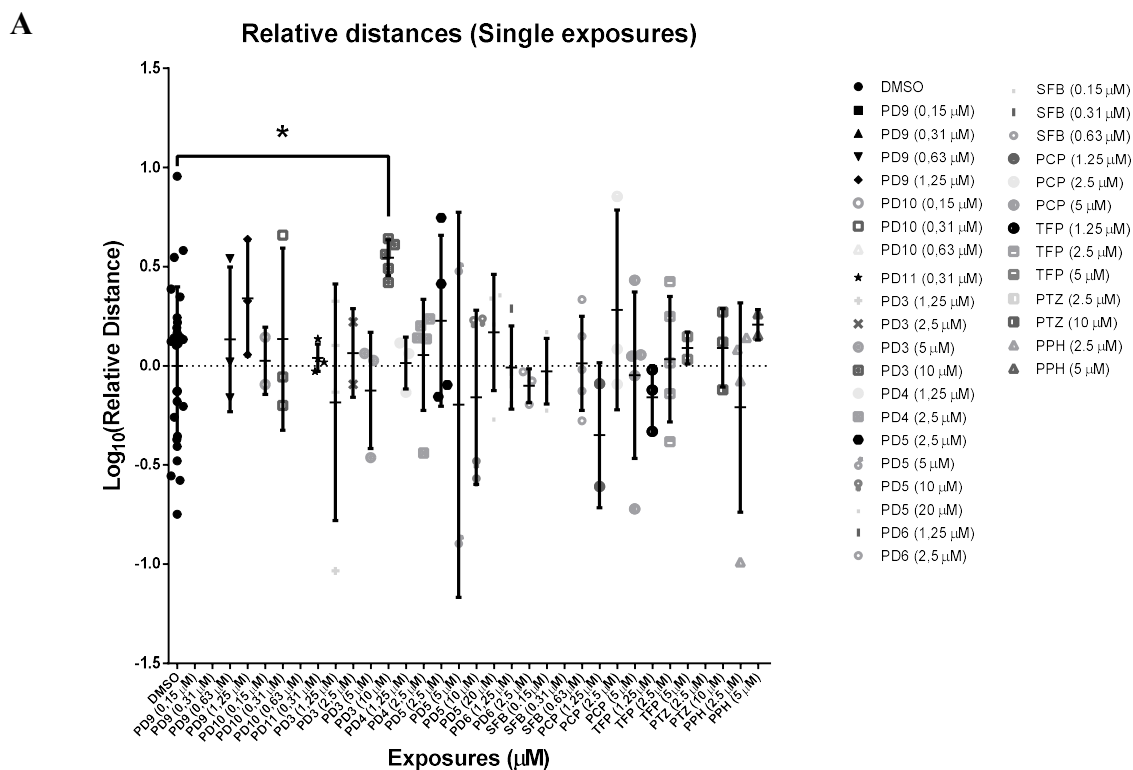


Figure 4.34 Locomotion distance analyses across single derivative and SFB combination exposures(A) Individual compounds, and (B) SFB 0.15 μM combinations of the derivatives. Comparisons and relative distance measurements were performed with respect to DMSO control group (0.5%) via one-way ANOVA/Dunnett statistics by using log transformed relative distances. (*: p-value<0.05)

4.2.7 RNAseq analyses of TFP-SFB combinations on Hep3B cell line

Combination effects further led us to investigate the molecular underlying of the synergism between two FDA approved compounds TFP and SFB. For that purpose, SFB (1 μ M and 2 μ M), TFP (12 μ M) and their combinations for the respective concentrations were exposed on Hep3B cell line for 48 hours. Then, the RNAseq evaluations were pursued. After processing the RNAseq data via Biojupies environment, we have evaluated how much the gene signatures of the exposures relate with each other on this cell line. For that purpose, PCA approach was utilized for the genes that show significant fold change differences in at least one of the samples (adj.p-val<0.05) (**Figure 4.35(A)** & **Figure Appendix B11**). Accordingly, The PC1 and PC2 dimensions were able to explain almost 90% variation across the samples and demonstrate the contrasts between each sample. We have observed that the biological duplicates of each DMSO control and TFP 12 μ M – SFB 1 μ M revealed greatly overlapping signatures within each group. Aside from that, TFP 12 μ M – SFB 2 μ M has shown distinctive profile with respect to its constituents TFP and SFB groups, reminding the impact of synergistic effects. Across the single SFB regimes largely deviating profiles were noticeable, further underlying concentration effects. However, single TFP and TFP 12 μ M – SFB 1 μ M groups represented relatively closer profiles to each other, suggesting that SFB 2 μ M would be the factor spiking the combination effect up. Despite of bringing some contrasts for the SFB concentration effects on combination, effect of 1 μ M SFB on the expression profile of the combination group remained mild. Therefore, logCPM based analyses demonstrated that Hep3B cell line can respond to the exposures distinctively, because the chemicals, the concentrations and the combination regimes could strongly matter.

Comparisons between the gene signatures of the exposures were additionally employed via hierarchical clustering and heatmap representation (**Figure 4.35 (B)**). In line with the PC1 axis, the combination groups clustered together, as in the case of the SFB 1 μ M and 2 μ M groups. Moreover, TFP 12 μ M sample remained aside from the SFB containing groups within the major single treatment branch. Henceforth, combination treatments were supported to give out differential expression profiles on Hep3B after 48-hour exposures.

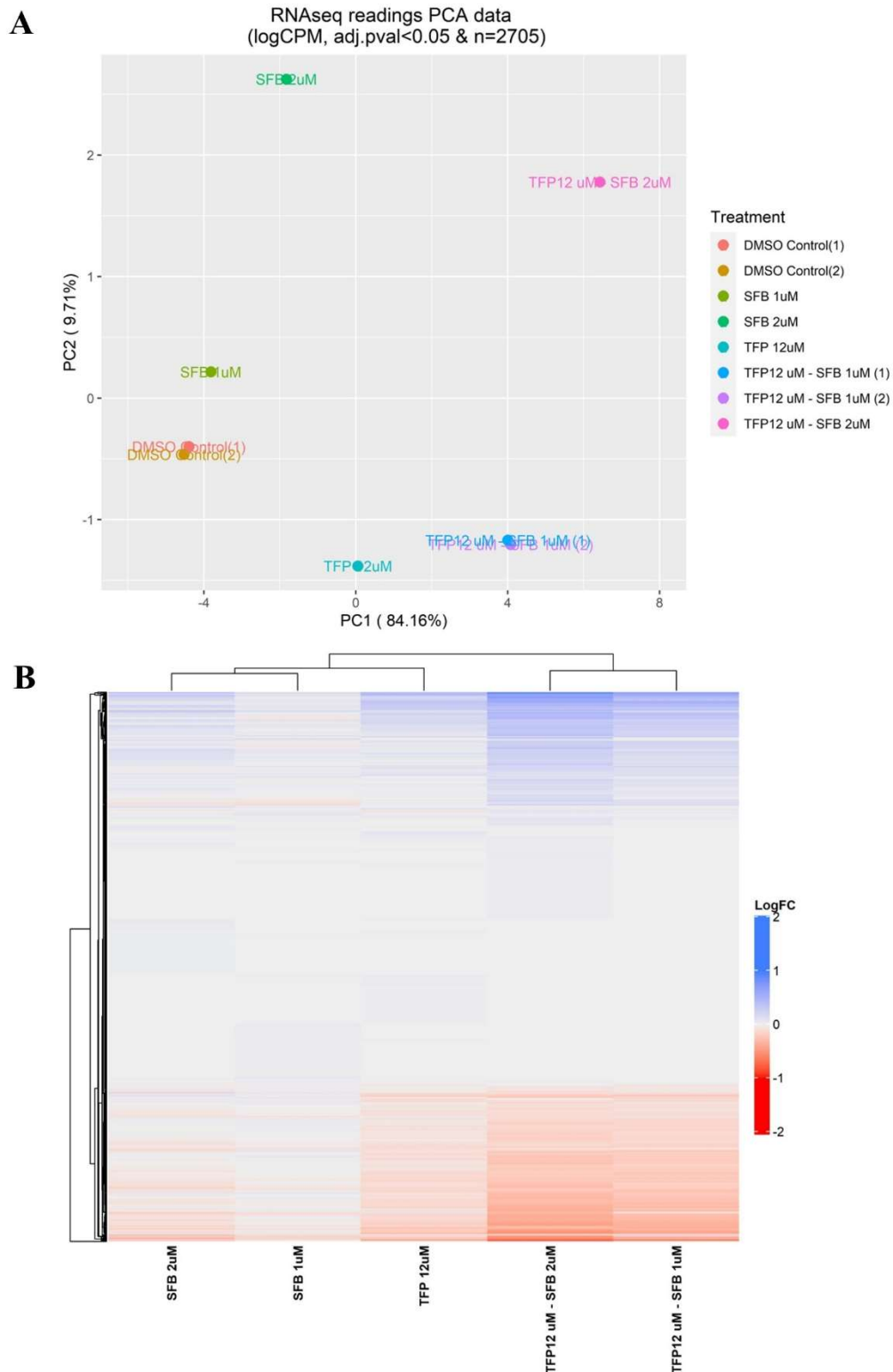


Figure 4.35 (A) PCA and (B) heatmap clusters of RNAseq data. PCA plot was generated by the LogCPM values of the genes that show significant fold change in either one of the samples in comparison to DMSO (0.1%) control group (adj. p-val<0.05, n=2705). Log FC values of the genes for each group were represented on the heatmap further where the clusters were formed by ward distances as blue and red color scales indicate decreasing and increasing amounts of the gene expressions, respectively.

Molecular mechanisms after the exposures, particularly in the case of combinations, were evaluated based via RNAseq and *limma* derived differentially expressed genes. For this purpose, KEGG pathway enrichments were evaluated (**Table 4.8**). Lists for genes affected by single SFB exposures remained limited, yet quite versatile by TFP, especially the combination groups. Spliceosome, cell-cycle, steroid biosynthesis pathways emerged strong by the combination treatments as FoxO signaling pathway was also noticeable by exposures.

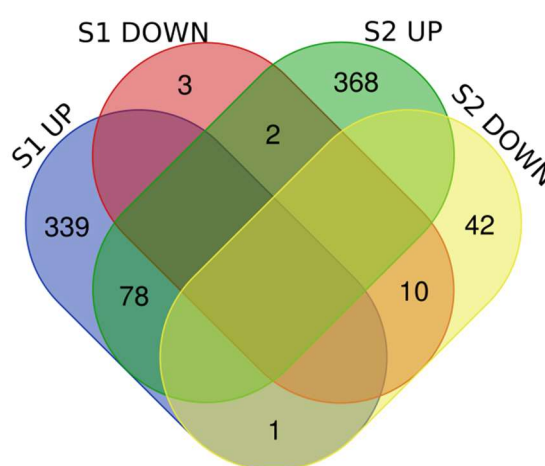
Table 4.8 Top 10 KEGG annotations (adj.p-value < 0.05)

Treatments	KEGG pathways	Overlapping gene ratios	P-value (<0.1)
SFB - 1 μM (n=433) KEGGs=3	Salivary secretion	6/90	0.013
	Morphine addiction	6/91	0.014
	Malaria	3/49	0.090
S2 (n=501) KEGGs=2	Allograft rejection	3/38	0.069
	Graft-versus-host disease	3/41	0.083
TFP 12 μM (n=560) KEGGs=7	Steroid biosynthesis	3/19	0.015
	Proteasome	4/45	0.037
	Malaria	4/49	0.048
	AGE-RAGE signaling pathway in diabetic complications	6/100	0.062
	Prion diseases	3/35	0.074
	FoxO signaling pathway	7/132	0.078
	African trypanosomiasis	3/37	0.084
TFP 12 μM –SFB 1 μM (n=776) KEGGs=68	Spliceosome	32/134	6.87E-17
	Cell cycle	22/124	2.22E-9
	Steroid biosynthesis	8/19	2.56E-7
	RNA transport	20/165	6.51E-6
	Pathogenic Escherichia coli infection	11/55	7.02E-6
	Proteasome	9/45	4.80E-5
	DNA replication	8/36	5.71E-5
	Antigen processing and presentation	11/77	1.81E-4
TFP 12 μM –SFB 2 μM (n=1772) KEGGs=40	Spliceosome	42/134	1.32E-13
	Cell cycle	32/124	2.24E-8
	DNA replication	14/36	1.02E-6
	Proteasome	15/45	4.08E-6
	RNA transport	33/165	7.08E-6
	Steroid biosynthesis	9/19	1.34E-5
	Pathogenic Escherichia coli infection	15/55	6.03E-5
	p53 signaling pathway	17/72	1.43E-4
	FoxO signaling pathway	24/132	5.34E-4
	Mismatch repair	8/23	5.44E-4

Next, gene signatures were compared between the groups. Fisher's exact tests for the genes that move either on the same or opposite directions between two samples showed significant

differences. Gene lists (minimum 9 genes) were utilized in detecting the pathways. In general, gene lists with the lengths between 15 and 500 are suggested by Broad Institute [315]. By decreasing numbers beyond this range, false positive rates increase. Besides that, inaccurate implementations can occur as the number gets higher above 500 due to increasing rates by the normalization errors. In the light of these criteria, we have initially observed that salivary secretion and actin cytoskeleton regulation were mutually regulated pathways by single SFB treatments (**Table 4.9**). NF-kappa B pathway and morphine addiction mechanisms were found to be affected differently by the exposures. Mutual genes were additionally utilized in Fisher's exact test analyses supporting the concentration-based difference between the SFB groups (p-value: 1.10e-10).

Table 4.9 SFB 1 μ M and SFB 2 μ M gene expression comparisons



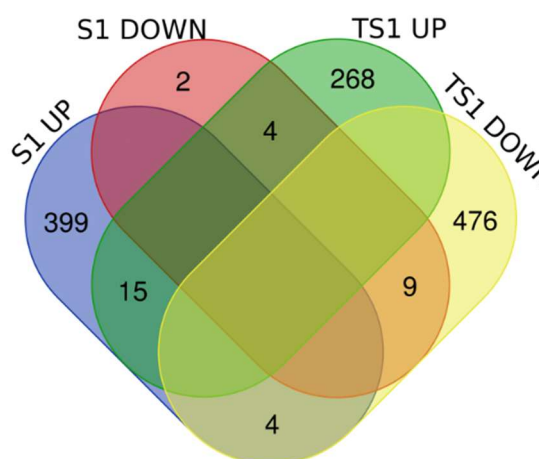
Clusters	KEGG pathways (p-value <0.05)	Overlapping gene ratios	P-value (<0.05)
Mutually increasing (n=78)	Salivary secretion	2/90	0.048
Mutually decreasing (n=10)	Regulation of actin cytoskeleton	2/214	0.005
	Shigellosis	1/65	0.032
	Melanoma	1/72	0.035
	AGE-RAGE signaling pathway in diabetic complications	1/100	0.049
Increasing in SFB 1 μM only (n=339)	Morphine addiction	5/91	0.019
Decreasing in SFB 2 μM only (n=42)	NF-kappa B signaling pathway	5/95	0.012
	Sphingolipid signaling pathway	2/119	0.026
	Lysosome	2/123	0.028

S1: SFB 1 μ M, S2: SFB 2 μ M; UP: upregulated, DOWN: downregulated genes. Fisher's exact test p-value: 1.104271e-10

Combination effect was initially investigated by comparing SFB 1 μ M and TFP 12 μ M - SFB 1 μ M groups and they represented different profiles (p-value: 0.011) (**Table 4.10**) [85].

Ferroptosis, Rap1, p53 and TGF-beta pathways seemed to be mutually affected by the exposures. Although the relationships of viability and these pathways were promising, numbers of genes relating with these pathways were relatively limited. Abundance of pathways after the combination exposures was noteworthy and reminded us that the signature of the synergism can differ from what we observe on single SFB treatments. Steroid metabolism, spliceosome, cell cycle, mTOR and various cell-death pathways were some leads in understanding the relationship between SFB 1 μ M and TFP 12 μ M - SFB 1 μ M groups.

Table 4.10 SFB 1 μ M and TFP 12 μ M-SFB 1 μ M gene expression comparisons



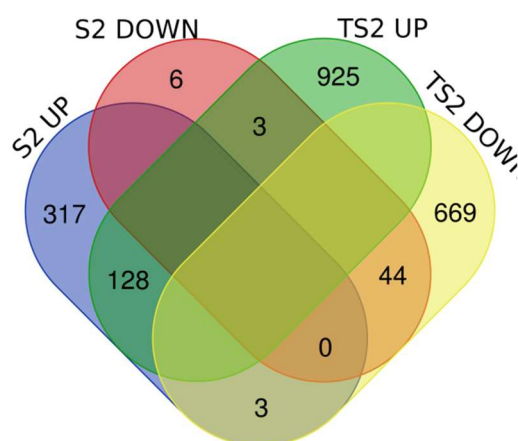
Clusters	KEGG pathways (p-value <0.05)	Overlapping gene ratios	P-value (<0.05)
Mutually increasing (n=15)	Ferroptosis	1/40	0.030
	Fat digestion and absorption	1/41	0.030
	Glutathione metabolism	1/56	0.041
Mutually decreasing (n=9)	Focal adhesion	2/199	0.003
	Rap1 signaling pathway	2/206	0.004
	Regulation of actin cytoskeleton	2/214	0.004
	PI3K-Akt signaling pathway	2/354	0.010
	Bladder cancer	1/41	0.018
	Malaria	1/49	0.022
	Shigellosis	1/65	0.029
	p53 signaling pathway	1/72	0.032
	Melanoma	1/72	0.032
Increasing in SFB 1 μM only (n=399)	Salivary secretion	6/90	0.009
	Morphine addiction	6/91	0.010
Increasing in TFP 12 μM – SFB 1 μM only (n=268)	Steroid biosynthesis	7/19	3.15E-9
	Terpenoid backbone biosynthesis	4/22	1.91E-4
	Renal cell carcinoma	6/69	3.24E-4

Table 4.10 SFB 1 μM and TFP 12 μM-SFB 1 μM gene expression comparisons (Cont'd)			
Clusters	KEGG pathways (p-value <0.05)	Overlapping gene ratios	P-value (<0.05)
Increasing in TFP 12 μM – SFB 1 μM only (n=268)	mTOR signaling pathway	8/152	0.001
	Other glycan degradation	3/18	0.002
	Central carbon metabolism in cancer	5/65	0.002
	Bladder cancer	4/41	0.002
	Phosphatidylinositol signaling system	6/99	0.002
	AMPK signaling pathway	6/120	0.006
	Endometrial cancer	4/58	0.008
	Autophagy	6/128	0.008
Decreasing in TFP 12 μM– SFB 1 μM only (n=476)	Spliceosome	32/134	3.37E-23
	Cell cycle	21/124	1.62E-12
	RNA transport	19/165	1.54E-8
	Proteasome	9/45	9.40E-7
	DNA replication	8/36	1.63E-6
	Pathogenic Escherichia coli infection	8/55	4.43E-5
	Oocyte meiosis	12/125	4.45E-5
	Viral carcinogenesis	15/201	9.91E-5
	Cellular senescence	12/160	4.61E-4
	Antigen processing and presentation	8/77	4.85E-4

S1: SFB 1 μ M, TS1: TFP 12 μ M – SFB 1 μ M; UP: upregulated, DOWN: downregulated genes. Fisher's exact test p-value: 0.011. Top 10 pathway lists are provided. For the extended version see **Table Appendix B12**

Combination effect was further investigated on the SFB 2 μ M levels and again represented significant differences between the groups (p-value: 2.09e-34), despite mutuality of some ferroptosis related mechanisms: the amino acid and glutathione metabolisms (**Table 4.11**)[316]. In contrast to previous SFB 1 μ M based comparisons, here cholesterol metabolism was also in mutuality further supporting the concentration dependent differences.

Table 4.11 SFB 2 μ M and TFP 12 μ M-SFB 2 μ M gene expression comparisons

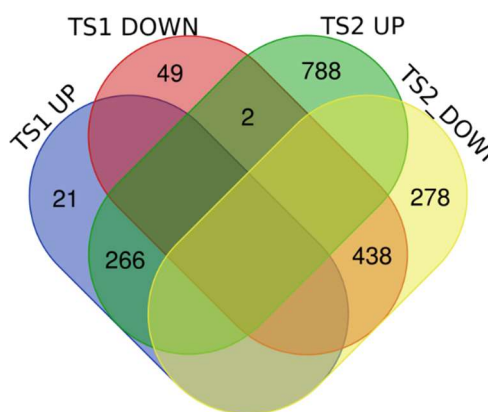


Clusters	KEGG pathways (p-value <0.05)	Overlapping gene ratios	P-value (<0.05)
Mutually increasing (n=128)	Natural killer cell mediated cytotoxicity	4/131	0.010
	Glycine, serine and threonine metabolism	2/40	0.027
	Graft-versus-host disease	2/41	0.028
	Cholesterol metabolism	2/50	0.041
	Glutathione metabolism	2/56	0.050
Mutually decreasing (n=44)	Lysosome	2/123	0.030
Increasing in TFP 12 μM - SFB 2 μM only (n=925)	Steroid biosynthesis	8/19	9.734E-7
	mTOR signaling pathway	17/152	6.81E-4
	Longevity regulating pathway	12/102	0.003
	Terpenoid backbone biosynthesis	5/22	0.003
	AMPK signaling pathway	13/120	0.004
	FoxO signaling pathway	13/132	0.008
	Aminoacyl-tRNA biosynthesis	8/66	0.011
	Phosphatidylinositol signaling system	10/99	0.016
	p53 signaling pathway	8/72	0.018
	Insulin resistance	10/108	0.028
Decreasing in TFP 12 μM - SFB 2 μM only (n=669)	Spliceosome	41/134	2.65E-28
	Cell cycle	28/124	6.71E-16
	DNA replication	14/36	3.69E-12
	RNA transport	27/165	8.04E-12
	Proteasome	15/45	8.54E-12
	Mismatch repair	8/23	4.72E-7
	Pathogenic Escherichia coli infection	11/55	1.69E-6
	Oocyte meiosis	16/125	4.33E-6
	Nucleotide excision repair	9/47	2.17E-5
	Human T-cell leukemia virus 1 infection	20/219	4.98E-5

S2: SFB 2 μ M, TS2: TFP 12 μ M – SFB 2 μ M; UP: upregulated, DOWN: downregulated genes. Fisher's exact test p-value: 2.09e-34. Top 10 pathway lists are provided. For the extended version see **Table Appendix B13**

The dose dependency was additionally interrogated on the combination levels. Two groups were able to separate from each other significantly supplementing PCA findings (p-value: 8.79e-198) (**Table 4.12**). Steroid, cholesterol metabolism, spliceosome, mTOR, cell cycle and various cell-death pathways emphasized combination effects. As in single SFB treatments, TGF-beta and Rap1 signaling pathways emerged for the combination groups suggesting an SFB originated effect on the expression. FoxO signaling and aminoacyl-tRNA biosynthesis pathways also drew attention for the involving pathways after combination therapies.

Table 4.12 TFP 12 μ M-SFB 1 μ M and TFP 12 μ M-SFB 2 μ M gene expression comparisons



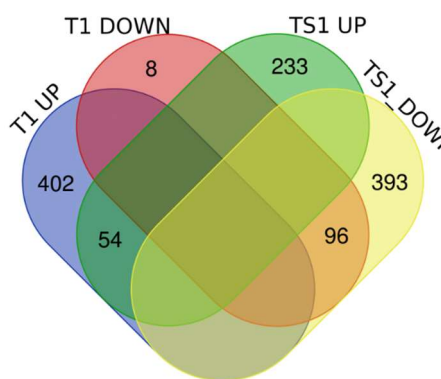
Clusters	KEGG pathways (p-value <0.05)	Overlapping gene ratios	P-value (<0.05)
Mutually increasing (n=266)	Steroid biosynthesis	8/19	5.87E-11
	Terpenoid backbone biosynthesis	4/22	1.85E-4
	Renal cell carcinoma	6/69	3.11E-4
	mTOR signaling pathway	8/152	9.94E-4
	Other glycan degradation	3/18	0.002
	Central carbon metabolism in cancer	5/65	0.002
	Glycerophospholipid metabolism	6/97	0.002
	Phosphatidylinositol signaling system	6/99	0.002
	Bladder cancer	4/41	0.002
	Autophagy	6/128	0.007
Mutually decreasing (n=438)	Spliceosome	32/134	2.59E-24
	Cell cycle	20/124	3.10E-12
	RNA transport	19/165	4.02E-9
	Proteasome	9/45	4.70E-7
	DNA replication	8/36	8.77E-7
	Oocyte meiosis	12/125	1.98E-5
	Viral carcinogenesis	14/201	1.46E-4
	Pathogenic Escherichia coli infection	7/55	1.89E-4
	Cellular senescence	12/160	2.18E-4
Antigen processing and presentation	8/77	2.79E-4	
Increasing in TFP 12 μM – SFB 1 μM only (n=21)	Mucin type O-glycan biosynthesis	1/31	0.032
	Fatty acid degradation	1/44	0.045
Decreasing in TFP 12 μM – SFB 1 μM only (n=49)	Ribosome biogenesis in eukaryotes	2/101	0.025

Clusters	KEGG pathways (p-value <0.05)	Overlapping gene ratios	P-value (<0.05)
Increasing in TFP 12 μM – SFB 2 μM only (n=788)	Longevity regulating pathway	9/102	0.019
	FoxO signaling pathway	10/132	0.036
	Aminoacyl-tRNA biosynthesis	6/66	0.045
Decreasing in TFP 12 μM – SFB 2 μM only (n=278)	Oxidative phosphorylation	10/133	1.72E-5
	Spliceosome	10/134	1.84E-5
	Parkinson disease	10/142	3.04E-5
	Proteasome	6/45	3.53E-5
	Huntington disease	11/193	8.55E-5
	Thermogenesis	12/231	9.98E-5
	Alzheimer disease	10/171	1.45E-4
	Non-alcoholic fatty liver disease (NAFLD)	9/149	2.44E-4
	Mismatch repair	4/23	2.63E-4
	Cell cycle	8/124	3.45E-4

TS1: TFP 12 μ M – SFB 1 μ M; TS2: TFP 12 μ M – SFB 2 μ M; UP upregulated, DOWN: downregulated genes. Fisher's exact test p-value: 8.79e-198. Top 10 pathway lists are provided. For the extended version see **Table Appendix B14**

Effect of TFP on the combination was evaluated by taking the TFP 12 μ M-SFB 1 μ M group into account (p-value: 4.01e-42) (**Table 4.13**). As in the comparisons between SFB and combinations, steroid, cholesterol and spliceosome metabolisms were found to be more related with the presence of TFP. In summary for RNAseq explorations, in addition to steroid, cholesterol and spliceosome mechanisms, cell cycle, mTOR, cell-death pathways, aminoacyl-tRNA biosynthesis, TGF-beta, Rap1 and FoxO demand additional evaluations in order to understand the synergistic effects that we have been observing for TFP and SFB pairs.

Table 4.13 TFP 12 μ M and TFP 12 μ M-SFB 1 μ M gene expression comparisons



Clusters	KEGG pathways (p-value <0.05)	Overlapping gene ratios	P-value (<0.05)
Mutually increasing (n=54)	Steroid biosynthesis	3/19	1.75E-5
	Renal cell carcinoma	3/69	8.60E-4
	Natural killer cell mediated cytotoxicity	3/131	0.005
	Cholesterol metabolism	2/50	0.008
	VEGF signaling pathway	2/59	0.011
	Focal adhesion	3/199	0.017
	ErbB signaling pathway	2/85	0.022
	Ras signaling pathway	3/232	0.025
	Synthesis and degradation of ketone bodies	1/10	0.027
	Taurine and hypotaurine metabolism	1/11	0.029

Table 4.13 TFP 12 μM and TFP 12 μM-SFB 1 μM gene expression comparisons (Cont'd)			
Clusters	KEGG pathways (p-value <0.05)	Overlapping gene ratios	P-value (<0.05)
Mutually decreasing (n=96)	Spliceosome	6/134	4.57E-5
	Proteasome	4/45	6.39E-5
	Epstein-Barr virus infection	6/201	4.18E-4
	Influenza A	4/171	0.009
	AGE-RAGE signaling pathway in diabetic complications	3/100	0.012
	Proteoglycans in cancer	4/201	0.016
	Bladder cancer	2/41	0.017
	Shigellosis	2/65	0.039
	Prolactin signaling pathway	2/70	0.045
	p53 signaling pathway	2/72	0.047
Increasing in TFP 12 μM only (n=402)	African trypanosomiasis	3/37	0.038
Increasing in TFP 12 μM – SFB 1 μM only (n=233)	Steroid biosynthesis	5/19	2.09E-6
	mTOR signaling pathway	8/152	4.19E-4
	Central carbon metabolism in cancer	5/65	9.62E-4
	Phosphatidylinositol signaling system	6/99	0.001
	Insulin resistance	6/108	0.002
	Terpenoid backbone biosynthesis	3/22	0.002
	AMPK signaling pathway	6/120	0.003
	Autophagy	6/128	0.004
	Endometrial cancer	4/58	0.005
Decreasing in TFP 12 μM – SFB 1 μM only (n=393)	Spliceosome	26/134	1.00E-18
	Cell cycle	20/124	4.23E-13
	RNA transport	17/165	2.90E-8
	DNA replication	7/36	5.47E-6
	Oocyte meiosis	12/125	6.70E-6
	Pathogenic Escherichia coli infection	8/55	1.12E-5
	Viral carcinogenesis	12/201	6.52E-4
	Antigen processing and presentation	7/77	7.91E-4
	Mismatch repair	4/23	9.67E-4
Cellular senescence	10/160	0.001	

T1: TFP 12 μ M, TS1: TFP 12 μ M – SFB 1 μ M; UP: upregulated, DOWN: downregulated genes. Fisher's exact test p-value: 4.01e-42. Top 10 pathway lists are provided. For the extended version see **Table Appendix B15**

RNAseq findings were evaluated via qPCR (**Figure 4.36**). Effects of combinations were found to be more profound in TFP 12 μ M-SFB 2 μ M combinations, confirming the gene level alterations on the genes of cell-cycle, DNA damage and alternative splicing pathways. In addition to these mechanisms, cholesterol pathways also showed alternating pattern in TFP containing groups. Nevertheless, the loss of significance for TFP 12 μ M-SFB 2 μ M GADD45A group from RNAseq to qPCR was unexpected. Although loss of significances by RRM2 and HMGCR were also eminent, direction of expression change was comparable between RNAseq and qPCR. Nonetheless, TFP 12 μ M-SFB 2 μ M combinations validated some crucial findings from the RNAseq approach, overall. As SFB concentration effect was partially addressed, validations demand some genes representative of functional annotation and within higher absolute logFC levels for each combination group.

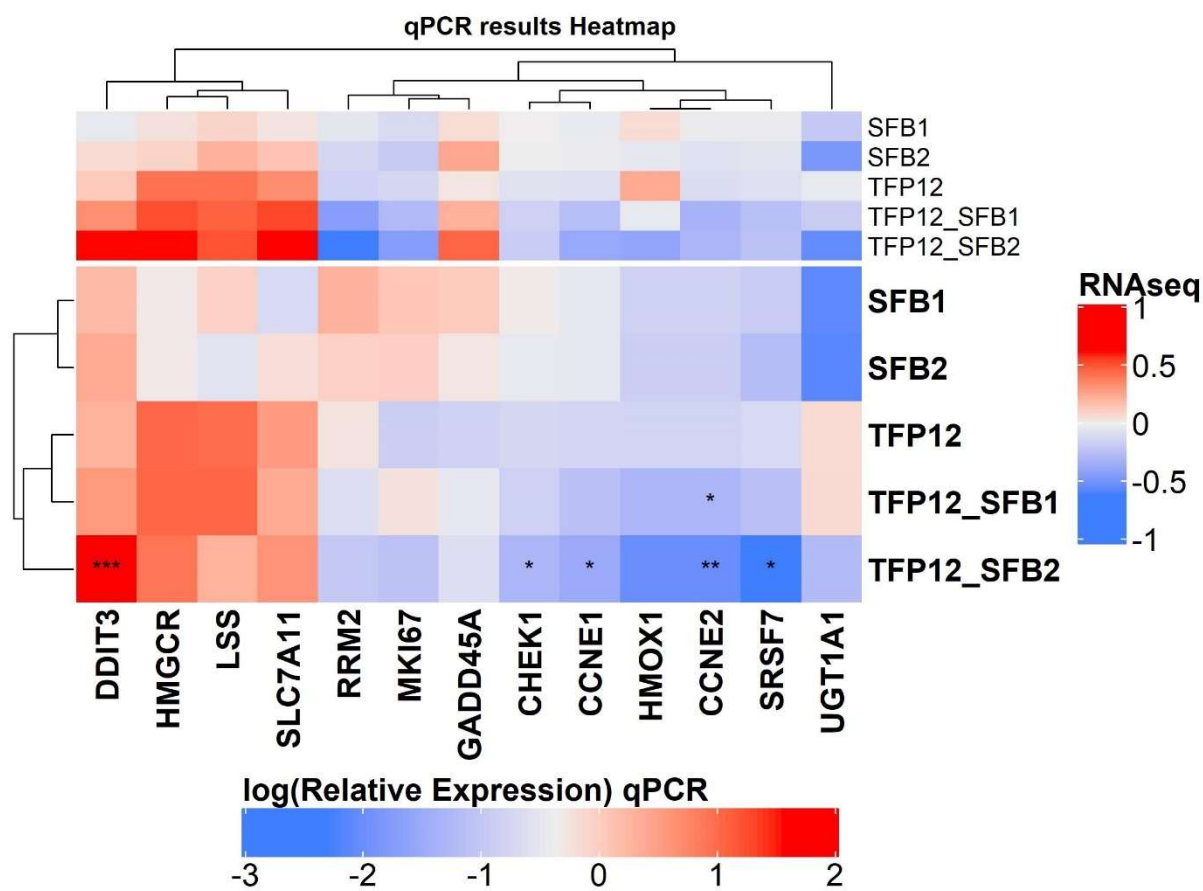


Figure 4.36 mRNA level changes after TFP-SFB combination exposures for 48 hours on Hep3B. Expression levels were derived by referring the TPT1 housekeeping gene and DMSO control (0.1%) groups, as the one-way ANOVA/Tukey statistics are provided on the heatmap on top of the color coding representing the $\log_2(\text{Relative Expression})$ levels (*: $p < 0.05$, **: $p < 0.01$ and ***: $p < 0.001$). In addition, the RNAseq data for the relevant genes are demonstrated as a top annotation with color coded logFC values.

CHAPTER 5: CONCLUSIONS AND DISCUSSION

BC and HCC demand novel therapeutic options with improved efficacies and safety profiles. The assessments are generally initiated by basic research and preclinical drug development stages, so most applicable therapies for clinic can be obtained. In this regard, *in vitro* and *in vivo* toxicity measurements as well as mechanistic understanding provide crucial insights for the advancement of preclinical stages. With this notion in mind, I have focused on evaluating the preclinical potentials of novel indole-benzimidazoles for BC therapy as well as generic and novel phenothiazine scaffolds for HCC using *in vitro*, *in vivo* and *in silico* approaches, and hence identified novel and effective candidates for future preclinical studies.

Screening strategies throughout the preliminary screening of both studies were kept limited to one (MCF7 in the case of indole-benzimidazoles) and two (Hep3B and SKHep1 in the case of phenothiazines) cell lines yet they were supported by the follow-up *in vitro* and *in vivo* screening approaches as well as mechanistic studies involving biochemical assays and comparative transcriptomics. Selection of MCF-7 as the primary model for novel indole-benzimidazoles was based on elimination of non-promising indole-benzimidazoles that were unlikely as novel SERMs. Since MCF-7 has also been accounted as the golden standard cell line for SERM development, its use on the preliminary stage can be considered as an effective strategy [317]. Moreover, inclusion of MDA-MB-231 and HepG2 further allowed us to validate the SERM-like properties of the selected drug candidates while demonstrating multi-target potential of these novel indole-benzimidazoles via comparative transcriptomics. Similarly, use of Hep3B (hepatoma) and SkHep1 (liver endothelial cancer) models have led us to prioritize phenothiazine derivatives effective in well differentiated and poorly differentiated liver cancer subtypes which were later tested on two other well differentiated HCC cell lines HepG2, Huh7 and a breast cancer cell line MCF-7. The large number of novel derivatives prioritized through the primary screens were tested in at least two and at most three other cell lines (excluding GFP-expression versions of some) helping us demonstrate the drugs' potential differences in their anticancer effects across the given cancers or cancer subtypes. Subsequently, functional assays and transcriptomic approaches and *in vivo* screens have supported the demonstrated anticancer activities and revealed interesting molecular properties of selected derivatives from both projects. Therefore, variabilities between the cell lines were assessed in detail which enabled us to pinpoint effective lead compounds as well as to discover the molecular pathways/subtypes/heterogeneity behind this variability if any. The above mentioned strategy has been a preferable methodology across multiple lines of studies

where applicabilities of the derivatives and selected candidates from a relatively large preliminary list were pursued [318-320]. Hence, the numbers of initial candidates could be shortened in a relatively time- and cost-effective manner, with detailed IC₅₀/EC₅₀ evaluations [321-323]. Accordingly in our case, 14 indole-benzimidazoles from a set of 37 molecules and 17 phenothiazines from a set of 34 compounds were subjected to secondary and more detailed screening across multiple cell lines, and hence structure-activity relationships could be evaluated. Moreover, *in vivo* studies in the zebrafish model throughout the secondary screening paradigms have become immensely helpful since they have been suggested as effective follow-ups for preclinical studies in the literature [324, 325].

Alternatively, screening across relatively large numbers of cell lines can also be pursued, after confirming the effects of prominent derivatives from a large scale study. In this regard, our indole-benzimidazole study was limited to three cell lines, whereas the number of cell lines studied with phenothiazines was five – in addition to eGFP monoclonal lines. Although limited in number, these cell lines were carefully selected for the purpose of identifying novel and more effective SERMS in the case of indole-benzimidazoles, and for testing phenothiazines together with sorafenib (SFB) as a synergizing combination therapy in liver cancer cell lines where effects of SFB have previously been studied in detail. On the other hand, utilizing a relatively higher number of cell lines can allow scrutinization of the sensitivity and heterogeneity profiles towards the derivatives in detail, leading to a more comprehensive estimation of their potential in clinics [326]. For instance, a kinase inhibitor, compound 10a, was initially identified from a large panel of pyrazolo[3,4-d]pyrimidine analogues by Radi and colleagues [327]. Later, screening the compound 10a across multiple melanoma cell lines were proven to be an effective strategy in deciding the sensitivity profiles of the cell lines and gene signatures [328]. Besides that, inclusion of more than 10 cell lines has improved the predictive abilities, as the study was mainly focused on a single compound. However this may not be time- and cost-efficient at all times where there are large number of compounds to secondarily screen. Therefore, there can be multiple strategies to be applied initially and as follow-up screening paradigms. Consequently we were also able to pursue molecule oriented comparisons, allowing us to evaluate structure-activity relationships and multi-target potential of derivatives. Yet, our approach can be improved by incorporating more heterogeneity to our panel of cell lines, especially for the most prominent compounds from indole-benzimidazoles and phenothiazines in future studies.

In the first line, novel indole-benzimidazole structures and influence of side-chain modifications were evaluated for their toxicity profiles *in vitro* and *in vivo*. Meanwhile, ER α relationship of the derivatives was under consideration which was remarkably complemented by transcriptomic analyses. Therefore, I was able gather essential understanding on the structural basis of the toxicities and possible mechanisms governing their actions. Key findings from this study are:

- 1) Novel derivatives exerted anti-cancer effects in a cell-line, dose and compound dependent manner;
- 2) R₁ position emerges as a key element on the cell proliferation rates;
- 3) Not only R₁: p-fluorobenzyl substitutions but also (i) R₁: -CH₃ x R₂: -Cl, (ii) R₁: -C₃H₇ x R₂: -Br and (iii) R₁: -3,4-difluorobenzyl x R₂: -OCH₃ modifications are implicative for further studies, and;
- 4) Although ER α modulation can be an important factor for the actions of the candidate compounds, their MoAs involve multiple targets and signaling cascades.

My second and third directions of this dissertation were comprised of evaluating anti-HCC potentials of generic and novel PTZ derivatives, respectively. Several preclinical strategies were used in profiling the derivatives. Repurposing has been the initial strategy to address if the privileged PTZ molecules can serve for HCC therapies. Secondly, novel and intermediary PTZ structures synthesized by Fikriye Zengin Karadayi and Murat Kisla at Prof. Dr. Zeynep Ateş-Alagöz lab in Ankara University were taken under investigation to identify novel molecules with enhanced activities against HCC. Furthermore, synergism of SFB with generic PTZs was also evaluated to understand if the SFB therapies can be enhanced by PTZ derivatives. Multiple lines of *in vitro* and *in vivo* toxicity assays, behavioral profiling and cholinesterase activity screenings as well as transcriptomic analyses supplemented these strategies.

Key findings from these repurposing studies are:

- 1) Toxicity profiles between the generic compounds vary across the cancer lines and on developing embryos
- 2) TFP emerges as a favorable compound due to tolerable ranges of toxicity based on *in vitro* and *in vivo* analyses and anti-cancer activities upon individual exposures,

- 3) Repurposing of TFP can be complemented with SFB, yet the synergistic effects can vary in a cell type and time dependent manner, and
- 4) TFP and SFB synergism indicate multiple levels of molecular events and cellular pathways.

In addition, key findings from the novel derivative screenings are:

- 1) Several novel and intermediary derivatives exert toxicities towards HCC and non-HCC cancer lines,
- 2) PD-5 emerges as a favorable compound due to no-observed-adverse-effect-levels (NOAEL) and SFB combination profiles. Additional tests and combination assessments are needed for PD-3, PD-28 and PD-29, and
- 3) MoA of the novel and intermediary derivatives can differ from the generic derivatives because of structural variations on the privileged PTZ scaffolds.
- 4) Cholinesterase activity is modulated by generic and novel derivatives in either direction depending on the type and dose of the drug.

Cumulatively, indole-benzimidazoles and phenothiazines both differ in their structures posing negligible bioisosteric properties between each other. As the antiproliferation was significantly influenced by the exposures, mechanisms of both derivative groups were thought to involve some alternative and mutual molecular pathways. Indeed, when we look at the list of pathways modulated in these two different classes of compounds arising from the transcriptomics studies (although one is in MCF-7, and the other one is in Hep3B) we have observed similarities as well as unique attributes. A few examples included cell cycle which was modulated in both the 50-51-53 trio as well as TFP+SFB combinations suggesting that genes involved in cell cycle machinery are common in both. It is known that cell cycle is tightly regulated and is expected to be common to compounds with antiproliferative aspects [329]. Ferroptosis and aminoacyl-tRNA biosynthesis have emerged as mutual mechanisms between indole-benzimidazoles study and phenothiazine project. On the other hand, spliceosome, cholesterol & steroid metabolisms, TGF-beta, FoxO signaling and mTOR pathways were found to be more related with the TFP and SFB exposures, implying distinctive gene signatures by the derivatives. Yet, further studies can examine the regulatory mechanisms leading to common signature patterns and distinctive features in both series of compounds. For this purpose, LINCS-Query analysis can become useful to see gene signatures associated with these two series as well as combination therapies. Furthermore,

disease and target oriented similarities of the treatments can be supplemented with additional network based analyses, protein interactome and disease based bipartite networks, such as protein-protein interaction networks (PIN) and “Open Target” tool [330, 331]. Accordingly, these approaches can further lead to novel aspects and new proposals for the uses of the derivatives in this study.

5.1 Anti-BC and antiestrogenic potentials of novel indole-benzimidazole derivatives

Initial toxicity screening on MCF-7 has demonstrated that some of the derivative groups can be promising leads for further evaluation. Then, they were subjected to secondary *in vitro* experiments, to better estimate their toxicity and cancer subtype dependencies. Therefore, a larger concentration scale was applied on MCF-7, MDA-MB-231 and HepG2.

Accordingly, toxicity assessments on multiple *in vitro* studies confirmed anti-cancer effects and mild relationship with estrogen receptor (ER) status. Intriguingly, the toxicities observed were not specific to MCF-7, and they overlapped with HepG2 profiles. Hence, importance of ER α emerged. In contrast to the preliminary screening performed on MCF-7, the derivatives **23**, **27** and **51** unexpectedly yielded some shifts in the activity levels on the secondary screening with MCF-7. As this can be due to batch effects, differences in the extend of dose scales might also have contributed these differences regarding the analyses of two different experiments. Although preliminary screenings and further transcriptomic analyses were representative of each other, validations on large scale dose responses are needed for R₁: -p-fluorobenzyl members. Nonetheless, MDA-MB-231 was also sensitive towards the candidate derivatives (including the R₁: -p-fluorobenzyl groups). As ER α modulation can be essential, cancer-type specificity is a remaining topic to consider for the indole-benzimidazole derivatives tested. Interestingly, compound **27** was found to inflict damage towards MCF-7 specifically with a considerable IC₅₀ value. Within the scope of the study, **27** demands toxicity validations for further preclinical studies.

In vivo survival and morphometric measurements have allowed testing the toxicities towards development and non-cancer organs. Survival rates and morphologies observed in response to the compounds were relatively similar with those in the controls, supporting the relatively high safety profiles of the R₁: p-fluorobenzyl substitutions. Nevertheless, hatching percentiles by 48 hpf were quite distinctive between the groups. Although this is suggestive for a developmental delay, 72 hpf profiles have demonstrated otherwise. Therefore, chorions might serve as a barrier, suggesting limited exposure levels than expected [332, 333]. Despite the

qPCR results indicative for presence of a perturbation, *in vivo* assays demand screenings after dechoriation of embryos

In addition to toxicity assays, the study provided basic information for further lead derivations and possible molecular mechanisms of the indole-benzimidazoles.

Although some derivatives have shown toxicity towards the cancer lines this remained within micromolar ranges, suggesting further improvements are needed on the structure of molecules. Varieties of sidechains have allowed deriving SAR interpretations which can be informative for future syntheses. Accordingly, R₁: -p-fluorobenzyl and alkyl groups emerged as structurally important components from the *in vitro* assays, as confirmatory *in vivo* developmental assays may be needed. Interaction between R₁ and R₂ was observable, but direct influence of each R₂ derivation was insignificant. On the one hand, **27** (R₁: -CH₃ x R₂: -Cl), **36** (R₁: -C₃H₇ x R₂: -Br) and **53** (R₁: -3,4-difluorobenzyl x R₂: -OCH₃) reduced the cancer cell proliferation robustly. On the other hand, other compounds from their respective R₁ or R₂ families could not perform as good as **27**, **36** or **53**. Nevertheless, R₂ groups were relatively limited in varieties, and sulfonyl side chains were solely attached with ethyl. Therefore, derivations on these positions can also bring about some improvements on the structures. For instance, diverse alkylation ranges or aryl substitutions on the sulfonyl structures can be positively influential [334]. Besides the sidechain modifications in this study, N-benzylations on indole-benzimidazoles may present a progress on the activities [172]. Moreover, primary and secondary cytotoxicity assays in this study provide a useful source for predicting the activities of next-generation derivatives. In this sense, pharmacophore modeling can be utilized as the structural features can be prioritized based on the activity profiles of the indole-benzimidazole derivatives screened in this thesis [335].

Besides SAR, transcriptome-based analyses have provided crucial insights into multifaceted nature of the indole-benzimidazoles.

Firstly, relationship between each indole-benzimidazole derivative were investigated to better understand molecular underlying of candidate exposures. Microarray signatures were found to overlap with each other, and they follow dose-dependency in line with cytotoxicity profiles. Initially, correlations of the gene signatures were evaluated across R₁: -p-fluorobenzyl members (**48**, **49**, **50** and **51**) and structurally related and cytotoxic compound **53** (R₁: -3,4-difluorobenzyl x R₂: -OCH₃) by 20 μM exposures. Relatively toxic molecules from the *in vitro* screenings have represented overlapping signatures on gene expression, as fewer toxic derivatives **48** and **49** formed a separate cluster. The distinction was further confirmed

between **48-49** and **50-51-53** sets, where genes for cell cycle, ESR1, DNA damage and stress response pathways were more pronounced in **50-51-53**. Later, qPCR analyses with 40 μ M exposures have presented a dispersion of the clusters previously observed by microarray analyses (20 μ M), since **48-49** also become significantly relevant with cell-cycle, DNA damage and stress response genes. The concentration dependency on gene expression was also supported by the E2 signaling gene (TFF1). Therefore, structurally resembling derivatives also revealed comparable gene signatures which is also dependent on the applied concentrations.

Molecular signatures of the indole-benzimidazoles have confirmed mutual relationships with ER modulation. The derivatives presented inverse relationship with E2-signaling, as they yield correlations with standard SERMs. In line with toxicity profiles between MCF-7 and HepG2, ER α status was supported to be an important factor for the actions of derivatives. However, the clusters of the indole-benzimidazoles were relatively separate from the SERMs, bringing additional pathways into question.

Enriched pathways were investigated for possible actions of the derivatives. Aminoacyl and amino acid metabolisms as well as ferroptosis have emerged from enrichment analyses. Interestingly, first two pathways can lead to ferroptosis, implying an aspect for the anti-cancer effects of the derivatives [316, 336, 337]. In addition, AhR signaling was considered due to its close relationship with E2 signaling, amino acid metabolism and ferroptosis [175, 338-340]. Thus, amino acid depletion (AA (-)) and AhR modulator dioxin signatures were examined. As possible E2, AA(-) and AhR interactions have supplemented the literature, correlations of the novel derivatives with AA(-) and dioxin were implicative for involvement of alternative pathways.

Use of large-scale public repositories further allowed to compare indole-benzimidazole expression profiles by means of gene and compound signatures. Hence, privileged components of the novel derivatives immensely came to light, indicating multiple targets and pathways. LINCS-Query perturbagen signatures were supportive in assigning multiple roles for the derivatives. Oxindole-I, which also possesses an indole structure, was the most similar one to our microarray compounds. Interestingly, oxindole-I based molecules were observed to participate in oxidative stress, ferroptosis and cell-death [341, 342]. The structures can influence the AhR signaling, hence multiple pathways that AhR interacts with [339]. Niguldipine was also strongly related with the derivatives in expression. Niguldipine can block calcium channels and cause unfolded protein and amino acid stress responses as well as

ferroptosis [312, 343]. Another agent FCCP works by uncoupling oxidative phosphorylation in mitochondria and antagonizes with ferroptosis process [344]. An indole-based structure ZK-164015 was also among the top list, and it serves as an ER antagonist. Furthermore, reserpine was recorded along the top compounds, as it contains indole ring and can modulate oxidative-stress pathway [345]. In accord with the literature suggestions, ER antagonists, tubulin and microtubule inhibitors presented high similarity scores with the novel indole-benzimidazoles. Structural similarities for these compounds were also eminent. Although *in silico* affinity profiles of the derivatives were lower than the standard ligand towards ER α and tubulin structures, overlapping patterns in gene expression suggested some interaction between the novel compounds and these targets [311]. Thus, multiple target proteins and mechanisms, besides ER α , have been implemented for the derivatives in this study. As structural changes may alter the affinity profiles in the future, currently the compounds were observed to be insufficient in strictly acting as SERMs.

5.2 Repurposing generic phenothiazines in combination with SFB for HCC therapies

Inverse associations between HCC and antipsychotics as well as repurposing potentials of PTZ derivatives have motivated us for this study. Cancer incidence and schizophrenia as well as use of antipsychotic therapies have also been noted across several clinical studies [233, 235, 236, 285, 291, 292]. These further led us to investigate their activities across HCC and non-HCC lines, as we also aimed to shed a light onto their mechanistic insights.

Anti-HCC potentials of the generic derivatives were initially addressed by MTT assays on HCC cells along with non-HCC SkHep1 liver cancer line and MCF-7 breast cancer cell line. Individual compounds were able to exert anti-proliferative abilities in a concentration, cell type, time and compound dependent manner. Furthermore, effects of the derivatives also changed across cell lines, indicating cell-type dependent effects of each molecule. Accordingly, TFP and PCP emerged as the most effective compounds with respect to PTZ and PPH. However, activities of TFP and PCP were in a broad spectrum where they influenced the viability percentiles of all HCC and non-HCC cell lines. Interestingly, effects of PPH was more profound on HepG2 where Huh7 and MCF-7 did not reflect any versatile IC₅₀ values. Therefore, repurposing potentials of TFP and PCP went beyond HCC, as PPH represented a more liver-like cancer oriented therapeutic option.

In vivo assays further complemented the *in vitro* studies, and prioritized TFP due to developmentally fewer toxic effects by 72 hpf. Although pharmacokinetic/pharmacodynamic (PK/PD) properties of the compounds were already established, PTZ, PPH and PCP implied

NOAEL by sub micromolar ranges on the tested embryos. Evident with affected embryo rates (dead/abnormal), TFP has yielded a more tolerable dose range upon the exposures. Considering the effective concentrations of the generics *in vitro*, TFP might yield better therapeutic settings. This was further supplemented with xenograft experiments with SkHep1^{eGFP} clones, where TFP (10 μ M) was able to keep the tumor size significantly lower than the control groups and PCP (10 μ M and 20 μ M) exposures.

In addition to repurposing strategy, SFB combination has been an important aspect of the studies. Preliminary evaluations by TFP and PCP (24 h) was in support of synergistic effects on the growth of Hep3B cell lines. Accordingly, TFP has emerged as the model combination drug with SFB, and it was tested across the liver cancer lines for 24 hours and 48 hours. Interestingly, the combination has presented a dual action, where synergistic and antagonistic effects can be observed across varying concentrations and the cell lines. Although synergism was prominent on Hep3B, the dual effects underlined the responses of HepG2 and Huh7 HCC lines. Furthermore, extended exposures were implicative for loss of synergistic dose ranges on HepG2 and gain of more synergistic attributes on Huh7. Moreover, a non-HCC liver cancer line SkHep1 has demonstrated major antagonistic profiles upon the exposures. As the results emphasize cell and time dependency on the actions of TFP-SFB combinations, varying degrees of synergistic and antagonistic effects implied dynamic cross-talks between TFP and SFB mediated signaling events.

Developmental effects of the SFB synergism with selected molecules were also assessed using zebrafish embryos. Surprisingly, combinations of PTZ, PPH and PCP were able to cause antagonistic effects, meaning that combination doses were less toxic towards the developing embryos than they would do additively. Since individual exposures were developmentally less tolerable than TFP, combination therapies may improve their therapeutic potentials. For that, SFB combinations with multiple cell line xenografts can be informative. Nonetheless, antagonistic range was minor in the TFP-SFB combinations, as they were greatly toxic beyond the concentrations of TFP 10 μ M and SFB 2 μ M, which can be a limiting factor for use of TFP scaffolds as SFB counterparts. In this sense, hepatotoxicity of the antipsychotic compounds by high doses should be also considered [236-238].

Although the derivatives overall can serve as dopaminergic ligands, there are multiple targets and receptors that the derivatives interact with. Due to unclear relationship of the dopaminergic system and *in vitro* cancer line cytotoxicity profiles, we also considered additional pathways, initially the cholinergic system. Accordingly, behavioral assays and

AChE activity profiles provided valuable insights for the actions of the derivatives. In line with literature findings, TFP and PCP were able to reduce overall motor responses, a common behavioral phenotype for antipsychotic compounds, such as haloperidol [314]. The photomotor response profiles (PMR) were also in close resemblance with anxiolytic compound diazepam, as shown by Kokel et.al (2010) [98]. In addition, cholinesterase activity assays have shown no significant changes on Hep3B and SkHep1, although activity change patterns were in opposite directions, suggesting differences on cholinesterase mechanisms between the cell lines. However, presence of multiple cholinesterases (AChE, BChE and their isoforms) in human sources should be born in mind. Furthermore, increasing AChE levels on zebrafish embryos were observed which may also rely on the applied concentrations of PCP and TFP. Interestingly, SFB 2 μ M was able to increase the activity levels of cholinesterase by 48 hours on Hep3B, where the changes were compensated by the presence of TFP 12 μ M. The influence of combination was additionally tested on PMR. Unlike the cholinesterase levels, no influence of the SFB 2 μ M was observed, which was thought to be due to concentration dependent effects. Moreover, increased cholinesterase levels were associated with HCC survival, since it has been suggested as a good prognostic marker by high levels [289, 290]. Despite a lack of mechanistic insight for AChE and HCC, compensation of the levels by TFP might be indicative for mechanisms involving TFP-SFB synergism. Nevertheless, dysregulation of cholinergic homeostasis has been also recorded on several cancer cases, besides annotation of AChE as a marker for apoptosis [346-349]. Although the findings do not clearly draw a functional relationship between AChE and anti-cancer effects, the mechanism can be considered in elucidating the TFP-SFB synergism, as well as for the actions of the novel derivatives in a dose-dependent manner. For this purpose, down-regulation of AChE, BChE and dopaminergic receptors can provide crucial insights for the mechanisms of derivative exposures.

RNAseq studies helped understanding the repurposing potential of TFP alone and in combination with SFB on gene expression level. Furthermore, KEGG pathway analyses were initiated to comprehend the synergism phenomena occurring between the treatments and combinations. Hence, we were able to relate the downstream effects, specific mechanisms and gene interactions regulated across the treatment groups and combinations. Initial assessments have shown distinct gene signatures of the combination groups from the individual compound exposures. The differences were more pronounced by the SFB 2 μ M combinations, despite enrichment of large numbers of pathways by the presence of TFP 12 μ M. Accordingly,

ferroptosis, p53 pathways, Rap1 signaling and TGF-beta pathways were presumed to be triggered by the presence of SFB in the combination, due to pathway mutuality between SFB and combination groups. In contrast, steroid, cholesterol, and spliceosome metabolisms were noticed to be more related with the presence of TFP. Some distinctive features emerging from the combination effect were found to relate with FoxO signaling, aminoacyl-tRNA biosynthesis and mTOR pathways. Although the analyses of the RNAseq findings are ongoing, initial findings were indicative for distinctive, yet partially additive, molecular profiles by the combinations. Validations of the RNAseq by qPCR pursued, but the range of the utilized primers were able to confirm the effects of TFP 12 μ M - SFB 2 μ M combinations. To address this relative inconsistency, multiple primers as well as a separate batch of RNA samples can be utilized in qPCR. Moreover, BioJupies environment can be further tested and supplemented with alignment-based algorithms like STAR and HISAT2, since they can be more informative on isoforms and lowly-abundant genes [350-352].

Lastly, SwissTargetPrediction has become insightful in conceiving the target ranges of privileged PTZ scaffolds can interact with. Interestingly, muscleblind-like proteins were also among the candidate targets for TFP. Considering the effect of TFP on spliceosome and interaction of documented relationship between muscleblind-like proteins and regulation of splicing can shed light onto MoA of TFP exposures [353].

As a result, generic PTZ derivatives have reflected some potentials towards the preclinical aspects in cancer therapy. Although HCC has been the major prospect, the derivatives can become applicable in non-HCC therapies. In this regard, the studies were supportive in repurposing PTZs. Specifically, TFP emerged as a prominent derivative, due to *in vitro* and *in vivo* toxicity profiles. On the other hand, remaining derivatives have reminded of some unfavorable safety issues as individual treatments. In addition, SFB combination trials provided novel aspects for repurposing PTZs. As TFP has shown some promising leads, xenograft works are needed to advance further in the preclinical studies. Furthermore, SFB synergism has not been fully addressed with other PTZ compounds, as developmental effects of PPH and PCP in SFB combinations were intriguing. So, *in vitro* and *in vivo* synergistic evaluations are needed to complement their toxicity data. Lastly, TFP-SFB RNAseq explorations were strongly implicative for major alterations on the molecular pathways. Therefore, in-depth analyses can be invaluable since the underlying mechanisms of synergism can reveal new directions for target-based therapies. Meanwhile, spliceosome and cholinesterase pathways can be also born in mind.

5.3 Preclinical evaluation of novel and synthesized derivatives

Cell type, compound type, concentration and time dependent effects were also observable on the novel derivatives. In contrast to generic derivatives, Hep3B and SkHep1 have shown significantly different profiles with each other, yet the responses of MCF-7 were more relevant with Hep3B. Similarly, effects of the derivatives also deviate across the cell lines, suggesting an interaction between the type of compounds and the type of cell lines. *In vitro* assessments of individual compounds pinpointed PD-3, PD-5, PD-9, PD-11, PD-28 and PD-29 as possible candidates for further evaluations with anti-cancer effects across multiple cancer types. Moreover, effects of PD-9 and PD-11 towards the proliferation of the cell lines were most effective even more than the generic compounds.

In vivo assays, however, were not favorable for PD-9 and PD-11 since they caused high developmental toxicity rates by low doses. Interestingly, adverse profiles were less observable by the compounds PD-3 and PD-5. Although their therapeutic potentials may be limited due to IC₅₀ values above 20 μ M, these molecules and PD-29 were able to reduce the xenograft tumor growth significantly. Hence, their structures can provide some references for further improvements as well.

SFB combinations were also tested with PD-5, where the synergistic effects were pronounced by 24 hours on Hep3B cell line. Comparable, even slightly higher, rates of synergistic scores supported the advance of PD-5. Synergistic evaluations on embryonic development were in favor of PD-3 and PD-5, due to antagonistic effects on the dual toxicities of the compound exposures during developmental stages. Despite *in vitro* toxicities in a micromolar range by individual exposures, PD-3, PD-5 and relatively recent compounds, PD-28 and PD-29, can be subjected for more synergistic evaluations in preclinic.

AChE level changes by PD-3 and PD-5 were in similar directions with TFP and PCP. However, PD-3 and PD-5 were able to result in a significant increase on cholinesterase activities, despite relatively minor significances of AChE levels in zebrafish. Distinctions in cholinesterase activity profiles can be resulted by affinities towards the enzyme, according to SwissTargetPrediction results indicating the novel derivatives as possible cholinesterase ligands.

Although PMR on the synthesized compounds are limited to PD-9 and PD-11, eye motor response changes were seemed to be confined in the excitation phase. As defined by Kokel et.al, magnitude stimulant phenotypes are representative for increased extend and height of

excitation peaks by the light stimulus [98]. Interestingly, the work of Kokel and colleagues has additionally suggested close relationship between magnitude stimulant compounds and monoamine oxidases, which were also predicted as possible targets of PD-9 and PD-11 by SwissTarget algorithm. This phenotypic behavior and targets are unlike TFP and PCP, affirming different structure-activity profiles between generic and synthesized derivatives. Multiple concentrations and use of PD-3, PD-5, PD-28 and PD-29 on PMR can be additionally informative.

To sum up, novel derivatives PD-3, PD-5, PD-28 and PD-29 have shown improvements on the basic PTZ scaffolds, yet limited on the cytotoxicity profiles by micromolar ranges ($IC_{50} > 20 \mu M$). Although PD-9 and PD-11 were seemed promising initially, they failed due to *in vivo* toxicities. Moreover, SFB synergism of PD-5 was remarkable for deriving further preclinical directions in the assessments of the novel candidates. However, possible functional differences with the generic compounds were noticeable, implying a need for thorough understanding for their mechanisms. Therefore, molecular signatures of the derivatives can become valuable resources upon supplementing efficacy and toxicity profiles, especially by means of SFB synergism. Although the chemical structures are not provided here, activity data of the phenothiazines allow new directions towards developing novel HCC therapies.

5.4 Future Perspectives

The findings of the study provided new directions for indole-benzimidazoles and phenothiazine derivatives.

The directions for indole-benzimidazoles are:

- Elucidation of multi-target profiles are needed. Accordingly, subtypes of ER and known targets of the top LINCS results can be prioritized. Multicomponent analyses can be insightful in predicting structure-activity relationships.
- Secondary assessments for the active members can be pursued *in vitro* and *in vivo*. Besides the validations, *in vivo* developmental assays after dechoriation and xenograft assays are needed for initial efficacy and safety estimations.
- Novel derivations can be followed to improve SERM and anti-cancer likelihood of the compound groups. Some of the derivations can be: (i) R_1 : p-fluorobenzyl, (ii) R_1 : -CH₃ x R_2 : -Cl, (iii) R_1 : -C₃H₇ x R_2 : -Br, (iv) R_1 : -3,4-difluorobenzyl x R_2 : -OCH₃, (v) additional R_2 groups and sulfonyl side-chain modifications (aryl and alkyl substitutions), and (iv) N-benzylation. Accordingly, the use of additional cell lines

that belong to different cancer subtypes can be informative for gaining more mechanistic insights and clinical perspectives.

- List of candidate next-generation derivatives can be further enriched via pharmacophore modeling approaches, since the activities of the derivatives in this thesis can be utilized.

The directions for generic and novel phenothiazines are:

- Xenograft studies are needed for SFB combinations with the candidate derivatives: TFP, PCP, PPH, PD-5, and, upon developmental toxicity assays, PD-29
- Morphometric measurements and organ toxicities can be utilized in providing better estimates on the safety profiles of the combinations.
- SFB combination trials with the candidate compounds across various and a larger scale of cancer subtypes *in vitro*, due to HCC and non-HCC effects.
- Evaluation of the synergism on transcriptome. As exploratory data analyses were promising, underlying synergy mechanisms need to be addressed both to understand TFP-SFB relationship and new targets for HCC therapy. In addition to KEGG pathway analyses that were pursued in the study, gene ontologies (GO) such as biological processes (BP) and network-based approaches such as ingenuity pathway analyses (IPA) can be informative on the underlying processes and mechanisms of the each treatment type [354].
- PMR assays for the candidates and SFB combinations by alternating doses. In addition to neurotoxicity profiling, the assay is also resourceful in providing mechanistic insights.
- The locomotor assay data needs further evaluations. Initial observations were suggestive for variations on motor responses.
- Target validations are needed. In consensus between activity data, RNAseq analyses and *in silico* target prediction algorithms, possible targets can be subjected to functional assays. Known ligands or transgenic/knockout or knockdown approaches (i.e. AChE, BChE and dopamine receptor siRNA treatments) would be utilized in deriving new directions towards HCC therapy. In addition, mRNA and protein level confirmations can be proceeded with.
- LINCS-Query analyses can be utilized for the RNAseq data to see gene signatures associated with exposures to drugs.

- Although SwissTargetPrediction tool has become immensely helpful, network-based analysis, protein interactome and disease based bipartite networks can be informative for identifying possible protein targets and disease relationships. Open Target tool can be implemented for further analyses.

REFERENCES

- [1] R.L. Siegel, K.D. Miller, A. Jemal, Cancer statistics, 2019, CA: a cancer journal for clinicians 69(1) (2019) 7-34.
- [2] S. Thakkar, D. Sharma, K. Kalia, R.K. Tekade, Tumor microenvironment targeted nanotherapeutics for cancer therapy and diagnosis: A review, Acta biomaterialia 101 (2020) 43-68.
- [3] K.D. Miller, L. Nogueira, A.B. Mariotto, J.H. Rowland, K.R. Yabroff, C.M. Alfano, A. Jemal, J.L. Kramer, R.L. Siegel, Cancer treatment and survivorship statistics, 2019, CA: a cancer journal for clinicians 69(5) (2019) 363-385.
- [4] D. Ho, Artificial intelligence in cancer therapy, Science 367(6481) (2020) 982-983.
- [5] R.C. Mohs, N.H. Greig, Drug discovery and development: Role of basic biological research, Alzheimer's & Dementia: Translational Research & Clinical interventions 3(4) (2017) 651-657.
- [6] FDA. <https://www.fda.gov/drugs/drug-approvals-and-databases/drugsfda-glossary-terms#Drug>. (Accessed September 9 2020).
- [7] K. Strebhardt, A. Ullrich, Paul Ehrlich's magic bullet concept: 100 years of progress, Nature Reviews Cancer 8(6) (2008) 473-480.
- [8] S. Harrer, P. Shah, B. Antony, J. Hu, Artificial intelligence for clinical trial design, Trends in pharmacological sciences 40(8) (2019) 577-591.
- [9] A.D. Hingorani, V. Kuan, C. Finan, F.A. Kruger, A. Gaulton, S. Chopade, R. Sofat, R.J. MacAllister, J.P. Overington, H. Hemingway, Improving the odds of drug development success through human genomics: modelling study, Scientific reports 9(1) (2019) 1-25.
- [10] D. Swinney, Phenotypic vs. target-based drug discovery for first-in-class medicines, Clinical Pharmacology & Therapeutics 93(4) (2013) 299-301.
- [11] E. Andrade, A. Bento, J. Cavalli, S. Oliveira, R. Schwanke, J. Siqueira, C. Freitas, R. Marcon, J. Calixto, Non-clinical studies in the process of new drug development-Part II: Good laboratory practice, metabolism, pharmacokinetics, safety and dose translation to clinical studies, Brazilian journal of medical and biological research 49(12) (2016).
- [12] N. Venkatesan, M. Ramanathan, Preclinical Toxicity Studies-Tool of Drug Discovery, PVPE 1 (2017) 1-7.
- [13] J.P. Hughes, S. Rees, S.B. Kalindjian, K.L. Philpott, Principles of early drug discovery, British journal of pharmacology 162(6) (2011) 1239-1249.

- [14] O.J. Wouters, M. McKee, J. Luyten, Estimated research and development investment needed to bring a new medicine to market, 2009-2018, *Jama* 323(9) (2020) 844-853.
- [15] J.D. McKinney, A. Richard, C. Waller, M.C. Newman, F. Gerberick, The practice of structure activity relationships (SAR) in toxicology, *Toxicological Sciences* 56(1) (2000) 8-17.
- [16] J. Blagg, Structure–activity relationships for in vitro and in vivo toxicity, *Annual Reports in medicinal chemistry* 41 (2006) 353-368.
- [17] R. Ritam, L. Sandeep, *Metabolic Screening in Drug Development, Vivo*, 2017.
- [18] A.D. Andricopulo, L.B. Salum, D.J. Abraham, Structure-based drug design strategies in medicinal chemistry, *Current topics in medicinal chemistry* 9(9) (2009) 771-790.
- [19] J. McKim, M. James, Building a tiered approach to in vitro predictive toxicity screening: a focus on assays with in vivo relevance, *Combinatorial chemistry & high throughput screening* 13(2) (2010) 188-206.
- [20] R. Guha, On exploring structure–activity relationships, In *silico* models for drug discovery, Springer2013, pp. 81-94.
- [21] G.T. Whiteside, J.D. Kennedy, Consideration of pharmacokinetic pharmacodynamic relationships in the discovery of new pain drugs, *Translational Pain Research: From Mouse to Man*. Boca Raton, FL: CRC Press/Taylor & Francis (2010).
- [22] L. Ni, H. Zhao, L. Tao, X. Li, Z. Zhou, Y. Sun, C. Chen, D. Wei, Y. Liu, G. Diao, Synthesis, in vitro cytotoxicity, and structure–activity relationships (SAR) of multidentate oxidovanadium (IV) complexes as anticancer agents, *Dalton Transactions* 47(30) (2018) 10035-10045.
- [23] M. Al-Refai, M.M. Ibrahim, M. Nurul Azmi, H. Osman, M.H. Abu Bakar, A. Geyer, The Synthesis, Characterization, Cytotoxic Activity Assessment and Structure-Activity Relationship of 4-Aryl-6-(2, 5-dichlorothiophen-3-yl)-2-methoxypyridine-3-carbonitriles, *Molecules* 24(22) (2019) 4072.
- [24] R.E. Mulvey, s-Block metal inverse crowns: synthetic and structural synergism in mixed alkali metal–magnesium (or zinc) amide chemistry, *Chemical Communications* (12) (2001) 1049-1056.
- [25] Q. Zhang, X. Liang, H. Chen, W. Yan, L. Shi, Y. Liu, J. Li, X. Zou, Identifying Key Structural Subunits and Their Synergism in Low-Iridium Triple Perovskites for Oxygen Evolution in Acidic Media, *Chemistry of Materials* 32(9) (2020) 3904-3910.
- [26] J. Hao, J.N. Ho, J.A. Lewis, K.A. Karim, R.N. Daniels, P.R. Gentry, C.R. Hopkins, C.W. Lindsley, C.C. Hong, In vivo structure– activity relationship study of dorsomorphin

analogues identifies selective VEGF and BMP inhibitors, *ACS chemical biology* 5(2) (2010) 245-253.

[27] D.K. Agrafiotis, J.J. Wiener, A. Skalkin, J. Kolpak, Single R-group polymorphisms (SRPs) and R-cliffs: An intuitive framework for analyzing and visualizing activity cliffs in a single analog series, *Journal of chemical information and modeling* 51(5) (2011) 1122-1131.

[28] X. Lin, X. Li, X. Lin, A review on applications of computational methods in drug screening and design, *Molecules* 25(6) (2020) 1375.

[29] A.C.L. Leite, J.W. Espíndola, M.V. de Oliveira Cardoso, G.B. de Oliveira Filho, Privileged structures in the design of potential drug candidates for neglected diseases, *Current Medicinal Chemistry* 26(23) (2019) 4323-4354.

[30] A. van der Vliet, K. Danyal, D.E. Heppner, Dual oxidase: a novel therapeutic target in allergic disease, *British Journal of Pharmacology* 175(9) (2018) 1401-1418.

[31] M.J. Naim, O. Alam, J. Alam, F. Bano, P. Alam, N. Shrivastava, Recent Review on Indole: A Privileged Structure Scaffold, *Int. J. Pharm. Sci. Res* 7 (2016) 51-62.

[32] S. Tahlan, S. Kumar, B. Narasimhan, Pharmacological significance of heterocyclic 1H-benzimidazole scaffolds: a review, *BMC chemistry* 13(1) (2019) 101.

[33] J.G. Moffat, F. Vincent, J.A. Lee, J. Eder, M. Prunotto, Opportunities and challenges in phenotypic drug discovery: an industry perspective, *Nature reviews Drug discovery* 16(8) (2017) 531-543.

[34] A.R. Neves, M. Correia-da-Silva, E. Sousa, M. Pinto, Structure–activity relationship studies for multitarget antithrombotic drugs, *Future medicinal chemistry* 8(18) (2016) 2305-2355.

[35] M.D. Siegelin, E. Schneider, M.-A. Westhoff, C.R. Wirtz, G. Karpel-Massler, Current state and future perspective of drug repurposing in malignant glioma, *Seminars in cancer biology*, Elsevier, 2019.

[36] F.H.C. Chou, K.Y. Tsai, H.C. Wu, S.P. Shen, Cancer in patients with schizophrenia: What is the next step?, *Psychiatry and Clinical Neurosciences* 70(11) (2016) 473-488.

[37] J. Huang, D. Zhao, Z. Liu, F. Liu, Repurposing psychiatric drugs as anti-cancer agents, *Cancer letters* 419 (2018) 257-265.

[38] J.K. Lee, D.H. Nam, J. Lee, Repurposing antipsychotics as glioblastoma therapeutics: Potentials and challenges, *Oncology letters* 11(2) (2016) 1281-1286.

[39] A.G. Lipman, *Drug repurposing and repositioning: workshop summary*, Taylor & Francis, 2015.

- [40] A. Neuberger, N. Oraiopoulos, D.L. Drakeman, Renovation as innovation: is repurposing the future of drug discovery research?, *Drug discovery today* 24(1) (2019) 1.
- [41] S. Pushpakom, F. Iorio, P.A. Eyers, K.J. Escott, S. Hopper, A. Wells, A. Doig, T. Guilleams, J. Latimer, C. McNamee, Drug repurposing: progress, challenges and recommendations, *Nature reviews Drug discovery* 18(1) (2019) 41-58.
- [42] Q. Duan, C. Flynn, M. Niepel, M. Hafner, J.L. Muhlich, N.F. Fernandez, A.D. Rouillard, C.M. Tan, E.Y. Chen, T.R. Golub, LINCS Canvas Browser: interactive web app to query, browse and interrogate LINCS L1000 gene expression signatures, *Nucleic acids research* 42(W1) (2014) W449-W460.
- [43] B. Li, C. Dai, L. Wang, H. Deng, Y. Li, Z. Guan, H. Ni, A novel drug repurposing approach for non-small cell lung cancer using deep learning, *Plos one* 15(6) (2020) e0233112.
- [44] A. Daina, O. Michielin, V. Zoete, SwissTargetPrediction: updated data and new features for efficient prediction of protein targets of small molecules, *Nucleic acids research* 47(W1) (2019) W357-W364.
- [45] Y. Budama-Kilinc, S. Kecel-Gunduz, B. Ozdemir, B. Bicak, G. Akman, B. Arvas, F. Aydogan, C. Yolacan, New nanodrug design for cancer therapy: Its synthesis, formulation, in vitro and in silico evaluations, *Archiv der Pharmazie* (2020) e2000137.
- [46] M. Rao, R. Gupta, M. Liguori, M. Hu, X. Huang, S. Mantena, S. Mittelstadt, E. Blomme, T. Van Vleet, Novel computational approach to predict off-target interactions for small molecules, *Front. Big Data* 2 (2019).
- [47] J.R.C. Rey, E.V. Cervino, M.L. Rentero, E.C. Crespo, A.O. Álvaro, M. Casillas, Raloxifene: mechanism of action, effects on bone tissue, and applicability in clinical traumatology practice, *The open orthopaedics journal* 3 (2009) 14.
- [48] S.J. Matthews, C. McCoy, Thalidomide: a review of approved and investigational uses, *Clinical therapeutics* 25(2) (2003) 342-395.
- [49] I. Amelio, M. Gostev, R. Knight, A. Willis, G. Melino, A. Antonov, DRUGSURV: a resource for repositioning of approved and experimental drugs in oncology based on patient survival information, *Cell death & disease* 5(2) (2014) e1051-e1051.
- [50] L. Aslostovar, A.L. Boyd, M. Almakadi, T.J. Collins, D.P. Leong, R.G. Tirona, R.B. Kim, J.A. Julian, A. Xenocostas, B. Leber, A phase 1 trial evaluating thioridazine in combination with cytarabine in patients with acute myeloid leukemia, *Blood advances* 2(15) (2018) 1935-1945.
- [51] R. W. Humphrey, L. M. Brockway-Lunardi, D. T. Bonk, K.M. Dohoney, J.H. Doroshow, S.J. Meech, M.J. Ratain, S.L. Topalian, D. M. Pardoll, Opportunities and challenges in the

- development of experimental drug combinations for cancer, *Journal of the National Cancer Institute* 103(16) (2011) 1222-1226.
- [52] R.c. therapies, Rationalizing combination therapies, *Nat Med* 23 (2017) 1113.
- [53] Z. Zhang, L. Zhou, N. Xie, E.C. Nice, T. Zhang, Y. Cui, C. Huang, Overcoming cancer therapeutic bottleneck by drug repurposing, *Signal Transduction and Targeted Therapy* 5(1) (2020) 1-25.
- [54] T.A. Yap, A. Omlin, J.S. De Bono, Development of therapeutic combinations targeting major cancer signaling pathways, *Journal of Clinical Oncology* 31(12) (2013) 1592-1605.
- [55] J. Lehár, A.S. Krueger, W. Avery, A.M. Heilbut, L.M. Johansen, E.R. Price, R.J. Rickles, G.F. Short Iii, J.E. Staunton, X. Jin, Synergistic drug combinations tend to improve therapeutically relevant selectivity, *Nature biotechnology* 27(7) (2009) 659-666.
- [56] R.B. Mokhtari, T.S. Homayouni, N. Baluch, E. Morgatskaya, S. Kumar, B. Das, H. Yeger, Combination therapy in combating cancer, *Oncotarget* 8(23) (2017) 38022.
- [57] J. Birkebak, L.A. Buckley, D. Dambach, E. Musvasva, K. Price, S. Ralston, A. Sacaan, Pharmaceutical industry perspective on combination toxicity studies: Results from an intra-industry survey conducted by IQ DruSafe Leadership Group, *Regulatory Toxicology and Pharmacology* 102 (2019) 40-46.
- [58] M.V. Blagosklonny, Analysis of FDA approved anticancer drugs reveals the future of cancer therapy, *Cell Cycle* 3(8) (2004) 1033-1040.
- [59] T.-C. Chou, Preclinical versus clinical drug combination studies, *Leukemia & lymphoma* 49(11) (2008) 2059-2080.
- [60] A. Ianevski, A.K. Giri, P. Gautam, A. Kononov, S. Potdar, J. Saarela, K. Wennerberg, T. Aittokallio, Prediction of drug combination effects with a minimal set of experiments, *Nature machine intelligence* 1(12) (2019) 568-577.
- [61] P.M. Haverty, E. Lin, J. Tan, Y. Yu, B. Lam, S. Lianoglou, R.M. Neve, S. Martin, J. Settleman, R.L. Yauch, Reproducible pharmacogenomic profiling of cancer cell line panels, *Nature* 533(7603) (2016) 333-337.
- [62] A. Ianevski, L. He, T. Aittokallio, J. Tang, SynergyFinder: a web application for analyzing drug combination dose–response matrix data, *Bioinformatics* 33(15) (2017) 2413-2415.
- [63] A. Ianevski, A.K. Giri, T. Aittokallio, SynergyFinder 2.0: visual analytics of multi-drug combination synergies, *Nucleic Acids Research* (2020).

- [64] A. Malyutina, M.M. Majumder, W. Wang, A. Pessia, C.A. Heckman, J. Tang, Drug combination sensitivity scoring facilitates the discovery of synergistic and efficacious drug combinations in cancer, *PLoS computational biology* 15(5) (2019) e1006752.
- [65] A. Ianevski, S. Timonen, A. Kononov, T. Aittokallio, A.K. Giri, SynToxProfiler: An interactive analysis of drug combination synergy, toxicity and efficacy, *PLoS computational biology* 16(2) (2020) e1007604.
- [66] H. Zhou, S. George, C. Li, S. Gurusamy, X. Sun, Z. Gong, H. Qian, Combined toxicity of prevalent mycotoxins studied in fish cell line and zebrafish larvae revealed that type of interactions is dose-dependent, *Aquatic toxicology* 193 (2017) 60-71.
- [67] G. Ding, J. Zhang, Y. Chen, L. Wang, M. Wang, D. Xiong, Y. Sun, Combined effects of PFOS and PFOA on zebrafish (*Danio rerio*) embryos, *Archives of environmental contamination and toxicology* 64(4) (2013) 668-675.
- [68] S. Brown, L.R. Fraga, G. Cameron, L. Erskine, N. Vargesson, The Primodos components Norethisterone acetate and Ethinyl estradiol induce developmental abnormalities in zebrafish embryos, *Scientific reports* 8(1) (2018) 1-14.
- [69] Z. Ju, S.-S. Liu, Y.-Q. Xu, K. Li, Combined toxicity of 2, 4-dichlorophenoxyacetic acid and its metabolites 2, 4-dichlorophenol (2, 4-DCP) on two nontarget organisms, *ACS omega* 4(1) (2019) 1669-1677.
- [70] J.R. Pritchard, P.M. Bruno, L.A. Gilbert, K.L. Capron, D.A. Lauffenburger, M.T. Hemann, Defining principles of combination drug mechanisms of action, *Proceedings of the National Academy of Sciences* 110(2) (2013) E170-E179.
- [71] H. Weber, J.R. Valbuena, M.A. Barbhuiya, S. Stein, H. Kunkel, P. García, C. Bizama, I. Riquelme, J.A. Espinoza, S.E. Kurtz, Small molecule inhibitor screening identified HSP90 inhibitor 17-AAG as potential therapeutic agent for gallbladder cancer, *Oncotarget* 8(16) (2017) 26169.
- [72] P.-P. Wong, F. Demircioglu, E. Ghazaly, W. Alrawashdeh, M.R. Stratford, C.L. Scudamore, B. Cereser, T. Crnogorac-Jurcevic, S. McDonald, G. Elia, Dual-action combination therapy enhances angiogenesis while reducing tumor growth and spread, *Cancer cell* 27(1) (2015) 123-137.
- [73] M. Hason, P. Bartůněk, Zebrafish models of cancer—new insights on modeling human cancer in a non-mammalian vertebrate, *Genes* 10(11) (2019) 935.
- [74] P. Letrado, I. de Miguel, I. Lamberto, R. Díez-Martínez, J. Oyarzabal, Zebrafish: speeding up the cancer drug discovery process, *Cancer research* 78(21) (2018) 6048-6058.

- [75] C. Santoriello, L.I. Zon, Hooked! Modeling human disease in zebrafish, *The Journal of clinical investigation* 122(7) (2012) 2337-2343.
- [76] L.I. Zon, R.T. Peterson, In vivo drug discovery in the zebrafish, *Nature reviews Drug discovery* 4(1) (2005) 35-44.
- [77] M. Chakraborty, K. Roy, A. Sedhain, P. Dhakal, G. Karunakaran, Zebrafish an emerging model for Preclinical Drug Discovery, *International Journal of Research in Pharmaceutical Sciences* 11(2) (2020) 1638-1648.
- [78] P. McGrath, C.-Q. Li, Zebrafish: a predictive model for assessing drug-induced toxicity, *Drug discovery today* 13(9-10) (2008) 394-401.
- [79] C. Parng, W.L. Seng, C. Semino, P. McGrath, Zebrafish: a preclinical model for drug screening, *Assay and drug development technologies* 1(1) (2002) 41-48.
- [80] C.H. Williams, C.C. Hong, Zebrafish small molecule screens: Taking the phenotypic plunge, *Computational and structural biotechnology journal* 14 (2016) 350-356.
- [81] C. Gutierrez-Lovera, A. Vazquez-Rios, J. Guerra-Varela, L. Sanchez, M. De la Fuente, The potential of zebrafish as a model organism for improving the translation of genetic anticancer nanomedicines, *Genes* 8(12) (2017) 349.
- [82] C.A. MacRae, R.T. Peterson, Zebrafish as tools for drug discovery, *Nature reviews Drug discovery* 14(10) (2015) 721-731.
- [83] J.R. Mathias, M.T. Saxena, J.S. Mumm, Advances in zebrafish chemical screening technologies, *Future medicinal chemistry* 4(14) (2012) 1811-1822.
- [84] M. Dang, R. Fogley, L. Zon, Cancer and zebrafish: mechanisms, techniques, and models: chemical genetics, *Advances in experimental medicine and biology* 916 (2016) 103.
- [85] S. Lantz-McPeak, X. Guo, E. Cuevas, M. Dumas, G.D. Newport, S.F. Ali, M.G. Paule, J. Kanungo, Developmental toxicity assay using high content screening of zebrafish embryos, *Journal of Applied Toxicology* 35(3) (2015) 261-272.
- [86] I.W. Selderslaghs, A.R. Van Rompay, W. De Coen, H.E. Witters, Development of a screening assay to identify teratogenic and embryotoxic chemicals using the zebrafish embryo, *Reproductive toxicology* 28(3) (2009) 308-320.
- [87] S. Jarque, M. Rubio-Brotons, J. Ibarra, V. Ordoñez, S. Dybala, R. Miñana, J. Terriente, Morphometric analysis of developing zebrafish embryos allows predicting teratogenicity modes of action in higher vertebrates, *Reproductive Toxicology* (2020).
- [88] X.-P. Gao, F. Feng, X.-Q. Zhang, X.-X. Liu, Y.-B. Wang, J.-X. She, Z.-H. He, M.-F. He, Toxicity assessment of 7 anticancer compounds in zebrafish, *International journal of toxicology* 33(2) (2014) 98-105.

- [89] X. Zhang, C. Li, Z. Gong, Development of a convenient in vivo hepatotoxin assay using a transgenic zebrafish line with liver-specific DsRed expression, *PloS one* 9(3) (2014) e91874.
- [90] C. Cornet, S. Calzolari, R. Miñana-Prieto, S. Dyballa, E. Van Doornmalen, H. Rutjes, T. Savy, D. D'Amico, J. Terriente, ZeGlobalTox: an innovative approach to address organ drug toxicity using zebrafish, *International Journal of Molecular Sciences* 18(4) (2017) 864.
- [91] D.M. Reif, L. Truong, D. Mandrell, S. Marvel, G. Zhang, R.L. Tanguay, High-throughput characterization of chemical-associated embryonic behavioral changes predicts teratogenic outcomes, *Archives of toxicology* 90(6) (2016) 1459-1470.
- [92] M.A. Cousin, J.O. Ebbert, A.R. Wiinamaki, M.D. Urban, D.P. Argue, S.C. Ekker, E.W. Klee, Larval zebrafish model for FDA-approved drug repositioning for tobacco dependence treatment, *PLoS One* 9(3) (2014) e90467.
- [93] J.J. Ingebretson, M.A. Masino, Quantification of locomotor activity in larval zebrafish: considerations for the design of high-throughput behavioral studies, *Frontiers in neural circuits* 7 (2013) 109.
- [94] T. Irons, R. MacPhail, D. Hunter, S. Padilla, Acute neuroactive drug exposures alter locomotor activity in larval zebrafish, *Neurotoxicology and teratology* 32(1) (2010) 84-90.
- [95] I.W. Selderslaghs, J. Hooyberghs, W. De Coen, H.E. Witters, Locomotor activity in zebrafish embryos: a new method to assess developmental neurotoxicity, *Neurotoxicology and teratology* 32(4) (2010) 460-471.
- [96] J. Jordi, D. Guggiana-Nilo, A.D. Bolton, S. Prabha, K. Ballotti, K. Herrera, A.J. Rennekamp, R.T. Peterson, T.A. Lutz, F. Engert, High-throughput screening for selective appetite modulators: A multibehavioral and translational drug discovery strategy, *Science advances* 4(10) (2018) eaav1966.
- [97] D. Kokel, R.T. Peterson, Using the zebrafish photomotor response for psychotropic drug screening, *Methods in cell biology*, Elsevier2011, pp. 517-524.
- [98] D. Kokel, J. Bryan, C. Laggner, R. White, C.Y.J. Cheung, R. Mateus, D. Healey, S. Kim, A.A. Werdich, S.J. Haggarty, Rapid behavior-based identification of neuroactive small molecules in the zebrafish, *Nature chemical biology* 6(3) (2010) 231-237.
- [99] W. van der Ent, C. Burrello, A.F. Teunisse, B.R. Ksander, P.A. van der Velden, M.J. Jager, A.G. Jochemsen, B.E. Snaar-Jagalska, Modeling of human uveal melanoma in zebrafish xenograft embryos, *Investigative ophthalmology & visual science* 55(10) (2014) 6612-6622.

- [100] D.-W. Jung, E.-S. Oh, S.-H. Park, Y.-T. Chang, C.-H. Kim, S.-Y. Choi, D.R. Williams, A novel zebrafish human tumor xenograft model validated for anti-cancer drug screening, *Molecular BioSystems* 8(7) (2012) 1930-1939.
- [101] M.G. Haney, L.H. Moore, J.S. Blackburn, Drug Screening of Primary Patient Derived Tumor Xenografts in Zebrafish, *JoVE* (158) (2020) e60996.
- [102] D. Hill, L. Chen, E. Snaar-Jagalska, B. Chaudhry, Embryonic zebrafish xenograft assay of human cancer metastasis, *FRResearch* 7 (2018).
- [103] C. Cornet, S. Dyballa, J. Terriente, V. Di Giacomo, ZeOncoTest: Refining and Automating the Zebrafish Xenograft Model for Drug Discovery in Cancer, *Pharmaceuticals* 13(1) (2020) 1.
- [104] L. Huiting, F. Laroche, H. Feng, The zebrafish as a tool to cancer drug discovery, *Austin journal of pharmacology and therapeutics* 3(2) (2015) 1069.
- [105] H.-S. Lin, Y.-L. Huang, Y.-R.S. Wang, E. Hsiao, T.-A. Hsu, H.-Y. Shiao, W.-T. Jiaang, B.P. Sampurna, K.-H. Lin, M.-S. Wu, Identification of novel anti-liver cancer small molecules with better therapeutic index than sorafenib via zebrafish drug screening platform, *Cancers* 11(6) (2019) 739.
- [106] C.-H. Tseng, Y.-R. Chen, C.-C. Tzeng, W. Liu, C.-K. Chou, C.-C. Chiu, Y.-L. Chen, Discovery of indeno [1, 2-b] quinoxaline derivatives as potential anticancer agents, *European journal of medicinal chemistry* 108 (2016) 258-273.
- [107] X.-Y. Zhu, D.-W. Guo, Q.-C. Lao, Y.-Q. Xu, Z.-K. Meng, B. Xia, H. Yang, C.-Q. Li, P. Li, Sensitization and synergistic anti-cancer effects of Furanodiene identified in zebrafish models, *Scientific reports* 9(1) (2019) 1-12.
- [108] G. Chimote, J. Sreenivasan, N. Pawar, J. Subramanian, H. Sivaramakrishnan, S. Sharma, Comparison of effects of anti-angiogenic agents in the zebrafish efficacy–toxicity model for translational anti-angiogenic drug discovery, *Drug design, development and therapy* 8 (2014) 1107.
- [109] S. Ridges, W.L. Heaton, D. Joshi, H. Choi, A. Eiring, L. Batchelor, P. Choudhry, E.J. Manos, H. Sofla, A. Sanati, Zebrafish screen identifies novel compound with selective toxicity against leukemia, *Blood advances* 119(24) (2012) 5621-5631.
- [110] D. Yamamoto, D. Sato, H. Nakayama, Y. Nakagawa, Y. Shimada, ZF-Mapper: Simple and complete freeware for fluorescence quantification in zebrafish images, *Zebrafish* 16(3) (2019) 233-239.

- [111] T.-H. Hsieh, C.-Y. Hsu, C.-F. Tsai, C.-C. Chiu, S.-S. Liang, T.-N. Wang, P.-L. Kuo, C.-Y. Long, E.-M. Tsai, A novel cell-penetrating peptide suppresses breast tumorigenesis by inhibiting β -catenin/LEF-1 signaling, *Scientific reports* 6(1) (2016) 1-12.
- [112] U. Ben-David, B. Siranosian, G. Ha, H. Tang, Y. Oren, K. Hinohara, C.A. Strathdee, J. Dempster, N.J. Lyons, R. Burns, Genetic and transcriptional evolution alters cancer cell line drug response, *Nature* 560(7718) (2018) 325-330.
- [113] W.L. Kaufman, I. Kocman, V. Agrawal, H.-P. Rahn, D. Besser, M. Gossen, Homogeneity and persistence of transgene expression by omitting antibiotic selection in cell line isolation, *Nucleic acids research* 36(17) (2008) e111-e111.
- [114] C.E. DeSantis, J. Ma, M.M. Gaudet, L.A. Newman, K.D. Miller, A. Goding Sauer, A. Jemal, R.L. Siegel, Breast cancer statistics, 2019, *CA: a cancer journal for clinicians* 69(6) (2019) 438-451.
- [115] J.J. Going, Ductal-lobar organisation of human breast tissue, its relevance in disease and a research objective: vector mapping of parenchyma in complete breasts (the Astley Cooper project), *Breast cancer research and treatment* 8(4) (2006) 107.
- [116] D.P. Arps, P. Healy, L. Zhao, C.G. Kleer, J.C. Pang, Invasive ductal carcinoma with lobular features: a comparison study to invasive ductal and invasive lobular carcinomas of the breast, *Breast cancer research and treatment* 138(3) (2013) 719-726.
- [117] J. Makki, Diversity of breast carcinoma: histological subtypes and clinical relevance, *Clinical Medicine Insights: Pathology* 8 (2015) CPath. S31563.
- [118] K. Polyak, Heterogeneity in breast cancer, *The Journal of clinical investigation* 121(10) (2011) 3786-3788.
- [119] C.M. Perou, T. Sørli, M.B. Eisen, M. Van De Rijn, S.S. Jeffrey, C.A. Rees, J.R. Pollack, D.T. Ross, H. Johnsen, L.A. Akslen, Molecular portraits of human breast tumours, *nature* 406(6797) (2000) 747-752.
- [120] S.M. Fragomeni, A. Sciallis, J.S. Jeruss, Molecular subtypes and local-regional control of breast cancer, *Surgical Oncology Clinics* 27(1) (2018) 95-120.
- [121] J. Kao, K. Salari, M. Bocanegra, Y.-L. Choi, L. Girard, J. Gandhi, K.A. Kwei, T. Hernandez-Boussard, P. Wang, A.F. Gazdar, Molecular profiling of breast cancer cell lines defines relevant tumor models and provides a resource for cancer gene discovery, *PloS one* 4(7) (2009) e6146.
- [122] L. Han, A new perspective on Estrogen Receptor beta in breast cancer progression, *Cancer biology & therapy* 11(7) (2011) 644-646.

- [123] L. He, Y. Lv, Y. Song, B. Zhang, The prognosis comparison of different molecular subtypes of breast tumors after radiotherapy and the intrinsic reasons for their distinct radiosensitivity, *Cancer Management and Research* 11 (2019) 5765.
- [124] X. Dai, H. Cheng, Z. Bai, J. Li, Breast cancer cell line classification and its relevance with breast tumor subtyping, *Journal of Cancer* 8(16) (2017) 3131.
- [125] F.J. Velloso, A.F. Bianco, J.O. Farias, N.E. Torres, P.Y. Ferruzo, V. Anschau, H.C. Jesus-Ferreira, T.H.-T. Chang, M.C. Sogayar, L.F. Zerbini, The crossroads of breast cancer progression: insights into the modulation of major signaling pathways, *OncoTargets and therapy* 10 (2017) 5491.
- [126] X. Dai, T. Li, Z. Bai, Y. Yang, X. Liu, J. Zhan, B. Shi, Breast cancer intrinsic subtype classification, clinical use and future trends, *American journal of cancer research* 5(10) (2015) 2929.
- [127] C. Curtis, S.P. Shah, S.-F. Chin, G. Turashvili, O.M. Rueda, M.J. Dunning, D. Speed, A.G. Lynch, S. Samarajiwa, Y. Yuan, The genomic and transcriptomic architecture of 2,000 breast tumours reveals novel subgroups, *Nature* 486(7403) (2012) 346-352.
- [128] T.O. Nielsen, J.S. Parker, S. Leung, D. Voduc, M. Ebbert, T. Vickery, S.R. Davies, J. Snider, I.J. Stijleman, J. Reed, A comparison of PAM50 intrinsic subtyping with immunohistochemistry and clinical prognostic factors in tamoxifen-treated estrogen receptor–positive breast cancer, *Clinical cancer research* 16(21) (2010) 5222-5232.
- [129] S. Guiu, S. Michiels, F. André, J. Cortes, C. Denkert, A. Di Leo, B. Hennessy, T. Sorlie, C. Sotiriou, N. Turner, Molecular subclasses of breast cancer: how do we define them? The IMPAKT 2012 Working Group Statement, *Annals of oncology* 23(12) (2012) 2997-3006.
- [130] M.C. Liu, B.N. Pitcher, E.R. Mardis, S.R. Davies, P.N. Friedman, J.E. Snider, T.L. Vickery, J.P. Reed, K. DeSchryver, B. Singh, PAM50 gene signatures and breast cancer prognosis with adjuvant anthracycline-and taxane-based chemotherapy: correlative analysis of C9741 (Alliance), *NPJ breast cancer* 2(1) (2016) 1-8.
- [131] M. Pu, K. Messer, S.R. Davies, T.L. Vickery, E. Pittman, B.A. Parker, M.J. Ellis, S.W. Flatt, C.R. Marinac, S.H. Nelson, based PAM50 signature and long-term breast cancer survival, *Breast cancer research and treatment* 179(1) (2020) 197-206.
- [132] H.G. Russnes, O.C. Lingjærde, A.-L. Børresen-Dale, C. Caldas, Breast cancer molecular stratification: from intrinsic subtypes to integrative clusters, *The American journal of pathology* 187(10) (2017) 2152-2162.

- [133] H. Hirschfield, C.B. Bian, T. Higashi, S. Nakagawa, T.Z. Zeleke, V.D. Nair, B.C. Fuchs, Y. Hoshida, In vitro modeling of hepatocellular carcinoma molecular subtypes for anti-cancer drug assessment, *Experimental & molecular medicine* 50(1) (2018) e419-e419.
- [134] J.M. Saunus, C.E. Smart, J.R. Kutasovic, R.L. Johnston, P. Kalita-de Croft, M. Miranda, E.N. Rozali, A.C. Vargas, L.E. Reid, E. Lorsy, Multidimensional phenotyping of breast cancer cell lines to guide preclinical research, *Breast cancer research and treatment* 167(1) (2018) 289-301.
- [135] G. Sflomos, V. Dormoy, T. Metsalu, R. Jeitziner, L. Battista, V. Scabia, W. Raffoul, J.-F. Delaloye, A. Treboux, M. Fiche, A preclinical model for ER α -positive breast cancer points to the epithelial microenvironment as determinant of luminal phenotype and hormone response, *Cancer cell* 29(3) (2016) 407-422.
- [136] A. Bouzekri, A. Esch, O. Ornatsky, Multidimensional profiling of drug-treated cells by Imaging Mass Cytometry, *FEBS open bio* 9(9) (2019) 1652-1669.
- [137] F.L. Nobrega, D. Ferreira, I.M. Martins, M. Suarez-Diez, J. Azeredo, L.D. Kluskens, L.R. Rodrigues, Screening and characterization of novel specific peptides targeting MDA-MB-231 claudin-low breast carcinoma by computer-aided phage display methodologies, *BMC cancer* 16(1) (2016) 881.
- [138] J. Wei, H. Sun, A. Zhang, X. Wu, Y. Li, J. Liu, Y. Duan, F. Xiao, H. Wang, M. Lv, A novel AXL chimeric antigen receptor endows T cells with anti-tumor effects against triple negative breast cancers, *Cellular Immunology* 331 (2018) 49-58.
- [139] M. Kucinska, M.-D. Giron, H. Piotrowska, N. Lisiak, W.H. Granig, F.-J. Lopez-Jaramillo, R. Salto, M. Murias, T. Erker, Novel promising estrogenic receptor modulators: cytotoxic and estrogenic activity of Benzanilides and Dithiobenzanilides, *Plos one* 11(1) (2016) e0145615.
- [140] B.K. Asare, E. Yawson, R.V. Rajnarayanan, Flexible small molecular anti-estrogens with N, N-dialkylated-2, 5-diethoxy-4-morpholinoaniline scaffold targets multiple estrogen receptor conformations, *Cell Cycle* 16(15) (2017) 1465-1477.
- [141] N. Fuentes, P. Silveyra, Estrogen receptor signaling mechanisms, *Advances in protein chemistry and structural biology*, Elsevier 2019, pp. 135-170.
- [142] J.Q. CHEN, J.D. Yager, Estrogen's effects on mitochondrial gene expression: mechanisms and potential contributions to estrogen carcinogenesis, *Annals of the New York Academy of Sciences* 1028(1) (2004) 258-272.
- [143] A.R. Frost, D.R. Hurst, L.A. Shevde, R.S. Samant, The influence of the cancer microenvironment on the process of metastasis, *Hindawi*, 2012.

- [144] H.-R. Lee, T.-H. Kim, K.-C. Choi, Functions and physiological roles of two types of estrogen receptors, ER α and ER β , identified by estrogen receptor knockout mouse, *Laboratory animal research* 28(2) (2012) 71-76.
- [145] N.J. Rothenberger, A. Somasundaram, L.P. Stabile, The role of the estrogen pathway in the tumor microenvironment, *International journal of molecular sciences* 19(2) (2018) 611.
- [146] I. Paterni, C. Granchi, J.A. Katzenellenbogen, F. Minutolo, Estrogen receptors alpha (ER α) and beta (ER β): subtype-selective ligands and clinical potential, *Steroids* 90 (2014) 13-29.
- [147] D.C. Rigeracciolo, A. Scarpelli, R. Lappano, A. Pisano, M.F. Santolla, S. Avino, P. De Marco, B. Bussolati, M. Maggiolini, E.M. De Francesco, GPER is involved in the stimulatory effects of aldosterone in breast cancer cells and breast tumor-derived endothelial cells, *Oncotarget* 7(1) (2016) 94.
- [148] M.F. Santolla, R. Lappano, P. De Marco, M. Pupo, A. Vivacqua, D. Sisci, S. Abonante, D. Iacopetta, A.R. Cappello, V. Dolce, G protein-coupled estrogen receptor mediates the up-regulation of fatty acid synthase induced by 17 β -estradiol in cancer cells and cancer-associated fibroblasts, *Journal of Biological Chemistry* 287(52) (2012) 43234-43245.
- [149] X. Zhou, S. Wang, Z. Wang, X. Feng, P. Liu, X.-B. Lv, F. Li, F.-X. Yu, Y. Sun, H. Yuan, Estrogen regulates Hippo signaling via GPER in breast cancer, *The Journal of clinical investigation* 125(5) (2019) 2123-2135.
- [150] E. Garcia Dos Santos, M.N.I. Dieudonne, R. Pecquery, V. Le Moal, Y. Giudicelli, D.I. Lacasa, Rapid nongenomic E2 effects on p42/p44 MAPK, activator protein-1, and cAMP response element binding protein in rat white adipocytes, *Endocrinology* 143(3) (2002) 930-940.
- [151] V. Mann, C. Huber, G. Kogianni, F. Collins, B. Noble, The antioxidant effect of estrogen and Selective Estrogen Receptor Modulators in the inhibition of osteocyte apoptosis in vitro, *Bone* 40(3) (2007) 674-684.
- [152] Z.-J. Chen, W. Wei, G.-M. Jiang, H. Liu, W.-D. Wei, X. Yang, Y.-M. Wu, H. Liu, C.K. Wong, J. Du, Activation of GPER suppresses epithelial mesenchymal transition of triple negative breast cancer cells via NF- κ B signals, *Molecular oncology* 10(6) (2016) 775-788.
- [153] D. Austin, N. Hamilton, Y. Elshimali, R. Pietras, Y. Wu, J. Vadgama, Estrogen receptor-beta is a potential target for triple negative breast cancer treatment, *Oncotarget* 9(74) (2018) 33912.
- [154] W. Wei, Z. Chen, K. Zhang, X. Yang, Y. Wu, X. Chen, H. Huang, H. Liu, S. Cai, J. Du, The activation of G protein-coupled receptor 30 (GPR30) inhibits proliferation of estrogen

receptor-negative breast cancer cells in vitro and in vivo, *Cell death & disease* 5(10) (2014) e1428-e1428.

[155] K. Zhou, P. Sun, Y. Zhang, X. You, P. Li, T. Wang, Estrogen stimulated migration and invasion of estrogen receptor-negative breast cancer cells involves an ezrin-dependent crosstalk between G protein-coupled receptor 30 and estrogen receptor beta signaling, *Steroids* 111 (2016) 113-120.

[156] M. Shen, H. Shi, Estradiol and estrogen receptor agonists oppose oncogenic actions of leptin in HepG2 cells, *Plos one* 11(3) (2016) e0151455.

[157] M. Shen, J. Cao, H. Shi, Effects of estrogen and estrogen receptors on transcriptomes of HepG2 Cells: A preliminary study using RNA sequencing, *International Journal of Endocrinology* 2018 (2018).

[158] M. Xue, K. Zhang, K. Mu, J. Xu, H. Yang, Y. Liu, B. Wang, Z. Wang, Z. Li, Q. Kong, Regulation of estrogen signaling and breast cancer proliferation by an ubiquitin ligase TRIM56, *Oncogenesis* 8(5) (2019) 1-14.

[159] R. Siersbæk, S. Kumar, J.S. Carroll, Signaling pathways and steroid receptors modulating estrogen receptor α function in breast cancer, *Genes & development* 32(17-18) (2018) 1141-1154.

[160] T. Utsumi, N. Kobayashi, H. Hanada, Recent perspectives of endocrine therapy for breast cancer, *Breast Cancer* 14(2) (2007) 194-199.

[161] T. de Villiers, Selective estrogen receptor modulators in the treatment of osteoporosis: a review of the clinical evidence, *Clinical Investigation* 1(5) (2011) 719-724.

[162] K.-C. An, Selective estrogen receptor modulators, *Asian spine journal* 10(4) (2016) 787.

[163] E.R. Prossnitz, M. Barton, Estrogen biology: new insights into GPER function and clinical opportunities, *Molecular and cellular endocrinology* 389(1-2) (2014) 71-83.

[164] S. Martinkovich, D. Shah, S.L. Planey, J.A. Arnott, Selective estrogen receptor modulators: tissue specificity and clinical utility, *Clinical interventions in aging* 9 (2014) 1437.

[165] L.-H. Hsu, N.-M. Chu, Y.-F. Lin, S.-H. Kao, G-protein coupled estrogen receptor in breast cancer, *International Journal of Molecular Sciences* 20(2) (2019) 306.

[166] Y.M. Yoo, E.B. Jeung, Melatonin-induced estrogen receptor α -mediated calbindin-D9k expression plays a role in H₂O₂-mediated cell death in rat pituitary GH3 cells, *Journal of pineal research* 47(4) (2009) 301-307.

- [167] B.G. Trogden, S.H. Kim, S. Lee, J.A. Katzenellenbogen, Tethered indoles as functionalizable ligands for the estrogen receptor, *Bioorganic & medicinal chemistry letters* 19(2) (2009) 485-488.
- [168] T. Golob, R. Liebl, E. von Angerer, Sulfamoyloxy-substituted 2-phenylindoles: antiestrogen-based inhibitors of the steroid sulfatase in human breast cancer cells, *Bioorganic & medicinal chemistry* 10(12) (2002) 3941-3953.
- [169] F. Payton-Stewart, S.L. Tilghman, L.G. Williams, L.L. Winfield, Benzimidazoles diminish ERE transcriptional activity and cell growth in breast cancer cells, *Biochemical and biophysical research communications* 450(4) (2014) 1358-1362.
- [170] S. Dettmann, K. Szymanowitz, A. Wellner, A. Schiedel, C.E. Müller, R. Gust, 2-Phenyl-1-[4-(2-piperidine-1-yl-ethoxy) benzyl]-1H-benzimidazoles as ligands for the estrogen receptor: Synthesis and pharmacological evaluation, *Bioorganic & medicinal Chemistry* 18(14) (2010) 4905-4916.
- [171] H.M. Refaat, Synthesis and anticancer activity of some novel 2-substituted benzimidazole derivatives, *European Journal of Medicinal Chemistry* 45(7) (2010) 2949-2956.
- [172] R. Singla, K.B. Gupta, S. Upadhyay, M. Dhiman, V. Jaitak, Design, synthesis and biological evaluation of novel indole-benzimidazole hybrids targeting estrogen receptor alpha (ER- α), *European journal of medicinal chemistry* 146 (2018) 206-219.
- [173] Z. Ates-Alagoz, N. Coleman, M. Martin, A. Wan, A. Adejare, Syntheses and In Vitro Anticancer Properties of Novel Radiosensitizers, *Chemical biology & drug design* 80(6) (2012) 853-861.
- [174] A. Adejare, I. Mercier, Z. Ates-Alagoz, Compounds and compositions for treatment of breast cancer, Google Patents, 2018.
- [175] Y. Cheng, U.-H. Jin, C.D. Allred, A. Jayaraman, R.S. Chapkin, S. Safe, Aryl hydrocarbon receptor activity of tryptophan metabolites in young adult mouse colonocytes, *Drug Metabolism and Disposition* 43(10) (2015) 1536-1543.
- [176] M.S. Denison, S.R. Nagy, Activation of the aryl hydrocarbon receptor by structurally diverse exogenous and endogenous chemicals, *Annual review of pharmacology and toxicology* 43(1) (2003) 309-334.
- [177] K. Kaur, V. Jaitak, Recent development in indole derivatives as anticancer agents for breast cancer, *Anti-Cancer Agents in Medicinal Chemistry* 19(8) (2019) 962-983.

- [178] Y. Li, J. Yang, L. Niu, D. Hu, H. Li, L. Chen, Y. Yu, Q. Chen, Structural insights into the design of indole derivatives as tubulin polymerization inhibitors, *Febs Letters* 594(1) (2020) 199-204.
- [179] N.S. Goud, P. Kumar, R.D. Bharath, Recent Developments of Target-Based Benzimidazole Derivatives as Potential Anticancer Agents, *Heterocycles-Synthesis and Biological Activities*, IntechOpen2020.
- [180] T.-T. Miao, X.-B. Tao, D.-D. Li, H. Chen, X.-Y. Jin, Y. Geng, S.-F. Wang, W. Gu, Synthesis and biological evaluation of 2-aryl-benzimidazole derivatives of dehydroabietic acid as novel tubulin polymerization inhibitors, *RSC advances* 8(31) (2018) 17511-17526.
- [181] K. Jiang, S. Al-Diffalha, B.A. Centeno, Primary Liver Cancers—Part 1: Histopathology, Differential Diagnoses, and Risk Stratification, *Cancer Control* 25(1) (2018) 1073274817744625.
- [182] D. Sia, A. Villanueva, S.L. Friedman, J.M. Llovet, Liver cancer cell of origin, molecular class, and effects on patient prognosis, *Gastroenterology* 152(4) (2017) 745-761.
- [183] P. Dasgupta, C. Henshaw, D.R. Youlden, P.J. Clark, J.F. Aitken, P.D. Baade, Global Trends in Incidence Rates of Primary Adult Liver Cancers: A Systematic Review and Meta-Analysis, *Frontiers in Oncology* 10 (2020) 171.
- [184] R.S. Finn, Overview and description of hepatocellular carcinoma, *Clinical Advances in Hematology and Oncology* 5(4) (2013) 4-7.
- [185] J. Calderaro, M. Ziol, V. Paradis, J. Zucman-Rossi, Molecular and histological correlations in liver cancer, *Journal of hepatology* 71(3) (2019) 616-630.
- [186] J. Calderaro, G. Couchy, S. Imbeaud, G. Amaddeo, E. Letouzé, J.-F. Blanc, C. Laurent, Y. Hajji, D. Azoulay, P. Bioulac-Sage, Histological subtypes of hepatocellular carcinoma are related to gene mutations and molecular tumour classification, *Journal of hepatology* 67(4) (2017) 727-738.
- [187] P.S. Tan, S. Nakagawa, N. Goossens, A. Venkatesh, T. Huang, S.C. Ward, X. Sun, W.M. Song, A. Koh, C. Canasto-Chibuque, Clinicopathological indices to predict hepatocellular carcinoma molecular classification, *Liver International* 36(1) (2016) 108-118.
- [188] B. Schmidt, L. Wei, D.K. DePeralta, Y. Hoshida, P.S. Tan, X. Sun, J.P. Sventek, M. Lanuti, K.K. Tanabe, B.C. Fuchs, Molecular subclasses of hepatocellular carcinoma predict sensitivity to fibroblast growth factor receptor inhibition, *International journal of cancer* 138(6) (2016) 1494-1505.
- [189] E.A.F.T.S.O.T. Liver, EASL clinical practice guidelines: management of hepatocellular carcinoma, *Journal of hepatology* 69(1) (2018) 182-236.

- [190] Y. Hoshida, S.M. Nijman, M. Kobayashi, J.A. Chan, J.-P. Brunet, D.Y. Chiang, A. Villanueva, P. Newell, K. Ikeda, M. Hashimoto, Integrative transcriptome analysis reveals common molecular subclasses of human hepatocellular carcinoma, *Cancer research* 69(18) (2009) 7385-7392.
- [191] J. Zucman-Rossi, A. Villanueva, J.-C. Nault, J.M. Llovet, Genetic landscape and biomarkers of hepatocellular carcinoma, *Gastroenterology* 149(5) (2015) 1226-1239. e4.
- [192] R. Xue, L. Chen, C. Zhang, M. Fujita, R. Li, S.-M. Yan, C.K. Ong, X. Liao, Q. Gao, S. Sasagawa, Genomic and transcriptomic profiling of combined hepatocellular and intrahepatic cholangiocarcinoma reveals distinct molecular subtypes, *Cancer Cell* 35(6) (2019) 932-947. e8.
- [193] A. Huang, X. Zhao, X.-R. Yang, F.-Q. Li, X.-L. Zhou, K. Wu, X. Zhang, Q.-M. Sun, Y. Cao, H.-M. Zhu, Circumventing intratumoral heterogeneity to identify potential therapeutic targets in hepatocellular carcinoma, *Journal of hepatology* 67(2) (2017) 293-301.
- [194] T. El Jabbour, S.M. Lagana, H. Lee, Update on hepatocellular carcinoma: Pathologists' review, *World journal of gastroenterology* 25(14) (2019) 1653.
- [195] B. Chen, M. Sirota, H. Fan-Minogue, D. Hadley, A.J. Butte, Relating hepatocellular carcinoma tumor samples and cell lines using gene expression data in translational research, *BMC medical genomics* 8(S2) (2015) S5.
- [196] Z.C. Nwosu, N. Battello, M. Rothley, W. Piorońska, B. Sitek, M.P. Ebert, U. Hofmann, J. Sleeman, S. Wölfl, C. Meyer, Liver cancer cell lines distinctly mimic the metabolic gene expression pattern of the corresponding human tumours, *Journal of Experimental & Clinical Cancer Research* 37(1) (2018) 211.
- [197] Y. Zhao, Y. Chen, Y. Hu, J. Wang, X. Xie, G. He, H. Chen, Q. Shao, H. Zeng, H. Zhang, Genomic alterations across six hepatocellular carcinoma cell lines by panel-based sequencing, *Transl. Cancer Res* 7 (2018) 231-239.
- [198] E. Lamy, A. Hertrampf, C. Herz, J. Schüler, M. Erlacher, D. Bertele, A. Bakare, M. Wagner, T. Weiland, U. Lauer, Preclinical evaluation of 4-methylthiobutyl isothiocyanate on liver cancer and cancer stem cells with different p53 status, *PloS one* 8(8) (2013) e70846.
- [199] F. Fondevila, C. Méndez-Blanco, P. Fernández-Palanca, J. González-Gallego, J.L. Mauriz, Anti-tumoral activity of single and combined regorafenib treatments in preclinical models of liver and gastrointestinal cancers, *Experimental & molecular medicine* 51(9) (2019) 1-15.

- [200] L. Xie, Y. Zeng, Z. Dai, W. He, H. Ke, Q. Lin, Y. Chen, J. Bu, D. Lin, M. Zheng, Chemical and genetic inhibition of STAT3 sensitizes hepatocellular carcinoma cells to sorafenib induced cell death, *International Journal of Biological Sciences* 14(5) (2018) 577.
- [201] Z. Ren, S. Chen, B. Ning, L. Guo, Use of liver-derived cell lines for the study of drug-induced liver injury, *Drug-Induced Liver Toxicity*, Springer2018, pp. 151-177.
- [202] G.-H. Qiu, X. Xie, F. Xu, X. Shi, Y. Wang, L. Deng, Distinctive pharmacological differences between liver cancer cell lines HepG2 and Hep3B, *Cytotechnology* 67(1) (2015) 1-12.
- [203] J. Dzieran, J. Fabian, T. Feng, C. Coulouarn, I. Ilkavets, A. Kyselova, K. Breuhahn, S. Dooley, N.M. Meindl-Beinker, Comparative analysis of TGF- β /Smad signaling dependent cytostasis in human hepatocellular carcinoma cell lines, *PloS one* 8(8) (2013) e72252.
- [204] R.S. Finn, A. Aleshin, J. Dering, P. Yang, C. Ginther, A. Desai, D. Zhao, E. von Euw, R.W. Busuttill, D.J. Slamon, Molecular subtype and response to dasatinib, an Src/Abl small molecule kinase inhibitor, in hepatocellular carcinoma cell lines in vitro, *Hepatology* 57(5) (2013) 1838-1846.
- [205] N. Charette, C. De Saeger, V. Lannoy, Y. Horsmans, I. Leclercq, P. Stärkel, Salirasib inhibits the growth of hepatocarcinoma cell lines in vitro and tumor growth in vivo through ras and mTOR inhibition, *Molecular cancer* 9(1) (2010) 256.
- [206] A.R. Singh, S. Joshi, A.M. Burgoyne, J.K. Sicklick, S. Ikeda, Y. Kono, J.R. Garlich, G.A. Morales, D.L. Durden, Single agent and synergistic activity of the “first-in-class” dual PI3K/BRD4 inhibitor SF1126 with sorafenib in hepatocellular carcinoma, *Molecular cancer therapeutics* 15(11) (2016) 2553-2562.
- [207] L. Guo, S. Dial, L. Shi, W. Branham, J. Liu, J.-L. Fang, B. Green, H. Deng, J. Kaput, B. Ning, Similarities and differences in the expression of drug-metabolizing enzymes between human hepatic cell lines and primary human hepatocytes, *Drug metabolism and disposition* 39(3) (2011) 528-538.
- [208] J.R. Eun, Y.J. Jung, Y. Zhang, Y. Zhang, B. Tschudy-Seney, R. Ramsamooj, Y.-J.Y. Wan, N.D. Theise, M.A. Zern, Y. Duan, Hepatoma SK Hep-1 cells exhibit characteristics of oncogenic mesenchymal stem cells with highly metastatic capacity, *PloS one* 9(10) (2014) e110744.
- [209] C.-Z. Huang, A.-M. Huang, J.-F. Liu, B. Wang, K.-C. Lin, Y.-B. Ye, Somatostatin Octapeptide Inhibits Cell Invasion and Metastasis in Hepatocellular Carcinoma Through PEBP1, *Cellular Physiology and Biochemistry* 47(6) (2018) 2340-2349.

- [210] S.C. Heffelfinger, H.H. Hawkins, J. Barrish, L. Taylor, G.J. Darlington, SK HEP-1: a human cell line of endothelial origin, *In Vitro Cellular & Developmental Biology-Animal* 28(2) (1992) 136-142.
- [211] Y. Tai, J.-H. Gao, C. Zhao, H. Tong, S.-P. Zheng, Z.-Y. Huang, R. Liu, C.-W. Tang, J. Li, SK-Hep1: not hepatocellular carcinoma cells but a cell model for liver sinusoidal endothelial cells, *International Journal of Clinical & Experimental Pathology* 11(5) (2018) 2931.
- [212] S. Rebouissou, J. Zucman-Rossi, R. Moreau, Z. Qiu, L. Hui, Note of caution: contaminations of hepatocellular cell lines, *Journal of hepatology* 67(5) (2017) 896-897.
- [213] Y. Cheng, R. Luo, H. Zheng, B. Wang, Y. Liu, D. Liu, J. Chen, W. Xu, A. Li, Y. Zhu, Synergistic anti-tumor efficacy of sorafenib and fluvastatin in hepatocellular carcinoma, *Oncotarget* 8(14) (2017) 23265.
- [214] J.-M. Zhai, X.-Y. Yin, Y.-R. Lai, X. Hou, J.-P. Cai, X.-Y. Hao, L.-J. Liang, L.-J. Zhang, Sorafenib enhances the chemotherapeutic efficacy of S-1 against hepatocellular carcinoma through downregulation of transcription factor E2F-1, *Cancer chemotherapy and pharmacology* 71(5) (2013) 1255-1264.
- [215] M. Badawi, J. Kim, A. Dauki, D. Sutaria, T. Motiwala, R. Reyes, N. Wani, S. Kolli, J. Jiang, C.C. Coss, CD44 positive and sorafenib insensitive hepatocellular carcinomas respond to the ATP-competitive mTOR inhibitor INK128, *Oncotarget* 9(40) (2018) 26032.
- [216] R.S. Finn, S. Qin, M. Ikeda, P.R. Galle, M. Ducreux, T.-Y. Kim, M. Kudo, V. Breder, P. Merle, A.O. Kaseb, Atezolizumab plus bevacizumab in unresectable hepatocellular carcinoma, *New England Journal of Medicine* 382(20) (2020) 1894-1905.
- [217] K.-F. Chen, H.-L. Chen, C.-Y. Liu, W.-T. Tai, K. Ichikawa, P.-J. Chen, A.-L. Cheng, Dovitinib sensitizes hepatocellular carcinoma cells to TRAIL and tigatuzumab, a novel anti-DR5 antibody, through SHP-1-dependent inhibition of STAT3, *Biochemical pharmacology* 83(6) (2012) 769-777.
- [218] J.M. Llovet, S. Ricci, V. Mazzaferro, P. Hilgard, E. Gane, J.-F. Blanc, A.C. De Oliveira, A. Santoro, J.-L. Raoul, A. Forner, Sorafenib in advanced hepatocellular carcinoma, *New England journal of medicine* 359(4) (2008) 378-390.
- [219] S.M. Wilhelm, J. Dumas, L. Adnane, M. Lynch, C.A. Carter, G. Schütz, K.H. Thierauch, D. Zopf, Regorafenib (BAY 73-4506): a new oral multikinase inhibitor of angiogenic, stromal and oncogenic receptor tyrosine kinases with potent preclinical antitumor activity, *International journal of cancer* 129(1) (2011) 245-255.

- [220] K. Ray, A combination therapy to keep hepatocellular carcinoma in check, Nature Publishing Group, 2020.
- [221] J.-J. Gao, Z.-Y. Shi, J.-F. Xia, Y. Inagaki, W. Tang, Sorafenib-based combined molecule targeting in treatment of hepatocellular carcinoma, *World journal of gastroenterology* 21(42) (2015) 12059.
- [222] A. Gomma, I. Waked, Management of advanced hepatocellular carcinoma: review of current and potential therapies, *practice* 17 (2017) 18.
- [223] D.W. Kim, C. Talati, R. Kim, Hepatocellular carcinoma (HCC): beyond sorafenib—chemotherapy, *Journal of gastrointestinal oncology* 8(2) (2017) 256.
- [224] X.-D. Zhu, H.-C. Sun, Emerging agents and regimens for hepatocellular carcinoma, *Journal of hematology & oncology* 12(1) (2019) 110.
- [225] R. Coriat, C. Nicco, C. Chereau, O. Mir, J. Alexandre, S. Ropert, B. Weill, S. Chaussade, F. Goldwasser, F. Batteux, Sorafenib-induced hepatocellular carcinoma cell death depends on reactive oxygen species production in vitro and in vivo, *Molecular cancer therapeutics* 11(10) (2012) 2284-2293.
- [226] N. Zhou, J. Bao, FerrDb: a manually curated resource for regulators and markers of ferroptosis and ferroptosis-disease associations, *Database* 2020 (2020).
- [227] G. Hu, Y. Zhang, K. Ouyang, F. Xie, H. Fang, X. Yang, K. Liu, Z. Wang, X. Tang, J. Liu, In vivo acquired sorafenib-resistant patient-derived tumor model displays alternative angiogenic pathways, multi-drug resistance and chromosome instability, *Oncology letters* 16(3) (2018) 3439-3446.
- [228] B. Duan, C. Huang, J. Bai, Y.L. Zhang, X. Wang, J. Yang, J. Li, Multidrug Resistance in Hepatocellular Carcinoma, *Exon Publications* (2019) 141-158.
- [229] C.Y. Lin, H.Y. Lane, T.T. Chen, Y.H. Wu, C.Y. Wu, V.Y. Wu, Inverse association between cancer risks and age in schizophrenic patients: A 12-year nationwide cohort study, *Cancer science* 104(3) (2013) 383-390.
- [230] A. Hwong, K. Wang, S. Bent, C. Mangurian, Breast cancer screening in women with schizophrenia: a systematic review and meta-analysis, *Psychiatric Services* 71(3) (2020) 263-268.
- [231] J. Ji, K. Sundquist, Y. Ning, K.S. Kendler, J. Sundquist, X. Chen, Incidence of cancer in patients with schizophrenia and their first-degree relatives: a population-based study in Sweden, *Schizophrenia bulletin* 39(3) (2013) 527-536.

- [232] G. Fond, A. Macgregor, J. Attal, A. Larue, M. Brittner, D. Ducasse, D. Capdevielle, Antipsychotic drugs: pro-cancer or anti-cancer? A systematic review, *Medical hypotheses* 79(1) (2012) 38-42.
- [233] K.-C. Huang, K.-C. Yang, H. Lin, T.T. Tsun-Hui, W.-K. Lee, S.-A. Lee, C.-Y. Kao, Analysis of schizophrenia and hepatocellular carcinoma genetic network with corresponding modularity and pathways: novel insights to the immune system, *BMC genomics* 14(S5) (2013) S10.
- [234] C. Abbruzzese, S. Matteoni, M. Persico, V. Villani, M.G. Paggi, Repurposing chlorpromazine in the treatment of glioblastoma multiforme: analysis of literature and forthcoming steps, *Journal of Experimental & Clinical Cancer Research* 39(1) (2020) 26.
- [235] D. Xu, G. Chen, L. Kong, W. Zhang, L. Hu, C. Chen, J. Li, C. Zhuo, Lower risk of liver cancer in patients with schizophrenia: a systematic review and meta-analysis of cohort studies, *Oncotarget* 8(60) (2017) 102328.
- [236] D. Telles-Correia, A. Barbosa, H. Cortez-Pinto, C. Campos, N.B. Rocha, S. Machado, Psychotropic drugs and liver disease: a critical review of pharmacokinetics and liver toxicity, *World journal of gastrointestinal pharmacology and therapeutics* 8(1) (2017) 26.
- [237] Q. Lv, Z. Yi, Antipsychotic drugs and liver injury, *Shanghai archives of psychiatry* 30(1) (2018) 47.
- [238] J.K. Aronson, *Meyler's side effects of psychiatric drugs*, Elsevier 2008.
- [239] Y.H. Hsieh, H.L. Chan, C.F. Lin, S.H.Y. Liang, M.L. Lu, R.S. McIntyre, Y. Lee, T.C. Lin, W.C. Chiu, V.C.H. Chen, Antipsychotic use is inversely associated with gastric cancer risk: A nationwide population-based nested case-control study, *Cancer medicine* 8(9) (2019) 4484-4496.
- [240] M. Abdelaleem, H. Ezzat, M. Osama, A. Megahed, W. Alaa, A. Gaber, A. Shafei, A. Refaat, Prospects for repurposing CNS drugs for cancer treatment, *Oncology reviews* 13(1) (2019).
- [241] J.-J. Chen, N. Cai, G.-Z. Chen, C.-C. Jia, D.-B. Qiu, C. Du, W. Liu, Y. Yang, Z.-J. Long, Q. Zhang, The neuroleptic drug pimozide inhibits stem-like cell maintenance and tumorigenicity in hepatocellular carcinoma, *Oncotarget* 8(11) (2017) 17593.
- [242] J.J. Chen, L.N. Zhang, N. Cai, Z. Zhang, K. Ji, Antipsychotic agent pimozide promotes reversible proliferative suppression by inducing cellular quiescence in liver cancer, *Oncology reports* 42(3) (2019) 1101-1109.

- [243] V. Fako, Z. Yu, C.J. Henrich, T. Ransom, A.S. Budhu, X.W. Wang, Inhibition of wnt/ β -catenin signaling in hepatocellular carcinoma by an antipsychotic drug pimozide, *International journal of biological sciences* 12(7) (2016) 768.
- [244] X.-N. Shi, H. Li, H. Yao, X. Liu, L. Li, K.-S. Leung, H.-f. Kung, D. Lu, M.-H. Wong, M.C.-m. Lin, In silico identification and in vitro and in vivo validation of anti-psychotic drug fluspirilene as a potential CDK2 inhibitor and a candidate anti-cancer drug, *PloS one* 10(7) (2015) e0132072.
- [245] S.K. Saha, Y. Yin, K. Kim, G.-M. Yang, A.A. Dayem, H.Y. Choi, S.-G. Cho, Valproic acid induces endocytosis-mediated doxorubicin internalization and shows synergistic cytotoxic effects in hepatocellular carcinoma cells, *International journal of molecular sciences* 18(5) (2017) 1048.
- [246] C.-M. Chang, M.-S. Hsieh, T.-C. Yang, V.C.-R. Hsieh, J.-H. Chiang, H.-H. Huang, C.-K. How, S.-Y. Hu, D.H.-T. Yen, Selective serotonin reuptake inhibitors and the risk of hepatocellular carcinoma in hepatitis B virus-infected patients, *Cancer management and research* 9 (2017) 709.
- [247] C.-H. Wu, L.-Y. Bai, M.-H. Tsai, P.-C. Chu, C.-F. Chiu, M.Y. Chen, S.-J. Chiu, J.-H. Chiang, J.-R. Weng, Pharmacological exploitation of the phenothiazine antipsychotics to develop novel antitumor agents—a drug repurposing strategy, *Scientific reports* 6 (2016) 27540.
- [248] L. Qi, Y. Ding, Potential antitumor mechanisms of phenothiazine drugs, *Science China Life Sciences* 56(11) (2013) 1020-1027.
- [249] S. Darvesh, I.R. Pottie, K.V. Darvesh, R.S. McDonald, R. Walsh, S. Conrad, A. Penwell, D. Mataija, E. Martin, Differential binding of phenothiazine urea derivatives to wild-type human cholinesterases and butyrylcholinesterase mutants, *Bioorganic & medicinal chemistry* 18(6) (2010) 2232-2244.
- [250] X. Chen, X. Luo, Y. Cheng, Trifluoperazine prevents FOXO1 nuclear excretion and reverses doxorubicin-resistance in the SHG44/DOX drug-resistant glioma cell line, *International journal of molecular medicine* 42(6) (2018) 3300-3308.
- [251] A. Messaoudi, Z. Basharat, A. Naqvi, High Throughput Screening and Molecular Docking of Calmodulin with Antagonists of Trifluoperazine and Phenothiazine Chemical Class, *Letters in Drug Design & Discovery* 15(2) (2018) 136-142.
- [252] S. Darvesh, I.R. Macdonald, E. Martin, Selectivity of phenothiazine cholinesterase inhibitors for neurotransmitter systems, *Bioorganic & medicinal chemistry letters* 23(13) (2013) 3822-3825.

- [253] A. Ashoor, D. Lorke, S.M. Nurulain, L. Al Kury, G. Petroianu, K.-H.S. Yang, M. Oz, Effects of phenothiazine-class antipsychotics on the function of $\alpha 7$ -nicotinic acetylcholine receptors, *European journal of pharmacology* 673(1-3) (2011) 25-32.
- [254] O. Wesołowska, D. Mosiądz, N. Motohashi, M. Kawase, K. Michalak, Phenothiazine maleates stimulate MRP1 transport activity in human erythrocytes, *Biochimica et Biophysica Acta -Biomembranes* 1720(1-2) (2005) 52-58.
- [255] A. Jaszczyszyn, K. Gąsiorowski, P. Świątek, W. Malinka, K. Cieślak-Boczula, J. Petrus, B. Czarnik-Matuszewicz, Chemical structure of phenothiazines and their biological activity, *Pharmacological Reports* 64(1) (2012) 16-23.
- [256] M.K. Sharma, J. Machhi, P. Murumkar, M.R. Yadav, New role of phenothiazine derivatives as peripherally acting CB1 receptor antagonizing anti-obesity agents, *Scientific reports* 8(1) (2018) 1-18.
- [257] R. Sivaramakarthikeyan, S. Iniyaval, K. Padmavathy, H.-S. Liew, C.-K. Looi, C.-W. Mai, C. Ramalingan, Phenothiazine and amide-ornamented dihydropyridines via a molecular hybridization approach: design, synthesis, biological evaluation and molecular docking studies, *New Journal of Chemistry* 43(43) (2019) 17046-17057.
- [258] I. Gil-Ad, B. Shtatif, Y. Levkovitz, M. Dayag, E. Zeldich, A. Weizman, Characterization of phenothiazine-induced apoptosis in neuroblastoma and glioma cell lines, *Journal of Molecular Neuroscience* 22(3) (2004) 189-198.
- [259] S.Y. Shin, C.G. Kim, S.H. Kim, Y.S. Kim, Y. Lim, Y.H. Lee, Chlorpromazine activates p21 Waf1/Cip1 gene transcription via early growth response-1 (Egr-1) in C6 glioma cells, *Experimental & molecular medicine* 42(5) (2010) 395-405.
- [260] Y. Luan, J. Liu, J. Gao, J. Wang, The Design and Synthesis of Novel Phenothiazine Derivatives as Potential Cytotoxic Agents, *Letters in Drug Design & Discovery* 17(1) (2020) 57-67.
- [261] S. Omoruyi, O. Ekpo, D. Semenya, A. Jardine, S. Prince, Exploitation of a novel phenothiazine derivative for its anti-cancer activities in malignant glioblastoma, *Apoptosis* (2020) 1-14.
- [262] S. Matsuyama, T. Kitamura, N. Enomoto, T. Fujita, A. Ishigami, S. Handa, N. Maruyama, D. Zheng, K. Ikejima, Y. Takei, Senescence marker protein-30 regulates Akt activity and contributes to cell survival in Hep G2 cells, *Biochemical and biophysical research communications* 321(2) (2004) 386-390.

- [263] E.D. Wiklund, V.S. Catts, S.V. Catts, T.F. Ng, N.J. Whitaker, A.J. Brown, L.H. Lutze-Mann, Cytotoxic effects of antipsychotic drugs implicate cholesterol homeostasis as a novel chemotherapeutic target, *International journal of cancer* 126(1) (2010) 28-40.
- [264] O.F. Kuzu, R. Gowda, M.A. Noory, G.P. Robertson, Modulating cancer cell survival by targeting intracellular cholesterol transport, *British journal of cancer* 117(4) (2017) 513-524.
- [265] R.G. Keynes, A. Karchevskaya, D. Riddall, C.H. Griffiths, T.C. Bellamy, A.E. Chan, D.L. Selwood, J. Garthwaite, N10-carbonyl-substituted phenothiazines inhibiting lipid peroxidation and associated nitric oxide consumption powerfully protect brain tissue against oxidative stress, *Chemical biology and drug design* 94(3) (2019) 1680-1693.
- [266] M. Conlon, C. Poltorack, G.C. Forcina, A. Wells, M. Mallais, A. Kahanu, L. Magtanong, D. Pratt, S.J. Dixon, A Compendium of Kinetic Cell Death Modulatory Profiles Identifies Ferroptosis Regulators, *bioRxiv* (2019) 826925.
- [267] K. Michalak, O. Wesolowska, N. Motohashi, J. Molnar, A. Hendrich, Interactions of phenothiazines with lipid bilayer and their role in multidrug resistance reversal, *Current drug targets* 7(9) (2006) 1095-1105.
- [268] D. Takács, Á. Csonka, Á. Horváth, T. Windt, M. Gajdács, Z. Riedl, G. Hajós, L. Amaral, J. Molnar, G. Spengler, Reversal of ABCB1-related multidrug resistance of colonic adenocarcinoma cells by phenothiazines, *Anticancer Research* 35(6) (2015) 3245-3251.
- [269] B. Varga, Á. Csonka, A. Csonka, J. Molnár, L. Amaral, G. Spengler, Possible biological and clinical applications of phenothiazines, *Anticancer Research* 37(11) (2017) 5983-5993.
- [270] I. Gil-Ad, B. Shtatif, Y. Levkovitz, J. Nordenberg, M. Taler, I. Korov, A. Weizman, Phenothiazines induce apoptosis in a B16 mouse melanoma cell line and attenuate in vivo melanoma tumor growth, *Oncology reports* 15(1) (2006) 107-112.
- [271] G. Spengler, D. Takács, Á. Horváth, Z. Riedl, G. Hajós, L. Amaral, J. Molnár, Multidrug resistance reversing activity of newly developed phenothiazines on P-glycoprotein (ABCB1)-related resistance of mouse T-lymphoma cells, *Anticancer Research* 34(4) (2014) 1737-1741.
- [272] A. Bisi, M. Meli, S. Gobbi, A. Rampa, M. Tolomeo, L. Dusonchet, Multidrug resistance reverting activity and antitumor profile of new phenothiazine derivatives, *Bioorganic medicinal chemistry* 16(13) (2008) 6474-6482.
- [273] A.A. Argyriou, A. Antonacopoulou, G. Iconomou, H.P. Kalofonos, Treatment options for malignant gliomas, emphasizing towards new molecularly targeted therapies, *Critical reviews in oncology/hematology* 69(3) (2009) 199-210.

- [274] C.W. Yde, M.P. Clausen, M.V. Bennetzen, A.E. Lykkesfeldt, O.G. Mouritsen, B. Guerra, The antipsychotic drug chlorpromazine enhances the cytotoxic effect of tamoxifen in tamoxifen-sensitive and tamoxifen-resistant human breast cancer cells, *Anti-Cancer Drugs* 20(8) (2009) 723-735.
- [275] Y. Zhang, Q. Zhang, S.X. Zeng, Q. Hao, H. Lu, Inauhzin sensitizes p53-dependent cytotoxicity and tumor suppression of chemotherapeutic agents, *Neoplasia* 15(5) (2013) 523-531.
- [276] M. Dehqan, S. Negintaji, F. Mirjalili, R. Bidaki, A. Mohammadi, A. Sahebnasagh, F. Saghafi, The Relationship between Antipsychotic Medications and Cancer: A Review Article, *Critical Comments in Biomedicine* (2020).
- [277] R.K. Cady, P.L. Durham, *Chronic Migraine: Diagnosis and Management, Headache and Migraine Biology and Management*, Elsevier 2015, pp. 99-122.
- [278] P.-A. Hals, H. Hall, S.G. Dahl, Muscarinic cholinergic and histamine H1 receptor binding of phenothiazine drug metabolites, *Life sciences* 43(5) (1988) 405-412.
- [279] A. Spinedi, L. Pacini, C. Limatola, P. Luly, R.N. Farias, Phenothiazines inhibit acetylcholinesterase by concentration-dependent-type kinetics: A study with trifluoperazine and perphenazine, *Biochemical pharmacology* 44(8) (1992) 1511-1514.
- [280] E.G. Thompson, H. Sontheimer, Acetylcholine receptor activation as a modulator of glioblastoma invasion, *Cells* 8(10) (2019) 1203.
- [281] S.-H. Jiang, L.-P. Hu, X. Wang, J. Li, Z.-G. Zhang, Neurotransmitters: emerging targets in cancer, *Oncogene* (2019) 1-13.
- [282] J. Chen, I.W. Cheuk, V.Y. Shin, A. Kwong, Acetylcholine receptors: Key players in cancer development, *Surgical oncology* 31 (2019) 46-53.
- [283] N. Dang, X. Meng, H. Song, Nicotinic acetylcholine receptors and cancer, *Biomedical reports* 4(5) (2016) 515-518.
- [284] X.-F. Liu, H.-J. Long, X.-Y. Miao, G.-L. Liu, H.-L. Yao, Fisetin inhibits liver cancer growth in a mouse model: Relation to dopamine receptor, *Oncology reports* 38(1) (2017) 53-62.
- [285] M. Lu, J. Li, Z. Luo, S. Zhang, S. Xue, K. Wang, Y. Shi, C. Zhang, H. Chen, Z. Li, Roles of dopamine receptors and their antagonist thioridazine in hepatoma metastasis, *OncoTargets and therapy* 8 (2015) 1543.
- [286] D.J. Brooks, P. Calabresi, S. Fox, T. Müller, W. Poewe, O. Rascol, F. Stocchi, *Expert Perspectives—Parkinson's Disease Pathophysiology and Management*.

- [287] D.B. Lester, T.D. Rogers, C.D. Blaha, Acetylcholine–dopamine interactions in the pathophysiology and treatment of CNS disorders, *CNS neuroscience & therapeutics* 16(3) (2010) 137-162.
- [288] B. Pérez-Aguilar, C.J. Vidal, G. Palomec, F. García-Dolores, M.C. Gutiérrez-Ruiz, L. Bucio, J.L. Gómez-Olivares, L.E. Gómez-Quiroz, Acetylcholinesterase is associated with a decrease in cell proliferation of hepatocellular carcinoma cells, *Biochimica et Biophysica Acta (BBA)-Molecular Basis of Disease* 1852(7) (2015) 1380-1387.
- [289] L. Zhou, J. Li, D.-L. Ai, J.-L. Fu, X.-M. Peng, L.-Z. Zhang, J.-Y. Wang, Y. Zhao, B. Yang, Q. Yu, Enhanced therapeutic efficacy of combined use of sorafenib and transcatheter arterial chemoembolization for treatment of advanced hepatocellular carcinoma, *Japanese journal of clinical oncology* 44(8) (2014) 711-717.
- [290] H. Takeda, H. Nishikawa, E. Iguchi, Y. Ohara, A. Sakamoto, K. Hatamaru, S. Henmi, S. Saito, A. Nasu, H. Komekado, Impact of pretreatment serum cholinesterase level in unresectable advanced hepatocellular carcinoma patients treated with sorafenib, *Molecular and Clinical Oncology* 1(2) (2013) 241-248.
- [291] M.-H. Chen, W.-L.R. Yang, K.-T. Lin, C.-H. Liu, Y.-W. Liu, K.-W. Huang, P.M.-H. Chang, J.-M. Lai, C.-N. Hsu, K.-M. Chao, Gene expression-based chemical genomics identifies potential therapeutic drugs in hepatocellular carcinoma, *PloS one* 6(11) (2011) e27186.
- [292] C.-Y. Huang, P.M.-H. Chang, K.-Y. Chen, C.-H. Wu, T.-S. Cheng, C.-H. Yu, Method for treating drug resistant cancer, Google Patents, 2017.
- [293] X.-H. Ma, N. Liu, J.-L. Lu, J. Zhao, X.-J. Zhang, Design, synthesis and antiproliferative activity of novel phenothiazine-1, 2, 3-triazole analogues, *Journal of Chemical Research* 41(12) (2017) 696-698.
- [294] K. Vögerl, N. Ong, J. Senger, D. Herp, K. Schmidtkunz, M. Marek, M. Müller, K. Bartel, T.B. Shaik, N.J. Porter, Synthesis and biological investigation of phenothiazine-based benzhydroxamic acids as selective histone deacetylase 6 inhibitors, *Journal of medicinal chemistry* 62(3) (2019) 1138-1166.
- [295] P.A. de Faria, F. Bettanin, R.L. Cunha, E.J. Paredes-Gamero, P. Homem-de-Mello, I.L. Nantes, T. Rodrigues, Cytotoxicity of phenothiazine derivatives associated with mitochondrial dysfunction: a structure-activity investigation, *Toxicology* 330 (2015) 44-54.
- [296] Y. Wen, Y. Zhang, J. Li, F. Luo, Z. Huang, K. Liu, Low concentration trifluoperazine promotes proliferation and reduces calcium-dependent apoptosis in glioma cells, *Scientific reports* 8(1) (2018) 1-10.

- [297] R.G. Armando, D.L. Mengual Gómez, D.E. Gomez, New drugs are not enough—drug repositioning in oncology: An update, *International Journal of Oncology* 56(3) (2020) 651-684.
- [298] J. Ryan, Cell cloning by serial dilution in 96 well plates protocol, *Life Sciences* (2008).
- [299] B. Jakic, M. Buszko, G. Cappellano, G. Wick, Elevated sodium leads to the increased expression of HSP60 and induces apoptosis in HUVECs, *PloS one* 12(6) (2017) e0179383.
- [300] N.A. Clark, M. Hafner, M. Kouril, E.H. Williams, J.L. Muhlich, M. Pilarczyk, M. Niepel, P.K. Sorger, M. Medvedovic, GRcalculator: an online tool for calculating and mining dose–response data, *BMC cancer* 17(1) (2017) 698.
- [301] J.S. Yuan, A. Reed, F. Chen, C.N. Stewart, Statistical analysis of real-time PCR data, *BMC bioinformatics* 7(1) (2006) 85.
- [302] L. Gautier, L. Cope, B.M. Bolstad, R.A. Irizarry, affy—analysis of Affymetrix GeneChip data at the probe level, *Bioinformatics* 20(3) (2004) 307-315.
- [303] M.E. Ritchie, B. Phipson, D. Wu, Y. Hu, C.W. Law, W. Shi, G.K. Smyth, limma powers differential expression analyses for RNA-sequencing and microarray studies, *Nucleic acids research* 43(7) (2015) e47-e47.
- [304] Z. Gu, R. Eils, M. Schlesner, Complex heatmaps reveal patterns and correlations in multidimensional genomic data, *Bioinformatics* 32(18) (2016) 2847-2849.
- [305] V. Stathias, A. Koleti, D. Vidović, D.J. Cooper, K.M. Jagodnik, R. Terry, M. Forlin, C. Chung, D. Torre, N. Ayad, Sustainable data and metadata management at the BD2K-LINCS Data Coordination and Integration Center, *Scientific data* 5 (2018) 180117.
- [306] D. Szklarczyk, A. Franceschini, S. Wyder, K. Forslund, D. Heller, J. Huerta-Cepas, M. Simonovic, A. Roth, A. Santos, K.P. Tsafou, STRING v10: protein–protein interaction networks, integrated over the tree of life, *Nucleic acids research* 43(D1) (2015) D447-D452.
- [307] B.E.G.V. UGent). <http://bioinformatics.psb.ugent.be/webtools/Venn/>. (Accessed September 9 2020).
- [308] D. Torre, A. Lachmann, A. Ma’ayan, BioJupies: automated generation of interactive notebooks for RNA-Seq data analysis in the cloud, *Cell systems* 7(5) (2018) 556-561. e3.
- [309] M.V. Kuleshov, M.R. Jones, A.D. Rouillard, N.F. Fernandez, Q. Duan, Z. Wang, S. Koplev, S.L. Jenkins, K.M. Jagodnik, A. Lachmann, Enrichr: a comprehensive gene set enrichment analysis web server 2016 update, *Nucleic acids research* 44(W1) (2016) W90-W97.

- [310] M. Kanehisa, M. Furumichi, M. Tanabe, Y. Sato, K. Morishima, KEGG: new perspectives on genomes, pathways, diseases and drugs, *Nucleic acids research* 45(D1) (2017) D353-D361.
- [311] F.Z. Karadayi, M. Yaman, M.M. Kislal, A.G. Keskus, O. Konu, Z. Ates-Alagoz, Design, Synthesis and Anticancer/Antiestrogenic Activities of Novel Indole-benzimidazoles, *Bioorganic Chemistry* (2020) 103929.
- [312] M. Niklasson, G. Maddalo, Z. Sramkova, E. Mutlu, S. Wee, P. Sekyrova, L. Schmidt, N. Fritz, I. Dehnisch, G. Kyriatzis, Membrane-depolarizing channel blockers induce selective glioma cell death by impairing nutrient transport and unfolded protein/amino acid responses, *Cancer research* 77(7) (2017) 1741-1752.
- [313] V. Nade, N. Shendye, L. Kawale, N. Patil, M. Khatri, Protective effect of nebivolol on reserpine-induced neurobehavioral and biochemical alterations in rats, *Neurochemistry international* 63(4) (2013) 316-321.
- [314] G. Bruni, A.J. Rennekamp, A. Velenich, M. McCarroll, L. Gendele, E. Fertsch, J. Taylor, P. Lakhani, D. Lensen, T. Evron, Zebrafish behavioral profiling identifies multitarget antipsychotic-like compounds, *Nature chemical biology* 12(7) (2016) 559.
- [315] The_GSEA/MSigDB_Team, GSEA. https://www.gsea-msigdb.org/gsea/doc/GSEAUserGuideFrame.html?Interpreting_GSEA. (Accessed September 9 2020).
- [316] X. Yu, Y.C. Long, Crosstalk between cystine and glutathione is critical for the regulation of amino acid signaling pathways and ferroptosis, *Scientific reports* 6(1) (2016) 1-11.
- [317] R. Callis, A. Rabow, M. Tonge, R. Bradbury, M. Challinor, K. Roberts, K. Jones, G. Walker, A screening assay cascade to identify and characterize novel selective estrogen receptor downregulators (SERDs), *Journal of biomolecular screening* 20(6) (2015) 748-759.
- [318] J.-R. Ioset, R. Brun, T. Wenzler, M. Kaiser, V. Yardley, Drug Screening for Kinetoplastids Diseases, *A Training Manual for Screening in Neglected Diseases* (2009).
- [319] N.C. Desai, B.Y. Patel, B.P. Dave, Synthesis and antimicrobial activity of novel quinoline derivatives bearing pyrazoline and pyridine analogues, *Medicinal Chemistry Research* 26(1) (2017) 109-119.
- [320] A. Kumar, M. Drozd, R. Pina-Mimbela, X. Xu, Y.A. Helmy, J. Antwi, J.R. Fuchs, C. Nislow, J. Templeton, P.J. Blackall, Novel anti-Campylobacter compounds identified using high throughput screening of a pre-selected enriched small molecules library, *Frontiers in microbiology* 7 (2016) 405.

- [321] E. Durieu, E. Prina, O. Leclercq, N. Oumata, N. Gaboriaud-Kolar, K. Vougianniopoulou, N. Aulner, A. Defontaine, J.H. No, S. Ruchaud, From drug screening to target deconvolution: a target-based drug discovery pipeline using *Leishmania casein kinase 1 isoform 2* to identify compounds with antileishmanial activity, *Antimicrobial agents and chemotherapy* 60(5) (2016) 2822-2833.
- [322] H. Brito, V. Marques, M.B. Afonso, D.G. Brown, U. Börjesson, N. Selmi, D.M. Smith, I.O. Roberts, M. Fitzek, N. Aniceto, Phenotypic high-throughput screening platform identifies novel chemotypes for necroptosis inhibition, *Cell Death Discovery* 6(1) (2020) 1-13.
- [323] A.L. Niles, R.A. Moravec, T.L. Riss, Update on in vitro cytotoxicity assays for drug development, *Expert opinion on drug discovery* 3(6) (2008) 655-669.
- [324] O.M. Lage, M.C. Ramos, R. Calisto, E. Almeida, V. Vasconcelos, F. Vicente, Current screening methodologies in drug discovery for selected human diseases, *Marine drugs* 16(8) (2018) 279.
- [325] H.L. Martin, M. Adams, J. Higgins, J. Bond, E.E. Morrison, S.M. Bell, S. Warriner, A. Nelson, D.C. Tomlinson, High-content, high-throughput screening for the identification of cytotoxic compounds based on cell morphology and cell proliferation markers, *PloS one* 9(2) (2014) e88338.
- [326] A. Eastman, Improving anticancer drug development begins with cell culture: misinformation perpetrated by the misuse of cytotoxicity assays, *Oncotarget* 8(5) (2017) 8854.
- [327] M. Radi, C. Brullo, E. Crespan, C. Tintori, F. Musumeci, M. Biava, S. Schenone, E. Dreassi, C. Zamperini, G. Maga, Identification of potent c-Src inhibitors strongly affecting the proliferation of human neuroblastoma cells, *Bioorganic medicinal chemistry letters* 21(19) (2011) 5928-5933.
- [328] B. Kucukkaraduman, C. Turk, A.L. Fallacara, M. Isbilen, K.M. Senses, Z.O. Ayyildiz, M.W. Akbar, M. Lotem, M. Botta, A.O. Gure, Predictive Gene Signature for Pyrazolopyrimidine Derivative c-Src Inhibitor 10a Sensitivity in Melanoma Cells, *ACS Medicinal Chemistry Letters* 11(5) (2020) 928-932.
- [329] E.M. Gordon, J.R. Ravicz, S. Liu, S.P. Chawla, F.L. Hall, Cell cycle checkpoint control: The cyclin G1/Mdm2/p53 axis emerges as a strategic target for broad-spectrum cancer gene therapy-A review of molecular mechanisms for oncologists, *Molecular and Clinical Oncology* 9(2) (2018) 115-134.

- [330] T. Hao, Q. Wang, L. Zhao, D. Wu, E. Wang, J. Sun, Analyzing of molecular networks for human diseases and drug discovery, *Current topics in medicinal chemistry* 18(12) (2018) 1007-1014.
- [331] D. Carvalho-Silva, A. Pierleoni, M. Pignatelli, C. Ong, L. Fumis, N. Karamanis, M. Carmona, A. Faulconbridge, A. Hercules, E. McAuley, Open Targets Platform: new developments and updates two years on, *Nucleic acids research* 47(D1) (2019) D1056-D1065.
- [332] Y. Nishimura, A. Inoue, S. Sasagawa, J. Koiwa, K. Kawaguchi, R. Kawase, T. Maruyama, S. Kim, T. Tanaka, Using zebrafish in systems toxicology for developmental toxicity testing, *Congenital Anomalies* 56(1) (2016) 18-27.
- [333] S. Vranic, Y. Shimada, S. Ichihara, M. Kimata, W. Wu, T. Tanaka, S. Boland, L. Tran, G. Ichihara, Toxicological evaluation of SiO₂ nanoparticles by zebrafish embryo toxicity test, *International journal of molecular sciences* 20(4) (2019) 882.
- [334] M. Fantacuzzi, B. De Filippis, M. Gallorini, A. Ammazalorso, L. Giampietro, C. Maccallini, Z. Aturki, E. Donati, R.S. Ibrahim, E. Shawky, Synthesis, biological evaluation, and docking study of indole aryl sulfonamides as aromatase inhibitors, *European journal of medicinal chemistry* 185 (2020) 111815.
- [335] S.-Y. Yang, Pharmacophore modeling and applications in drug discovery: challenges and recent advances, *Drug discovery today* 15(11-12) (2010) 444-450.
- [336] M. Gao, P. Monian, N. Quadri, R. Ramasamy, X. Jiang, Glutaminolysis and transferrin regulate ferroptosis, *Molecular cell* 59(2) (2015) 298-308.
- [337] M. Hayano, W. Yang, C. Corn, N. Pagano, B. Stockwell, Loss of cysteinyl-tRNA synthetase (CARS) induces the transsulfuration pathway and inhibits ferroptosis induced by cystine deprivation, *Cell Death & Differentiation* 23(2) (2016) 270-278.
- [338] P. Gong, Z. Madak-Erdogan, J.A. Flaws, D.J. Shapiro, J.A. Katzenellenbogen, B.S. Katzenellenbogen, Estrogen receptor- α and aryl hydrocarbon receptor involvement in the actions of botanical estrogens in target cells, *Molecular and cellular endocrinology* 437 (2016) 190-200.
- [339] T.D. Hubbard, I.A. Murray, W.H. Bisson, T.S. Lahoti, K. Gowda, S.G. Amin, A.D. Patterson, G.H. Perdew, Adaptation of the human aryl hydrocarbon receptor to sense microbiota-derived indoles, *Scientific reports* 5(1) (2015) 1-13.
- [340] E. Zgheib, A. Limonciel, X. Jiang, A. Wilmes, S. Wink, B. Van De Water, A. Kopp-Schneider, F.Y. Bois, P. Jennings, Investigation of Nrf2, AhR and ATF4 activation in toxicogenomic databases, *Frontiers in genetics* 9 (2018) 429.

- [341] Y. Hirata, C. Yamada, Y. Ito, S. Yamamoto, H. Nagase, K. Oh-hashii, K. Kiuchi, H. Suzuki, M. Sawada, K. Furuta, Novel oxindole derivatives prevent oxidative stress-induced cell death in mouse hippocampal HT22 cells, *Neuropharmacology* 135 (2018) 242-252.
- [342] Y. Hirata, T. Iwasaki, Y. Makimura, S. Okajima, K. Oh-hashii, H. Takemori, Inhibition of double-stranded RNA-dependent protein kinase prevents oxytosis and ferroptosis in mouse hippocampal HT22 cells, *Toxicology* 418 (2019) 1-10.
- [343] P. Maher, K. van Leyen, P.N. Dey, B. Honrath, A. Dolga, A. Methner, The role of Ca²⁺ in cell death caused by oxidative glutamate toxicity and ferroptosis, *Cell Calcium* 70 (2018) 47-55.
- [344] J. Lewerenz, G. Ates, A. Methner, M. Conrad, P. Maher, Oxytosis/ferroptosis—(Re-) emerging roles for oxidative stress-dependent non-apoptotic cell death in diseases of the central nervous system, *Frontiers in Neuroscience* 12 (2018) 214.
- [345] B. Hong, Z. Su, C. Zhang, Y. Yang, Y. Guo, W. Li, A.-N.T. Kong, Reserpine inhibit the JB6 P⁺ cell transformation through epigenetic reactivation of Nrf2-mediated anti-oxidative stress pathway, *The AAPS journal* 18(3) (2016) 659-669.
- [346] H.J. Xi, R.P. Wu, J.J. Liu, L.J. Zhang, Z.S. Li, Role of acetylcholinesterase in lung cancer, *Thoracic cancer* 6(4) (2015) 390-398.
- [347] J.R. Friedman, S.D. Richbart, J.C. Merritt, K.C. Brown, N.A. Nolan, A.T. Akers, J.K. Lau, Z.R. Robateau, S.L. Miles, P. Dasgupta, Acetylcholine signaling system in progression of lung cancers, *Pharmacology & therapeutics* 194 (2019) 222-254.
- [348] A.C. Castillo-González, S. Nieto-Cerón, J.P. Pelegrín-Hernández, M.F. Montenegro, J.A. Noguera, M.F. López-Moreno, J.N. Rodríguez-López, C.J. Vidal, D. Hellín-Meseguer, J. Cabezas-Herrera, Dysregulated cholinergic network as a novel biomarker of poor prognostic in patients with head and neck squamous cell carcinoma, *BMC cancer* 15(1) (2015) 385.
- [349] X.-J. Zhang, D.S. Greenberg, Acetylcholinesterase involvement in apoptosis, *Frontiers in molecular neuroscience* 5 (2012) 40.
- [350] A. Dobin, C.A. Davis, F. Schlesinger, J. Drenkow, C. Zaleski, S. Jha, P. Batut, M. Chaisson, T.R. Gingeras, STAR: ultrafast universal RNA-seq aligner, *Bioinformatics* 29(1) (2013) 15-21.
- [351] D. Kim, J.M. Paggi, C. Park, C. Bennett, S.L. Salzberg, Graph-based genome alignment and genotyping with HISAT2 and HISAT-genotype, *Nature biotechnology* 37(8) (2019) 907-915.
- [352] D.C. Wu, J. Yao, K.S. Ho, A.M. Lambowitz, C.O. Wilke, Limitations of alignment-free tools in total RNA-seq quantification, *BMC genomics* 19(1) (2018) 510.

- [353] P. Konieczny, E. Stepniak-Konieczna, K. Sobczak, MBNL proteins and their target RNAs, interaction and splicing regulation, *Nucleic acids research* 42(17) (2014) 10873-10887.
- [354] S. Farashi, T. Kryza, J. Batra, Pathway Analysis of Genes Identified through Post-GWAS to Underpin Prostate Cancer Aetiology, *Genes* 11(5) (2020) 526.

APPENDIX A

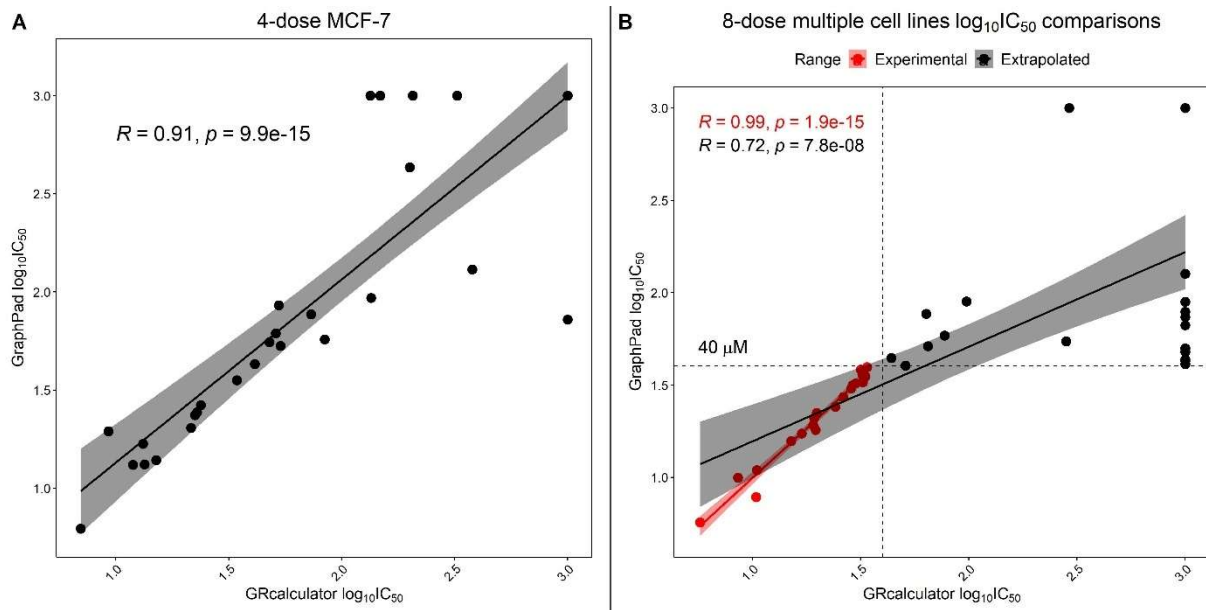


Figure Appendix A1 Pearson's correlations between GraphPad Prism and GRcalculator derived IC_{50} values. Comparisons for (A) preliminary 4-dose MCF-7, and (B) 8-dose multiple cell line MTT assays are provided, as the GraphPad IC_{50} values are retrieved from the PhD thesis of Fikriye Zengin Karadayı (2019). Black color corresponds to total $\log IC_{50}$ values from the tools, as red color represents the values within the dose scales that were followed through the MTT assays.

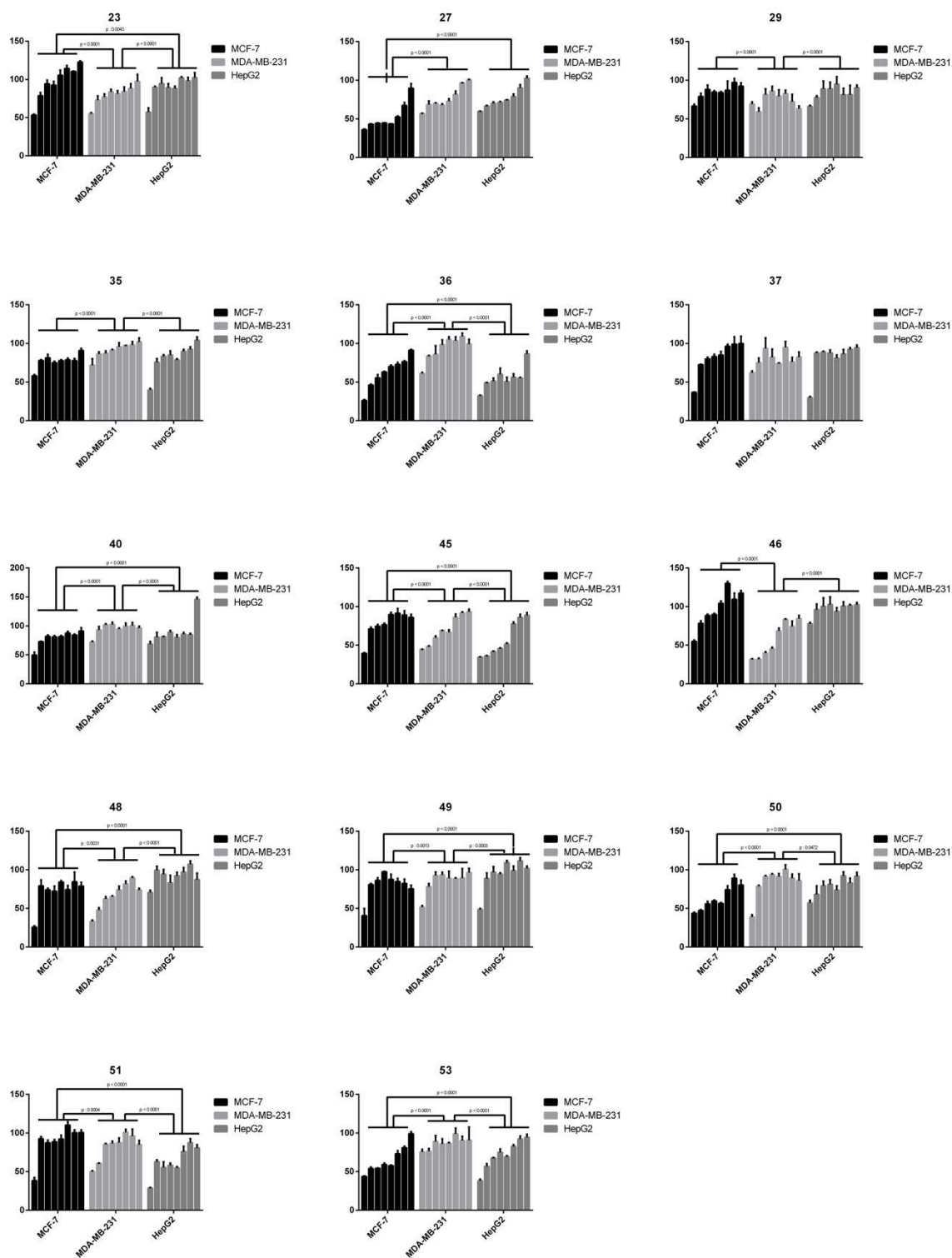


Figure Appendix A2 Viability percentile-based cell line effect comparisons across varying concentrations of the candidate indole-benzimidazoles. Two-way ANOVA/Tukey methodology was applied, ns: not significant. Retrieved from Karadayi F.Z. & Yaman M. *et al.*, 2020. *Bioorganic Chemistry* [311].

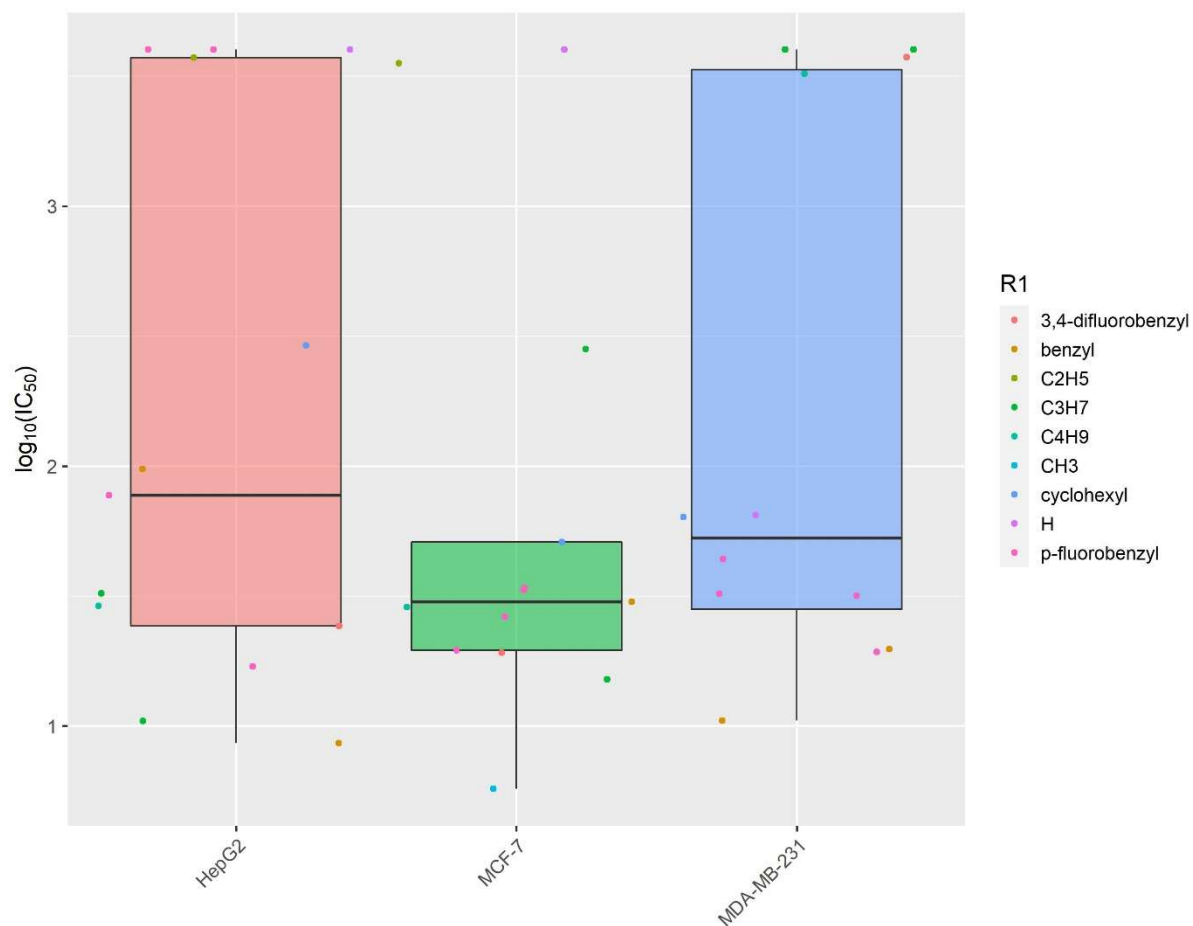


Figure Appendix A3 Representation of cell line based $\log_{10}(\text{IC}_{50})$ values (μM) (GRcalculator). Retrieved from Karadayi F.Z. & Yaman M. et al., 2020. *Bioorganic Chemistry* [311].

Table Appendix A4 List of Reactome Pathways as represented on **Figure 4.4 (C)**

STRING Database - Reactome Pathways
50-51-53 up (3)
PERK regulates gene expression Unfolded Protein Response (UPR) Basigin interactions
50-51-53 down (51)
NoRC negatively regulates rRNA expression E2F-enabled inhibition of pre-replication complex formation Pre-NOTCH Expression and Processing Early Phase of HIV Life Cycle RNA Polymerase I Chain Elongation Meiotic synapsis Transcriptional regulation by the AP-2 (TFAP2) family of transcription factors TP53 Regulates Transcription of Genes Involved in G2 Cell Cycle Arrest Signaling by Rho GTPases RHO GTPase Effectors RHO GTPases Activate Formins Activated PKN1 stimulates transcription of AR (androgen receptor) regulated genes KLK2 and KLK3 RNA Polymerase I Promoter Opening Resolution of Sister Chromatid Cohesion Termination of translesion DNA synthesis Removal of the Flap Intermediate from the C-strand Meiosis Translesion synthesis by POLI Translesion synthesis by REV1 ERCC6 (CSB) and EHMT2 (G9a) positively regulate rRNA expression TFAP2 (AP-2) family regulates transcription of growth factors and their receptors Polo-like kinase mediated events SIRT1 negatively regulates rRNA expression SCF(Skp2)-mediated degradation of p27/p21 Cyclin D associated events in G1 Separation of Sister Chromatids Transcriptional Regulation by E2F6 Recognition of DNA damage by PCNA-containing replication complex B-WICH complex positively regulates rRNA expression G2/M DNA damage checkpoint Resolution of D-loop Structures through Synthesis-Dependent Strand Annealing (SDSA) Resolution of D-loop Structures through Holliday Junction Intermediates Apoptotic execution phase Metabolism of nucleotides Formation of the beta-catenin:TCF transactivating complex Pre-NOTCH Transcription and Translation Meiotic recombination Mitotic Anaphase Translesion synthesis by POLK Translesion Synthesis by POLH Inhibition of replication initiation of damaged DNA by RB1/E2F1 DNA Damage Bypass Mitotic Prometaphase RUNX1 regulates transcription of genes involved in differentiation of HSCs Deregulated CDK5 triggers multiple neurodegenerative pathways in Alzheimer's disease models SUMOylation of intracellular receptors HDACs deacetylate histones CDK-mediated phosphorylation and removal of Cdc6 Amplification of signal from unattached kinetochores via a MAD2 inhibitory signal RMTs methylate histone arginines Transcription of E2F targets under negative control by p107 (RBL1) and p130 (RBL2) in complex with HDAC1

Table Appendix A4 List of Reactome Pathways as represented on Figure 4.4 (C) (<i>Cont'd</i>)
48-49 down (2)
Diseases of Mismatch Repair (MMR) Signaling by ERBB4
48-49 up vs 50-51-53 up (1)
Cytosolic tRNA aminoacylation
48-49 down vs 50-51-53 up (1)
Cellular responses to external stimuli
48-49 down vs 50-51-53 down (70)
p53-Dependent G1 DNA Damage Response Estrogen-dependent gene expression Telomere C-strand (Lagging Strand) Synthesis Transcriptional Regulation by TP53 CDT1 association with the CDC6:ORC:origin complex DNA Damage/Telomere Stress Induced Senescence Cell Cycle Checkpoints HDR through Single Strand Annealing (SSA) Chromosome Maintenance G2/M Checkpoints G0 and Early G1 Assembly of the pre-replicative complex Cellular Senescence TP53 Regulates Transcription of Genes Involved in G1 Cell Cycle Arrest Activation of ATR in response to replication stress Processing of DNA double-strand break ends DNA Replication Pre-Initiation DNA strand elongation Switching of origins to a post-replicative state E2F mediated regulation of DNA replication G2 Phase PCNA-Dependent Long Patch Base Excision Repair Activation of E2F1 target genes at G1/S Synthesis of DNA Orc1 removal from chromatin Polymerase switching Regulation of TP53 Activity Gene expression (Transcription) Generic Transcription Pathway S Phase Mismatch repair (MMR) directed by MSH2:MSH6 (MutSalpha) M Phase Cyclin A:Cdk2-associated events at S phase entry Cellular responses to stress Formation of Senescence-Associated Heterochromatin Foci (SAHF) Cyclin E associated events during G1/S transition HDR through Homologous Recombination (HRR) or Single Strand Annealing (SSA) Mitotic Prophase Mitotic G1-G1/S phases Unwinding of DNA HDR through Homologous Recombination (HRR) Cell Cycle Deposition of new CENPA-containing nucleosomes at the centromere Presynaptic phase of homologous DNA pairing and strand exchange Condensation of Prophase Chromosomes Activation of the pre-replicative complex PRC2 methylates histones and DNA Regulation of TP53 Activity through Phosphorylation

Table Appendix A4 List of Reactome Pathways as represented on Figure 4.4 (C) 48-49 down vs 50-51-53 down (70) (Cont'd)
DNA Repair
TP53 Regulates Transcription of Cell Cycle Genes
CDC6 association with the ORC:origin complex
Fanconi Anemia Pathway
Lagging Strand Synthesis
Removal of the Flap Intermediate
DNA Replication
Senescence-Associated Secretory Phenotype (SASP)
PTK6 Regulates Cell Cycle
Phosphorylation of proteins involved in G1/S transition by active Cyclin E:Cdk2 complexes
G1/S DNA Damage Checkpoints
DNA methylation
Homology Directed Repair
Signaling by Nuclear Receptors
Oxidative Stress Induced Senescence
Apoptosis
G1/S Transition
Transcription of E2F targets under negative control by DREAM complex
Cell Cycle, Mitotic
Mismatch repair (MMR) directed by MSH2:MSH3 (MutSbeta)
Telomere Maintenance
Polymerase switching on the C-strand of the telomere

Retrieved from Karadayi F.Z. & Yaman M. et al., 2020. *Bioorganic Chemistry* [311].

Table Appendix A5 Compound 51 KEGG pathway annotations ($|\log_{2}FC| > 1$; adjusted p-value < 0.05 (n=202 genes))

#term ID	Term description	Observed gene count	Background gene count	FDR
hsa05418	Fluid shear stress and atherosclerosis	9	133	0.0031
hsa00970	Aminoacyl-tRNA biosynthesis	5	44	0.0137
hsa04010	MAPK signaling pathway	11	293	0.0199
hsa04210	Apoptosis	7	135	0.0318
hsa04115	p53 signaling pathway	5	68	0.0354
hsa04216	Ferroptosis	4	40	0.0354

Retrieved from Karadayi F.Z. & Yaman M. et al., 2020. *Bioorganic Chemistry* [311].

Table Appendix A6 Compounds 50-51-53 KEGG pathway annotations($|\log_{2}FC| > 0.5$ & $n=1109$ genes).

#term ID	Term description	Observed gene count	Background gene count	FDR
hsa03030	DNA replication	24	36	4.10E-13
hsa04110	Cell cycle	38	123	8.30E-13
hsa03430	Mismatch repair	12	23	1.36E-05
hsa00240	Pyrimidine metabolism	21	100	0.00012
hsa03460	Fanconi anemia pathway	15	51	0.00012
hsa03410	Base excision repair	12	33	0.00014
hsa03420	Nucleotide excision repair	13	46	0.00047
hsa04114	Oocyte meiosis	21	116	0.00047
hsa03440	Homologous recombination	11	40	0.0021
hsa05322	Systemic lupus erythematosus	17	94	0.0025
hsa04115	p53 signaling pathway	14	68	0.0028
hsa05206	MicroRNAs in cancer	22	149	0.003
hsa00230	Purine metabolism	24	173	0.0033
hsa04218	Cellular senescence	22	156	0.0047
hsa04914	Progesterone-mediated oocyte maturation	15	94	0.0136
hsa00620	Pyruvate metabolism	9	39	0.0162
hsa05203	Viral carcinogenesis	22	183	0.0263
hsa05222	Small cell lung cancer	14	92	0.0263
hsa00970	Aminoacyl-tRNA biosynthesis	9	44	0.0283
hsa05034	Alcoholism	18	142	0.0344
hsa01100	Metabolic pathways	95	1250	0.0453
hsa04210	Apoptosis	17	135	0.0453
hsa05166	HTLV-I infection	26	250	0.0488

Retrieved from Karadayi F.Z. & Yaman M. et al., 2020. *Bioorganic Chemistry* [311].

Table Appendix A7 KEGG pathways-based contingency table where the genes show mutual or opposite direction in expression fold changes between 51 and E2, dioxin and AA (-) metadata

-Treatment type -Total No of genes -Fisher's exact p-value	Direction	51	
		Up	Down
E2 2177 genes p-value < 2.2e-16	Up	(293 genes) ---	(950 genes) DNA replication Cell cycle Mismatch repair Pyrimidine metabolism Spliceosome Nucleotide excision repair Homologous recombination Fanconi anemia pathway Base excision repair Purine metabolism Progesterone-mediated oocyte maturation Oocyte meiosis Cellular senescence p53 signaling pathway HTLV-I infection Metabolic pathways RNA polymerase Epstein-Barr virus infection Proteasome mRNA surveillance pathway Cysteine and methionine metabolism Small cell lung cancer RNA transport
	Down	(659 genes) TGF-beta signaling pathway	(275 genes) ---
Dioxin 111 genes p-value: 4.415e-05	Up	(33 genes) Ferroptosis MicroRNAs in cancer Tryptophan metabolism mTOR signaling pathway Ovarian steroidogenesis Steroid hormone biosynthesis Metabolism of xenobiotics by cytochrome P450 Chemical carcinogenesis	(17 genes) Aldosterone-regulated sodium reabsorption Insulin secretion Salivary secretion Protein digestion and absorption
	Down	(16 genes) ---	(45 genes) Estrogen signaling pathway
AA(-) 1480 genes p-value < 2.2e-16	Up	(493 genes) MAPK signaling pathway MicroRNAs in cancer Ferroptosis p53 signaling pathway Aminoacyl-tRNA biosynthesis Thyroid hormone signaling pathway Mitophagy - animal Endocrine resistance Autophagy - animal mTOR signaling pathway Cellular senescence Focal adhesion Transcriptional misregulation in cancer Proteoglycans in cancer Glioma Fluid shear stress and atherosclerosis HIF-1 signaling pathway Salmonella infection Breast cancer Apoptosis Pathways in cancer Chronic myeloid leukemia	(248 genes) Lysosome Apelin signaling pathway

Table Appendix A7 KEGG pathways-based contingency table
where the genes show mutual or opposite direction in expression fold changes between 51 and E2, dioxin and AA (-) metadata
(Cont'd)

-Treatment type -Total No of genes -Fisher's exact p-value	Direction	Up	Down
AA(-) 1480 genes p-value < 2.2e-16	Down	(117 genes) Mineral absorption	(622 genes) Cell cycle DNA replication Metabolic pathways Mismatch repair Nucleotide excision repair Pyrimidine metabolism Base excision repair Purine metabolism Homologous recombination Spliceosome Oocyte meiosis Progesterone-mediated oocyte maturation Epstein-Barr virus infection Cysteine and methionine metabolism p53 signaling pathway Huntington's disease Carbon metabolism Pyruvate metabolism Fanconi anemia pathway Cellular senescence Parkinson's disease Citrate cycle (TCA cycle) HTLV-I infection Proteasome Biosynthesis of amino acids Fatty acid degradation Small cell lung cancer Arginine and proline metabolism Fatty acid metabolism MicroRNAs in cancer Pathogenic Escherichia coli infection Hepatitis B Viral carcinogenesis 2-Oxocarboxylic acid metabolism Pentose phosphate pathway Lysine degradation Alzheimer's disease Oxidative phosphorylation RNA degradation RNA polymerase Fructose and mannose metabolism Valine, leucine and isoleucine degradation Peroxisome N-Glycan biosynthesis

Retrieved from Karadayi F.Z. & Yaman M. et al., 2020. *Bioorganic Chemistry* [311].

Table Appendix A 8 Molecular docking scores of the derivatives and ligands

Compounds	ER α	Tubulin	vEGFR2 kinase domain
48	-7.776	-5.851	-6.348
49	-7.726	-5.575	-6.786
50	Unsuccessful binding	Unsuccessful binding	-6.435
51	-7.802	-5.458	-6.131
53	-6.610	-5.662	-6.813
Vincristine	-	-8.1	-
Tivozanib	-	-	-10.265
Bazedoxifene	-9.852	-	-

Courtesy of Mehmet Murat Kisla. Retrieved from Karadayi F.Z. & Yaman M. et al., 2020. *Bioorganic Chemistry* [311]

APPENDIX B

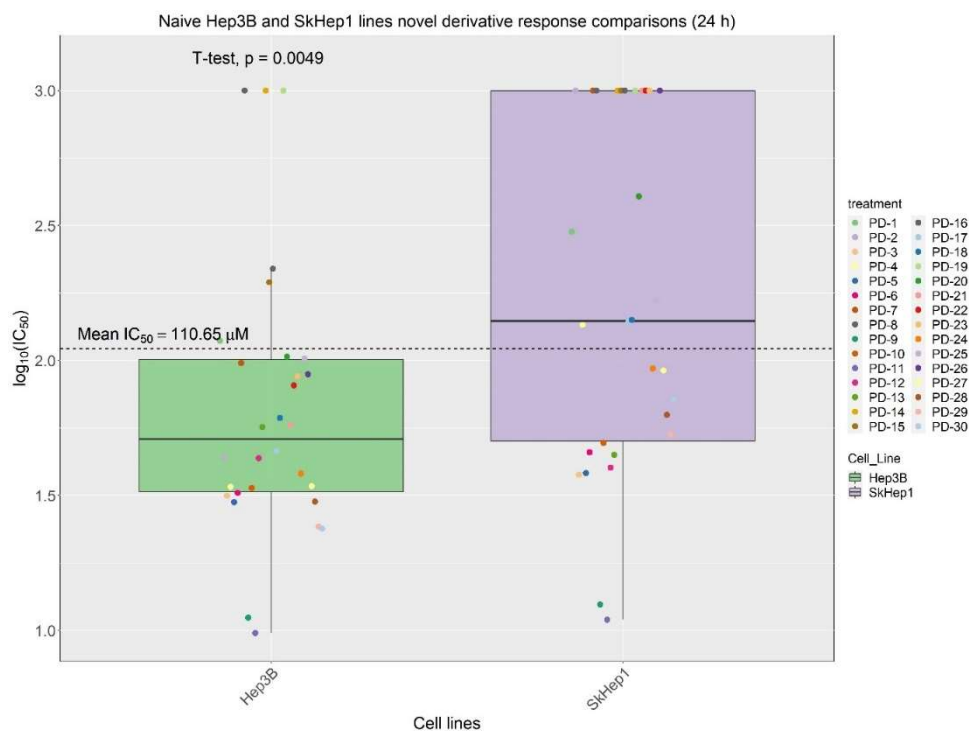


Figure Appendix B1 Non-generic PTZ derivative log₁₀IC₅₀ response t-test comparisons between Hep3B and SkHep1 cell lines. (A) Screenings with the novel compounds, (B) naive vs eGFP assessments, and (C) time-dependency evaluations. Compound wise comparisons were performed via n-way ANOVA approach as the comparisons regarding eGFP status and time-dependency were evaluated through t-tests.

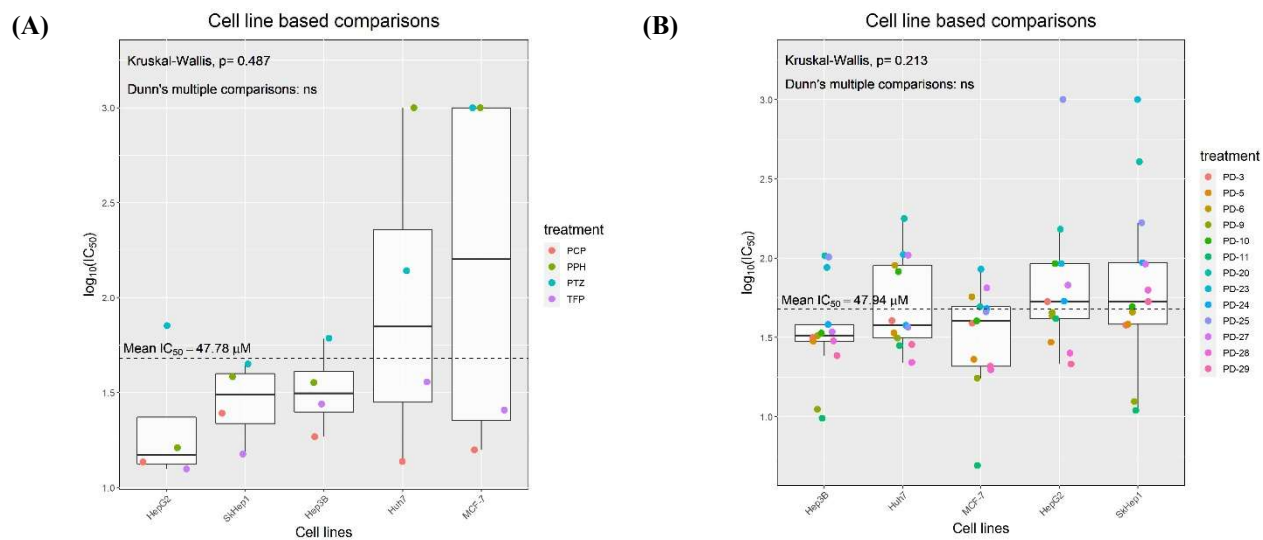


Figure Appendix B2 Cell line-based comparisons for the PTZ derivatives. (A) Generic compounds, and (B) Novel molecules. Kruskal-Wallis/Dunn statistics were used in comparing the logIC₅₀ values for the groups with the respective cell-lines (ns: not significant).

Table Appendix B3 Zebrafish images after exposures to individual derivatives. One image for each time-concentration group was provided for representative purposes.

PTZ								
Time/ Concentration	0 μ M	0.63 μ M	1.25 μ M	2.5 μ M	5 μ M	10 μ M	20 μ M	40 μ M
30 hpf								
54 hpf								
72 hpf								
PPH								
Time/ Concentration	0 μ M	0.63 μ M	1.25 μ M	2.5 μ M	5 μ M	10 μ M	20 μ M	40 μ M
30 hpf								
54 hpf								
72 hpf							-	-
PCP								
Time/ Concentration	0 μ M	0.63 μ M	1.25 μ M	2.5 μ M	5 μ M	10 μ M	20 μ M	40 μ M
30 hpf								
54 hpf								

Table Appendix B3 PCP (Cont'd)								
Time/ Concentration	0 μ M	0.63 μ M	1.25 μ M	2.5 μ M	5 μ M	10 μ M	20 μ M	40 μ M
72 hpf								-
TFP								
Time/ Concentration	0 μ M	0.63 μ M	1.25 μ M	2.5 μ M	5 μ M	10 μ M	20 μ M	40 μ M
30 hpf								
54 hpf								
72 hpf								-
PD-3								
Time/ Concentration	0 μ M	0.63 μ M	1.25 μ M	2.5 μ M	5 μ M	10 μ M	20 μ M	40 μ M
30 hpf								
54 hpf								
72 hpf								
96 hpf								
120 hpf								

Table Appendix B3 PD-4 (Cont'd)								
Time/ Concentration	0 μ M	0.63 μ M	1.25 μ M	2.5 μ M	5 μ M	10 μ M	20 μ M	40 μ M
30 hpf								
54 hpf								
72 hpf								
96 hpf								
120 hpf								-
PD-5								
Time/ Concentration	0 μ M	0.63 μ M	1.25 μ M	2.5 μ M	5 μ M	10 μ M	20 μ M	40 μ M
30 hpf								
54 hpf								
72 hpf								
96 hpf								
120 hpf								

Table Appendix B3 PD-6 (Cont'd)								
Time/ Concentration	0 μ M	0.63 μ M	1.25 μ M	2.5 μ M	5 μ M	10 μ M	20 μ M	40 μ M
30 hpf								
54 hpf								
72 hpf								
96 hpf								
120 hpf								-
PD-9								
Time/ Concentration	0 μ M	0.31 μ M	0.63 μ M	1.25 μ M	2.5 μ M	5 μ M	10 μ M	20 μ M
30 hpf								
54 hpf								-
72 hpf							-	-
96 hpf								-
120 hpf							-	-

Table Appendix B3 PD-10 (Cont'd)								
Time/ Concentration	0 μ M	0.31 μ M	0.63 μ M	1.25 μ M	2.5 μ M	5 μ M	10 μ M	20 μ M
30 hpf								
54 hpf								-
72 hpf							-	-
96 hpf							-	-
120 hpf							-	-

Table Appendix B3 PD-11								
Time/ Concentration	0 μ M	0.31 μ M	0.63 μ M	1.25 μ M	2.5 μ M	5 μ M	10 μ M	20 μ M
30 hpf								
54 hpf								-
72 hpf								-
96 hpf								-
120 hpf								-

Table Appendix B3 PD-21 (Cont'd)								
Time/ Concentration	0 μ M	0.63 μ M	1.25 μ M	2.5 μ M	5 μ M	10 μ M	20 μ M	40 μ M
30 hpf								
54 hpf								
72 hpf								
96 hpf								
120 hpf								
PD-22								
Time/ Concentration	0 μ M	0.63 μ M	1.25 μ M	2.5 μ M	5 μ M	10 μ M	20 μ M	40 μ M
30 hpf								
54 hpf								
72 hpf								
96 hpf								
120 hpf								

Table Appendix B3 PD-23 (Cont'd)								
Time/ Concentration	0 μ M	0.63 μ M	1.25 μ M	2.5 μ M	5 μ M	10 μ M	20 μ M	40 μ M
30 hpf								
54 hpf								
72 hpf								
96 hpf								
120 hpf								
PD-24								
Time/ Concentration	0 μ M	0.63 μ M	1.25 μ M	2.5 μ M	5 μ M	10 μ M	20 μ M	40 μ M
30 hpf								
54 hpf								
72 hpf								
96 hpf								-
120 hpf								-

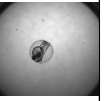
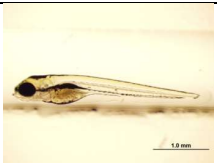
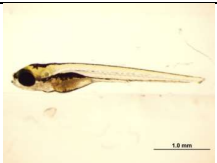
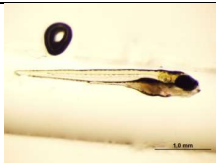
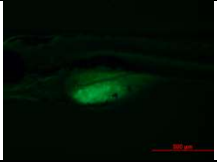
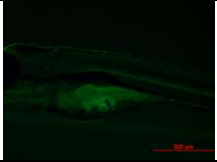
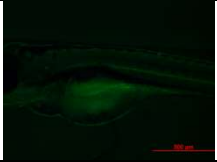
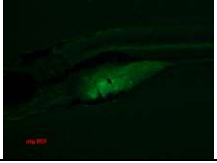
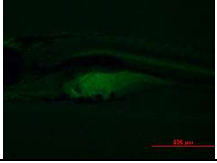
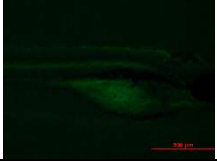
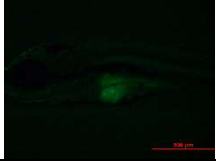
Table Appendix B3 SFB (Cont'd)								
Time/ Concentration	0 μ M	0.0625 μ M	0.125 μ M	0.25 μ M	0.5 μ M	1 μ M	2 μ M	4 μ M
30 hpf								
54 hpf								
72 hpf								

Table Appendix B4 Representative images for xenograft experiments

		Exposure (Concentration) - Normal / Affected (abnormal or dead)			
PCP & TFP	Microscopy /Exposures	DMSO (%0.5) - 8/8	PCP (10 μM) - 11/9	PCP (20 μM) - 4/15	TFP (10 μM) - 7/13
	Brightfield				
	GFP filter				
	Brightfield + GFP				
PD-3 & PD-29	Microscopy /Exposures	DMSO (%0.5) - 9/2	PD-3 (20 μM) - 5/6	PD-29 (20 μM) - 5/6	
	Brightfield				
	GFP filter				
	Brightfield + GFP				
PD-5, PD-9 & PD-11	Microscopy /Exposures	DMSO (%0.5) - 9/1	PD-3 (10 μM) - 11/0	PD-9 (5 μM) - 2/9	PD-11 (5 μM) - 8/3
	Brightfield				
	GFP filter				
	Brightfield + GFP				

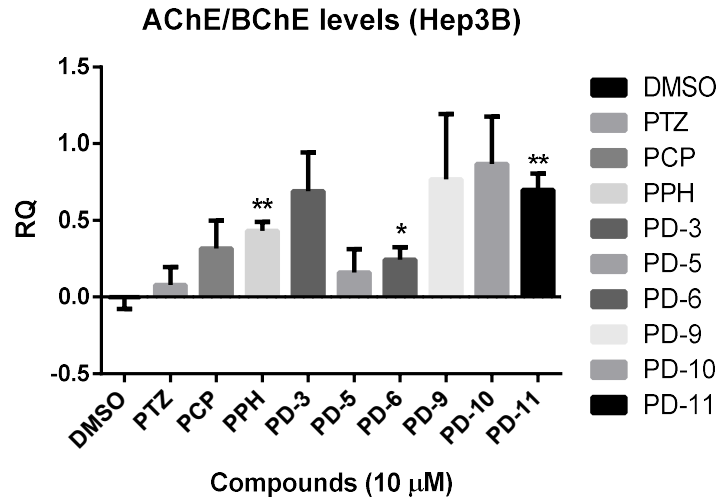


Figure Appendix B5 Validation experiment on the direction of AChE/BChE activities on Hep3B

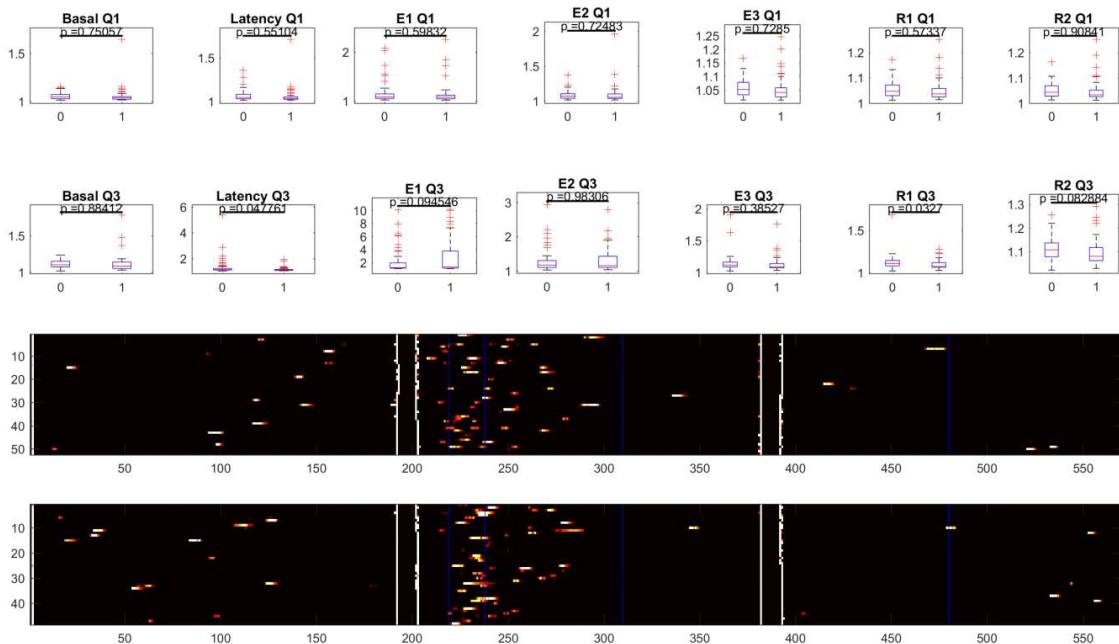


Figure Appendix B6 PCP (20 μM) versus PCP (20 μM) - SFB (2 μM) PMR results. Boxplots represent ANOVA statistics for each phase by contrasting with DMSO control. Heatmaps represent PMR intensities along the 6 seconds measurements where red indicates the highest, yellow modest and black no response. Upper panel heatmaps belong to the PCP (20 μM) group as the lower panel to the PCP (20 μM) - SFB (2 μM) group.

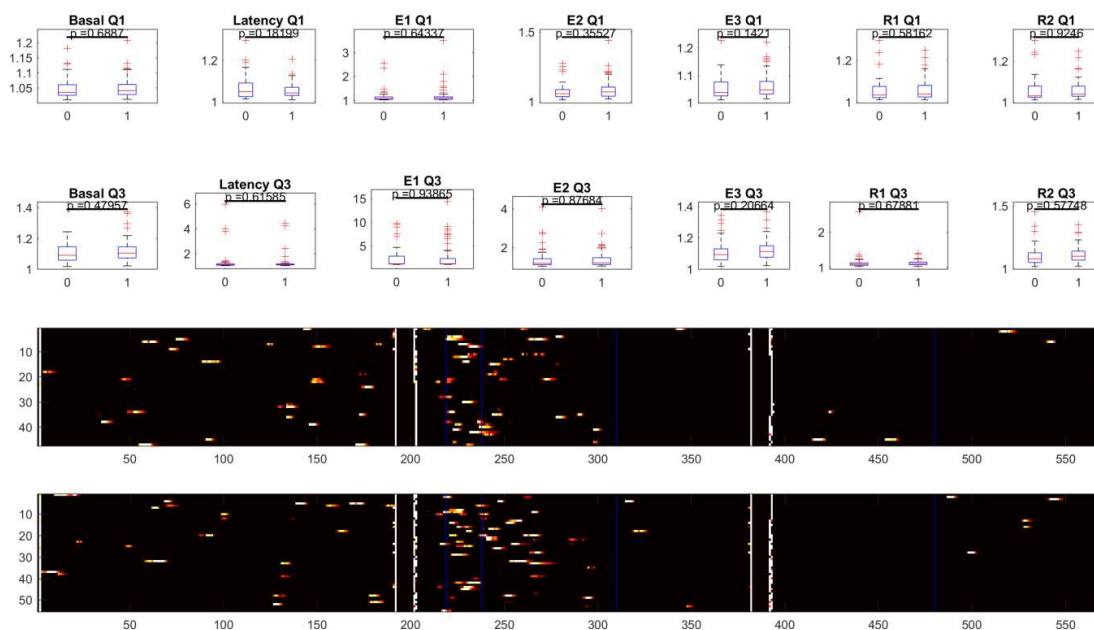


Figure Appendix B7 TFP (20 μM) versus TFP (20 μM) - SFB (2 μM) PMR results. Boxplots represent ANOVA statistics for each phase by contrasting with DMSO control. Heatmaps represent PMR intensities along the 6 seconds measurements where red indicates the highest, yellow modest and black no response. Upper panel heatmaps belong to the TFP (20 μM) group as the lower panel to the PCP (20 μM) - SFB (2 μM) group.

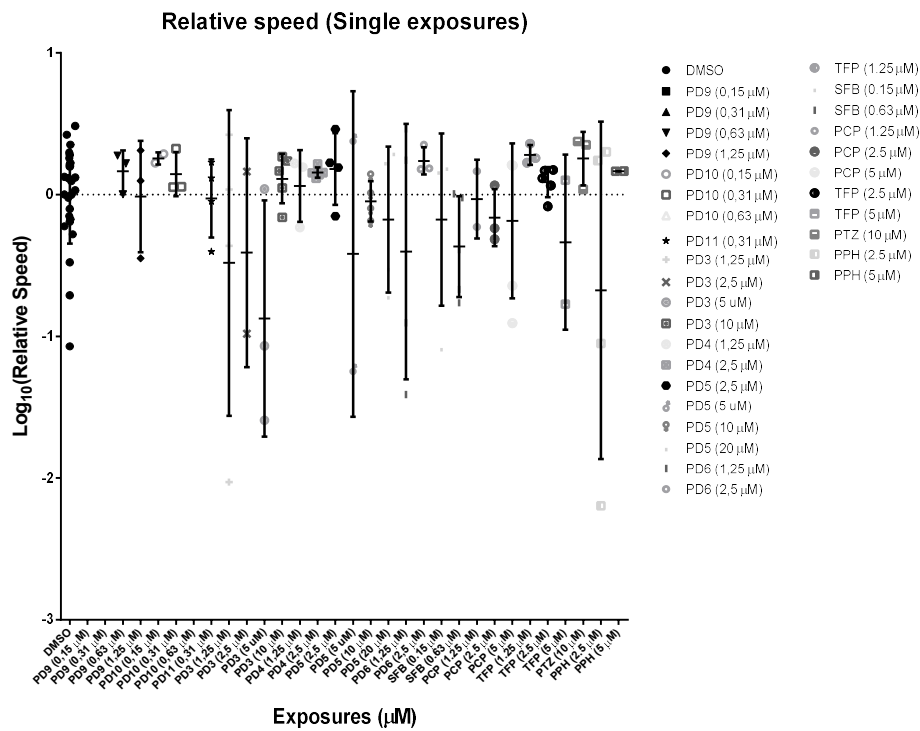
Table Appendix B8 n-way ANOVA results for the effects of treatment, concentration, combination and their interactions on the raw distance data

	Df	Sum Sq	Mean Sq	F-value	Pr(>F)
Treatment	12	0.909	0.07578	0.646	0.8
Concentration	8	0.997	0.12464	1.063	0.392
Combination	1	0.026	0.02607	0.222	0.638
Treatment:Concentration	22	2.584	0.11745	1.001	0.466
Treatment:Combination	9	0.58	0.06441	0.549	0.837
Concentration:Combination	1	0.041	0.04057	0.346	0.557
Treatment:Concentration:Combination	4	0.383	0.09583	0.817	0.516
Residuals	159	18.649	0.11729		

Table Appendix B9 n-way ANOVA results for the effects of treatment, concentration, combination and their interactions on the raw speed data. (p-value: * < 0.05)

	Df	Sum Sq	Mean Sq	F-value	Pr(>F)	Significancy
Treatment	12	3.87	0.3221	1.58	0.1022	
Concentration	8	1.42	0.1774	0.87	0.5431	
Combination	1	0.01	0.0055	0.027	0.8696	
Treatment:Concentration	22	4.03	0.1831	0.898	0.5975	
Treatment:Combination	9	3.81	0.4237	2.078	0.0344	*
Concentration:Combination	1	0.17	0.1682	0.825	0.3652	
Treatment:Concentration:Combination	4	0.88	0.221	1.084	0.3663	
Residuals	159	32.42	0.2039			

A



B

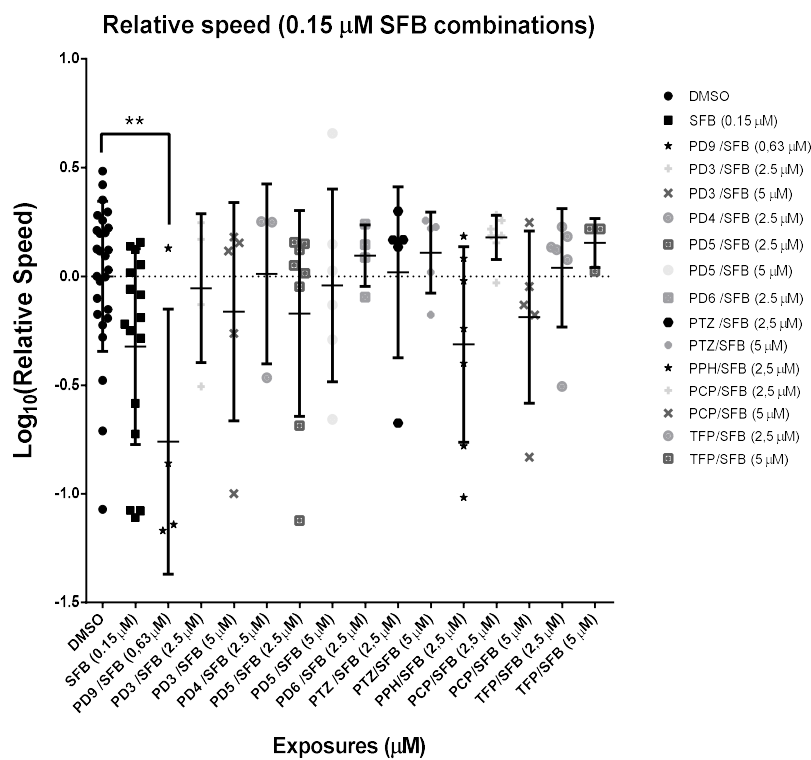


Figure Appendix B10 Locomotion speed analyses across single derivative and SFB combination exposures. (A) Individual compound exposures, and (B) SFB 0.15 μ M combinations of the derivatives. Comparisons and relative distance measurements were performed with respect to DMSO control group (0.5%) via one-way ANOVA/Dunnett statistics by using log transformed relative speeds. (*: p-value<0.05)

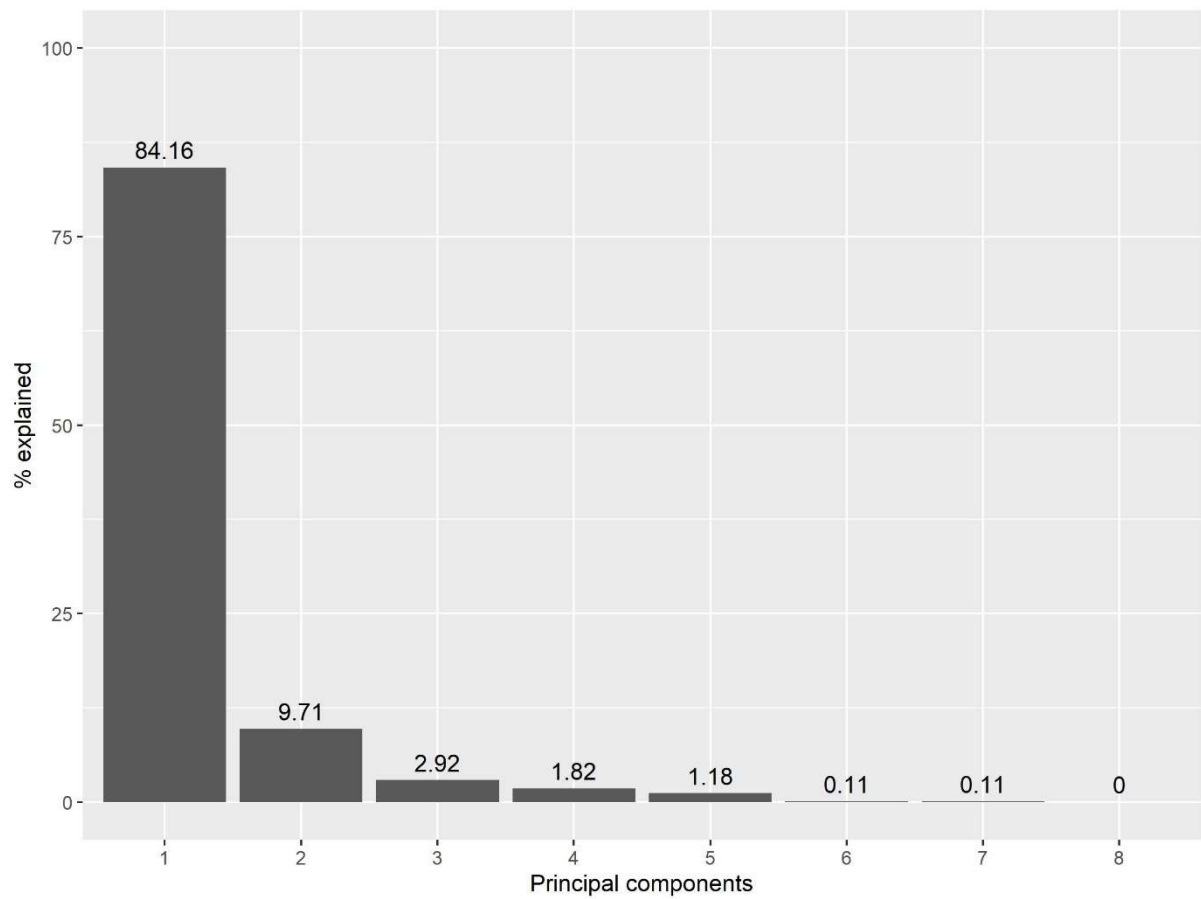


Figure Appendix B11 Percentiles of each principal component generated by the PCA approach at **Figure 4.35**

Table Appendix B12 SFB 1 μ M and TFP 12 μ M-SFB 1 μ M gene expression comparisons

Clusters	KEGG pathways (p-value <0.05)	Overlap- ping gene ratios	P-value (<0.05)	Overlapping genes with the relevant pathways	
Mutually increasing (n=15)	Ferroptosis	1/40	0.030	GPX4	
	Fat digestion and absorption	1/41	0.030	SLC27A4	
	Glutathione metabolism	1/56	0.041	GPX4	
Mutually decreasing (n=9)	Focal adhesion	2/199	0.003	DIAPH1;THBS1	
	Rap1 signaling pathway	2/206	0.004	FGF19;THBS1	
	Regulation of actin cytoskeleton	2/214	0.004	DIAPH1;FGF19	
	PI3K-Akt signaling pathway	2/354	0.010	FGF19;THBS1	
	Bladder cancer	1/41	0.018	THBS1	
	Malaria	1/49	0.022	THBS1	
	Shigellosis	1/65	0.029	DIAPH1	
	p53 signaling pathway	1/72	0.032	THBS1	
	Melanoma	1/72	0.032	FGF19	
	ECM-receptor interaction	1/82	0.036	THBS1	
	TGF-beta signaling pathway	1/90	0.040	THBS1	
Increasing in SFB 1 μM only (n=399)	AGE-RAGE signaling pathway in diabetic complications	1/100	0.044	DIAPH1	
	Salivary secretion	6/90	0.009	PRKCG;CHRM3;DMBT1;CALML3;BEST2;STATH	
Increasing in TFP 12 μM – SFB 1 μM only (n=268)	Morphine addiction	6/91	0.010	GABRR3;PRKCG;GABRA1;PDE10A;PDE1C;PDE4B	
	Steroid biosynthesis	7/19	3.15E-9	SQLE;EBP;NSDHL;CYP51A1;MSMO1;DHCR7;FDFT1	
	Terpenoid backbone biosynthesis	4/22	1.91E-4	IDH1;HMGCS1;MVD;HMGR	
	Renal cell carcinoma	6/69	3.24E-4	FLCN;PAK1;EGLN3;RAPGEF1;PIK3CD;VEGFA	
	mTOR signaling pathway	8/152	0.001	FLCN;SLC7A5;DDIT4;GRB10;PTEN;PIK3CD;ULK1;LPIN1	
	Other glycan degradation	3/18	0.002	GLB1;NEU1;GBA2	
	Central carbon metabolism in cancer	5/65	0.002	SLC7A5;IDH1;PTEN;PIK3CD;TP53	
	Bladder cancer	4/41	0.002	CDH1;DAPK2;TP53;VEGFA	
	Phosphatidylinositol signaling system	6/99	0.002	DGKD;DGKQ;PTEN;PIK3CD;MTMR7;PIK3C2B	
	AMPK signaling pathway	6/120	0.006	TBC1D1;CPT1A;PIK3CD;ULK1;HMGR;EEF2	
	Endometrial cancer	4/58	0.008	CDH1;PTEN;PIK3CD;TP53	
	Autophagy	6/128	0.008	DAPK2;TP53INP2;DDIT4;PTEN;PIK3CD;ULK1	
	Glycerolipid metabolism	4/61	0.009	DGKD;DGKQ;PNPLA3;LPIN1	
	Glycerophospholipid metabolism	5/97	0.010	DGKD;PCYT2;DGKQ;LCAT;LPIN1	
	Choline metabolism in cancer	5/99	0.011	DGKD;DGKQ;PIK3CD;RALGDS;WASF2	
	Mitophagy	4/65	0.011	BNIP3L;ULK1;TBC1D17;TP53	
	Insulin resistance	5/108	0.015	SLC27A1;CPT1A;PTEN;PIK3CD;PPARA	
	Melanoma	4/72	0.016	CDH1;PTEN;PIK3CD;TP53	
	Bacterial invasion of epithelial cells	4/74	0.017	SHC2;CDH1;PIK3CD;WASF2	
	Inositol phosphate metabolism	4/74	0.017	PTEN;PIK3CD;PIK3C2B;MTMR7	
	Glioma	4/75	0.018	SHC2;PTEN;PIK3CD;TP53	
	Pancreatic cancer	4/75	0.018	PIK3CD;TP53;RALGDS;VEGFA	
	Sphingolipid metabolism	3/47	0.025	GLB1;NEU1;GBA2	
	One carbon pool by folate	2/20	0.029	SHMT2;MTHFR	
	Cholesterol metabolism	3/50	0.029	NPC1;PCSK9;LCAT	
	Natural killer cell mediated cytotoxicity	5/131	0.032	SHC2;PAK1;SH3BP2;PIK3CD;MICA	
	Axon guidance	6/181	0.035	PAK1;CXCL12;TRPC1;PIK3CD;NGEF;PLXNA3	
	Ras signaling pathway	7/232	0.037	PAK1;SHC2;FLT3LG;PIK3CD;RALGDS;RGL2;VEGFA	
	Pathogenic Escherichia coli infection	3/55	0.037	TUBA1A;CDH1;ARHGEP2	
	VEGF signaling pathway	3/59	0.045	SHC2;PIK3CD;VEGFA	
	Phospholipase D signaling pathway	5/148	0.050	SHC2;DGKD;DGKQ;PIK3CD;RALGDS	
	Decreasing in TFP 12 μM– SFB 1 μM only (n=476)	Spliceosome	32/134	3.37E-23	RBM25;SF3B3;RBM8A;SRSF1;PRPF19;EFTUD2;SNRPD2;SNRPD1;U2AF2;TRA2B;HNRNPA1;SF3A3;HSPA8;NCBP1;ALYREF;HSPA2;PLRG1;WBP11;LSM5;LSM3;CHERP;HNRNPM;SNW1;PHF5A;SRSF2;SRSF3;SNRPA1;PRPF31;SNRPF;SNRPA;HSPA1B;SNRNP
		Cell cycle	21/124	1.62E-12	HDAC2;PCNA;YWHAB;PLK1;BUB1B;CDC20;CCNA2;CCNB1;CCND1;PTTG1;ORC1;YWHAQ;ESPL1;CHEK2;CHEK1;MCM3;E2F4;SKP2;BUB1;SKP1;MCM2
		RNA transport	19/165	1.54E-8	EIF4A1;EIF5B;PRMT5;RBM8A;NCBP1;POP4;ALYREF;RANGAP1;SUMO1;NUP85;SUMO3;NUP50;NUP62;SUMO2;XPO5;GEMIN5;SAP18;RAN;EIF3B
Proteasome		9/45	9.40E-7	PSMC5;PSMA3;PSMD11;PSMA1;PSMD13;PSMA2;PSMD2;PSME3;PSMD3	
DNA replication		8/36	1.63E-6	FEN1;RFC3;PCNA;RFC4;RPA3;MCM3;DNA2;MCM2	
Pathogenic Escherichia coli infection		8/55	4.43E-5	CDC42;TUBA1B;YWHAQ;NCL;ARPC5L;TUBB4B;CLDN1;ACTB	
Oocyte meiosis		12/125	4.45E-5	CDC20;PPP2CA;CCNB1;PTTG1;YWHAQ;ESPL1;YWHAB;PLK1;CALM1;BUB1;SKP1;AURKA	
Viral carcinogenesis		15/201	9.91E-5	LYN;HDAC2;ATF6B;YWHAB;ACTN1;GTF2H3;CDC20;CCNA2;CDC42;SNW1;CCND1;YWHAQ;CHEK1;VDAC3;SKP2	
Cellular senescence		12/160	4.61E-4	CCNA2;CCNB1;CCND1;CHEK2;CHEK1;VDAC3;VDAC1;E2F4;CALM1;FOXO1;MAPK14;TGFB2	
Antigen processing and presentation		8/77	4.85E-4	HSPA8;HSP90AA1;HSP90AB1;HSPA4;PSME3;HSPA2;IFI30;HSPA1B	

Table Appendix B12 SFB 1 μM and TFP 12 μM-SFB 1 μM gene expression comparisons (Cont'd)				
Clusters	KEGG pathways (p-value <0.05)	Overlapping gene ratios	P-value (<0.05)	Overlapping genes with the relevant pathways
Decreasing in TFP 12 μM- SFB 1 μM only (n=476)	Protein processing in endoplasmic reticulum	12/165	6.08E-4	DNAJA1;HSPA8;DNAJB1;VCP;HSP90AA1;HSPH1;HSP90AB1;ATF6B;HSPA2;CRYAB;HSPA1B;SKP1
	Ribosome biogenesis in eukaryotes	9/101	6.84E-4	UTP6;TCOF1;UTP4;POP4;NAT10;DROSHA;UTP18;GTPBP4;RAN
	Tight junction	12/170	7.91E-4	PPP2CA;CDC42;TUBA1B;PCNA;CCND1;HSPA4;ACTN1;CLDN1;YBX3;ACTB;RAB8A;RAB8B
	mRNA surveillance pathway	8/91	0.001	PPP2CA;NCBP1;RBM8A;CSTF3;ALYREF;CSTF2;CSTF2T;SAP18
	Necroptosis	11/162	0.002	GLUD2;HSP90AA1;HSP90AB1;PARP1;H2AFZ;FAF1;VDAC3;VDAC1;PGAM5;HMGB1;DNM1L
	Fluid shear stress and atherosclerosis	10/139	0.002	HSP90AA1;HSP90AB1;SUMO1;DUSP1;SUMO3;SUMO2;CALM1;MAPK14;ACTB;KLF2
	Mismatch repair	4/23	0.002	RFC3;PCNA;RFC4;RPA3
	Human T-cell leukemia virus 1 infection	13/219	0.002	ATF6B;BUB1B;TGFB2;CDC20;CCNA2;CCND1;PTTG1;ESPL1;CHEK2;CHEK1;VDAC3;VDAC1;RAN
	Progesterone-mediated oocyte maturation	8/99	0.003	CCNA2;CCNB1;HSP90AA1;HSP90AB1;PLK1;MAPK14;BUB1;AURKA
	Influenza A	11/171	0.003	IVNS1ABP;HSPA8;DNAJB1;HNRNPUL1;VDAC1;HSPA2;KPN2;MAPK14;ACTB;HSPA1B;AGFG1
	Non-homologous end-joining	3/13	0.003	FEN1;XRCC6;XRCC5
	Epstein-Barr virus infection	12/201	0.003	LYN;CCNA2;PSMC5;HDAC2;SNW1;PSMD11;CCND1;PSMD13;PSMD2;PSMD3;SKP2;MAPK14
	Nucleotide excision repair	5/47	0.005	RFC3;PCNA;RFC4;RPA3;GTF2H3
	Glyoxylate and dicarboxylate metabolism	4/30	0.005	GCSH;CS;GLDC;PCCB
	TGF-beta signaling pathway	7/90	0.006	PPP2CA;ID1;ID3;E2F4;HAMP;SKP1;TGFB2
	Base excision repair	4/33	0.008	FEN1;PCNA;PARP1;HMGB1
	Fanconi anemia pathway	5/54	0.009	FANCD2;RPA3;USP1;FANCB;FANCG
	Pyrimidine metabolism	5/57	0.011	CDA;RRM1;RRM2;CTPS1;NME1
	FoxO signaling pathway	8/132	0.014	CCNB1;CCND1;HOMER2;PLK1;SKP2;MAPK14;KLF2;TGFB2
	Hepatitis B	9/163	0.016	CCNA2;PCNA;YWHAQ;ATF6B;YWHAB;VDAC3;BIRC5;MAPK14;TGFB2
	Estrogen signaling pathway	8/137	0.017	HSPA8;HSP90AA1;HSP90AB1;ATF6B;HSPA2;FKBP4;CALM1;HSPA1B
	Adherens junction	5/72	0.028	CDC42;ACTN1;ACTB;TGFB2;FGFR1
	p53 signaling pathway	5/72	0.028	CCNB1;RRM2;CCND1;CHEK2;CHEK1
	Longevity regulating pathway	6/102	0.035	HSPA8;HDAC2;ATF6B;HSPA2;CRYAB;HSPA1B
	Hippo signaling pathway	8/160	0.038	PPP2CA;CCND1;YWHAQ;YWHAB;ID1;BIRC5;ACTB;TGFB2
	RNA degradation	5/79	0.040	EXOSC6;EXOSC5;EXOSC10;LSM5;LSM3
	Legionellosis	4/55	0.042	HSPA8;VCP;HSPA2;HSPA1B
	Glutathione metabolism	4/56	0.044	GPX2;RRM1;RRM2;ODC1
	Drug metabolism	6/108	0.044	CDA;CYP2C9;RRM1;RRM2;UGT2B4;NME1
	Ubiquitin mediated proteolysis	7/137	0.046	CDC20;UBE2C;SKP2;SAE1;PRPF19;SKP1;RHOTB2

S1: SFB 1 μ M, TS1: TFP 12 μ M - SFB 1 μ M; UP: upregulated, DOWN: downregulated genes. Fisher's exact test p-value: 0.011

Table Appendix B13 SFB 2 μ M and TFP 12 μ M-SFB 2 μ M gene expression comparisons

Clusters	KEGG pathways (p-value <0.05)	Overlapping gene ratios	P-value (<0.05)	Overlapping genes with the relevant pathways
Mutually increasing (n=128)	Natural killer cell mediated cytotoxicity	4/131	0.010	SHC2;PAK1;SH3BP2;KLRC1
	Glycine, serine and threonine metabolism	2/40	0.027	SHMT2;PHGDH
	Graft-versus-host disease	2/41	0.028	CD80;KLRC1
	Cholesterol metabolism	2/50	0.041	NPC1;PCSK9
	Glutathione metabolism	2/56	0.050	GPX4;GPX7
Mutually decreasing (n=44)	Lysosome	2/123	0.030	MCOLN1;LITAF
Increasing in TFP 12 μM - SFB 2 μM only (n=925)	Steroid biosynthesis	8/19	9.734E-7	SQLE;EBP;NSDHL;CYP51A1;SC5D;MSMO1;DHCR7;FDF1
	mTOR signaling pathway	17/152	6.81E-4	PRKCG;WDR59;FZD4;INSR;PTEN;PIK3CD;SLC3A2;F LCN;SLC7A5;SESN2;DDIT4;GRB10;EIF4EBP1;DVL2; ULK1;LPIN1;EIF4B
	Longevity regulating pathway	12/102	0.003	PRK- AB2;INSR;SESN2;EIF4EBP1;PIK3CD;ULK1;FOXO3;T P53;PPARGC1A;SIRT1;ATF4;FOXA2
	Terpenoid backbone biosynthesis	5/22	0.003	ID1;HMGCS1;MVD;HMGR;ACAT2
	AMPK signaling pathway	13/120	0.004	PRK- AB2;INSR;PIK3CD;PPP2R3B;HMGR;FOXO3;EEF2;S I RT1;TBC1D1;EIF4EBP1;ULK1;PPARGC1A;PCK2
	FoxO signaling pathway	13/132	0.008	IL10;PRKAB2;SMAD4;GADD45A;INSR;PTEN;FOXO6; PIK3CD;CSNK1E;FOXO3;SIRT1;CCNG2;PCK2
	Aminoacyl-tRNA biosynthesis	8/66	0.011	CARS;NARS;MARS;SARS;GARS;IARS;EPRS;AARS
	Phosphatidylinositol signaling system	10/99	0.016	PRKCG;DGKD;DGKQ;PLCG2;PTEN;PIK3CD;ITPR3;M TMR4;MTMR7;PIK3C2B
	p53 signaling pathway	8/72	0.018	GADD45A;CCNG2;SESN2;SIAH1;PTEN;MDM4;TP53; BBC3
	Insulin resistance	10/108	0.028	SLC27A1;PRKAB2;INSR;PTEN;PIK3CD;TRIB3;PPAR A;PPARGC1A;SLC27A5;PCK2
	Mitophagy	7/65	0.030	BNIP3L;TOMM7;ULK1;FOXO3;TBC1D17;TP53;ATF4
	HIF-1 signaling pathway	9/100	0.042	PRKCG;EGLN3;INSR;MKNK2;EIF4EBP1;PLCG2;PIK3 CD;TLR4;VEGFA
	Other glycan degradation	3/18	0.048	GLB1;NEU1;GBA2
	Decreasing in TFP 12 μM - SFB 2 μM only (n=669)	Spliceosome	41/134	2.65E-28
Cell cycle		28/124	6.71E-16	PCNA;YWHAB;BUB1B;ANAPC11;CDC20;CCNB1;CC ND1;PTTG1;ORC1;YWHAQ;CDC26;CHEK2;CHEK1;E 2F4;BUB3;SKP2;BUB1;SKP1;PLK1;CDC6;CDC25C;CC NA2;CDK6;ESPL1;CDK2;MCM3;MCM6;MCM2
DNA replication		14/36	3.69E-12	FEN1;RFC3;PCNA;RFC4;LIG1;RPA1;RPA2;POLA2;RP A3;MCM3;MCM6;SSBP1;DNA2;MCM2
RNA transport		27/165	8.04E-12	POP5;EIF4A1;NUP107;RBM8A;POP4;EIF4A3;SUMO1; NUP85;SUMO3;NUP62;SUMO2;XPO5;SAP18;EIF4E;N DC1;EIF5B;PRMT5;NCBP1;ALYREF;RANGAP1;SNUP N;NUP50;TACC3;GEMIN5;RAN;EIF4G1;EIF3B
Proteasome		15/45	8.54E-12	PSMD11;PSMD13;PSMB6;PSMB4;PSMC5;PSMA3;PS MB2;PSMC3;PSMA1;PSMB3;PSMA2;PSMD2;PSME3;P SMD3;PSMD1
Mismatch repair		8/23	4.72E-7	RFC3;PCNA;RFC4;LIG1;RPA3;RPA1;RPA2;SSBP1
Pathogenic Escherichia coli infection		11/55	1.69E-6	CDC42;TUBA1C;TUBA1B;YWHAQ;TUBB;NCL;ARPC 1A;ARPC5L;TUBB4B;ACTB;TUBA4A
Oocyte meiosis		16/125	4.33E-6	YWHAB;PLK1;CDC25C;ANAPC11;AURKA;CDC20;PP P2CA;CCNB1;PTTG1;YWHAQ;ESPL1;CDC26;CDK2;C ALM1;BUB1;SKP1
Nucleotide excision repair		9/47	2.17E-5	RFC3;PCNA;RFC4;LIG1;RPA3;RPA1;RPA2;GTF2H3;R AD23B
Human T-cell leukemia virus 1 infection		20/219	4.98E-5	RANBP1;ATF6B;BUB1B;ANAPC11;TGFB2;CDC20;C CNA2;CCND1;PTTG1;ESPL1;CDC26;CHEK2;CHEK1; CDK2;VDAC3;VDAC1;BUB3;TLN1;RAN;BCL2L1
Fanconi anemia pathway		9/54	6.87E-5	FAN- CI;FANCD2;RPA3;USP1;RPA1;RPA2;FANCC;FANCB; FANCG
Base excision repair		7/33	9.08E-5	FEN1;NEIL3;PCNA;LIG1;PARP1;HMGB1;UNG
Cellular senescence		16/160	9.58E-5	LIN9;FOXM1;MAPK14;TGFB2;CCNA2;CCNB1;CDK 6;CCND1;CHEK2;CHEK1;CDK2;VDAC3;VDAC1;MYB L2;E2F4;CALM1
Progesterone-mediated oocyte maturation		12/99	1.15E-4	CCNA2;CCNB1;HSP90AA1;HSP90AB1;CDC26;PLK1; CDK2;CDC25C;MAPK14;BUB1;ANAPC11;AURKA
Viral carcinogenesis		18/201	1.50E-4	RANBP1;ATF6B;YWHAB;ACTN1;STAT3;GTF2H3;CD C20;CCNA2;CDC42;HNRNPK;SNW1;CDK6;CCND1;Y WHAQ;CHEK1;CDK2;VDAC3;SKP2
mRNA surveillance pathway		11/91	2.25E-4	PPP2CA;NCBP1;RBM8A;PCF11;CSTF3;ALYREF;EIF4 A3;CSTF2;CSTF2T;SAP18;GSPT1

Table Appendix B13 SFB 2 μ M and TFP 12 μ M-SFB 2 μ M gene expression comparisons (Cont'd)

Clusters	KEGG pathways (p-value <0.05)	Overlapping gene ratios	P-value (<0.05)	Overlapping genes with the relevant pathways
Decreasing in TFP 12 μ M - SFB 2 μ M only (n=669)	p53 signaling pathway	9/72	6.45E-4	CCNB1;RRM2;CDK6;CCND1;CHEK2;CHEK1;CDK2;T HBS1;BCL2L1
	Necroptosis	14/162	0.001	HSP90AA1;HSP90AB1;PARP1;H2AFZ;H2AFX;STAT3; H2AFV;HMGB1;HIST2H2AC;GLUD2;VDAC3;VDAC1; DNM1L;FTL
	Pyrimidine metabolism	7/57	0.003	CDA;DUT;RRM1;RRM2;CTPS1;UMPS;NME1
	Parkinson disease	12/142	0.003	COX8A;COX7B;NDUFA11;UBB;NDUFS5;NDUFA2;V DAC3;UQCRFS1;NDUFC2;VDAC1;SDHB;COX6B1
	Epstein-Barr virus infection	15/201	0.003	PSMD11;PSMD13;STAT3;MAPK14;CCNA2;PSMC5;SN W1;CDK6;PSMC3;CCND1;PSMD2;PSMD3;CDK2;PSM D1;SKP2
	Antigen processing and presentation	8/77	0.004	HSPA8;HSP90AA1;HSP90AB1;HSPA4;PSME3;RFX5;H SPA2;HSPA1B
	Tight junction	13/170	0.005	PCNA;HSPA4;ACTN1;YBX3;ACTB;TUBA4A;PPP2CA; CDC42;TUBA1C;TUBA1B;CCND1;AMOTL1;RAB8A
	FoxO signaling pathway	11/132	0.005	PLK4;CCNB1;CCND1;PLK1;CDK2;STAT3;SKP2;SGK1 ;MAPK14;KLF2;TGFB2
	Thermogenesis	16/231	0.005	COX8A;COX7B;COA1;NDUFA11;COX16;NDUFA2;N DUFC2;MAPK14;SDHB;ACTB;COX6B1;ADCY10;ND UFS5;AKT1S1;UQCRFS1;FGFR1
	Huntington disease	14/193	0.006	COX8A;COX7B;NDUFA11;NDUFA2;NDUFC2;NRF1;S DHB;COX6B1;NDUFS5;VDAC3;UQCRFS1;VDAC1;TG M2;POLR2L
	Ribosome biogenesis in eukaryotes	9/101	0.007	POP5;TCOF1;IMP3;POP4;GAR1;NAT10;DROSHA;UTP 18;RAN
	Non-homologous end-joining	3/13	0.008	FEN1;XRCC6;XRCC5
	Protein processing in endoplasmic reticulum	12/165	0.010	DNAJA1;HSPA8;DNAJB1;VCP;HSP90AA1;HSP90AB1; ATF6B;HSPA2;RAD23B;CRYAB;HSPA1B;SKP1
	Drug metabolism	9/108	0.010	CDA;DUT;RRM1;UGT2B11;RRM2;NAT1;UGT2B4;UM PS;NME1
	Alzheimer disease	12/171	0.013	COX8A;COX7B;NDUFA11;CDK5;NDUFS5;NDUFA2; UQCRFS1;NDUFC2;NAE1;CALM1;SDHB;COX6B1
	Phagosome	11/152	0.013	TU- BA1C;TUBA1B;TUBB;ATP6V1B2;TLR6;TUBB4B;TH BS1;ACTB;TUBA4A;DYNC111;MBL2
	Oxidative phosphorylation	10/133	0.014	COX8A;COX7B;NDUFA11;NDUFS5;NDUFA2;ATP6V 1B2;UQCRFS1;NDUFC2;SDHB;COX6B1
	Systemic lupus erythematosus	10/133	0.014	SSB;SNRPD1;H2AFZ;ACTN1;H3F3A;H2AFX;H2AFV; HIST1H3C;SNRPB;HIST2H2AC
	Cardiac muscle contraction	7/78	0.015	COX8A;COX7B;TPM3;TPM1;UQCRFS1;ATP1B3;COX 6B1
	Fluid shear stress and atherosclerosis	10/139	0.019	HSP90AA1;HSP90AB1;SUMO1;DUSP1;SUMO3;SUMO 2;CALM1;MAPK14;ACTB;KLF2
	Hepatitis B	11/163	0.021	CCNA2;PCNA;YWHAQ;ATF6B;YWHAB;CDK2;STAT 3;VDAC3;BIRC5;MAPK14;TGFB2
	Non-alcoholic fatty liver disease (NAFLD)	10/149	0.028	COX8A;CDC42;COX7B;NDUFA11;NDUFS5;NDUFA2; UQCRFS1;NDUFC2;SDHB;COX6B1
	TGF-beta signaling pathway	7/90	0.031	PPP2CA;ID1;ID3;E2F4;THBS1;SKP1;TGFB2
	Ribosome	10/153	0.033	RPS15;MRPS17;MRPS15;MRPL18;MRPS12;MRPL16; MRPS7;MRPL13;RPL6;MRPL11
	Glutathione metabolism	5/56	0.039	RRM1;RRM2;ODC1;SMS;CHAC2
	Pancreatic cancer	6/75	0.039	CDC42;CDK6;CCND1;STAT3;TGFB2;BCL2L1
	Estrogen signaling pathway	9/137	0.041	HSPA8;HSP90AA1;HSP90AB1;ATF6B;KRT23;HSPA2; FKBP4;CALM1;HSPA1B
Ubiquitin mediated proteolysis	9/137	0.041	CDC20;UBE2C;CDC26;SKP2;SAE1;PRPF19;SKP1;AN APC11;RHOTB2	
Homologous recombination	4/41	0.047	RPA3;RPA1;RPA2;SSBP1	
RNA degradation	6/79	0.049	EXOSC6;EXOSC5;EXOSC10;LSM5;DCPS;LSM3	

S2: SFB 2 μ M, TS2: TFP 12 μ M - SFB 2 μ M; UP: upregulated, DOWN: downregulated genes. Fisher's exact test p-value: 2.09e-34

Table Appendix B14 TFP 12 μ M-SFB 1 μ M and TFP 12 μ M-SFB 2 μ M gene expression comparisons

Clusters	KEGG pathways (p-value <0.05)	Overlapping gene ratios	P-value (<0.05)	Overlapping genes with the relevant pathways
Mutually increasing (n=266)	Steroid biosynthesis	8/19	5.87E-11	SQLE;EBP;NSDHL;CYP51A1;CYP2R1;MSMO1;DHCR7;FDFT1
	Terpenoid backbone biosynthesis	4/22	1.85E-4	ID11;HMGCS1;MVD;HMGR
	Renal cell carcinoma	6/69	3.11E-4	FLCN;PAK1;EGLN3;RAPGEF1;PIK3CD;VEGFA
	mTOR signaling pathway	8/152	9.94E-4	FLCN;SLC7A5;DDIT4;GRB10;PTEN;PIK3CD;ULK1;LPI N1
	Other glycan degradation	3/18	0.002	GLB1;NEU1;GBA2
	Central carbon metabolism in cancer	5/65	0.002	SLC7A5;IDH1;PTEN;PIK3CD;TP53
	Glycerophospholipid metabolism	6/97	0.002	DGKD;PCYT2;PNPLA7;DGKQ;LCAT;LPIN1
	Phosphatidylinositol signaling system	6/99	0.002	DGKD;DGKQ;PTEN;PIK3CD;MTMR7;PIK3C2B
	Bladder cancer	4/41	0.002	CDH1;DAPK2;TP53;VEGFA
	Autophagy	6/128	0.007	DAPK2;TP53INP2;DDIT4;PTEN;PIK3CD;ULK1
	Endometrial cancer	4/58	0.007	CDH1;PTEN;PIK3CD;TP53
	Glycerolipid metabolism	4/61	0.009	DGKD;DGKQ;PNPLA3;LPIN1
	Choline metabolism in cancer	5/99	0.010	DGKD;DGKQ;PIK3CD;RALGDS;WASF2
	Axon guidance	7/181	0.011	PAK1;CXCL12;UNC5B;TRPC1;PIK3CD;NGEF;PLXNA3
	Mitophagy	4/65	0.011	BNIP3L;ULK1;TBC1D17;TP53
	Insulin resistance	5/108	0.015	SLC27A1;PTEN;PIK3CD;PPARA;SLC27A4
	Melanoma	4/72	0.016	CDH1;PTEN;PIK3CD;TP53
	Ribosome	6/153	0.017	RPL18A;RPLP0;RPL13A;RPS20;RPL28;RPS12
	Bacterial invasion of epithelial cells	4/74	0.017	SHC2;CDH1;PIK3CD;WASF2
	Inositol phosphate metabolism	4/74	0.017	PTEN;PIK3CD;PIK3C2B;MTMR7
	Glioma	4/75	0.018	SHC2;PTEN;PIK3CD;TP53
	Pancreatic cancer	4/75	0.018	PIK3CD;TP53;RALGDS;VEGFA
	AMPK signaling pathway	5/120	0.022	TBC1D1;PIK3CD;ULK1;HMGR;EEF2
	Sphingolipid metabolism	3/47	0.025	GLB1;NEU1;GBA2
	One carbon pool by folate	2/20	0.029	SHMT2;MTHFR
	Cholesterol metabolism	3/50	0.029	NPC1;PCSK9;LCAT
	Natural killer cell mediated cytotoxicity	5/131	0.031	SHC2;PAK1;SH3BP2;PIK3CD;MICA
	Ras signaling pathway	7/232	0.036	PAK1;SHC2;FLT3LG;PIK3CD;RALGDS;RGL2;VEGFA
	Pathogenic Escherichia coli infection	3/55	0.037	TUBA1A;CDH1;ARHGFE2
	Glutathione metabolism	3/56	0.038	GGT7;GPX4;IDH1
VEGF signaling pathway	3/59	0.044	SHC2;PIK3CD;VEGFA	
Phospholipase D signaling pathway	5/148	0.048	SHC2;DGKD;DGKQ;PIK3CD;RALGDS	
Mutually decreasing (n=438)	Spliceosome	32/134	2.59E-24	RBM25;SF3B3;RBM8A;SRSF1;PRPF19;EFTUD2;SNRPD2;SNRPD1;U2AF2;TRA2B;HNRNP1A1;SF3A3;HSPA8;NCBP1;ALYREF;HSPA2;PLRG1;WBP11;LSM5;LSM3;CHERP;HNRNPM;SNW1;PHF5A;SRSF2;SRSF3;SNRPA1;PRPF31;SNRPF;SNRPA;HSPA1B;SNRPB
	Cell cycle	20/124	3.10E-12	PCNA;YWHAB;PLK1;BUB1B;CDC20;CCNA2;CCNB1;CCND1;PTTG1;ORC1;YWHAQ;ESPL1;CHEK2;CHEK1;MCM3;E2F4;SKP2;BUB1;SKP1;MCM2
	RNA transport	19/165	4.02E-9	EIF4A1;EIF5B;PRMT5;RBM8A;NCBP1;POP4;ALYREF;RAN;GAP1;SUMO1;NUP85;SUMO3;NUP50;NUP62;SUMO2;XPO5;GEMIN5;SAP18;RAN;EIF3B
	Proteasome	9/45	4.70E-7	PSMC5;PSMA3;PSMD11;PSMA1;PSMD13;PSMA2;PSMD2;PSME3;PSMD3
	DNA replication	8/36	8.77E-7	FEN1;RFC3;PCNA;RFC4;RPA3;MCM3;DNA2;MCM2
	Oocyte meiosis	12/125	1.98E-5	CDC20;PPP2CA;CCNB1;PTTG1;YWHAQ;ESPL1;YWHAB;PLK1;CALM1;BUB1;SKP1;AURKA
	Viral carcinogenesis	14/201	1.46E-4	LYN;ATF6B;YWHAB;ACTN1;GTF2H3;CDC20;CCNA2;CDC42;SNW1;CCND1;YWHAQ;CHEK1;VDAC3;SKP2
	Pathogenic Escherichia coli infection	7/55	1.89E-4	CDC42;TUBA1B;YWHAQ;NCL;ARPC5L;TUBB4B;ACTB
	Cellular senescence	12/160	2.18E-4	CCNA2;CCNB1;CCND1;CHEK2;CHEK1;VDAC3;VDAC1;E2F4;CALM1;FOXO1;MAPK14;TGFB2
	Antigen processing and presentation	8/77	2.79E-4	HSPA8;HSP90AA1;HSP90AB1;HSPA4;PSME3;HSPA2;IFI30;HSPA1B
	Protein processing in endoplasmic reticulum	12/165	2.89E-4	DNAJA1;HSPA8;DNAJB1;VCP;HSP90AA1;HSPH1;HSP90AB1;ATF6B;HSPA2;CRYAB;HSPA1B;SKP1
	mRNA surveillance pathway	8/91	8.63E-4	PPP2CA;NCBP1;RBM8A;CSTF3;ALYREF;CSTF2;CSTF2T;SAP18
	Fluid shear stress and atherosclerosis	10/139	9.91E-4	HSP90AA1;HSP90AB1;SUMO1;DUSP1;SUMO3;SUMO2;CALM1;MAPK14;ACTB;KLF2
	Human T-cell leukemia virus 1 infection	13/219	0.001	ATF6B;BUB1B;TGFB2;CDC20;CCNA2;CCND1;PTTG1;ESPL1;CHEK2;CHEK1;VDAC3;VDAC1;RAN
	Tight junction	11/170	0.001	PPP2CA;CDC42;TUBA1B;PCNA;CCND1;HSPA4;ACTN1;YBX3;ACTB;RAB8A;RAB8B
	Mismatch repair	4/23	0.001	RFC3;PCNA;RFC4;RPA3
	Progesterone-mediated oocyte maturation	8/99	0.001	CCNA2;CCNB1;HSP90AA1;HSP90AB1;PLK1;MAPK14;BUB1;AURKA
	Non-homologous end-joining	3/13	0.003	FEN1;XRCC6;XRCC5
	Nucleotide excision repair	5/47	0.004	RFC3;PCNA;RFC4;RPA3;GTF2H3
	TGF-beta signaling pathway	7/90	0.004	PPP2CA;ID1;ID3;E2F4;THBS1;SKP1;TGFB2

Table Appendix B14 TFP 12 μM-SFB 1 μM and TFP 12 μM-SFB 2 μM gene expression comparisons (Cont'd)				
Clusters	KEGG pathways (p-value <0.05)	Overlapping gene ratios	P-value (<0.05)	Overlapping genes with the relevant pathways
	Influenza A	10/171	0.005	HSPA8;DNAJB1;HNRNPUL1;VDAC1;HSPA2;KPNA2;MAPK14;ACTB;HSPA1B;AGFG1
	Epstein-Barr virus infection	11/201	0.005	LYN;CCNA2;PSMC5;SNW1;PSMD11;CCND1;PSMD13;PSMD2;PSMD3;SKP2;MAPK14
	p53 signaling pathway	6/72	0.005	CCNB1;RRM2;CCND1;CHEK2;CHEK1;THBS1
	Base excision repair	4/33	0.006	FEN1;PCNA;PARP1;HMGB1
	Fanconi anemia pathway	5/54	0.006	FANCD2;RPA3;USP1;FANCB;FANCG
	Ribosome biogenesis in eukaryotes	7/101	0.007	UTP6;TCOF1;POP4;NAT10;DROSHA;UTP18;RAN
	Pyrimidine metabolism	5/57	0.008	CDA;RRM1;RRM2;CTPS1;NME1
	Necroptosis	9/162	0.010	GLUD2;HSP90AA1;HSP90AB1;PARP1;H2AFZ;VDAC3;VDAC1;HMGB1;DNM1L
	Hepatitis B	9/163	0.010	CCNA2;PCNA;YWHAQ;ATF6B;YWHAB;VDAC3;BIRC5;MAPK14;TGFB2
	Estrogen signaling pathway	8/137	0.011	HSPA8;HSP90AA1;HSP90AB1;ATF6B;HSPA2;FKBP4;CALM1;HSPA1B
	Shigellosis	5/65	0.014	CDC42;DIAPH1;ARPC5L;MAPK14;ACTB
	Adherens junction	5/72	0.021	CDC42;ACTN1;ACTB;TGFB2;FGFR1
	AGE-RAGE signaling pathway in diabetic complications	6/100	0.023	CDC42;DIAPH1;CCND1;PLCE1;MAPK14;TGFB2
	Hippo signaling pathway	8/160	0.025	PPP2CA;CCND1;YWHAQ;YWHAB;IDL1;BIRC5;ACTB;TGFB2
	FoxO signaling pathway	7/132	0.026	CCNB1;CCND1;PLK1;SKP2;MAPK14;KLF2;TGFB2
	Glyoxylate and dicarboxylate metabolism	3/30	0.027	GCSH;CS;GLDC
	RNA degradation	5/79	0.030	EXOSC6;EXOSC5;EXOSC10;LSM5;LSM3
	Ubiquitin mediated proteolysis	7/137	0.031	CDC20;UBE2C;SKP2;SAE1;PRPF19;SKP1;RHOTB2
	Legionellosis	4/55	0.032	HSPA8;VCP;HSPA2;HSPA1B
	Glutathione metabolism	4/56	0.034	GPX2;RRM1;RRM2;ODC1
	Rap1 signaling pathway	9/206	0.038	CDC42;FGF19;IDL1;PLCE1;CALM1;MAPK14;THBS1;ACTB;FGFR1
	Endocytosis	10/244	0.043	CDC42;HSPA8;CAPZB;ARPC5L;HSPA2;SNX5;RAB8A;ARF5;HSPA1B;TGFB2
	Human immunodeficiency virus 1 infection	9/212	0.044	CCNB1;APIG1;LIMK2;CHEK1;APIB1;CALM1;SAMHD1;MAPK14;SKP1
Increasing in TFP 12 μM – SFB 1 μM only (n=21)	Mucin type O-glycan biosynthesis	1/31	0.032	B4GALT5
	Fatty acid degradation	1/44	0.045	CPT1A
Decreasing in TFP 12 μM – SFB 1 μM only (n=49)	Ribosome biogenesis in eukaryotes	2/101	0.025	UTP4;GTPBP4
Increasing in TFP 12 μM – SFB 2 μM only (n=788)	Longevity regulating pathway	9/102	0.019	PRKAB2;INSR;SESN2;EIF4EBP1;FOXO3;PPARGC1A;SIRT1;ATF4;FOXA2
	FoxO signaling pathway	10/132	0.036	IL10;PRKAB2;SMAD4;GADD45A;INSR;FOXO6;CSNK1E;FOXO3;SIRT1;PCK2
	Aminoacyl-tRNA biosynthesis	6/66	0.045	CARS;NARS;SARS;GARS;IARS;EPRS
	Oxidative phosphorylation	10/133	1.72E-5	POLA2;LIG1;RPA1;RPA2;MCM6;SSBP1
	Spliceosome	10/134	1.84E-5	COX8A;COX7B;NDUFA11;NDUF55;NDUFA2;ATP6V1B2;UQCRRF1;NDUFC2;SDHB;COX6B1
	Parkinson disease	10/142	3.04E-5	PPIL1;HNRNPA3;HNRNPK;EIF4A3;DDX23;SNRPG;HNRNPU;SNRPE;HNRNPC;SRSF7
	Proteasome	6/45	3.53E-5	COX8A;COX7B;NDUFA11;UBB;NDUF55;NDUFA2;UQCRRF1;NDUFC2;SDHB;COX6B1
	Huntington disease	11/193	8.55E-5	PSMB6;PSMB4;PSMB2;PSMC3;PSMB3;PSMD1
	Thermogenesis	12/231	9.98E-5	COX8A;COX7B;NDUFA11;NDUF55;NDUFA2;UQCRRF1;NDUFC2;NRF1;SDHB;TGM2;COX6B1
	Alzheimer disease	10/171	1.45E-4	COX8A;ADCY10;COX7B;NDUFA11;COX16;NDUF55;AKT1S1;NDUFA2;UQCRRF1;NDUFC2;SDHB;COX6B1
	Non-alcoholic fatty liver disease (NAFLD)	9/149	2.44E-4	COX8A;COX7B;NDUFA11;CDK5;NDUF55;NDUFA2;UQCRRF1;NDUFC2;SDHB;COX6B1
Decreasing in TFP 12 μM – SFB 2 μM only (n=278)	Mismatch repair	4/23	2.63E-4	COX8A;COX7B;NDUFA11;NDUF55;NDUFA2;UQCRRF1;NDUFC2;SDHB;COX6B1
	Cell cycle	8/124	3.45E-4	LIG1;RPA1;RPA2;SSBP1
	RNA transport	8/165	0.002	CDK6;CDC26;CDK2;CDC6;MCM6;BUB3;CDC25C;ANAPC11
	Nucleotide excision repair	4/47	0.004	NDC1;POP5;NUP107;EIF4A3;TACC3;EIF4E;SNUPN;EIF4G1
	Cardiac muscle contraction	5/78	0.005	LIG1;RPA1;RPA2;RAD23B
	Fanconi anemia pathway	4/54	0.007	COX8A;COX7B;UQCRRF1;ATP1B3;COX6B1
	Pathogenic Escherichia coli infection	4/55	0.007	FANCI;RPA1;RPA2;FANCC
	Base excision repair	3/33	0.011	TUBA1C;TUBB;ARPC1A;TUBA4A
	Homologous recombination	3/41	0.020	NEIL3;LIG1;UNG
	Phagosome	6/152	0.020	RPA1;RPA2;SSBP1
	Vasopressin-regulated water reabsorption	3/44	0.023	TUBA1C;TUBB;ATP6V1B2;TUBA4A;DYNCIII1;MBL2
	Human T-cell leukemia virus 1 infection	7/219	0.034	ARHGDI1;DYNLL1;DYNC1I1
	Small cell lung cancer	4/93	0.041	RANBP1;CDC26;CDK2;BUB3;TLN1;ANAPC11;BCL2L1
	Progesterone-mediated oocyte maturation	4/99	0.049	CDK6;CDK2;CKS1B;BCL2L1

TS1: TFP 12 μ M – SFB 1 μ M; TS2: TFP 12 μ M – SFB 2 μ M; UP upregulated, DOWN: downregulated genes. Fisher's exact test p-value: 8.79e-198

Table Appendix B15 TFP 12 μ M and TFP 12 μ M-SFB 1 μ M gene expression comparisons

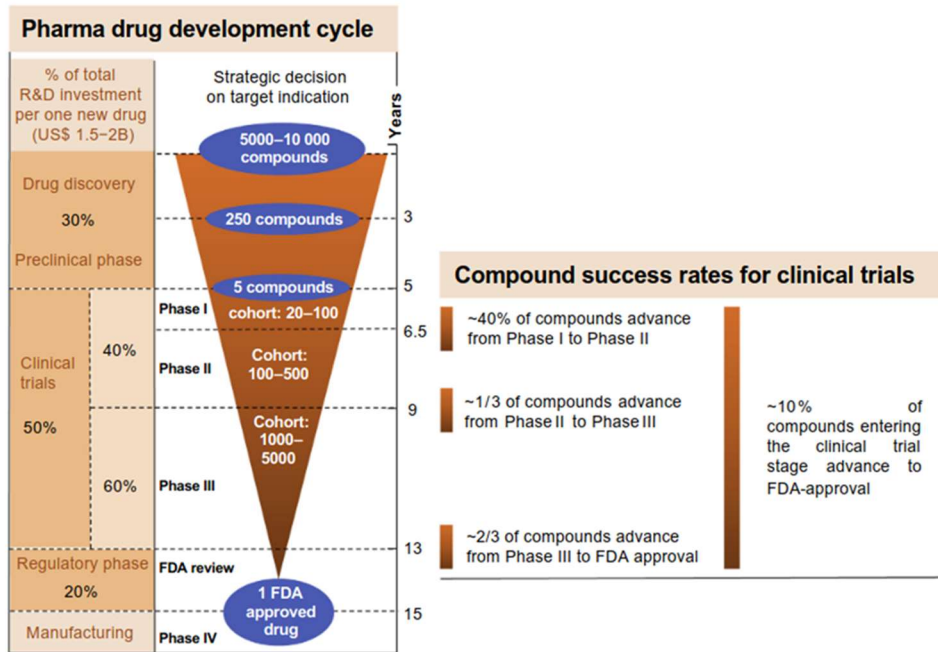
Clusters	KEGG pathways (p-value <0.05)	Overlapping gene ratios	P-value (<0.05)	Overlapping genes with the relevant pathways	
Mutually increasing (n=54)	Steroid biosynthesis	3/19	1.75E-5	NSDHL;CYP51A1;DHCR7	
	Renal cell carcinoma	3/69	8.60E-4	PAK1;EGLN3;VEGFA	
	Natural killer cell mediated cytotoxicity	3/131	0.005	SHC2;PAK1;SH3BP2	
	Cholesterol metabolism	2/50	0.008	NPC1;PCSK9	
	VEGF signaling pathway	2/59	0.011	SHC2;VEGFA	
	Focal adhesion	3/199	0.017	SHC2;PAK1;VEGFA	
	ErbB signaling pathway	2/85	0.022	SHC2;PAK1	
	Ras signaling pathway	3/232	0.025	SHC2;PAK1;VEGFA	
	Synthesis and degradation of ketone bodies	1/10	0.027	HMGCS1	
	Taurine and hypotaurine metabolism	1/11	0.029	GGT7	
	HIF-1 signaling pathway	2/100	0.030	EGLN3;VEGFA	
	Lysosome	2/123	0.044	NPC1;NEU1	
	Other glycan degradation	1/18	0.048	NEU1	
	Relaxin signaling pathway	2/130	0.048	SHC2;VEGFA	
	Mutually decreasing (n=96)	Spliceosome	6/134	4.57E-5	SF3A3;SNW1;U2AF2;ALYREF;PRPF19;HNRNPA1
Proteasome		4/45	6.39E-5	PSMC5;PSMD11;PSMA1;PSMD3	
Epstein-Barr virus infection		6/201	4.18E-4	PSMC5;PSMD11;SNW1;CCND1;PSMD3;MAPK14	
Influenza A		4/171	0.009	IVNS1ABP;HNRNPUL1;KPNA2;MAPK14	
AGE-RAGE signaling pathway in diabetic complications		3/100	0.012	DIAPH1;CCND1;MAPK14	
Proteoglycans in cancer		4/201	0.016	CCND1;DROSHA;MAPK14;THBS1	
Bladder cancer		2/41	0.017	CCND1;THBS1	
Shigellosis		2/65	0.039	DIAPH1;MAPK14	
Prolactin signaling pathway		2/70	0.045	CCND1;MAPK14	
p53 signaling pathway		2/72	0.047	CCND1;THBS1	
Melanoma		2/72	0.047	CCND1;FGF19	
Increasing in TFP 12 μM only (n=402)					IL10;IL6;FASLG
Increasing in TFP 12 μM – SFB 1 μM only (n=233)		African trypanosomiasis	3/37	0.038	
Decreasing in TFP 12 μM – SFB 1 μM only (n=393)		Steroid biosynthesis	5/19	2.09E-6	SOLE;EBP;CYP2R1;MSMO1;FDFT1
	mTOR signaling pathway	8/152	4.19E-4	FLCN;SLC7A5;DDIT4;GRB10;PTEN;PIK3CD;ULK1;LIPIN1	
	Central carbon metabolism in cancer	5/65	9.62E-4	SLC7A5;IDH1;PTEN;PIK3CD;TP53	
	Phosphatidylinositol signaling system	6/99	0.001	DGKD;DGKQ;PTEN;PIK3CD;MTMR7;PIK3C2B	
	Insulin resistance	6/108	0.002	SLC27A1;CPT1A;PTEN;PIK3CD;PPARA;SLC27A4	
	Terpenoid backbone biosynthesis	3/22	0.002	IDH1;MVD;HMGR	
	AMPK signaling pathway	6/120	0.003	TBC1D1;CPT1A;PIK3CD;ULK1;HMGR;EEF2	
	Autophagy	6/128	0.004	DAPK2;TP53INP2;DDIT4;PTEN;PIK3CD;ULK1	
	Endometrial cancer	4/58	0.005	CDH1;PTEN;PIK3CD;TP53	
	Spliceosome	26/134	1.00E-18	RBM25;SF3B3;RBM8A;SRSF1;EFTUD2;SNRPD2;SNRPD1;TRA2B;HSPA8;NCBP1;HSPA2;PLRG1;WBP11;LSM5;LSM3;CHERP;HNRNPM;PHF5A;SRSF2;SRSF3;SNRPA1;PRPF31;SNRPF;SNRPA;HSPA1B;SNRPB	
Cell cycle	20/124	4.23E-13	HDAC2;PCNA;YWHAB;PLK1;BUB1B;CDC20;CCNA2;CCNB1;PTTG1;ORC1;YWHAQ;ESPL1;CHEK2;CHEK1;MCM3;E2F4;SKP2;BUB1;SKP1;MCM2		
RNA transport	17/165	2.90E-8	EIF4A1;EIF5B;PRMT5;RBM8A;NCBP1;POP4;RANGAP1;SUMO1;SUMO3;NUP50;NUP62;SUMO2;XPO5;GEMIN5;SAP18;RAN;EIF3B		
DNA replication	7/36	5.47E-6	FEN1;RFC3;PCNA;RFC4;RPA3;MCM3;MCM2		
Oocyte meiosis	12/125	6.70E-6	CDC20;PPP2CA;CCNB1;PTTG1;YWHAQ;ESPL1;YWHAB;PLK1;CALM1;BUB1;SKP1;AURKA		
Pathogenic Escherichia coli infection	8/55	1.12E-5	CDC42;TUBA1B;YWHAQ;NCL;ARPC5L;TUBB4B;CLDN1;ACTB		
Viral carcinogenesis	12/201	6.52E-4	CDC20;LYN;CCNA2;CDC42;HDAC2;YWHAQ;ATF6B;YWHAB;ACTN1;CHEK1;VDAC3;SKP2		
Antigen processing and presentation	7/77	7.91E-4	HSPA8;HSP90AA1;HSPA4;PSME3;HSPA2;IFI30;HSPA1B		
Mismatch repair	4/23	9.67E-4	RFC3;PCNA;RFC4;RPA3		
Cellular senescence	10/160	0.001	CCNA2;CCNB1;CHEK2;CHEK1;VDAC3;VDAC1;E2F4;CALM1;FOXM1;TGFB2		
Human T-cell leukemia virus 1 infection	12/219	0.001	CDC20;CCNA2;PTTG1;ESPL1;ATF6B;CHEK2;CHEK1;VDAC3;BUB1B;VDAC1;RAN;TGFB2		
Necroptosis	10/162	0.001	GLUD2;HSP90AA1;PARP1;H2AFZ;FAF1;VDAC3;VDAC1;PGAM5;HMGB1;DNM1L		
Protein processing in endoplasmic reticulum	10/165	0.002	DNAJA1;HSPA8;DNAJB1;VCP;HSP90AA1;ATF6B;HSPA2;CRYAB;HSPA1B;SKP1		
Proteasome	5/45	0.002	PSMA3;PSMD13;PSMA2;PSMD2;PSME3		
Non-homologous end-joining	3/13	0.002	FEN1;XRCC6;XRCC5		
Tight junction	10/170	0.002	PPP2CA;CDC42;TUBA1B;PCNA;HSPA4;ACTN1;CLDN1;YBX3;ACTB;RAB8A		
mRNA surveillance pathway	7/91	0.002	PPP2CA;NCBP1;RBM8A;CSTF3;CSTF2;CSTF2T;SAP18		
Glyoxylate and dicarboxylate metabolism	4/30	0.003	GCSH;CS;GLDC;PCCB		
Ribosome biogenesis in eukaryotes	7/101	0.004	TCOF1;UTP4;POP4;NAT10;UTP18;GTPBP4;RAN		
Base excision repair	4/33	0.004	FEN1;PCNA;PARP1;HMGB1		

Decreasing in TFP 12 μM – SFB 1 μM only (n=393)	Fanconi anemia pathway	5/54	0.004	FANCD2;RPA3;USP1;FANCB;FANCG
	Pyrimidine metabolism	5/57	0.005	CDA;RRM1;RRM2;CTPS1;NME1
	Fluid shear stress and atherosclerosis	8/139	0.006	HSP90AA1;SUMO1;DUSP1;SUMO3;SUMO2;CALM1;ACTB;KLF2
	TGF-beta signaling pathway	6/90	0.009	PPP2CA;ID1;E2F4;HAMP;SKP1;TGFB2
	Progesterone-mediated oocyte maturation	6/99	0.013	CCNA2;CCNB1;HSP90AA1;PLK1;BUB1;AURKA
	Nucleotide excision repair	4/47	0.013	RFC3;PCNA;RFC4;RPA3
	Adherens junction	5/72	0.014	CDC42;ACTN1;ACTB;TGFB2;FGFR1
	Longevity regulating pathway	6/102	0.015	HSPA8;HDAC2;ATF6B;HSPA2;CRYAB;HSPA1B
	Hepatitis B	8/163	0.015	CCNA2;PCNA;YWHAQ;ATF6B;YWHAB;VDAC3;BIRC5;TGFB2
	Estrogen signaling pathway	7/137	0.019	HSPA8;HSP90AA1;ATF6B;HSPA2;FKBP4;CALM1;HSPA1B
	RNA degradation	5/79	0.020	EXOSC6;EXOSC5;EXOSC10;LSM5;LSM3
	Drug metabolism	6/108	0.020	CDA;CYP2C9;RRM1;RRM2;UGT2B4;NME1
	Legionellosis	4/55	0.023	HSPA8;VCP;HSPA2;HSPA1B
	Glutathione metabolism	4/56	0.024	GPX2;RRM1;RRM2;ODC1
	Ribosome	7/153	0.032	RPS15;MRPS17;RPL24;MRPS7;MRPL13;MRPL32;MRPL11
	Hippo signaling pathway	7/160	0.040	PPP2CA;YWHAQ;YWHAB;ID1;BIRC5;ACTB;TGFB2
FoxO signaling pathway	6/132	0.050	CCNB1;HOMER2;PLK1;SKP2;KLF2;TGFB2	

T1: TFP 12 μ M, TS1: TFP 12 μ M – SFB 1 μ M; UP: upregulated, DOWN: downregulated genes. Fisher's exact test p-value: 4.01e-42

COPYRIGHTS AND PERMISSIONS

Figure 1.1 Drug development stages representing the expenses and amounts of screened compounds on each stage



Copyright Clearance Center RightsLink®

Home ? Email Support Sign In Create Account

Trends in Pharmacological Sciences
Artificial Intelligence for Clinical Trial Design
 Author: Stefan Harrer, Pratik Shah, Bhavna Antony, Jianying Hu
 Publication: Trends in Pharmacological Sciences
 Publisher: Elsevier
 Date: August 2019
 © 2019 The Author(s). Published by Elsevier Ltd.

Creative Commons Attribution-NonCommercial-No Derivatives License (CC BY NC ND)

This article is published under the terms of the Creative Commons Attribution-NonCommercial-No Derivatives License (CC BY NC ND). For non-commercial purposes you may copy and distribute the article, use portions or extracts from the article in other works, and text or data mine the article, provided you do not alter or modify the article without permission from Elsevier. You may also create adaptations of the article for your own personal use only, but not distribute these to others. You must give appropriate credit to the original work, together with a link to the formal publication through the relevant DOI, and a link to the Creative Commons user license above. If changes are permitted, you must indicate if any changes are made but not in any way that suggests the licensor endorses you or your use of the work.

Permission is not required for this non-commercial use. For commercial use please continue to request permission via Rightslink.

BACK CLOSE WINDOW

CC BY-NC-ND 4.0

Attribution-NonCommercial-NoDerivatives 4.0 International (CC BY-NC-ND 4.0)

This is a human-readable summary of (and not a substitute for) the license. [View full license](#)

You are free to:

- Share — copy and redistribute the material in any medium or format

The licensor cannot revoke these freedoms as long as you follow the license terms.

Under the following terms:

- Attribution** — You must give appropriate credit, provide a link to the license, and indicate if changes were made. You may do so in any reasonable manner, but not in any way that suggests the licensor endorses you or your use.
- NonCommercial** — You may not use the material for commercial purposes.
- NoDerivatives** — If you remix, transform, or build upon the material, you may not distribute the modified material.

No additional restrictions — You may not apply legal terms or technological measures that legally restrict others from doing anything the license permits.

Table 1.1 Molecular subtypes of BC and status of each molecular marker

Molecular subtypes	Estrogen receptor α (ERα)	Progesterone receptor (PgR)	Human epidermal growth factor receptor 2 (HER2)	Ki67
Luminal A	+	+/-	-	<14%
Luminal B	+	+/-	+/-	\geq 14%
HER2+	-	-	+	\geq 14%
TNBC	-	-	-	\geq 14%

Journal List > Cancer Manag Res > v.11, 2019 > PMC6612049



Cancer Manag Res. 2019; 11: 5765-5775. PMID: PMC6612049
 Published online 2019 Jun 28. doi: 10.2147/CMAR.S213663 PMID: 31303789

The prognosis comparison of different molecular subtypes of breast tumors after radiotherapy and the intrinsic reasons for their distinct radiosensitivity

Lin He,¹ Yang Lv,² Yuhua Song,¹ and Bijuan Zhang³

- Author information - Article notes - Copyright and License information [Disclaimer](#)

Copyright © 2019 He et al.

This work is published and licensed by Dove Medical Press Limited. The full terms of this license are available at <https://www.dovepress.com/terms.php> and incorporate the Creative Commons Attribution – Non Commercial (unported, v3.0) License (<http://creativecommons.org/licenses/by-nc/3.0/>). By accessing the work you hereby accept the Terms. Non-commercial uses of the work are permitted without any further permission from Dove Medical Press Limited, provided the work is properly attributed. For permission for commercial use of this work, please see paragraphs 4.2 and 5 of our Terms (<https://www.dovepress.com/terms.php>).

Cancer Manag Res

Attribution-NonCommercial 3.0 Unported (CC BY-NC 3.0)

This is a human-readable summary of (and not a substitute for) the license. [Disagree?](#)

You are free to:

- Share** — copy and redistribute the material in any medium or format.
- Adapt** — remix, transform, and build upon the material.

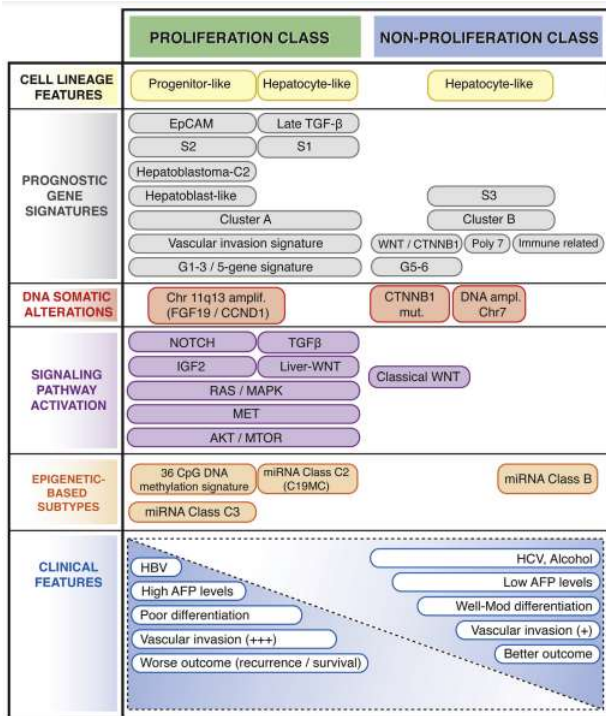
The licensor cannot revoke these freedoms as long as you follow the license terms.

Under the following terms:

- Attribution** — You must give appropriate credit, provide a link to the license, and indicate if changes were made. You may do so in any reasonable manner, but not in any way that suggests the licensor endorses you or your use.
- NonCommercial** — You may not use the material for commercial purposes.

No additional restrictions — You may not apply legal terms or technological measures that legally restrict others from doing anything the license permits.

Figure 1.2 Molecular classes and related histological and clinical features of HCCs.



RightsLink®

My Orders My Library My Profile Welcome murat.yaman@bilkent.edu.tr Log out Help

My Orders > Orders > All Orders

My Orders

Orders Billing History Payable Invoices

SEARCH

Order Number:

Date Range: From 4-Jun-2020 To 4-Sep-2020

View: All On Hold Response Required Pending Completed Canceled Denied Credited

Results: 1-1 of 1

Order Date	Article Title	Publication	Type Of Use	Price	Order Status	Expiration Date	Order Number
4-Sep-2020	Genetic Landscape and Biomarkers of Hepatocellular Carcinoma	Gastroenterology	reuse in a thesis/dissertation	0.00 \$	Completed		4901951483383

Authored publication [311]



RightsLink®



Home



Help



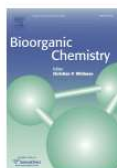
Email Support



Sign In



Create Account



Design, synthesis and anticancer/antiestrogenic activities of novel indole-benzimidazoles

Author: Fikriye Zengin Karadayi, Murat Yaman, Mehmet Murat Kislá, Ayse G. Keskus, Ozlen Konu, Zeynep Ates-Alagoz

Publication: Bioorganic Chemistry

Publisher: Elsevier

Date: July 2020

© 2020 Elsevier Inc. All rights reserved.

Please note that, as the author of this Elsevier article, you retain the right to include it in a thesis or dissertation, provided it is not published commercially. Permission is not required, but please ensure that you reference the journal as the original source. For more information on this and on your other retained rights, please visit: <https://www.elsevier.com/about/our-business/policies/copyright#Author-rights>

BACK

CLOSE WINDOW

For subscription articles	For open access articles
<p>Authors transfer copyright to the publisher as part of a journal publishing agreement, but have the right to:</p> <ul style="list-style-type: none">• Share their article for Personal Use, Internal Institutional Use and Scholarly Sharing purposes, with a DOI link to the version of record on ScienceDirect (and with the Creative Commons CC-BY-NC-ND license for author manuscript versions)• Retain patent, trademark and other intellectual property rights (including research data).• Proper attribution and credit for the published work.	<p>Authors sign an exclusive license agreement, where authors have copyright but license exclusive rights in their article to the publisher**. In this case authors have the right to:</p> <ul style="list-style-type: none">• Share their article in the same ways permitted to third parties under the relevant user license (together with Personal Use rights) so long as it contains a CrossMark logo, the end user license, and a DOI link to the version of record on ScienceDirect.• Retain patent, trademark and other intellectual property rights (including research data).• Proper attribution and credit for the published work.

*Please note that society or third party owned journals may have different publishing agreements. Please see the journal's guide for authors for journal specific copyright information.

This includes the right for the publisher to make and authorize **commercial use, please see "**Rights granted to Elsevier**" for more details.



Design, synthesis and anticancer/antiestrogenic activities of novel indole-benzimidazoles

Fikriye Zengin Karadayi^{a,1}, Murat Yaman^{c,1}, Mehmet Murat Kisla^{a,2}, Ayse G. Keskus^{c,2}, Ozlen Konu^{b,c,d,*}, Zeynep Ates-Alagoz^{a,*}

^a Department of Pharmaceutical Chemistry, Faculty of Pharmacy, Ankara University, 06100 Ankara, Turkey

^b Department of Molecular Biology and Genetics, Bilkent University, 06800 Ankara, Turkey

^c Interdisciplinary Program in Neuroscience, Bilkent University, 06800 Ankara, Turkey

^d UNAM-Institute of Materials Science and Nanotechnology, Bilkent University, 06800 Ankara, Turkey

ARTICLE INFO

InChIKeys:

NKANXQFJJICGDU-QPLCGJKRSA-N

GZUITABIAMVPG-UHFFFAOYSA-N

UCJGJABZCDBEDK-UHFFFAOYSA-N

Indole-benzimidazole

Molecular docking

Comparative transcriptomics

Estrogen signaling

ABSTRACT

Indole-benzimidazoles have recently gained attention due to their antiproliferative and antiestrogenic effects. However, their structural similarities and molecular mechanisms shared with selective estrogen receptor modulators (SERMs) have not yet been investigated. In this study, we synthesized novel ethylsulfonyl indole-benzimidazole derivatives by substituting the first (R₁) and fifth (R₂) positions of benzimidazole and indole groups, respectively. Subsequently, we performed ¹H NMR, ¹³C NMR, and Mass spectral and *in silico* docking analyses, and anticancer activity screening studies of these novel indole-benzimidazoles. The antiproliferative effects of indole-benzimidazoles were found to be more similar between the estrogen (E2) responsive cell lines MCF-7 and HEPG2 in comparison to the Estrogen Receptor negative (ER-) cell line MDA-MB-231. R₁:p-fluorobenzyl group members were selected as lead compounds for their potent anticancer effects and moderate structural affinity to ER. Microarray expression profiling and gene enrichment analyses (GSEA) of the selected compounds (R₁:p-fluorobenzyl: **48**, **49**, **50**, **51**; R₁:3,4-difluorobenzyl: **53**) helped determine the similarly modulated cellular signaling pathways among derivatives. Moreover, we identified known compounds that have significantly similar gene signatures to that of **51** via queries performed in LINCS database; and further transcriptomics comparisons were made using public GEO datasets (GSE35428, GSE7765, GSE62673). Our results strongly demonstrate that these novel indole-benzimidazoles can modulate ER target gene expression as well as dioxin-mediated aryl hydrocarbon receptor and amino acid deprivation-mediated integrated stress response signaling in a dose-dependent manner.

1. Introduction

Breast cancer, which is among the most prevalent cancer types affecting women all over the world, can be conventionally subtyped according to the presence of estrogen receptor (ER), progesterone receptor (PR), and/or human epidermal growth factor receptor 2 (HER2/ERBB2) activity. These subtypes possess differential characteristics regarding prognosis, incidence, therapeutic response and tumor aggressiveness. The heterogeneous nature and adverse effects associated with therapeutic targeting of such diverse and crucial pathways bring challenges into the therapy and hence makes the discovery of novel, more effective, and subtype specific anticancer molecules invaluable [1].

Estrogens (E2) play crucial roles in breast cancer development, consequently a considerable amount of research has been done either to block their synthesis or to modulate their activity [2]. Therefore, drugs that function as antiestrogens in mammary tissue have been frequently used for the treatment of hormone-dependent breast cancers. Nuclear receptors ER α and ER β , through E2 binding, take part in multiple cellular activities such as proliferation and differentiation. In addition, they can be found at an equilibrium [2–4] and differentially regulate their downstream elements upon exposure to selective estrogen receptor modulators (SERMs) [5]. Moreover, their expression levels differ among various tissues while the expression of ER α is tightly associated with breast cancer physiology [6] as well as prognosis of breast tumors

* Corresponding authors at: Department of Pharmaceutical Chemistry, Faculty of Pharmacy, Ankara University, 06100 Ankara, Turkey (Z. Ates-Alagoz), Department of Molecular Biology and Genetics, Bilkent University, 06800 Ankara, Turkey (O. Konu).

E-mail addresses: konu@fen.bilkent.edu.tr (O. Konu), zeynep.ates@pharmacy.ankara.edu.tr (Z. Ates-Alagoz).

¹ Equal contributors.

² Equal contributors.

<https://doi.org/10.1016/j.bioorg.2020.103929>

Received 27 March 2020; Received in revised form 6 May 2020; Accepted 8 May 2020

Available online 17 May 2020

0045-2068/ © 2020 Elsevier Inc. All rights reserved.

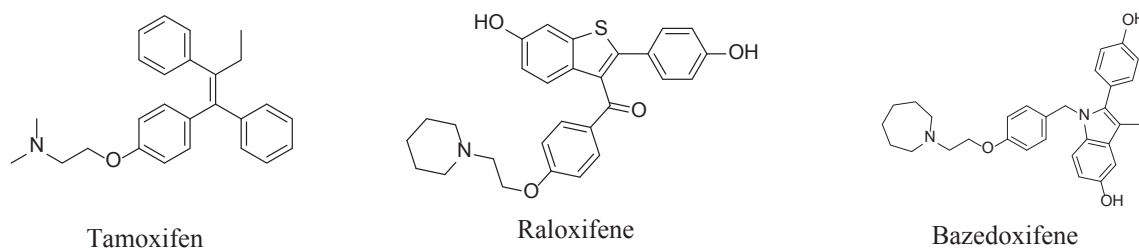
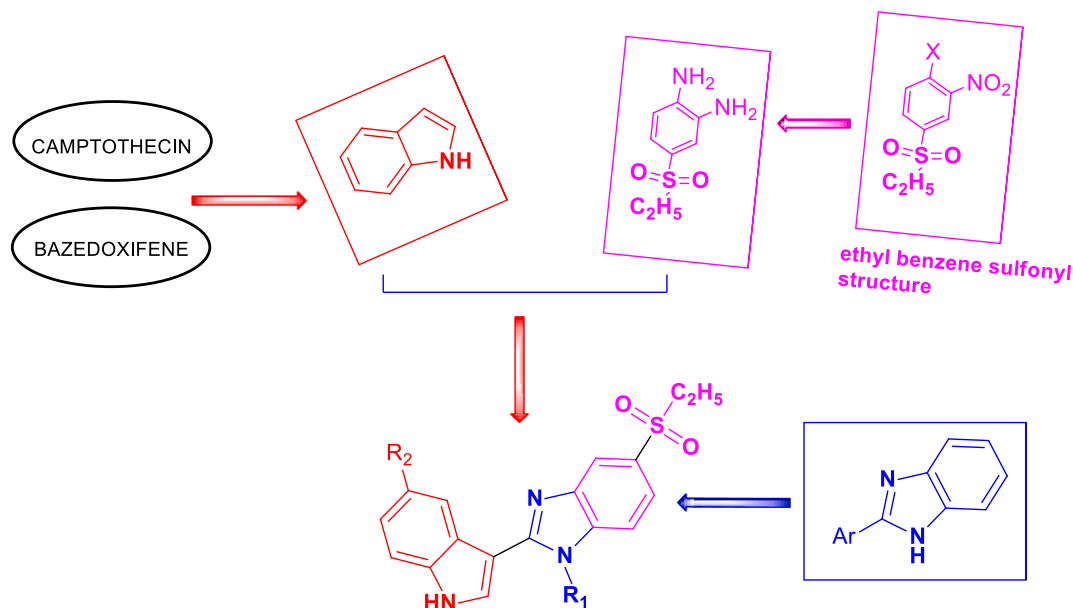


Fig. 1. Chemical structure of tamoxifen, raloxifene and bazedoxifene.



Scheme 1. Scheme showing previous studies and starting point of the new syntheses.

[7]. ER β on the other hand has been implicated in tumor suppression and breast carcinogenesis [8].

Multiple SERMs have been designed and assessed over the years for breast cancer treatment [9]. Moreover, ER α and ER β binding affinities and downstream effects of these SERMs might differ leading to variable outcomes [5,10,11]. Accordingly, tamoxifen (Fig. 1) belonging to the first generation of SERMs has been shown to significantly reduce the incidence of breast cancer. Raloxifene (Fig. 1) is a second-generation SERM exhibiting a role similar to tamoxifen yet it functions as a pure antagonist in the uterus and a partial agonist against tamoxifen-resistant breast cancers [12]. ICI 182780 acts antagonistically in ER positive (ER+) MCF-7 cells and can outperform raloxifene [13]. A third-generation SERM called bazedoxifene (Fig. 1) that has been introduced for the treatment of breast cancer and osteoporosis [14] is based on the pharmacophore of raloxifene. Indole based derivatives (bazedoxifene, melatonin and KB9520), as well as methyl and naphthyl-substituted benzimidazole derivatives also exhibit different modes of actions on breast cancer cell lines some of which could be through actions similar to SERMs [2,15–17]. Accordingly, a combination of affinity studies with toxicological approaches as well as molecular profiling could be highly beneficial to help identify more selective/effective breast cancer therapeutic agents [18–21].

Indole and benzimidazole rings, which are bioavailable molecules, constitute structures found in current drugs. These two ring structures are also isosteres of DNA bases that carry purine and pyrimidine cores, and they can as well be purine antimetabolites. For this reason, indole and benzimidazole rings are thought to interact easily with biopolymers in biosystems [22]. Benzimidazole and its derivatives are effective agents against cancer [23,24], inflammation [25] and oxidative stress [26,27] while also having antiviral [28] and antibacterial [28–30] effects. Indole core has already been used to obtain novel derivatives with

antiproliferative activity [31,32]. Aside from several crucial bioactive compounds (tryptophan, serotonin and melatonin), some of the anti-neoplastic compounds, such as vinblastine sulfate, vincristine sulfate, vinorelbine ditartrate and lanreotide carry indole ring systems [33]. In addition, phenyl-indole derivatives have been shown to inhibit breast cancer development through different mechanisms [34–36]. Similarly, recent studies on benzimidazoles reveal that different heterocycles at 2-position yield to potent anticancer agents for various carcinoma cell lines [37,38]. Furthermore, indole-benzimidazole hybrids have been designed and synthesized by fusing the indole nucleus with benzimidazole to develop novel selective ER modulators. These indole-benzimidazoles can represent novel potent ER α antagonist properties and provide promising insight into the discovery of novel SERMs for the management of breast cancer [39]. For instance, in our previous studies, we have discovered a small molecule with benzene sulfonyl structure exhibiting selectivity toward breast cancer cells while sparing normal surrounding cells [40]. Also, benzene sulfonyl structures have been shown to exhibit higher anticancer activity than doxorubicin in breast and prostate cancers [41,42]. However, the molecular mechanism of action of novel indole-benzimidazoles carrying benzene sulfonyl structures has not yet been assessed. Because of the above and the need for new compounds with better anticancer and anti-estrogenic properties, we designed, synthesized and tested a series of indole-benzimidazoles possessing ethylsulfonyl moiety (Scheme 1).

2. Material and methods

2.1. Chemistry

Melting points were determined with Buchi SMP-20 (BuchiLabortechnik, Flawil, Switzerland) and Electrotermal 9100

capillary melting point apparatus (Electrothermal, Essex, U.K.) and are uncorrected. The ^1H NMR spectra in $\text{DMSO}-d_6$ using Varian Mercury-400 FT-NMR spectrometer (Varian Inc., Palo Alto, CA, USA), and the Mass spectra based on ESI(+) method using Waters ZQ micromass LC-MS spectrometer (Waters Corporation, Milford, MA, USA) were recorded. For elemental analysis we used LECO 932 CHNS (Leco-932, St. Joseph, MI, USA) instrument. Silica gel 60 (40–63 mm particle size) was used for column chromatography.

2.1.1. General procedure for synthesis of 3–12

To a solution of 4-(ethylsulfonyl)-1-chloro-2-nitrobenzene (**2**) (5 mmol) in ethanol (5 mL), amine derivative (15 mmol) was added and heated under reflux, until the starting material was consumed (determined by TLC, 8–48 h). Upon cooling the mixture, water was added. The resultant yellow residue was crystallized from ethanol or purified by column chromatography (cc) by using a mixture of hexane and ethyl acetate in varying concentrations as eluent (Table 1) [43].

2.1.2. General procedure for synthesis of 13–22

Compounds **3–12** (3.5 mmol) in EtOH (75 mL) reduced by hydrogenation using 40 psi of H_2 and 10% Pd/C (40 mg) until cessation of H_2 uptake to obtain the catalyst before filtering off on a bed of celite and washing with EtOH; and concentrating the filtrate in vacuo [44]. The crude amine was used without purification (Table 1).

2.1.3. General procedure for synthesis of 23–59

A mixture of the appropriate o-phenylenediamine (1 mmol), related indole derivative (1 mmol) and $\text{Na}_2\text{S}_2\text{O}_5$ (40%) (2 mL) in EtOH (4 mL), was refluxed until starting materials were consumed (determined by TLC, 4–12 h). The precipitate was obtained upon pouring the reaction mixture and then filtering and washing. The residue was purified by column chromatography to give final product [45].

2.1.3.1. 5-(ethylsulfonyl)-2-(1H-indole-3-yl)-1H-benzo[d]imidazole (23). Compound **23** was prepared according to general methods starting from 4-ethylsulfonyl-benzene-1,2-diamine (1.35 mmol, 0.27 g) and indole-3-carboxaldehyde (1.35 mmol, 0.195 g). The residue was purified by cc using the mixture of ethyl acetate-hexane (1:1) as eluent to give a light yellow solid, m.p. 157 °C (0.058 g, 13% yield). ^1H NMR (400 MHz, $\text{DMSO}-d_6$): δ ppm 1.10 (t, 3H), 3.27 (q, 2H), 7.23 (dd, $J = 8.8$ Hz, $J = 2$ Hz, 1H), 7.53 (d, $J = 8.8$ Hz, 1H), 7.64 (m, 2H), 7.83–8.26 (m, 3H), 8.51 (d, $J = 1.6$ Hz, 1H), 11.91 (brd s, 1H, NH), 12.99 (brd d, 1H, NH). ^{13}C NMR (CD_3OD): 8.02, 52.02, 106.93, 113.20, 114.42, 121.25, 123.03, 124.36, 125.67, 127.47, 128.20, 129.74, 132.78, 132.90, 136.59, 136.96, 154.36. MS (ESI+) m/z : 326. $\text{C}_{17}\text{H}_{15}\text{N}_3\text{O}_2\text{S}\cdot 0.9\text{H}_2\text{O}$: C, 59.77; H, 4.95; N, 12.30; S, 9.38 and found C, 59.42; H, 5.23; N, 11.91; S, 9.10.

2.1.3.2. 2-(5-bromo-1H-indol-3-yl)-5-(ethylsulfonyl)-1H-benzo[d]imidazole (24). Compound **24** was prepared according to general methods starting from 4-ethylsulfonyl-benzene-1,2-diamine (0.87 mmol, 0.175 g) and 5-bromo-indole-3-carboxaldehyde (0.87 mmol, 0.195 g). The residue was purified by cc using the chloroform/ethyl acetate (1:1) as eluent to give a white solid, m.p. 192 °C (0.128 g, 36% yield). ^1H NMR (400 MHz, $\text{DMSO}-d_6$): δ ppm 1.11 (t, 3H), 3.29 (q, 2H), 7.37 (d, $J = 8.4$ Hz, 1H), 7.51 (d, $J = 8.8$ Hz, 1H), 7.63–7.71 (m, 2H), 7.88 (m, 1H), 8.27 (s, 1H), 8.68 (s, 1H), 11.97 (brd d, 1H, NH), 13.04 (brd d, 1H, NH). MS (ESI+) m/z : 404. Anal. calcd. For $\text{C}_{17}\text{H}_{14}\text{BrN}_3\text{O}_2\text{S}\cdot \text{H}_2\text{O}$: C, 48.35; H, 3.82; N, 9.95; S, 7.59 and found C, 48.16; H, 3.86; N, 9.68; S, 7.45.

2.1.3.3. 5-(ethylsulfonyl)-2-(1H-indol-3-yl)-1-methyl-1H-benzo[d]imidazole (25). Compound **25** was prepared according to general methods starting from N^1 -methyl-4-ethylsulfonyl-benzene-1,2-diamine (0.99 mmol, 0.211 g) and indole-3-carboxaldehyde (0.99 mmol, 0.143 g). The residue was purified by cc using the ethyl acetate/hexane (1:1) as

eluent to give a white solid, m.p. 273 °C (0.095 g, 28% yield). ^1H NMR (400 MHz, $\text{DMSO}-d_6$): δ ppm 1.11 (t, 3H), 3.31 (q, 2H), 4.06 (s, 3H), 7.19–7.28 (m, 2H), 7.54 (d, $J = 7.6$ Hz, 1H), 7.72 (dd, $J = 8.4$ Hz, $J = 2$ Hz, 1H), 7.84 (d, $J = 8.4$ Hz, 1H), 8.13 (d, $J = 1.6$ Hz, 1H), 8.20 (d, $J = 2.8$ Hz, 1H), 8.44 (d, $J = 7.6$ Hz, 1H), 11.93 (brd s, 1H, NH). ^{13}C NMR ($\text{DMSO}-d_6$): 7.43, 32.01, 49.77, 104.33, 110.39, 111.81, 118.21, 120.52, 120.61, 121.53, 122.54, 126.29, 127.76, 131.26, 136.08, 139.35, 142.54, 152.90. MS (ESI+) m/z : 340. Anal. calcd. For $\text{C}_{18}\text{H}_{17}\text{N}_3\text{O}_2\text{S}\cdot 0.3\text{H}_2\text{O}$: C, 62.69; H, 5.14; N, 12.18; S, 9.29 and found C, 62.57; H, 5.06; N, 12.21; S, 9.08.

2.1.3.4. 5-(ethylsulfonyl)-2-(5-methoxy-1H-indol-3-yl)-1-methyl-1H-benzo[d]imidazole (26). Compound **26** was prepared according to general methods starting from N^1 -methyl-4-ethylsulfonyl-benzene-1,2-diamine (0.92 mmol, 0.2197 g) and 5-methoxy-indole-3-carboxaldehyde (0.92 mmol, 0.161 g). The residue was purified by cc using the ethyl acetate/hexane (1:1) as eluent to give a light yellow solid, m.p. 198 °C (0.125 g, 37% yield). ^1H NMR (400 MHz, $\text{DMSO}-d_6$): δ ppm 1.11 (t, 3H), 3.30 (q, 2H), 3.82 (s, 3H), 4.05 (s, 3H), 6.90 (dd, $J = 8.8$ Hz, $J = 2$ Hz, 1H), 7.43 (d, $J = 8.8$ Hz, 1H), 7.71 (dd, $J = 8.4$ Hz, $J = 2$ Hz, 1H), 7.82 (d, $J = 8.4$ Hz, 1H), 7.97 (d, $J = 2.4$ Hz, 1H), 8.14 (d, $J = 2$ Hz, 1H), 8.15 (s, 1H), 11.80 (brd s, 1H, NH). ^{13}C NMR ($\text{DMSO}-d_6$): 7.44, 32.03, 49.77, 55.38, 103.24, 104.10, 110.30, 112.55, 112.69, 118.21, 120.55, 126.93, 128.08, 131.13, 131.19, 139.33, 142.53, 153.07, 154.53. MS (ESI+) m/z : 370. Anal. calcd. For $\text{C}_{19}\text{H}_{19}\text{N}_3\text{O}_3\text{S}$: C, 61.77; H, 5.18; N, 11.37; S, 8.67 and found C, 61.21; H, 5.43; N, 11.52; S, 8.63.

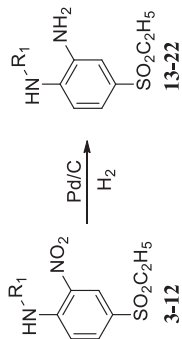
2.1.3.5. 2-(5-chloro-1H-indol-3-yl)-5-(ethylsulfonyl)-1-methyl-1H-benzo[d]imidazole (27). Compound **27** was prepared according to general methods starting from N^1 -methyl-4-ethylsulfonyl-benzene-1,2-diamine (1.15 mmol, 0.247 g) and 5-chloro-indole-3-carboxaldehyde (1.15 mmol, 0.206 g). The residue was purified by cc using the ethyl acetate/hexane (1:2) as eluent to give a light yellow solid, m.p. 264 °C (0.098 g, 23% yield). ^1H NMR (400 MHz, $\text{DMSO}-d_6$): δ ppm 1.11 (t, 3H), 3.32 (q, 2H), 4.07 (s, 3H), 7.26 (dd, $J = 8.8$ Hz, $J = 2.4$ Hz, 1H), 7.56 (d, $J = 8.4$ Hz, 1H), 7.72 (dd, $J = 8.4$ Hz, $J = 2$ Hz, 1H), 7.85 (d, $J = 8.8$ Hz, 1H), 8.17 (d, $J = 1.6$ Hz, 1H), 8.30 (s, 1H), 8.50 (d, $J = 2$ Hz, 1H). ^{13}C NMR ($\text{DMSO}-d_6$): 7.44, 32.02, 49.70, 104.08, 110.42, 113.58, 118.33, 120.69, 120.71, 122.53, 125.20, 127.47, 129.35, 131.37, 134.74, 139.27, 142.41, 152.34. MS (ESI+) m/z : 374. Anal. calcd. For $\text{C}_{18}\text{H}_{16}\text{ClN}_3\text{O}_2\text{S}\cdot 0.4\text{H}_2\text{O}$: C, 56.73; H, 4.44; N, 11.02; S, 8.41; Found: C, 56.48; H, 4.38; N, 11.02; S, 8.26.

2.1.3.6. 2-(5-bromo-1H-indol-3-yl)-5-(ethylsulfonyl)-1-methyl-1H-benzo[d]imidazole (28). Compound **28** was prepared according to general methods starting from N^1 -methyl-4-ethylsulfonyl-benzene-1,2-diamine (1.65 mmol, 0.228 g) and 5-bromo-indole-3-carboxaldehyde (1.65 mmol, 0.238 g). The residue was purified by cc using the ethyl acetate/hexane (1:1) as eluent to give a light yellow solid, m.p. 259 °C (0.052 g, 8% yield). ^1H NMR (400 MHz, $\text{DMSO}-d_6$): δ ppm 1.11 (t, 3H), 3.31 (q, 2H), 4.06 (s, 3H), 7.35 (d, $J = 8.4$ Hz, 1H), 7.54 (d, $J = 8$ Hz, 1H), 7.71 (d, $J = 8.8$ Hz, 1H), 7.83 (d, $J = 8.4$ Hz, 1H), 8.17 (s, 1H), 8.26 (s, 1H), 8.64 (s, 1H). ^{13}C NMR ($\text{DMSO}-d_6$): 7.54, 31.96, 49.72, 103.76, 110.30, 113.05, 114.14, 118.22, 120.59, 123.60, 124.81, 128.16, 129.38, 131.35, 135.22, 139.24, 142.43, 152.42. MS (ESI+) m/z : 418. Anal. calcd. For $\text{C}_{18}\text{H}_{16}\text{BrN}_3\text{O}_2\text{S}\cdot 0.35\text{H}_2\text{O}$: C, 50.91; H, 3.96; N, 9.89; S, 7.55; Found: C, 50.85; H, 3.94; N, 10.27; S, 7.45.

2.1.3.7. 1-ethyl-5-(ethylsulfonyl)-2-(1H-indol-3-yl)-1H-benzo[d]imidazole (29). Compound **29** was prepared according to general methods starting from N^1 -ethyl-4-ethylsulfonyl-benzene-1,2-diamine (1 mmol, 0.240 g) and indole-3-carboxaldehyde (1 mmol, 0.152 g). The residue was purified by cc using the ethyl acetate/metanol (4:0.5) as eluent to give a white solid, m.p. 254 °C (0.130 g, 37% yield). ^1H NMR (400 MHz, $\text{DMSO}-d_6$): δ ppm 1.13 (t, 3H), 1.42 (t, 3H), 3.32 (q, 2H), 4.56 (q, 2H), 7.19–7.28 (m, 2H), 7.54 (d, $J = 8$ Hz, 1H), 7.73 (dd, $J = 8.4$ Hz,

Table 1
Physicochemical data for compounds 3–22.

Comp.	R ₁	¹ H NMR	M.p. (°C)	Yield %	Comp.	Mass
3	-H	1.29 (t, 3H), 3.11 (q, 2H), 6.96 (d, J = 9.2 Hz, 1H), 7.77 (dd, J = 9.2 Hz, J = 2 Hz, 1H), 8.68 (d, J = 2 Hz, 1H).	143	88	13	201
4	-CH ₃	1.12 (t, 3H), 3.03 (d, 3H), 3.28 (q, 2H), 7.18 (d, J = 8.8 Hz, 1H), 7.89 (dd, J = 9 Hz, J = 2.4 Hz, 1H), 8.45 (d, J = 2 Hz, 1H), 8.68 (d, 1H, NH).	138	83	14	215
5	-C ₂ H ₅	1.09 (t, 3H), 1.2 (t, 3H), 1.64 (m, 2H), 3.25 (q, 2H), 3.46 (m, 2H), 7.22 (d, J = 8.8 Hz, 1H), 7.83 (dd, J = 9.2 Hz, J = 2.4 Hz, 1H), 8.42 (d, J = 1.6 Hz, 1H), 8.59 (t, 1H, NH).	125	84	15	229
6	-C ₆ H ₇	0.94 (t, 3H), 1.12 (t, 3H), 1.64 (m, 2H), 3.28 (q, 2H), 3.40 (q, 2H), 7.25 (d, J = 9.2 Hz, 1H), 7.84 (dd, J = 9.2 Hz, J = 2.4 Hz, 1H), 8.44 (d, J = 2.4 Hz, 1H), 8.61 (t, 1H, NH).	90	81	16	243
7	-C ₄ H ₉	0.92 (t, 3H), 1.11 (t, 3H), 1.38 (m, 2H), 1.61 (m, 2H), 3.26 (q, 2H), 3.44 (q, 2H), 7.25 (d, J = 8.8 Hz, 1H), 7.85 (dd, J = 8.8 Hz, J = 2 Hz, 1H), 8.44 (d, J = 2 Hz, 1H), 8.60 (t, 1H, NH).	76	82	17	257
8	-cyclohexyl	1.11 (t, 3H), 1.26 (m, 1H), 1.43 (m, 4H), 1.61 (d, 1H), 1.71 (m, 2H), 1.95 (m, 2H), 3.27 (q, 2H), 3.75 (m, 1H), 7.34 (d, J = 9.6 Hz, 1H), 7.85 (dd, J = 9.2 Hz, J = 2.4 Hz, 1H), 8.32 (d, J = 8 Hz, 1H), 8.55 (d, J = 2.4 Hz, 1H).	154	80	18	283
9	-benzyl	1.09 (t, 3H), 3.25 (q, 2H), 4.72 (d, 2H), 7.10 (d, J = 9.2 Hz, 1H), 7.30 (m, 5H), 7.79 (dd, J = 9.4 Hz, J = 2.4 Hz, 1H), 8.47 (d, J = 2 Hz, 1H), 9.18 (t, 1H, NH).	120	75	19	291
10	-p-fluorobenzyl	1.08 (t, 3H), 3.26 (q, 2H), 4.70 (d, 2H), 7.09 (d, J = 9.2 Hz, 1H), 7.17 (m, 2H), 7.43 (m, 2H), 7.79 (dd, J = 9.2 Hz, J = 1.6 Hz, 1H), 8.46 (d, J = 2.4 Hz, 1H), 9.19 (t, 1H, NH).	114	73	20	309
11	-3,4-difluorobenzyl	1.08 (t, 3H), 3.26 (q, 2H), 4.70 (d, 2H), 7.07 (d, J = 9.2 Hz, 1H), 7.25 (m, 1H), 7.37–7.52 (m, 2H), 7.79 (dd, J = 9.2 Hz, J = 2 Hz, 1H), 8.46 (d, J = 2.4 Hz, 1H), 9.20 (t, 1H, NH).	121	71	21	357
12	-3,4-dichlorobenzyl	1.28 (t, 3H), 3.09 (q, 2H), 4.58 (d, 2H), 6.85 (d, J = 8.8 Hz, 1H), 7.18 (dd, J = 8 Hz, J = 1.2 Hz, 1H), 7.43 (m, 2H), 7.80 (dd, J = 9 Hz, J = 2 Hz, 1H), 8.73 (d, J = 2 Hz, 1H), 8.79 (t, 1H, NH).	145	76	22	390



$J = 1.6$ Hz, 1H), 7.86 (d, $J = 8.8$ Hz, 1H), 8.09 (d, $J = 1.6$ Hz, 1H), 8.15 (d, $J = 1.6$ Hz, 1H), 8.40 (d, $J = 8$ Hz, 1H), 11.90 (brd s, 1H, NH). ^{13}C NMR (DMSO- d_6): 7.36, 14.61, 49.69, 104.04, 110.39, 111.79, 118.30, 120.43, 120.70, 121.44, 122.46, 126.35, 126.73, 131.40, 136.04, 138.33, 142.65, 151.89. MS (ESI+) m/z : 354. Anal. calcd. For $\text{C}_{19}\text{H}_{19}\text{N}_3\text{O}_2\text{S}$: C, 64.57; H, 5.41; N, 11.88; S, 9.07; Found: C, 64.67; H, 5.14; N, 11.57; S, 8.84.

2.1.3.8. 1-ethyl-5-(ethylsulfonyl)-2-(5-methoxy-1H-indol-3-yl)-1H-benzo[d]imidazole (30). Compound 30 was prepared according to general methods starting from N^1 -ethyl-4-ethylsulfonylbenzene-1,2-diamine (1.22 mmol, 0.280 g) and 5-methoxy-indole-3-carboxaldehyde (1.22 mmol, 0.214 g). The residue was purified by cc using the ethyl acetate as eluent to give a light yellow solid, m.p. 249 °C (0.165 g, 36% yield). ^1H NMR (400 MHz, DMSO- d_6): δ ppm 1.12 (t, 3H), 1.41 (t, 3H), 3.30 (q, 2H), 3.82 (s, 3H), 4.55 (q, 2H), 6.90 (dd, $J = 8.8$ Hz, $J = 2.4$ Hz, 1H), 7.43 (d, $J = 8.8$ Hz, 1H), 7.71 (dd, $J = 8.8$ Hz, $J = 1.6$ Hz, 1H), 7.85 (d, $J = 8.8$ Hz, 1H), 7.95 (d, $J = 2.4$ Hz, 1H), 8.04 (d, $J = 3.2$ Hz, 1H), 8.15 (d, $J = 1.6$ Hz, 1H), 11.76 (brd d, 1H, NH). ^{13}C NMR (DMSO- d_6): 7.43, 14.66, 49.76, 55.35, 103.19, 103.87, 110.37, 112.57, 112.72, 118.36, 120.71, 127.05, 127.13, 131.14, 131.41, 138.39, 142.69, 152.13, 154.52. MS (ESI+) m/z : 384. Anal. calcd. For $\text{C}_{20}\text{H}_{21}\text{N}_3\text{O}_3\text{S}$: C, 60.10; H, 5.74; N, 10.51; S, 8.02; Found: C, 60.05; H, 5.75; N, 10.12; S, 7.85;

2.1.3.9. 2-(5-chloro-1H-indol-3-yl)-1-ethyl-5-(ethylsulfonyl)-1H-benzo[d]imidazole (31). Compound 31 was prepared according to general methods starting from N^1 -ethyl-4-ethylsulfonylbenzene-1,2-diamine (1.5 mmol, 0.342 g) and 5-chloro-indole-3-carboxaldehyde (1.5 mmol, 0.269 g). The residue was purified by cc using the ethyl acetate as eluent to give a light yellow solid, m.p. 280 °C (0.273 g, 47% yield). ^1H NMR (400 MHz, DMSO- d_6): δ ppm 1.10 (t, 3H), 1.40 (t, 3H), 3.29 (q, 2H), 4.55 (q, 2H), 7.25 (dd, $J = 8.8$ Hz, $J = 2$ Hz, 1H), 7.54 (d, $J = 7.6$ Hz, 1H), 7.71 (dd, $J = 8.4$ Hz, $J = 1.6$ Hz, 1H), 7.84 (d, $J = 8$ Hz, 1H), 8.17 (t, 2H), 8.47 (d, $J = 2$ Hz, 1H), 12.07 (brd s, 1H, NH). ^{13}C NMR (DMSO- d_6): 7.41, 14.63, 49.69, 103.92, 110.46, 113.50, 118.51, 120.79, 120.88, 122.62, 125.28, 127.57, 128.29, 131.62, 134.63, 138.34, 142.57, 151.31. MS (ESI+) m/z : 388. Anal. calcd. For $\text{C}_{19}\text{H}_{18}\text{ClN}_3\text{O}_2\text{S}$: C, 58.83; H, 4.67; N, 10.83; S, 8.26; Found: C, 58.56; H, 4.67; N, 10.64; S, 8.13.

2.1.3.10. 2-(5-bromo-1H-indol-3-yl)-1-ethyl-5-(ethylsulfonyl)-1H-benzo[d]imidazole (32). Compound 32 was prepared according to general methods starting from N^1 -ethyl-4-ethylsulfonylbenzene-1,2-diamine (1.8 mmol, 0.406 g) and 5-bromo-indole-3-carboxaldehyde (1.8 mmol, 0.401 g). The residue was purified by cc using the ethyl acetate as eluent to give a light yellow solid, m.p. 288 °C (0.370 g, 48% yield). ^1H NMR (400 MHz, DMSO- d_6): δ ppm 1.10 (t, 3H), 1.40 (t, 3H), 3.29 (q, 2H), 4.55 (q, 2H), 7.36 (dd, $J = 8.8$ Hz, $J = 2$ Hz, 1H), 7.50 (d, $J = 9.2$ Hz, 1H), 7.71 (dd, $J = 8.4$ Hz, $J = 1.6$ Hz, 1H), 7.84 (d, $J = 8.4$ Hz, 1H), 8.17 (t, 2H), 8.62 (d, $J = 2$ Hz, 1H), 12.08 (brd s, 1H, NH). ^{13}C NMR (DMSO- d_6): 7.36, 14.57, 49.63, 103.74, 110.40, 113.23, 113.89, 118.47, 120.84, 123.74, 125.10, 128.06, 128.14, 131.57, 134.81, 138.28, 142.50, 151.22. MS (ESI+) m/z : 434. Anal. calcd. For $\text{C}_{19}\text{H}_{18}\text{BrN}_3\text{O}_2\text{S}$: C, 52.78; H, 4.19; N, 9.71; S, 7.41; Found: C, 52.48; H, 3.98; N, 9.58; S, 7.39.

2.1.3.11. 5-(ethylsulfonyl)-2-(1H-indol-3-yl)-1-propyl-1H-benzo[d]imidazole (33). Compound 33 was prepared according to general methods starting from N^1 -(propyl)-4-ethylsulfonylbenzene-1,2-diamine (1.04 mmol, 0.253 g) and indole-3-carboxaldehyde (1.04 mmol, 0.152 g). The residue was purified by cc using the chloroform/ethyl acetate/hexane (2:1:1) as eluent to give a white solid, m.p. 182 °C (0.199 g, 52% yield). ^1H NMR (400 MHz, DMSO- d_6): δ ppm 0.89 (t, 3H), 1.13 (t, 3H), 1.78–1.84 (m, 2H), 3.32 (q, 2H), 4.49 (t, 2H), 7.18–7.27 (m, 2H), 7.53–7.55 (m, 1H), 7.72 (dd,

$J = 8.4$ Hz, $J = 1.6$ Hz, 1H), 7.78 (d, $J = 8.8$ Hz, 1H), 8.07 (s, 1H), 8.14 (d, $J = 1.6$ Hz, 1H), 8.39 (m, 1H), 11.85 (brd s, 1H). ^{13}C NMR (DMSO- d_6): 7.40, 10.92, 22.36, 45.57, 49.74, 104.24, 110.73, 111.85, 118.37, 120.48, 120.71, 121.46, 122.49, 126.45, 126.75, 131.43, 136.05, 138.91, 142.55, 152.20. MS (ESI+) m/z : 368. Anal. calcd. For $\text{C}_{20}\text{H}_{21}\text{N}_3\text{O}_2\text{S}$: C, 65.22; H, 6.03; N, 11.54; S, 8.68; Found: C, 65.37; H, 5.76; N, 11.44; S, 8.72.

2.1.3.12. 5-(ethylsulfonyl)-2-(5-methoxy-1H-indol-3-yl)-1-propyl-1H-benzo[d]imidazole (34). Compound 34 was prepared according to general methods starting from N^1 -(propyl)-4-ethylsulfonylbenzene-1,2-diamine (1.06 mmol, 0.258 g) and 5-methoxy-indole-3-carboxaldehyde (1.06 mmol, 0.187 g). The residue was purified by cc using the chloroform/ethyl acetate/hexane (2:1:1) as eluent to give a white solid, m.p. 159 °C (0.175 g, 41% yield). ^1H NMR (400 MHz, DMSO- d_6): δ ppm 0.90 (t, 3H), 1.13 (t, 3H), 1.79–1.84 (m, 2H), 3.32 (q, 2H), 3.82 (s, 3H), 4.48 (t, 2H), 6.90 (dd, $J = 8.4$ Hz, $J = 2.4$ Hz, 1H), 7.44 (d, $J = 8.4$ Hz, 1H), 7.71 (dd, $J = 8.8$ Hz, $J = 1.6$ Hz, 1H), 7.87 (d, $J = 8.8$ Hz, 1H), 7.95 (d, $J = 2.4$ Hz, 1H), 8.02 (d, $J = 2.8$ Hz, 1H), 8.15 (d, $J = 2$ Hz, 1H) 11.8 (brd s, 1H). ^{13}C NMR (DMSO- d_6): 7.40, 10.93, 22.34, 45.57, 49.73, 55.35, 103.20, 103.99, 110.62, 112.55, 112.67, 118.35, 120.66, 127.08, 131.08, 131.36, 138.91, 142.51, 152.36, 154.51. MS (ESI+) m/z : 398. Anal. calcd. For $\text{C}_{21}\text{H}_{23}\text{N}_3\text{O}_3\text{S}$: C, 63.46; H, 5.83; N, 10.57; S, 8.07; Found: C, 63.18; H, 5.99; N, 10.50; S, 7.93.

2.1.3.13. 5-(ethylsulfonyl)-2-(5-chloro-1H-indol-3-yl)-1-propyl-1H-benzo[d]imidazole (35). Compound 35 was prepared according to general methods starting from N^1 -(propyl)-4-ethylsulfonylbenzene-1,2-diamine (0.82 mmol, 0.199 g) and 5-chloro-indole-3-carboxaldehyde (0.82 mmol, 0.147 g). The residue was purified by cc using the chloroform/ethyl acetate/hexane (2:1:1) as eluent to give a white solid, m.p. 232 °C (0.050 g, 15% yield). ^1H NMR (400 MHz, DMSO- d_6): δ ppm 0.88 (t, 3H), 1.10 (t, 3H), 1.76–1.82 (m, 2H), 3.30 (q, 2H), 4.48 (t, 2H), 7.24 (dd, $J = 8.8$ Hz, $J = 2$ Hz, 1H), 7.54 (d, $J = 8.8$ Hz, 1H), 7.70 (dd, $J = 8.8$ Hz, $J = 1.6$ Hz, 1H), 7.86 (d, $J = 8.4$ Hz, 1H), 8.15–8.17 (m, 2H), 8.46 (d, $J = 2$ Hz, 1H), 12.03 (brd s, 1H). ^{13}C NMR (DMSO- d_6): 7.34, 10.87, 22.30, 45.48, 49.60, 103.97, 110.69, 113.45, 118.46, 120.71, 120.78, 122.54, 125.20, 127.56, 128.19, 131.50, 134.51, 138.82, 142.34, 151.49. MS (ESI+) m/z : 402. Anal. calcd. For $\text{C}_{20}\text{H}_{20}\text{ClN}_3\text{O}_2\text{S}$: C, 59.77; H, 5.02; N, 10.46; S, 7.98; Found: C, 59.85; H, 5.20; N, 10.54; S, 7.77.

2.1.3.14. 5-(ethylsulfonyl)-2-(5-bromo-1H-indol-3-yl)-1-propyl-1H-benzo[d]imidazole (36). Compound 36 was prepared according to general methods starting from N^1 -(propyl)-4-ethylsulfonylbenzene-1,2-diamine (1.11 mmol, 0.269 g) and 5-bromo-indole-3-carboxaldehyde (1.11 mmol, 0.249 g). The residue was purified by cc using the chloroform/ethyl acetate/hexane (2:1:1) as eluent to give a white solid, m.p. 234 °C (0.079 g, 16% yield). ^1H NMR (400 MHz, DMSO- d_6): δ ppm 0.87 (t, 3H), 1.11 (t, 3H), 1.76–1.82 (m, 2H), 3.29 (q, 3H), 4.47 (t, 2H) 7.35 (d, $J = 8$ Hz, 1H), 7.49 (d, $J = 8.8$ Hz, 1H), 7.7 (d, $J = 8.4$ Hz, 1H), 7.84 (d, $J = 8.4$ Hz, 1H), 8.11 (s, 1H), 8.16 (s, 1H), 8.6 (s, 1H), 11.98 (brd s, 1H). ^{13}C NMR (DMSO- d_6): 7.39, 10.92, 22.35, 45.54, 49.66, 103.93, 110.76, 113.28, 113.95, 118.52, 120.85, 123.77, 125.14, 128.09, 128.24, 131.59, 134.81, 138.87, 142.40, 151.52. MS (ESI+) m/z : 446. Anal. calcd. For $\text{C}_{20}\text{H}_{20}\text{BrN}_3\text{O}_2\text{S}$: C, 53.81; H, 4.51; N, 9.41; S, 7.18; Found: C, 53.26; H, 4.51; N, 9.56; S, 6.98.

2.1.3.15. 5-(ethylsulfonyl)-2-(1H-indol-3-yl)-1-butyl-1H-benzo[d]imidazole (37). Compound 37 was prepared according to general methods starting from N^1 -(butyl)-4-ethylsulfonylbenzene-1,2-diamine (0.89 mmol, 0.228 g) and indole-3-carboxaldehyde (0.89 mmol, 0.129 g). The residue was purified by cc using the chloroform/ethyl acetate/hexane (2:1:1) as eluent to give a white solid, m.p. 177 °C

(0.044 g, 13% yield). $^1\text{H NMR}$ (400 MHz, $\text{DMSO}-d_6$): δ ppm 0.82 (t, 3H), 1.10 (t, 3H), 1.29 (m, 2H), 1.71–1.75 (m, 2H), 3.30 (q, 2H), 4.50 (t, 2H), 7.15–7.24 (m, 2H), 7.51 (d, $J = 7.6$ Hz, 1H), 7.70 (dd, $J = 8.8$ Hz, $J = 1.6$ Hz, 1H), 7.85 (d, $J = 8.4$ Hz, 1H), 8.06 (d, $J = 2.4$ Hz, 1H), 8.12 (d, $J = 1.6$ Hz, 1H), 8.34 (d, $J = 8$ Hz, 1H), 11.84 (brd s, 1H). $^{13}\text{C NMR}$ ($\text{DMSO}-d_6$): 7.33, 13.42, 19.31, 31.02, 43.90, 49.65, 104.16, 110.62, 111.79, 118.31, 120.41, 120.67, 121.36, 122.43, 126.36, 126.71, 131.35, 135.96, 138.77, 142.50, 152.10. **MS** (ESI+) m/z : 382. **Anal. calcd.** For $\text{C}_{21}\text{H}_{23}\text{N}_3\text{O}_2\text{S}\cdot 0.2\text{H}_2\text{O}$: C, 65.49; H, 6.12; N, 10.91; S, 8.30; Found: C, 65.20; H, 6.11; N, 11.10; S, 8.30.

2.1.3.16. 5-(ethylsulfonyl)-2-(5-chloro-1H-indol-3-yl)-1-butyl-1H-benzo[d]imidazole (38). Compound **38** was prepared according to general methods starting from N^1 -(butyl)-4-ethylsulfonyl-benzene-1,2-diamine (1.08 mmol, 0.277 g) and 5-chloro-indole-3-carboxaldehyde (1.08 mmol, 0.194 g). The residue was purified by cc using the chloroform/ethyl acetate/hexane (2:1:1) as eluent to give a white solid, m.p. 221 °C (0.065 g, 14% yield). $^1\text{H NMR}$ (400 MHz, $\text{DMSO}-d_6$): δ ppm 0.87 (t, 3H), 1.13 (t, 3H), 1.32–1.37 (m, 2H), 1.75–1.79 (m, 2H), 3.30 (q, 2H), 4.51 (t, 2H), 7.28 (dd, $J = 8.4$ Hz, $J = 2.4$ Hz, 1H), 7.58 (d, $J = 8.4$ Hz, 1H), 7.74 (dd, $J = 8.4$ Hz, $J = 2$ Hz, 1H), 7.88 (d, $J = 8.8$ Hz, 1H), 8.2 (s, 2H), 8.48 (d, $J = 2.4$ Hz, 1H), 12.08 (brd s, 1H). $^{13}\text{C NMR}$ ($\text{DMSO}-d_6$): 7.45, 13.58, 19.44, 31.14, 44.01, 49.69, 104.05, 110.76, 113.57, 118.57, 120.78, 120.90, 122.65, 125.31, 127.63, 128.33, 131.59, 134.60, 138.84, 142.45, 151.55. **MS** (ESI+) m/z : 416. **Anal. calcd.** For $\text{C}_{21}\text{H}_{22}\text{ClN}_3\text{O}_2\text{S}$: C, 60.64; H, 5.33; N, 10.10; S, 7.71; Found: C, 60.23; H, 5.37; N, 10.38; S, 7.62.

2.1.3.17. 5-(ethylsulfonyl)-2-(5-bromo-1H-indol-3-yl)-1-butyl-1H-benzo[d]imidazole (39). Compound **39** was prepared according to general methods starting from N^1 -(butyl)-4-ethylsulfonyl-benzene-1,2-diamine (0.86 mmol, 0.220 g) and 5-bromo-indole-3-carboxaldehyde (0.86 mmol, 0.194 g). The residue was purified by cc using the chloroform/ethyl acetate/hexane (2:2:1) as eluent to give a white solid, m.p. 235 °C (0.040 g, 10% yield). $^1\text{H NMR}$ (400 MHz, $\text{DMSO}-d_6$): δ ppm 0.86 (t, 3H), 1.13 (t, 3H), 1.30–1.39 (m, 2H), 1.73–1.80 (m, 2H), 3.33 (q, 2H), 4.54 (t, 2H), 7.38 (dd, $J = 8.8$ Hz, $J = 1.6$ Hz, 1H), 7.53 (d, $J = 8.4$ Hz, 1H), 7.78 (dd, $J = 8.4$ Hz, $J = 1.6$ Hz, 1H), 7.88 (d, $J = 8.8$ Hz, 1H), 8.17 (s, 1H), 8.2 (d, $J = 1.6$ Hz, 1H), 8.62 (d, $J = 2$ Hz, 1H), 12.06 (brd s, 1H). $^{13}\text{C NMR}$ ($\text{DMSO}-d_6$): 7.40, 13.52, 19.39, 31.09, 43.98, 49.66, 103.92, 110.72, 113.28, 113.96, 118.54, 120.86, 123.73, 125.14, 128.11, 128.23, 131.59, 134.81, 138.79, 142.42, 151.48. **MS** (ESI+) m/z : 460. **Anal. calcd.** For $\text{C}_{21}\text{H}_{22}\text{BrN}_3\text{O}_2\text{S}$: C, 54.78; H, 4.81; N, 9.12; S, 6.96; Found: C, 54.28; H, 4.67; N, 9.51; S, 6.96.

2.1.3.18. 1-cyclohexyl-5-(ethylsulfonyl)-2-(1H-indol-3-yl)-1H-benzo[d]imidazole (40). Compound **40** was prepared according to general methods starting from N^1 -cyclohexyl-4-ethylsulfonyl-benzene-1,2-diamine (0.94 mmol, 0.265 g) and indole-3-carboxaldehyde (0.94 mmol, 0.136 g). The residue was purified by cc using the chloroform/ethyl acetate (1:1) as eluent to give a light yellow solid, m.p. 250 °C (0.263 g, 69% yield). $^1\text{H NMR}$ (400 MHz, $\text{DMSO}-d_6$): δ ppm 1.14 (t, 3H), 1.32–1.43 (m, 3H), 1.66 (d, 1H), 1.85–1.98 (m, 4H), 2.29–2.37 (m, 2H), 3.30 (q, 2H), 4.62–4.68 (m, 1H), 7.15–7.26 (m, 2H), 7.55 (d, $J = 8.4$ Hz, 1H), 7.68 (dd, $J = 8.8$ Hz, $J = 1.6$ Hz, 1H), 7.84 (d, $J = 2.8$ Hz, 1H), 7.97 (d, $J = 8$ Hz, 1H), 8.10 (d, $J = 8.8$ Hz, 1H), 8.14 (d, $J = 1.6$ Hz, 1H), 11.79 (brd s, 1H, NH). $^{13}\text{C NMR}$ ($\text{DMSO}-d_6$): 7.28, 24.32, 25.47, 30.49, 49.70, 56.58, 104.18, 111.96, 113.11, 118.84, 120.12, 120.29, 122.27, 126.46, 127.13, 131.29, 136.05, 136.85, 143.42, 152.21. **MS** (ESI+) m/z : 408. **Anal. calcd.** For $\text{C}_{23}\text{H}_{25}\text{N}_3\text{O}_2\text{S}\cdot 0.3\text{H}_2\text{O}$: C, 66.89; H, 6.25; N, 10.18; S, 7.74; Found: C, 66.57; H, 5.95; N, 9.94; S, 7.97.

2.1.3.19. 1-cyclohexyl-5-(ethylsulfonyl)-2-(5-methoxy-1H-indol-3-yl)-1H-

benzo[d]imidazole (41). Compound **41** was prepared according to general methods starting from N^1 -cyclohexyl-4-ethylsulfonyl-benzene-1,2-diamine (1.05 mmol, 0.297 g) and 5-methoxy-indole-3-carboxaldehyde (1.05 mmol, 0.184 g). The residue was purified by cc using the chloroform/ethyl acetate (1:1) as eluent to give a light yellow solid, m.p. 163 °C (0.061 g, 13% yield). $^1\text{H NMR}$ (400 MHz, $\text{DMSO}-d_6$): δ ppm 1.13 (t, 3H), 1.32–1.44 (m, 3H), 1.66 (d, 1H), 1.85–1.98 (m, 4H), 2.30–2.36 (m, 2H), 3.31 (q, 2H), 3.77 (s, 3H), 4.60–4.66 (m, 1H), 6.89 (dd, $J = 8.8$ Hz, $J = 2.4$ Hz, 1H), 7.45 (m, 2H), 7.67 (dd, $J = 8.8$ Hz, $J = 1.6$ Hz, 1H), 7.79 (d, $J = 2.8$ Hz, 1H), 8.09 (d, $J = 8.8$ Hz, 1H), 8.14 (d, $J = 1.6$ Hz, 1H), 11.68 (brd s, 1H, NH). $^{13}\text{C NMR}$ ($\text{DMSO}-d_6$): 7.37, 14.04, 24.38, 25.56, 30.55, 49.72, 55.24, 56.63, 59.71, 101.51, 104.01, 112.74, 112.82, 113.17, 118.88, 120.31, 126.95, 127.66, 131.10, 131.25, 136.92, 143.49, 152.45, 154.43. **MS** (ESI+) m/z : 438. **Anal. calcd.** For $\text{C}_{24}\text{H}_{27}\text{N}_3\text{O}_3\text{S}\cdot 0.9\text{H}_2\text{O}$: C, 63.52; H, 6.40; N, 9.26; S, 7.05; Found: C, 63.60; H, 6.40; N, 8.86; S, 6.81.

2.1.3.20. 2-(5-chloro-1H-indol-3-yl)-1-cyclohexyl-5-(ethylsulfonyl)-1H-benzo[d]imidazole (42). Compound **42** was prepared according to general methods starting from N^1 -cyclohexyl-4-ethylsulfonyl-benzene-1,2-diamine (1.12 mmol, 0.315 g) and 5-chloro-indole-3-carboxaldehyde (1.12 mmol, 0.200 g). The residue was purified by cc using the chloroform/ethyl acetate (2:1) as eluent to give a white solid, m.p. 182 °C (0.201 g, 41% yield). $^1\text{H NMR}$ (400 MHz, $\text{DMSO}-d_6$): δ ppm 1.14 (t, 3H), 1.38–1.43 (m, 3H), 1.67–2.00 (m, 5H), 2.30–2.35 (m, 2H), 3.33 (q, 2H), 4.63–4.69 (m, 1H), 7.26 (dd, $J = 8.8$ Hz, $J = 2$ Hz, 1H), 7.59 (d, $J = 9.2$ Hz, 1H), 7.71–7.73 (m, 1H), 7.98 (d, $J = 2$ Hz, 1H), 8.05 (d, $J = 1.6$ Hz, 1H), 8.14–8.19 (m, 2H), 12.06 (brd s, 1H, NH). $^{13}\text{C NMR}$ ($\text{DMSO}-d_6$): 7.35, 24.33, 25.43, 30.42, 49.65, 56.94, 103.06, 113.64, 113.78, 118.48, 119.64, 120.88, 122.60, 125.31, 127.56, 129.22, 131.93, 134.68, 136.47, 141.93, 151.22. **MS** (ESI+) m/z : 442. **Anal. calcd.** For $\text{C}_{23}\text{H}_{24}\text{ClN}_3\text{O}_2\text{S}$: C, 62.50; H, 5.47; N, 9.51; S, 7.25; Found: C, 62.23; H, 5.71; N, 8.94; S, 7.12.

2.1.3.21. 2-(5-bromo-1H-indol-3-yl)-1-cyclohexyl-5-(ethylsulfonyl)-1H-benzo[d]imidazole (43). Compound **43** was prepared according to general methods starting from N^1 -cyclohexyl-4-ethylsulfonyl-benzene-1,2-diamine (1.10 mmol, 0.311 g) and 5-bromo-indole-3-carboxaldehyde (1.10 mmol, 0.246 g). The residue was purified by cc using the chloroform/ethyl acetate (1:1) as eluent to give a white solid, m.p. 184 °C (0.335 g, 79% yield). $^1\text{H NMR}$ (400 MHz, $\text{DMSO}-d_6$): δ ppm 1.13 (t, 3H), 1.40 (m, 3H), 1.67 (s, 1H), 1.86–1.98 (m, 4H), 2.29–2.35 (m, 2H), 3.31 (q, 2H), 4.63–4.69 (m, 1H), 7.36 (dd, $J = 8.4$ Hz, $J = 1.6$ Hz, 1H), 7.53 (d, $J = 8.4$ Hz, 1H), 7.68 (dd, $J = 8.4$ Hz, $J = 2$ Hz, 1H), 7.93 (d, $J = 2.8$ Hz, 1H), 8.10 (d, $J = 8.8$ Hz, 1H), 8.20 (dd, $J = 11.2$ Hz, $J = 1.6$ Hz, 2H), 11.99 (brd s, 1H, NH). $^{13}\text{C NMR}$ ($\text{DMSO}-d_6$): 7.27, 24.32, 25.41, 30.45, 49.65, 56.65, 103.78, 113.05, 113.21, 114.00, 118.91, 120.40, 122.70, 124.92, 128.30, 128.40, 131.47, 134.83, 136.76, 143.23, 151.43. **MS** (ESI+) m/z : 488. **Anal. calcd.** For $\text{C}_{23}\text{H}_{24}\text{BrN}_3\text{O}_2\text{S}\cdot 0.45\text{H}_2\text{O}$: C, 55.86; H, 5.07; N, 8.49; S, 6.48; Found: C, 55.85; H, 4.85; N, 8.15; S, 6.43.

2.1.3.22. 1-benzyl-5-(ethylsulfonyl)-2-(1H-indol-3-yl)-1H-benzo[d]imidazole (44). Compound **44** was prepared according to general methods starting from N^1 -benzyl-4-ethylsulfonyl-benzene-1,2-diamine (0.80 mmol, 0.230 g) and indole-3-carboxaldehyde (0.80 mmol, 0.115 g). The residue was purified by cc using the chloroform/ethyl acetate (1:1) as eluent to give a white solid, m.p. 252 °C (0.066 g, 20% yield). $^1\text{H NMR}$ (400 MHz, $\text{DMSO}-d_6$): δ ppm 1.14 (t, 3H), 3.31 (q, 2H), 5.85 (s, 2H), 7.09 (d, $J = 7.2$ Hz, 2H), 7.19–7.34 (m, 5H), 7.49 (d, $J = 7.2$ Hz, 1H), 7.68–7.78 (m, 3H), 8.19 (s, 1H), 8.44 (d, $J = 7.2$ Hz, 1H), 11.77 (brd s, 1H, NH). $^{13}\text{C NMR}$ ($\text{DMSO}-d_6$): 7.38, 47.38, 49.68, 103.92, 110.74, 111.87, 118.48, 120.63, 121.09, 121.50, 122.63, 125.96, 126.33, 126.84, 127.48, 128.93, 131.90, 135.98, 136.57, 139.12, 142.69, 152.61. **MS** (ESI+) m/z : 416. **Anal. calcd.** For

C₂₄H₂₁N₃O₂S.0,5C₄H₈O₂.0,5H₂O: C, 66.65; H, 5.59; N, 8.97; S, 6.84; Found: C, 66.68; H, 5.40; N, 8.98; S, 6.90.

2.1.3.23. 1-benzyl-5-(ethylsulfonyl)-2-(5-methoxy-1H-indol-3-yl)-1H-benzo[d]imidazole (45). Compound 45 was prepared according to general methods starting from N¹-benzyl-4-ethylsulfonyl-benzene-1,2-diamine (0.70 mmol, 0.203 g) and 5-methoxy-indole-3-carboxaldehyde (0.70 mmol, 0.123 g). The residue was purified by cc using the chloroform/ethyl acetate (1:1) as eluent to give a white solid, m.p. 296 °C (0.036 g, 12% yield). ¹H NMR (400 MHz, DMSO-d₆): δ ppm 1.13 (t, 3H), 3.32 (q, 2H), 3.80 (s, 3H), 5.83 (s, 2H), 6.88 (dd, J = 8.8 Hz, J = 2.4 Hz, 1H), 7.09 (d, J = 7.2 Hz, 2H), 7.23–7.39 (m, 4H), 7.67–7.74 (m, 3H), 7.96 (d, J = 2.4 Hz, 1H), 8.19 (d, J = 1.2 Hz, 1H), 11.64 (brd s, 1H, NH). ¹³C NMR (DMSO-d₆): 7.89, 47.89, 60.18, 55.81, 103.62, 104.17, 111.15, 113.09, 113.29, 118.98, 121.52, 126.47, 127.44, 127.72, 127.96, 129.43, 131.47, 132.32, 137.08, 139.62, 143.19, 153.31, 155.07. MS (ESI+) m/z: 446. Anal. calcd. For C₂₅H₂₃N₃O₃S: C, 67.39; H, 5.20; N, 9.43; S, 7.19; Found: C, 67.29; H, 5.45; N, 9.30; S, 7.16.

2.1.3.24. 1-benzyl-2-(5-chloro-1H-indol-3-yl)-5-(ethylsulfonyl)-1H-benzo[d]imidazole (46). Compound 46 was prepared according to general methods starting from N¹-benzyl-4-ethylsulfonylbenzene-1,2-diamine (0.85 mmol, 0.246 g) and 5-chloro-indole-3-carboxaldehyde (0.85 mmol, 0.152 g). The residue was purified by cc using the chloroform/ethyl acetate (1:1) as eluent to give a white solid, m.p. 265 °C (0.139 g, 36% yield). ¹H NMR (400 MHz, DMSO-d₆): δ ppm 1.15 (t, 3H), 3.32 (q, 2H), 5.86 (s, 2H), 7.09 (d, J = 7.6 Hz, 2H), 7.25–7.34 (m, 4H), 7.52 (d, J = 8.8 Hz, 1H), 7.70–7.78 (m, 2H), 7.8 (s, 1H), 8.25 (s, 1H), 8.51 (d, J = 2 Hz, 1H), 11.95 (brd s, 1H, NH). ¹³C NMR (DMSO-d₆): 7.31, 47.33, 49.62, 103.71, 110.71, 113.48, 118.61, 120.70, 121.16, 122.66, 125.34, 125.90, 127.45, 128.24, 128.89, 132.05, 134.46, 136.38, 139.05, 142.53, 151.95. MS (ESI+) m/z: 450. Anal. calcd. For C₂₄H₂₀ClN₃O₂S: C, 64.06; H, 4.48; N, 9.33; S, 7.12; Found: C, 63.47; H, 4.46; N, 9.19; S, 7.05.

2.1.3.25. 1-benzyl-2-(5-bromo-1H-indol-3-yl)-5-(ethylsulfonyl)-1H-benzo[d]imidazole (47). Compound 47 was prepared according to general methods starting from N¹-benzyl-4-ethylsulfonyl-benzene-1,2-diamine (0.83 mmol, 0.240 g) and 5-bromo-indole-3-carboxaldehyde (0.83 mmol, 0.185 g). The residue was purified by cc using the chloroform/ethyl acetate (1:1) as eluent to give a white solid, m.p. 267 °C (0.226 g, 55% yield). ¹H NMR (400 MHz, DMSO-d₆): δ ppm 1.13 (t, 3H), 3.33 (q, 2H), 5.87 (s, 2H), 7.08 (d, J = 7.2 Hz, 2H), 7.25–7.38 (m, 4H), 7.48 (d, J = 8.8 Hz, 1H), 7.69–7.78 (m, 2H), 7.87 (s, 1H), 8.25 (s, 1H), 8.66 (d, J = 1.6 Hz, 1H), 11.97 (brd s, 1H, NH). ¹³C NMR (DMSO-d₆): 7.38, 47.34, 49.63, 103.61, 110.75, 113.41, 113.97, 118.68, 121.23, 123.77, 125.25, 125.94, 127.50, 128.10, 128.13, 128.95, 132.05, 134.73, 136.43, 139.10, 142.55, 151.95. MS (ESI+) m/z: 496. Anal. calcd. For C₂₄H₂₀BrN₃O₂S.0,3H₂O: C, 57.67; H, 4.15; N, 8.40; S, 6.41; Found: C, 57.66; H, 4.12; N, 8.17; S, 6.13.

2.1.3.26. 5-(ethylsulfonyl)-1-(4-fluorobenzyl)-2-(1H-indol-3-yl)-1H-benzo[d]imidazole (48). Compound 48 was prepared according to general methods starting from N¹-(4-fluorobenzyl)-4-ethylsulfonyl-benzene-1,2-diamine (0.68 mmol, 0.210 g) and indole-3-carboxaldehyde (0.68 mmol, 0.099 g). The residue was purified by cc using the chloroform/ethyl acetate (2:1) as eluent to give a white solid, m.p. 234 °C (0.080 g, 27% yield). ¹H NMR (400 MHz, DMSO-d₆): δ ppm 1.13 (t, 3H), 3.31 (q, 2H), 5.82 (s, 2H), 7.08–7.24 (m, 6H), 7.48 (d, J = 7.2 Hz, 1H), 7.69 (dd, J = 8.4 Hz, J = 1.6 Hz, 1H), 7.71 (d, J = 8.8 Hz, 1H), 7.80 (d, J = 2.4 Hz, 1H), 8.17 (d, J = 1.2 Hz, 1H), 8.41 (d, J = 8.4 Hz, 1H), 11.73 (brd s, 1H, NH). ¹³C NMR (DMSO-d₆): 7.31, 46.68, 49.62, 103.80, 110.66, 111.82, 115.69 (d, J = 21.3 Hz), 118.46, 120.57, 121.07, 121.45, 122.57, 126.26, 126.81, 128.04 (d, J = 8.4 Hz), 131.90, 132.65 (d, J = 3.1 Hz), 135.94, 138.95, 142.66,

152.47, 161.32 (d, J = 242.3 Hz), 170.23. MS (ESI+) m/z: 434. Anal. calcd. For C₂₄H₂₀FN₃O₂S.0,5C₄H₈O₂: C, 65.39; H, 5.06; N, 8.79; S, 6.71; Found: C, 65.18; H, 5.02; N, 8.71; S, 6.68.

2.1.3.27. 5-(ethylsulfonyl)-1-(4-fluorobenzyl)-2-(5-methoxy-1H-indol-3-yl)-1H-benzo[d]imidazole (49). Compound 49 was prepared according to general methods starting from N¹-(4-fluorobenzyl)-4-ethylsulfonyl-benzene-1,2-diamine (0.54 mmol, 0.168 g) and 5-methoxy-indole-3-carboxaldehyde (0.54 mmol, 0.095 g). The residue was purified by cc using the chloroform/ethyl acetate (2:1) as eluent to give a light yellow solid, m.p. 260 °C (0.044 g, 18% yield). ¹H NMR (400 MHz, DMSO-d₆): δ ppm 1.13 (t, 3H), 3.32 (q, 2H), 3.80 (s, 3H), 5.82 (s, 2H), 6.89 (dd, J = 8.8 Hz, J = 2.4 Hz, 1H), 7.10–7.18 (m, 4H), 7.39 (d, J = 8.8 Hz, 1H), 7.67–7.77 (m, 3H), 7.96 (d, J = 2.4 Hz, 1H), 8.19 (d, J = 1.6 Hz, 1H), 11.66 (brd s, 1H, NH). ¹³C NMR (DMSO-d₆): 7.31, 46.68, 49.60, 55.24, 103.08, 103.55, 110.55, 112.53, 112.72, 115.68 (d, J = 21.7 Hz), 118.43, 120.98, 126.87, 127.16, 128.03 (d, J = 8.4 Hz), 130.92, 131.84, 132.64 (d, J = 3.5 Hz), 138.93, 142.64, 152.64, 154.51, 161.30 (d, J = 242.3 Hz). MS (ESI+) m/z: 464. Anal. calcd. For C₂₅H₂₂FN₃O₃S.0,2H₂O: C, 64.27; H, 4.83; N, 9.00; S, 6.85; Found: C, 64.02; H, 4.98; N, 8.69; S, 6.62.

2.1.3.28. 2-(5-chloro-1H-indol-3-yl)-5-(ethylsulfonyl)-1-(4-fluorobenzyl)-1H-benzo[d]imidazole (50). Compound 50 was prepared according to general methods starting from N¹-(4-fluorobenzyl)-4-ethylsulfonyl-benzene-1,2-diamine (0.52 mmol, 0.162 g) and 5-chloro-indole-3-carboxaldehyde (0.52 mmol, 0.094 g). The residue was purified by cc using the chloroform/ethyl acetate (2:1) as eluent to give a white solid, m.p. 230 °C (0.097 g, 40% yield). ¹H NMR (400 MHz, DMSO-d₆): δ ppm 1.12 (t, 3H), 3.32 (q, 2H), 5.83 (s, 2H), 7.08–7.15 (m, 4H), 7.24 (dd, J = 8.8 Hz, J = 2 Hz, 1H), 7.50 (d, J = 8.4 Hz, 1H), 7.69 (dd, J = 8.4 Hz, J = 2 Hz, 1H), 7.76 (d, J = 8.4 Hz, 1H), 7.9 (s, 1H), 8.22 (d, J = 1.6 Hz, 1H), 8.48 (d, J = 2.4 Hz, 1H), 11.96 (brd s, 1H, NH). ¹³C NMR (DMSO-d₆): 7.31, 46.44, 49.55, 103.61, 110.68, 113.49, 115.72 (d, J = 21.1 Hz), 118.62, 120.69, 121.20, 122.66, 125.33, 127.41, 128.03 (d, J = 7.7 Hz), 128.28, 132.04, 132.52 (d, J = 2.6 Hz), 134.43, 138.92, 142.51, 151.82, 161.32 (d, J = 240 Hz). MS (ESI+) m/z: 468. Anal. calcd. For C₂₄H₁₉ClFN₃O₂S: C, 61.60; H, 4.09; N, 8.98; S, 6.85; Found: C, 61.51; H, 4.10; N, 9.00; S, 6.86.

2.1.3.29. 2-(5-bromo-1H-indol-3-yl)-5-(ethylsulfonyl)-1-(4-fluorobenzyl)-1H-benzo[d]imidazole (51). Compound 51 was prepared according to general methods starting from N¹-(4-fluorobenzyl)-4-ethylsulfonyl-benzene-1,2-diamine (0.66 mmol, 0.202 g) and 5-bromo-indole-3-carboxaldehyde (0.66 mmol, 0.146 g). The residue was purified by cc using the chloroform/ethyl acetate/hexane (2:1:1) as eluent to give a white solid, m.p. 240 °C (0.099 g, 29% yield). ¹H NMR (400 MHz, DMSO-d₆): δ ppm 1.13 (t, 3H), 3.32 (q, 2H), 5.86 (s, 2H), 7.10–7.18 (m, 4H), 7.38 (dd, J = 8.8 Hz, J = 2 Hz, 1H), 7.48 (d, J = 8.4 Hz, 1H), 7.71 (dd, J = 8.4 Hz, J = 1.6 Hz, 1H), 7.78 (d, J = 8.4 Hz, 1H), 7.91 (d, J = 2.8 Hz, 1H), 8.25 (d, J = 1.6 Hz, 1H), 8.66 (d, J = 2 Hz, 1H), 11.99 (brd s, 1H, NH). ¹³C NMR (DMSO-d₆): 7.31, 46.64, 49.64, 103.49, 110.68, 113.34, 113.92, 115.72 (d, J = 21.2 Hz), 118.63, 121.20, 123.70, 125.20, 127.97, 128.02 (d, J = 8.3 Hz), 128.113, 132.05, 132.51 (d, J = 3.2 Hz), 134.67, 138.91, 142.50, 151.79, 161.32 (d, J = 241.5 Hz). MS (ESI+) m/z: 514. Anal. calcd. For C₂₄H₁₉BrFN₃O₂S: C, 56.26; H, 3.74; N, 8.20; S, 6.25; Found: C, 56.51; H, 4.02; N, 7.72; S, 5.84.

2.1.3.30. 5-(ethylsulfonyl)-1-(3,4-difluorobenzyl)-2-(1H-indol-3-yl)-1H-benzo[d]imidazole (52). Compound 52 was prepared according to general methods starting from N¹-(3,4-difluorobenzyl)-4-ethylsulfonyl-benzene-1,2-diamine (0.64 mmol, 0.209 g) and indole-3-carboxaldehyde (0.64 mmol, 0.093 g). The residue was purified by cc using the chloroform/ethyl acetate/hexane (2:1.5:1) as eluent to give a white solid, m.p. 262 °C (0.175 g, 61% yield). ¹H NMR (400 MHz,

DMSO-*d*₆): δ ppm 1.11 (t, 3H), 3.31 (q, 2H), 5.82 (s, 2H), 6.77 (d, $J = 8.4$ Hz, 1H), 7.16–7.36 (m, 4H), 7.48 (d, $J = 7.6$ Hz, 1H), 7.69 (dd, $J = 8.8$ Hz, $J = 1.6$ Hz, 1H), 7.75 (d, $J = 8.4$ Hz, 1H), 7.80 (d, $J = 2.8$ Hz, 1H), 8.18 (d, $J = 1.6$ Hz, 1H), 8.41 (d, $J = 8.4$ Hz, 1H), 11.77 (brd s, 1H). **MS (ESI+)** m/z : 452. **Anal. calcd. For C₂₄H₁₉F₂N₃O₂S**: C, 63.85; H, 4.24; N, 8.42; S, 7.10; Found: C, 63.61; H, 4.41; N, 8.97; S, 6.91

2.1.3.31. 5-(ethylsulfonyl)-1-(3,4-difluorobenzyl)-2-(5-methoxy-1H-indol-3-yl)-1H-benzod[*j*]imidazole (53). Compound **53** was prepared according to general methods starting from N¹-(3,4-difluorobenzyl)-4-ethylsulfonyl-benzene-1,2-diamine (0.71 mmol, 0.233 g) and 5-methoxy-indole-3-carboxaldehyde (0.71 mmol, 0.125 g). The residue was purified by cc using the chloroform/ethyl acetate/hexane (2:1:1) as eluent to give a white solid, m.p. 271 °C (0.151 g, 44% yield). **¹H NMR (400 MHz, DMSO-*d*₆)**: δ ppm 1.11 (t, 3H), 3.30 (q, 2H), 3.79 (s, 3H), 5.80 (s, 2H), 6.78 (d, 1H), 6.87 (dd, $J = 9$ Hz, $J = 2.4$ Hz, 1H), 7.24–7.39 (m, 3H), 7.67–7.76 (m, 3H), 7.94 (d, 1H), 8.19 (d, $J = 1.2$ Hz, 1H), 11.65 (brd s, 1H). **MS (ESI+)** m/z : 482. **Anal. calcd. For C₂₅H₂₁F₂N₃O₃S**: C, 62.36; H, 4.40; N, 8.73; S, 6.66; Found: C, 61.94; H, 4.60; N, 8.61; S, 6.68.

2.1.3.32. 5-(ethylsulfonyl)-1-(3,4-difluorobenzyl)-2-(5-chloro-1H-indol-3-yl)-1H-benzod[*j*]imidazole (54). Compound **54** was prepared according to general methods starting from N¹-(3,4-difluorobenzyl)-4-ethylsulfonyl-benzene-1,2-diamine (0.89 mmol, 0.293 g) and 5-chloro-indole-3-carboxaldehyde (0.89 mmol, 0.160 g). The residue was purified by cc using the chloroform/ethyl acetate/hexane (2:1:1) as eluent to give a white solid, m.p. 258 °C (0.209 g, 48% yield). **¹H NMR (400 MHz, DMSO-*d*₆)**: δ ppm 1.11 (t, 3H), 3.30 (q, 2H), 5.83 (s, 2H), 6.76 (d, 1H), 7.22–7.36 (m, 3H), 7.50 (d, $J = 8.4$ Hz, 1H), 7.70 (dd, $J = 8.6$ Hz, $J = 1.6$ Hz, 1H), 7.76 (d, $J = 8.4$ Hz, 1H), 7.9 (d, $J = 1.6$ Hz, 1H), 8.23 (d, $J = 1.6$ Hz, 1H), 8.47 (d, $J = 2.4$ Hz, 1H), 11.96 (brd s, 1H). **MS (ESI+)** m/z : 486. **Anal. calcd. For C₂₄H₁₈ClF₂N₃O₂S**: C, 59.32; H, 3.73; N, 8.65; S, 6.60; Found: C, 59.01; H, 3.74; N, 8.45; S, 6.45

2.1.3.33. 5-(ethylsulfonyl)-1-(3,4-difluorobenzyl)-2-(5-bromo-1H-indol-3-yl)-1H-benzod[*j*]imidazole (55). Compound **55** was prepared according to general methods starting from N¹-(3,4-difluorobenzyl)-4-ethylsulfonyl-benzene-1,2-diamine (0.72 mmol, 0.234 g) and 5-bromo-indole-3-carboxaldehyde (0.72 mmol, 0.160 g). The residue was purified by cc using the chloroform/ethyl acetate/hexane (2:2:1) as eluent to give a white solid, m.p. 248 °C (0.141 g, 37% yield). **¹H NMR (400 MHz, DMSO-*d*₆)**: δ ppm 1.14 (t, 3H), 3.33 (q, 2H), 5.86 (s, 2H), 6.80 (d, 1H), 7.29–7.39 (m, 3H), 7.49 (d, $J = 8.8$ Hz, 1H), 7.75 (dd, $J = 8.4$ Hz, $J = 1.6$ Hz, 1H), 7.79 (d, $J = 8.8$ Hz, 1H), 7.91 (d, $J = 2.8$ Hz, 1H), 8.26 (d, $J = 1.2$ Hz, 1H), 8.65 (d, $J = 2$ Hz, 1H), 12.00 (brd s, 1H). **MS (ESI+)** m/z : 532. **Anal. calcd. For C₂₄H₁₈BrF₂N₃O₂S**: C, 54.35; H, 3.42; N, 7.92; S, 6.04; Found: C, 54.43; H, 3.20; N, 7.84; S, 6.01.

2.1.3.34. 5-(ethylsulfonyl)-1-(3,4-dichlorobenzyl)-2-(1H-indol-3-yl)-1H-benzod[*j*]imidazole (56). Compound **56** was prepared according to general methods starting from N¹-(3,4-dichlorobenzyl)-4-ethylsulfonyl-benzene-1,2-diamine (0.44 mmol, 0.158 g) and indole-3-carboxaldehyde (0.44 mmol, 0.064 g). The residue was purified by cc using the chloroform/ethyl acetate (2:1) as eluent to give a white solid, m.p. 247 °C (0.070 g, 33% yield). **¹H NMR (400 MHz, DMSO-*d*₆)**: δ ppm 1.15 (t, 3H), 3.34 (q, 2H), 5.88 (s, 2H), 6.90 (dd, $J = 8.2$ Hz, $J = 2.4$ Hz, 1H), 7.20–7.27 (m, 2H), 7.49–7.60 (m, 3H), 7.71 (dd, $J = 8.2$ Hz, $J = 2$ Hz, 1H), 7.78 (d, $J = 8.8$ Hz, 1H), 7.82 (d, $J = 2.8$ Hz, 1H), 8.21 (d, $J = 1.6$ Hz, 1H), 8.45 (d, $J = 7.2$ Hz, 1H), 11.81 (brd s, 1H). **¹³C NMR (DMSO-*d*₆)**: 7.30, 46.30, 49.61, 103.62, 110.58, 111.84, 118.52, 120.62, 121.45, 122.63, 126.04, 126.85, 128.37, 130.07, 130.80, 131.09, 131.41, 132.07, 135.95, 137.73, 138.88, 142.65,

152.43, 161.22. **MS (ESI+)** m/z : 484. **Anal. calcd. For C₂₄H₁₉Cl₂N₃O₂S·0.5 H₂O**: C, 58.42; H, 4.08; N, 8.51; S, 6.49; Found: C, 58.30; H, 4.31; N, 8.78; S, 6.04.

2.1.3.35. 5-(ethylsulfonyl)-1-(3,4-dichlorobenzyl)-2-(5-methoxy-1H-indol-3-yl)-1H-benzod[*j*]imidazole (57). Compound **57** was prepared according to general methods starting from N¹-(3,4-dichlorobenzyl)-4-ethylsulfonyl-benzene-1,2-diamine (1.01 mmol, 0.363 g) and 5-methoxy-indole-3-carboxaldehyde (1.01 mmol, 0.177 g). The residue was purified by cc using the chloroform/ethyl acetate (2:1) as eluent to give a white solid, m.p. 242 °C (0.065 g, 12% yield). **¹H NMR (400 MHz, DMSO-*d*₆)**: δ ppm 1.11 (t, 3H), 3.31 (q, 2H), 3.79 (s, 3H), 5.83 (s, 2H), 6.89 (m, 2H), 7.37 (d, $J = 8.8$ Hz, 1H), 7.46 (d, $J = 2$ Hz, 1H), 7.53 (d, $J = 8.4$ Hz, 1H), 7.67–7.76 (m, 3H), 7.95 (d, $J = 2.4$ Hz, 1H), 8.19 (d, $J = 1.6$ Hz, 1H), 11.65 (brd s, 1H). **¹³C NMR (DMSO-*d*₆)**: 7.31, 46.30, 49.61, 55.25, 103.08, 103.39, 110.50, 112.57, 112.79, 118.52, 121.15, 126.06, 126.87, 127.20, 128.37, 130.05, 130.94, 131.09, 131.40, 132.08, 137.74, 138.87, 142.64, 152.61, 154.57. **MS (ESI+)** m/z : 514. **Anal. calcd. For C₂₅H₂₁Cl₂N₃O₃S**: C, 58.37; H, 4.11; N, 8.17; S, 6.23; Found: C, 58.04; H, 4.06; N, 7.83; S, 5.98.

2.1.3.36. 5-(ethylsulfonyl)-1-(3,4-dichlorobenzyl)-2-(5-chloro-1H-indol-3-yl)-1H-benzod[*j*]imidazole (58). Compound **58** was prepared according to general methods starting from N¹-(3,4-dichlorobenzyl)-4-ethylsulfonyl-benzene-1,2-diamine (0.56 mmol, 0.202 g) and 5-chloro-indole-3-carboxaldehyde (0.56 mmol, 0.101 g). The residue was purified by cc using the chloroform/ethyl acetate (2:1) as eluent to give a white solid, m.p. 278 °C (0.045 g, 15% yield). **¹H NMR (400 MHz, DMSO-*d*₆)**: δ ppm 1.12 (t, 3H), 3.32 (q, 2H), 5.86 (s, 2H), 6.86 (dd, $J = 8.4$ Hz, $J = 2$ Hz, 1H), 7.24 (dd, $J = 8.8$ Hz, $J = 2$ Hz, 1H), 7.47–7.53 (m, 3H), 7.71 (dd, $J = 8.2$ Hz, $J = 1.6$ Hz, 1H), 7.77 (d, $J = 8.4$ Hz, 1H), 7.90 (d, $J = 3.2$ Hz, 1H), 8.24 (d, $J = 1.6$ Hz, 1H), 8.49 (d, $J = 2$ Hz, 1H), 11.96 (brd s, 1H). **¹³C NMR (DMSO-*d*₆)**: 7.31, 46.26, 49.55, 103.44, 110.61, 113.52, 118.69, 120.69, 121.35, 122.72, 125.39, 125.99, 127.39, 128.32, 128.39, 130.09, 131.11, 131.42, 132.21, 134.45, 137.60, 138.85, 142.51, 151.80. **MS (ESI+)** m/z : 518. **Anal. calcd. For C₂₄H₁₈Cl₃N₃O₂S**: C, 55.56; H, 3.50; N, 8.10; S, 6.18; Found: C, 55.19; H, 3.35; N, 7.92; S, 5.98.

2.1.3.37. 5-(ethylsulfonyl)-1-(3,4-dichlorobenzyl)-2-(5-bromo-1H-indol-3-yl)-1H-benzod[*j*]imidazole (59). Compound **59** was prepared according to general methods starting from N¹-(3,4-dichlorobenzyl)-4-ethylsulfonyl-benzene-1,2-diamine (0.78 mmol, 0.280 g) and 5-bromo-indole-3-carboxaldehyde (0.78 mmol, 0.174 g). The residue was purified by cc using the chloroform/ethyl acetate (2:1) as eluent to give a white solid, m.p. 156 °C (0.055 g, 12% yield). **¹H NMR (400 MHz, DMSO-*d*₆)**: δ ppm 1.13 (t, 3H), 3.33 (q, 2H), 5.89 (s, 2H), 6.88 (dd, $J = 8.4$ Hz, $J = 1.6$ Hz, 1H), 7.38 (dd, $J = 8.8$ Hz, $J = 2$ Hz, 1H), 7.48–7.56 (m, 3H), 7.73 (dd, $J = 8.2$ Hz, $J = 1.6$ Hz, 1H), 7.80 (d, $J = 8.8$ Hz, 1H), 7.91 (d, $J = 3.2$ Hz, 1H), 8.27 (d, $J = 0.8$ Hz, 1H), 8.66 (d, $J = 1.6$ Hz, 1H), 12.00 (brd s, 1H). **¹³C NMR (DMSO-*d*₆)**: 12.45, 47.26, 56.68, 103.65, 110.68, 113.47, 118.45, 120.69, 121.03, 122.65, 125.31, 125.87, 127.40, 127.42, 128.23, 128.88, 132.60, 134.41, 136.37, 139.00, 142.47, 151.90. **MS (ESI+)** m/z : 564. **Anal. calcd. For C₂₄H₁₈BrCl₂N₃O₂S·0.5H₂O**: C, 50.52; H, 3.35; N, 7.37; S, 5.60; Found: C, 50.14; H, 3.05; N, 7.12; S, 5.35.

2.2. Biological activity assays

2.2.1. Cytotoxic assays on human cancer lines

3-(4,5-Dimethylthiazol-2-yl)-2,5-diphenyltetrazolium Bromide (MTT) (Molecular Probes) was used to measure cell viability. Cell lines (MCF-7, MDA-MB-231 and HEPG2) were seeded onto 96-well plates with 10,000 cells/well in phenol-free media (DMEM-low-glucose, GIBCO). After 24 h, the cells were exposed to compounds listed in [Table 2](#) with different concentrations for another day. All compounds

were tested first at 0.25 μM , 2 μM , 16 μM and 40 μM doses using MCF-7 cells. At each dose, percent cell viability was calculated in relationship to the DMSO control for each concentration. Selected compounds were further studied using three different cell lines (MCF-7, MDA-MB-231, and HEPG2) at eight different concentrations to calculate IC_{50} values. Camptothecin was used as a positive control (0.25 and 2 μM) as there was a DMSO group for calibration for each drug concentration. Cells were then fixed according to the manufacturer's instructions and intensities were measured spectrophotometrically (BIO-TEK/ μ Quant Universal Microplate Spectrophotometer and BIO-TEK/KC junior software (v.1.418)). Percent viability was calculated at each dose, separately, by dividing the blank subtracted average OD values of each treated sample with the blank subtracted average ODs of corresponding DMSO treated counterparts; and the resulting values were multiplied by 100 to obtain percentile viabilities. One-way ANOVA followed by multiple comparisons (MATLAB R2016a) were used to test differences in group means between the drug and DMSO control groups at each concentration. For clustering the MTT data, percentiles were divided by 100 and logarithmically transformed at base two before performing hierarchical clustering. For testing the significance of mean differences between groups from the MCF-7 four-concentration screening, raw data from each plate of compounds were statistically compared with respect to their corresponding DMSO control values at each concentration, separately. For wider dose screens, IC_{50} values for each cell line were calculated using GraphPad Prism (v. 6.05). Further statistical analyses were performed by using the viability values obtained from MCF-7 and other cell lines, to determine any relationship between the viability and R_1 or R_2 status of the derivatives. n -way ANOVA analyses with \log_2 transformed viability values (in R environment), and one-sided Wilcoxon-rank sum test and $\log\text{IC}_{50}$ (GRcalculator [46]) were performed by taking into account the triplicate values of viability scores and corresponding treatment concentrations. In GRcalculator analyses, sigmoidal fit and capping GR values below 1 were used. Additionally, two-way ANOVA with Tukey's multiple comparisons was performed to test the significance of difference between specific groups of compounds in GraphPad Prism (v. 6.05), by using cell viability values in triplicates. Principal component analysis (PCA) was used for further investigating the effect of cell line and concentration; and \log_2 transformed cell viability was used for the analysis.

2.3. Molecular docking analyses with multiple targets

$\text{ER}\alpha$ ligand-binding domain (PDB ID:1a52, resolution: 2.8 Å) file was obtained from the RCSB Protein database website [47]. Additional proteins were tested to analyze the selectivity of compounds against $\text{ER}\alpha$. These compounds were protein kinase C beta II (PDB ID:1pfq, resolution: 1.9 Å), glycogen synthase kinase 3 (PDB ID:1io9, resolution: 2.7 Å), platelet-derived growth factor receptor beta (PDB ID:3mjg, resolution: 2.3 Å), tubulin (PDB ID:1sa0, resolution: 3.58 Å) and vEGFR2 kinase domain (PDB ID:2xir, resolution:1.5 Å), respectively. Proteins were prepared with Maestro's Protein Preparation Wizard [48] and the gridbox was prepared via the Receptor Grid Generation module of Maestro [49]. Binding sites of co-ligands were used for gridbox generation. 2D builder was used to draw the ligands and same ligands were minimized and prepared with the LigPrep module [50]. Tautomers and conformers were generated to maximize the number of conformers. For all the complexes, bound ligands were used. Structures of these compounds were procured from DrugBank [51], and were subjected to the identical LigPrep procedure. After this, Ligand Docking process of the Glide program was initiated [52]. Precision was set to SP (Standard precision) and Ligand Sampling was set to Flexible. 10 poses were generated for each ligand and poses having the least binding energies amongst them were evaluated. 2D-interaction diagrams were visualized via Ligand Interactions. Additionally, molecular descriptors of these compounds were calculated via the QikProp module and assessed accordingly [53].

2.4. Microarray analyses of novel-indole benzimidazole derivatives and comparative transcriptomics

MCF-7 cells were exposed to compounds 48, 49, 50, 51, and 53 for 24 h at a dose of 20 μM . Total RNA was extracted from each sample where DMSO control and 51, each, had two biological replicates (RNeasy Mini Kit (QIAGEN)) before performing microarray experiments using HuGene 2.0 ST platform (Affymetrix). Data were normalized via Transcriptome Analysis Console Software (V3.0.0.466) using default Affymetrix analysis parameters and *rma* using affy package [54]. For differential expression analysis of 51 ($n = 2$) in comparison with DMSO ($n = 2$), the *limma* toolbox of R was used [55]. Volcano plot of statistical significance against fold change between control and 51 treated MCF-7 cells was generated in MATLAB. For multiple probes hitting the same gene, the probe with the lowest adjusted p-value was used.

GSEA was performed for each compound separately with default parameters to calculate the KEGG pathway enrichment using MSigDB [56]. Significantly enriched pathways were chosen (false discovery rate (FDR) q value < 0.25); and commonly enriched KEGG pathways were reported. LINCS database was used to identify compounds with the most and least similar expression profiles to significantly up- and down-regulated gene lists obtained from 51 (top 150 and bottom 150 ranked genes according to their $\log\text{FC}$ values) [57].

Limma analyses were performed between expression profiles of 48–49 and those of 50–51–53 compound series to identify the significantly differentially expressed genes at the adjusted p-value < 0.05 . Pathway enrichment was done on the significantly up- and down-regulated genes between groups via STRING database with Reactome Pathways option while Venn Diagrams of unique and variably affected pathways were also shown [58,59].

For comparative transcriptomics, GSE35428, GSE7765 and GSE62673 were retrieved and normalized with *rma* [60]. Differential expression analyses of normalized dataset were done using *limma* between groups as follows: for GSE35428: E2, tamoxifen (4OHT), ICI 182780, Lasofoxifene, Bazedoxifene or Raloxifene and EtOH (control) treatments; for GSE7765: Dioxin and DMSO (control) treatments; and for GSE62673: AA depletion (AA (-)) and control samples. For GSE7765, the results from hgu133A and hgu133B were merged. For multiple probes hitting the same gene, the probe with the lowest adjusted p-value was used. For GSE35428 and for GSE62673 best jetset probesets were selected for further analysis [61].

Venn diagrams were generated to represent the expression pattern (i.e., \log_2 fold changes) of the significantly altered genes ($N = 2177$, p-value < 0.05 between 51 & E2; $N = 111$, p-value < 0.05 between 51 & Dioxin; $N = 1480$, p-value < 0.05 between 51 & AA (-)). KEGG pathway enrichment analysis was performed using the STRING database; and Venn diagrams were generated based on the lists of significantly enriched pathways. Obtained diagrams were further utilized to form contingency tables where counts of shared and unique up-regulated or downregulated genes were used in performing Fisher's exact test in R.

Genes altered more than one-fold (FDR adj p-value < 0.05), in response to treatment with 51, were selected for the correlation analysis. The Pearson's correlation coefficient between each pair of treatments was used for the hierarchical clustering and heatmap was performed using ComplexHeatmap toolbox in R [62].

2.5. RT-QPCR assays for validation of treatment effects in MCF-7

Differential effects of candidate compounds on selected genes, known to be modulated by E2, dioxin, AA depletion, and/or to have roles in cell cycle, DNA damage/repair, drug metabolism were evaluated via RT-QPCR (LightCycler 480 II–Roche) in MCF-7 breast cancer cells exposed to 40 μM of each compound for 24 h. Following exposure, total mRNA was isolated and collected using the RNeasy Mini Kit

(QIAGEN) according to the manufacturer's instructions. Total RNA was then converted into cDNA using RevertAid First Strand cDNA Synthesis Kit (Thermo Scientific). Logarithmically transformed relative expression ($-\Delta\Delta Ct$) levels were calculated based on *TPT1* as the reference gene and DMSO treatment as the control group. The results were analyzed via either One-way ANOVA followed by Tukey's multiple comparisons to evaluate the compound-based effects or a Two-way ANOVA to assess dose-dependent effects (GraphPad Prism (v. 6.05)). ComplexHeatmap toolbox in R was utilized; and GSE35428 (E2), GSE7765 (dioxin), and GSE62673 (AA (-)) logFC data for the tested genes were annotated on top of the RT-QPCR data, for comparative representation. A list of primers was given in Table A. 1.

3. Results

3.1. Design and synthesis of indole-benzimidazole derivatives

The synthesis of compounds (Scheme 2) was initiated from 4-chloro-benzenesulfonyl chloride. 4-(ethylsulfonyl)-1-chlorobenzene (**1**) and 4-(ethylsulfonyl)-1-chloro-2-nitrobenzene (**2**) were synthesized according our previous publication [42]. To a solution of 4-(ethylsulfonyl)-1-chloro-2-nitrobenzene (**2**) (5 mmol) in ethanol (5 mL), amine derivative (15 mmol) was added and heated under reflux until the starting material was consumed (determined by TLC, 8–48 h). Upon cooling the mixture, water was added. The resultant yellow residue was crystallized from ethanol or purified by column chromatography (cc) by using a mixture of hexane and ethyl acetate in varying concentrations as eluent (Table 1) [43]. 5-methoxy-indole-3-carboxaldehyde was synthesized from 5-methoxy-indole, *N,N*-dimethylformamide, and phosphorus oxychloride [63].

Compounds **3–12** (3.5 mmol) in EtOH (75 mL) were reduced by hydrogenation using 40 psi of H₂ and 10% Pd/C (40 mg) until cessation of H₂ uptake to obtain the catalyst before filtering off on a bed of celite and washing with EtOH, and concentrating the filtrate in vacuo [44]. The crude amine was used without purification (**13–22**) (see for details Experimental Section). A mixture of the appropriate *o*-phenylenediamine (1 mmol), related indole derivative (1 mmol) and Na₂S₂O₅ (40%) (2 mL) in EtOH (4 mL), was refluxed until starting materials were

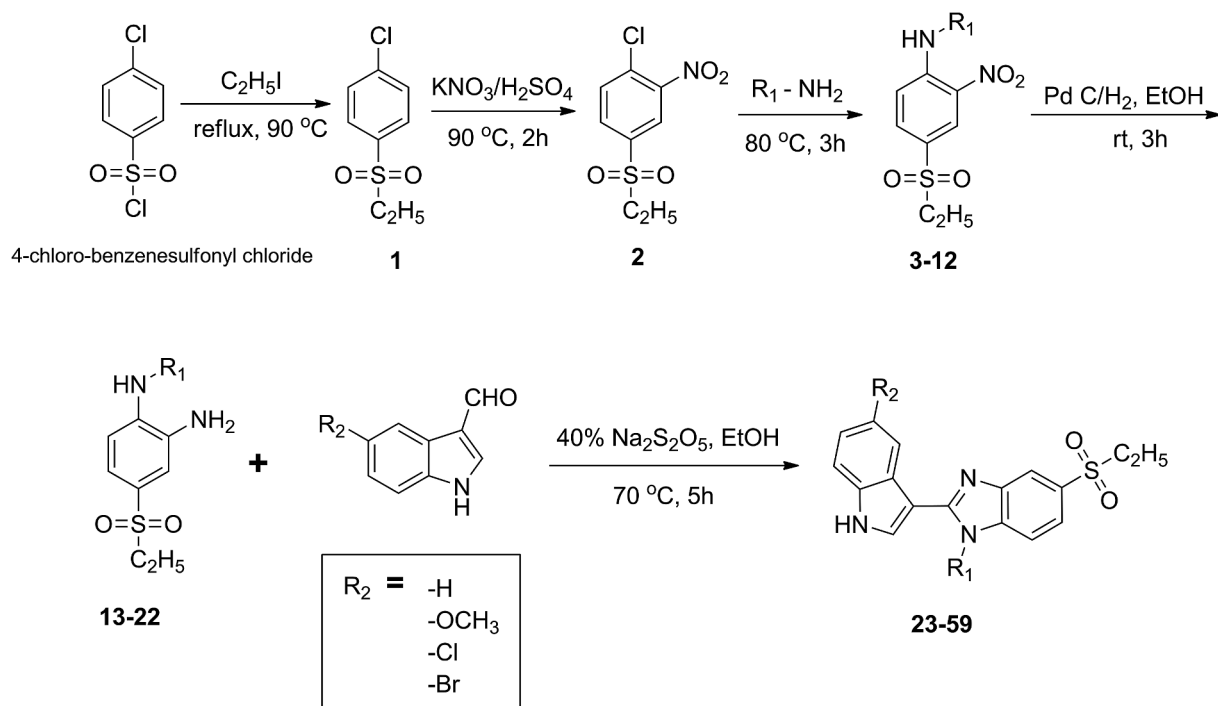
consumed (determined by TLC, 4–12 h). The precipitate was obtained upon pouring the reaction mixture and then filtering and washing. The residue was purified by cc to obtain the final product (**23–59**) [45]. The synthesis details of the compounds were provided in the Experimental Section.

3.2. Biological evaluation of indole-benzimidazole derivatives

3.2.1. Anti-cancer activity of novel indole-benzimidazole compounds in MCF-7 cell line

All ethylsulfonyl derivatives were analyzed for their cytotoxicity using MTT assays. A four-dose (0.25 μM, 2 μM, 16 μM and 40 μM) screening panel in MCF-7, an ER+ and TP53 (p53) wild-type breast cancer cell line, was used to identify highly effective compounds. This allowed us to screen large numbers of derivatives before pursuing selected compounds in more detail. As a result, the primary anticancer activity screening in MCF-7 showed that most of the compounds exhibited significance at one or more of the concentrations (Table 2). Hierarchical clustering of the compound relative cell viabilities (at log₂ scale) helped summarize similarities between activities across doses (Fig. 2). Accordingly, molecules numbered **23**, **35**, **53**, **36**, **27**, **29**, **45**, **37**, **50** and **51** clustered together, since they were highly effective at the highest dose, and one or more of the other three concentrations. The remaining compounds were less effective than the above-mentioned compounds with respect to their level of activity. In addition, compound **49** was highly effective at the highest dose, i.e., 40 μM, yet was not effective at lower doses (Fig. 2). None of the molecules exhibited activity at the lowest dose (0.25 μM).

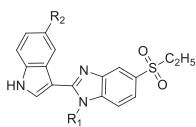
Synthesized compounds had either -H, -OCH₃, -Cl, or -Br at their R₂ position for each of the R₁ (Table 2). Therefore, the most active molecule could be determined for each of the R₁. According to the *n*-way ANOVA, molecular substitutions by R₁ and R₂ resulted in alterations on cytotoxic activities of the sulfonyl ethyl structures (p-value < 2e-16) where the R₁ group was the major predictor (p-value < 2e-16) of anticancer activity rather than the R₂ group (p-value: 0.0885). However, there was a significant interaction between R₁ and R₂ groups based on the cell viability scores (R_{1x2} interaction p-value < 2e-16) suggesting that substitution on indoles could modify the activity of



Scheme 2. Synthesis of new indole-benzimidazoles (23–59).

Table 2

Relative cell viability from four-dose screening with the ethylsulfonyl derivatives in MCF-7 cells. p-values were calculated using One-Way ANOVA followed by multiple comparisons.



No	R ₁	R ₂	% Relative viabilities				p-values			
			40 μM	16 μM	2 μM	0.25 μM	40 μM	16 μM	2 μM	0.25 μM
23	-H	-H	24.36	67.57	100	110.16	0.0000	0.0005	1.0000	0.2498
24	-H	-Br	67.53	85.44	90.04	105.73	0.0055	0.0391	0.2914	0.9979
25	-CH ₃	-H	64.68	72.12	94.01	95.39	0.0000	0.0293	0.9361	0.9238
26	-CH ₃	-OCH ₃	63.70	65.96	87.64	111.74	0.0028	0.0002	0.1572	0.9931
27	-CH ₃	-Cl	40.38	48.75	60.56	86.70	0.0001	0.0000	0.0000	0.1723
28	-CH ₃	-Br	69.58	79.32	94.45	92.97	0.0000	0.0089	0.0426	0.5252
29	-C ₂ H ₅	-H	44.16	45.09	77.02	87.82	0.0000	0.0000	0.0150	0.2749
30	-C ₂ H ₅	-OCH ₃	72.80	74.36	93.02	97.33	0.0112	0.0000	0.3659	0.9644
31	-C ₂ H ₅	-Cl	66.03	79.80	85.35	86.52	0.0000	0.0102	0.0001	0.1001
32	-C ₂ H ₅	-Br	58.80	58.13	85.41	111.86	0.0012	0.0000	0.0862	0.9742
33	-C ₃ H ₇	-H	69.52	98.64	101.48	112.94	0.0000	0.9871	0.9979	0.1720
34	-C ₃ H ₇	-OCH ₃	69.76	99.09	91.76	91.25	0.0000	0.9961	0.7629	0.4445
35	-C ₃ H ₇	-Cl	26.90	68.60	92	97.79	0.0000	0.0003	0.7776	0.9773
36	-C ₃ H ₇	-Br	32.85	48.06	77.12	89.86	0.0000	0.0000	0.0089	0.3313
37	-C ₄ H ₉	-H	43.76	55.21	91.36	101.55	0.0000	0.0000	0.3874	0.9919
38	-C ₄ H ₉	-Cl	89.88	81.38	94.29	110.80	0.0760	0.0021	0.6895	0.2854
39	-C ₄ H ₉	-Br	62.15	88.91	100.98	101.15	0.0009	0.4355	0.9990	0.9993
40	-cyclohexyl	-H	42.19	83.28	103.84	108.25	0.0005	0.8736	0.1878	0.9742
41	-cyclohexyl	-OCH ₃	64.12	85.42	91.05	102.61	0.0000	0.0008	0.3503	0.9805
42	-cyclohexyl	-Cl	63.80	82.62	97.92	105.45	0.0025	0.0498	0.9865	0.9742
43	-cyclohexyl	-Br	68.96	80.98	88.39	93.54	0.0000	0.0001	0.1768	0.7885
44	-benzyl	-H	89.26	95.42	104.85	99.40	0.0957	0.5882	0.3247	0.9979
45	-benzyl	-OCH ₃	39.58	54.85	84.41	95.28	0.0000	0.0000	0.0585	0.9010
46	-benzyl	-Cl	80.60	109.71	93.24	92.42	0.0700	0.3435	0.7116	0.9931
47	-benzyl	-Br	79.31	85.37	91.90	91.11	0.0456	0.0000	0.2589	0.4536
48	-p-fluoro benzyl	-H	59.55	92.02	92.69	93.24	0.0012	0.4955	0.6626	0.9979
49	-p-fluoro benzyl	-OCH ₃	52.00	92.06	105.67	105.33	0.0000	0.0124	0.1202	0.7249
50	-p-fluoro benzyl	-Cl	40.52	46.74	96.32	109.39	0.0000	0.0000	0.3942	0.3171
51	-p-fluoro benzyl	-Br	45.69	46.37	97.05	106.44	0.0000	0.0000	0.5654	0.6023
52	-3,4-difluorobenzyl	-H	73.53	92.77	85.60	101.92	0.0190	0.8907	0.3750	0.9918
53	-3,4-difluorobenzyl	-OCH ₃	33.53	43.94	86.09	95.01	0.0000	0.0000	0.0748	0.8098
54	-3,4-difluorobenzyl	-Cl	65.13	70.69	91.71	90.78	0.0000	0.0003	0.3661	0.4076
55	-3,4-difluorobenzyl	-Br	66.23	75.12	93.55	95.20	0.0000	0.0009	0.5591	0.8262
56	-3,4-dichlorobenzyl	-H	84.14	91.57	104.71	99.27	0.1014	0.6394	0.9074	0.9998
57	-3,4-dichlorobenzyl	-OCH ₃	86.39	90.78	90.94	106.51	0.0110	0.2980	0.3872	0.8039
58	-3,4-dichlorobenzyl	-Cl	73.06	72.70	100.18	115.78	0.0001	0.0022	1.0000	0.2061
59	-3,4-dichlorobenzyl	-Br	81.31	71.81	94.90	100.67	0.0016	0.0018	0.7792	0.9997

benzimidazoles differentially. Analysis by GRcalculator tool indicated that p-fluorobenzyl R₁ group was one of the most effective R₁ moiety outstanding from the rest of the substitutions (p-value: 0.023) and other cyclic aromatic side chain groups (p-value: 0.012) (Fig. 3; Fig. A.1). In addition to the p-fluorobenzyl, the substitutions of methyl (as in compound 27) and propyl on R₁ exhibited anti-proliferative trends.

3.2.2. Anti-cancer activity of selected compounds on different cell lines

Upon analysis of Table 2, we selected, for further screening, several compounds that were highly effective in reducing viability at the highest dose 40 μM (compounds: 23 (24.36%); 27 (40.38%); 29 (44.16%); 35 (26.90%); 36 (32.85%); and 37 (43.76%)); 40 (42.19%); 45 (39.58%); 48 (59.55%); 49 (52.00%); 50 (40.52%); 51 (45.69%); 53 (33.53%) and a control molecule with relatively less cytotoxic activity (compound 46 (80.60%)). Among these, 48–51 spanning the full -p-fluorobenzyl series exhibited similar activity at 40 μM whereas 50 and 51 were also significantly antiproliferative at a relatively lower concentration of 16 μM along with another related compound 53 containing 3,4-difluorobenzyl group. In the wider dose panel, IC₅₀ values of these 13 molecules across multiple cell lines (Table 3) were studied along with *n*-way ANOVA. Overall, R₁ chain (p-value < 2e–16) had

significant effects on viability while the effect of the R₂ side chain was also significant (p-value < 2e–16) and varied depending on the type of R₁ (R₁×2 interaction p-value < 2e–16). Moreover, there was also a significant cell line effect (p-value: 2.62e–08) as well as a treatment effect (p-value < 2e–16). Additional analyses with two-way ANOVA and multiple comparison tests have implied possible trends by cell line and R₂ (Table 3; Fig. 4; Fig. A.3; Fig. A.4). Cell line specific effects in response to treatments were observable via Principal Component Analysis (PCA) where both MCF-7 and HEPG2 lines interestingly yielded parallel profiles in comparison to MDA-MB-231 (Fig. 4). PCA showed that E2 responsive cell lines MCF-7 and HEPG2 were more similar to each other than they were to the ER- MDA-MB-231 cells at lower concentrations (up to 16 μM) while at the highest dose tested (40 μM) each cell line assumed a relatively distinct response profile. In particular, the compound 53 exhibited low IC₅₀ values for the TP53 wild-type MCF-7 and HEPG2 cells (19.23 μM and 24.10 μM, respectively) while it was not as effective in MDA-MB-231, a cell line with a mutant TP53 allele. In accord with two-way ANOVA comparisons, most of the candidate compounds exhibited a cell-line dependency, but not compound 37 with butyl (R₁) and -H (R₂) substitutions (Table 3; Fig. A.4). Nonetheless, GRcalculator assessments showed that MCF-7 was the cell

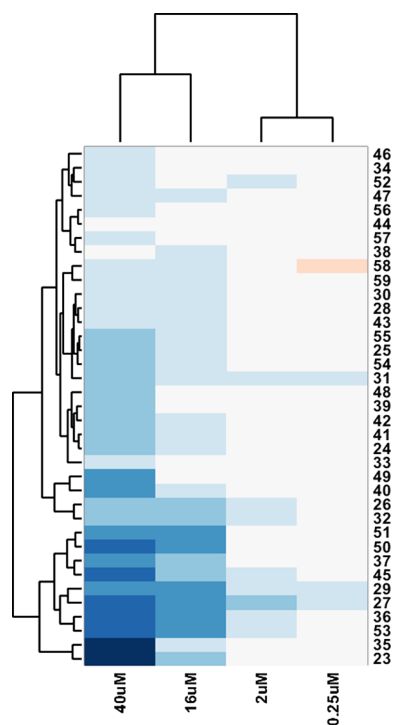


Fig. 2. Hierarchical clustering of anti-cancer activity of the novel indole-benzimidazoles. Darker tones of blue indicate stronger inhibition of cell growth. Euclidean distance and complete linkage were used for clustering (MATLAB®).

line that seemed to be affected the most by the compounds, whereas -Br carrying R_2 moieties on the Table 2 compounds were also observed to have more effect on viability (Fig. A.2; Fig. A.3). After obtaining the toxicity data, we continued with docking studies and transcriptomic

analyses in order to get an understanding on the mechanisms of action.

3.3. Molecular docking studies

Structurally related R_1 groups with relatively high potencies were taken into docking analyses. On the basis of the literature on indoles and benzimidazoles as well as PCA clusters in this study, we primarily focused on ER α , and assessed dockings of R_1 :p-fluorobenzyl derivatives and **53**. Compound based statistical comparisons between the cell lines were also in accord with these observations (Fig. A.2). Our indole-benzimidazole derivatives tended to exhibit increased affinity to ER α , VEGFR2, and tubulin rather than the other ones which were discussed in Section 2.3, such as Protein kinase C beta II, glycogen synthase kinase 3, Platelet-derived growth factor receptor beta.

Based on the structural analysis (Fig. 5) ER α ligand binding domain mainly consists of hydrophobic residues. Therefore, utilization of hydrophobic moieties such as indole and benzimidazole may play a key role in inhibiting or activating this receptor. The binding mode of 4-hydroxytamoxifen with ER α suggested that a hydrogen donor group could be important for H-bond interaction with polar residue Gly521 in this cavity. This interaction's distance was 2.28 Å. In the literature, these residues including Glu353, Arg394, Phe404 and Lys529 take part in the modulation of this receptor. Hydrophobic interactions with Phe404 and Trp383, H-bond interactions with Glu353 and Arg394, also a salt bridge interaction with Asp351 are important according to both bazedoxifene and 4-hydroxytamoxifen's patterns [64]. List of molecular properties and ER α docking energies for all compounds were given in Table A. 10.

One of the prominent compounds that stood out in transcriptomic analyses, compound **51**, created halogen bond interactions with both Glu353 and Arg394. In the case of the another potent ligand **53**, Phe404 joins a Pi-Pi interaction with an indole ring while the sulfonyl group acts as the hydrogen bond donor (Fig. 6). Both ligands have provided necessary interactions in the reference study. Their energy values were relatively close to that of standard compound bazedoxifene.

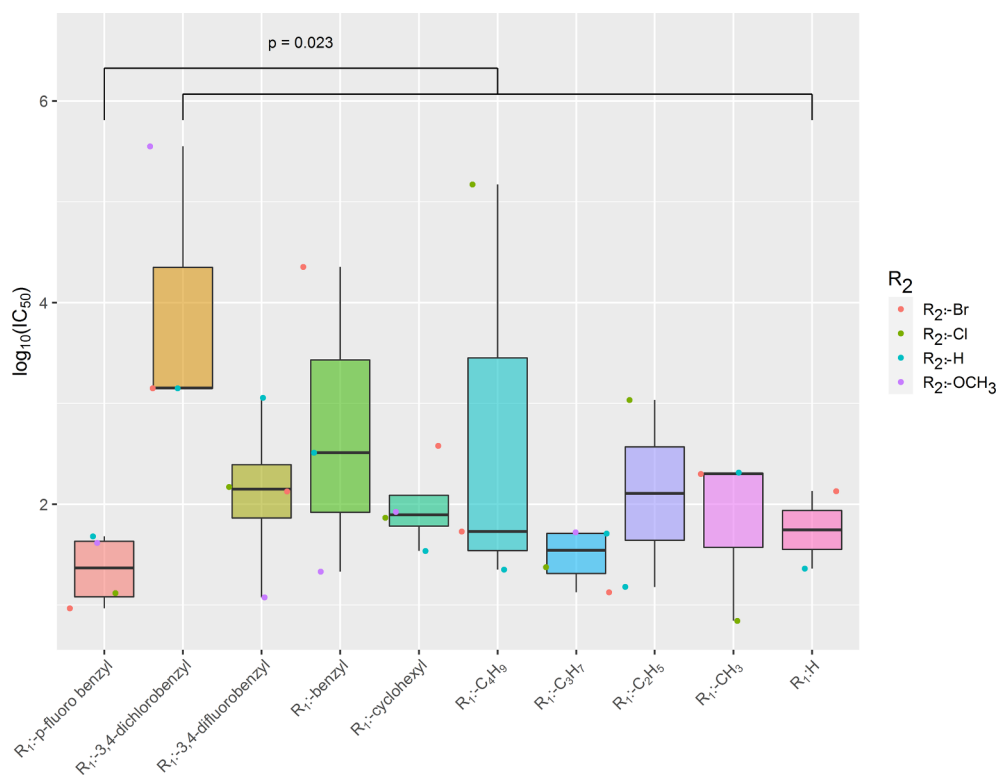


Fig. 3. Log₁₀(IC₅₀) based representation and comparison of R_1 carrying derivatives (GRcalculator tool was used for this purpose and comparisons between all derivatives versus p-fluorobenzyl substituted compounds were made with a built-in one-sided Wilcoxon rank-sum test).

Table 3

IC₅₀ (μM) values and two-way ANOVA cell line specific p-value for each selected candidate tested on MCF-7, MDA-MB-231 and HEPG2 cells (NA: Unmeasurable IC₅₀ values, ns: not significant).

Comp.	IC ₅₀			Cell line effect p-value	Comp.	IC ₅₀			Cell line effect p-value
	MCF-7	MDA-MB-231	HEPG2			MCF-7	MDA-MB-231	HEPG2	
23	42.9536	51.4043	47.9733	< 0.0001	45	32.2849	22.3872	9.9540	< 0.0001
27	5.71	NA	NA	< 0.0001	46	43.4510	10.9396	89.54	< 0.0001
29	89.3305	NA	73.7904	< 0.0001	48	27.2270	20.8450	78.70	< 0.0001
35	54.4503	126.7652	32.7341	< 0.0001	49	39.5367	44.2588	41.11	< 0.0001
36	15.7398	49.8884	7.8163	< 0.0001	50	18.0717	36.1410	58.6138	< 0.0001
37	30.4089	66.6807	31.5500	0.3538 (ns)	51	35.1560	38.2825	17.2584	< 0.0001
40	40.2717	76.9130	NA	< 0.0001	53	19.2309	NA	24.0991	< 0.0001

According to the glide docking score results in Table 4, compounds 48, 49 and 51 have exhibited favorable affinity value against ER when compared with those against tubulin and vEGFR2.

3.4. Gene level alterations upon exposure to indole-benzimidazoles

3.4.1. Transcriptomics analysis of compounds 48–51 and 53

Based on Fig. 3, derivatives with p-fluorobenzyl and the structurally related compound 53 represented strong candidates for understanding the molecular mechanisms of action of the effective novel indole-benzimidazoles. For that purpose, we initiated gene level analyses in a parallel line with molecular docking studies. *Limma* analysis of expression data obtained upon exposure to compound 51 demonstrated that MCF-7 transcriptome was significantly modulated leading to up-regulation and downregulation of a considerable number of genes (Fig. 7; Table 5).

Additionally, the STRING protein-protein interaction network and KEGG pathway analyses for the compound 51 were implemented to reveal various molecular pathways that might be involved in the anticancer effects of the derivatives (Table A. 2). Accordingly, stress mechanisms, apoptosis and ferroptosis, as well as p53 and cellular signaling via MAPK pathway, were observed in addition to the metabolic process of aminoacyl-tRNA biosynthesis. List of these pathways were also common when the gene signatures of the compounds 50, 51 and 53 are compared, confirming similarity of the derivative exposures on molecular level (Table A. 3). In addition to that, overall comparisons with all the microarrayed compounds together resulted in a relatively limited set of mutual pathways such as cell cycle and DNA replication (Table A. 4) which might be due to milder effects on the expression by

the compounds 48 and 49 at 20 μM. Candidate pathways as well as dose-dependent effects were further taken into account in understanding the mechanisms of action of these derivatives. We compared the expression profiles of compounds 48–49 with those of 50–51–53 showing that 553 genes were differentially expressed between these two groups (adjusted p-value < 0.05). Pathway enrichment by STRING – Reactome Pathways demonstrated that compounds 50–51–53 led to significantly more reduction in expression of genes related with cell cycle and ESR1 signaling while increasing the stress response in MCF-7 cells (Fig. A.5; Table A. 5).

3.4.2. LINC analysis

Query of the top 150 up- and 150 down-regulated genes by 51 against a large collection of compounds, gene knockdown and gene overexpression datasets obtained from MCF-7 cells was performed using LINC database and the most positively and negatively correlated compounds were provided (Table 6; Table A. 6). Among the compounds most similar to 51 were the inhibitors of various classes such as ER antagonists, calcium channel inhibitors (niguldipine, an amino acid (AA) response/integrated stress response activator [65]), tubulin and microtubule inhibitors. Besides, three out of the top ten compounds also were carrying indole or benzimidazole backbones. Interestingly, the top compound oxindole-I and an ER antagonist, i.e., ZK-164015, were among them. Many of the tubulin and microtubule inhibitors from this analysis were also found to carry either an indole or benzimidazole scaffold (Table A. 6).

3.4.3. Comparative transcriptomics

Comparative transcriptomics analysis of the selected indole-

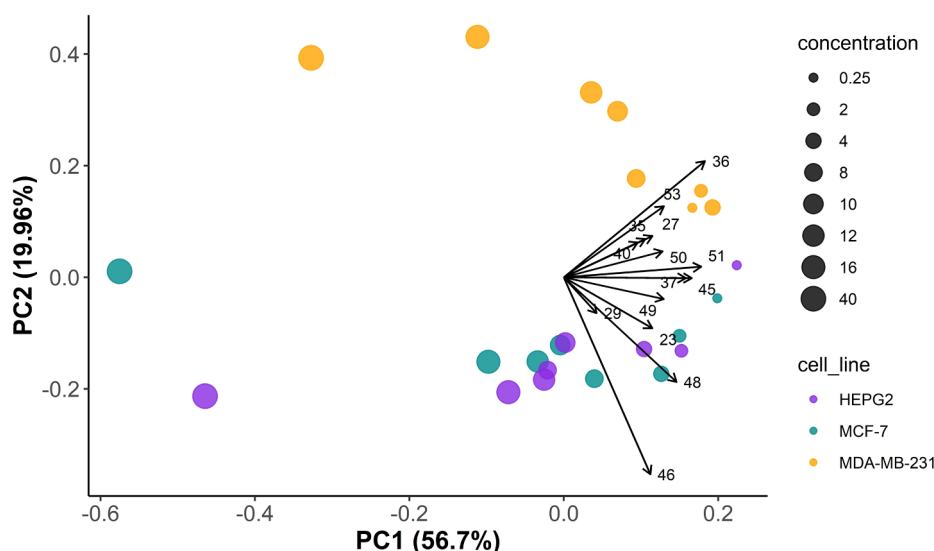


Fig. 4. PCA representation on cell viabilities of the cell lines upon exposure to varying concentrations of novel derivatives.

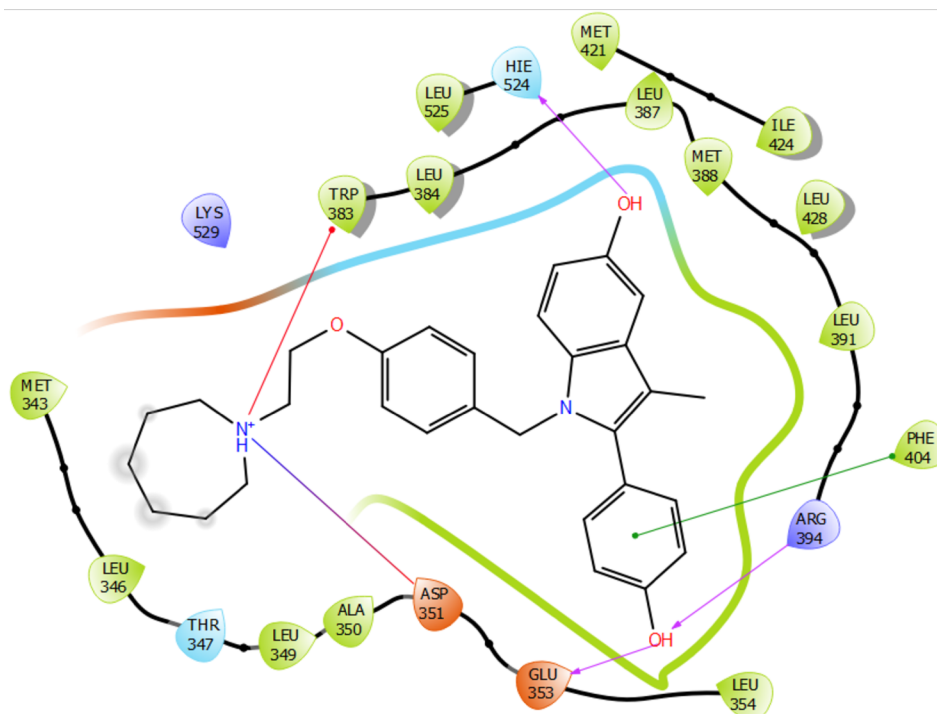


Fig. 5. 2D diagram of amino acid interactions of bazedoxifene with ER α ligand-binding domain. Hydrophobic interactions are shown as green, whereas the red line represents Pi-cation interactions. H-bond interactions are depicted as purple. Red-blue represents salt bridge interaction.

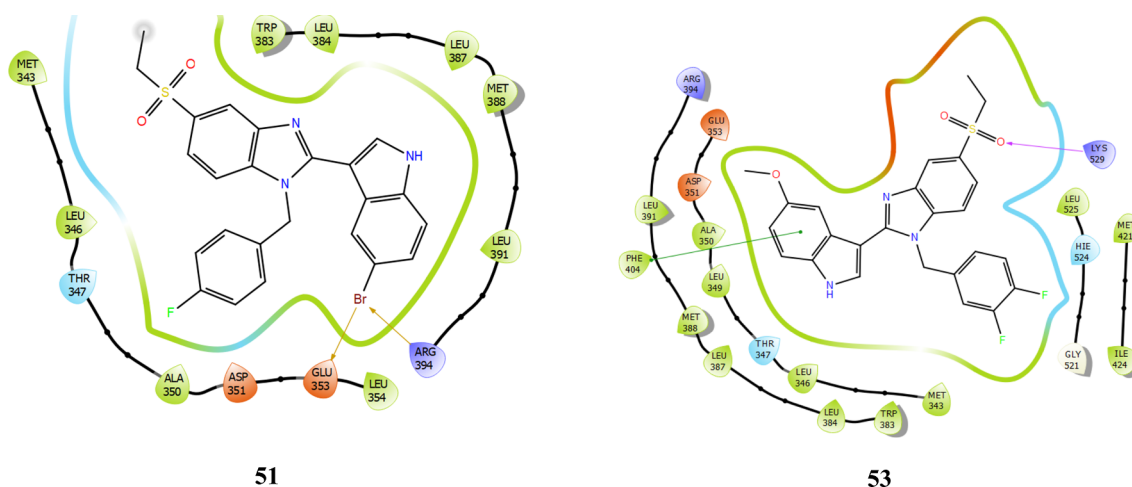


Fig. 6. 2D interaction diagrams of the two most potent compounds against MCF-7 and in microarray analyses. Brown arrow indicates halogen bond interaction and purple one indicate hydrogen bond interaction, whilst green line represents Pi-Pi steric interaction.

Table 4

Data showing the glide scores of microarrayed compounds against different proteins.

Compounds	ER α	Tubulin	vEGFR2 kinase domain
48	-7.776	-5.851	-6.348
49	-7.726	-5.575	-6.786
50	Unsuccessful binding	Unsuccessful binding	-6.435
51	-7.802	-5.458	-6.131
53	-6.610	-5.662	-6.813
Vincristine	-	-8.1	-
Tivozanib	-	-	-10.265
Bazedoxifene	-9.852	-	-

benzimidazoles was performed using public microarray datasets for AA (-) and exposure to E2/SERMs or dioxin, an aryl hydrocarbon activator known to be activated by plant-based estrogens [66–68]. This approach has further demonstrated a pattern of inverse correlation with E2 and positive correlations with SERMs, AhR/dioxin, and AA (-) signatures (Fig. 8). AA deprivation was the most closely associated treatment followed by dioxin and SERMs while indole-benzimidazoles formed the tightest cluster. Our results showed that novel indole-benzimidazoles exhibited transcript-level effects that were more pronounced than the generic SERMs on reverting E2 driven expression modulation. Furthermore, compounds 50, 51 and 53 were found in the same cluster while compounds 48 and 49 formed another cluster which was placed closer to the generic SERMs. In accord with this expression profile based clustering, compounds 48 (R₂: -H) and 49 (R₂: -OCH₃) had higher IC₅₀ values, thus lower drug effectivity than 50 (R₂: -Cl), 51 (R₂: -Br) and 53 (R₁: 3,4-difluorobenzyl; R₂: -OCH₃) (Fig. A.4).

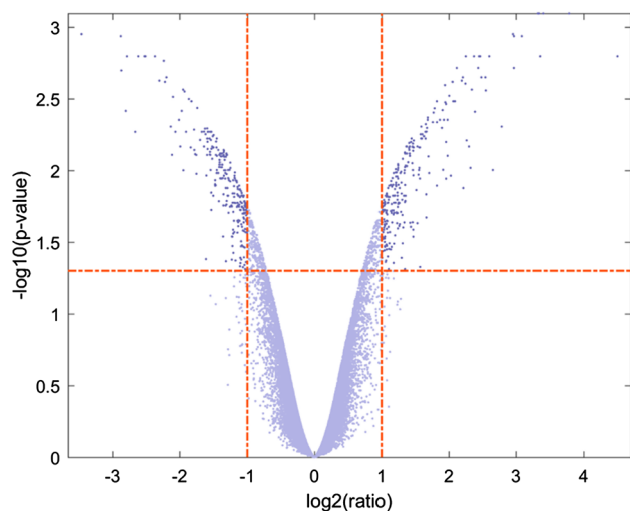


Fig. 7. Volcano plot of statistical significance against fold change between control and compound **51** treated MCF-7 cells. 546 genes were statistically altered more than two folds (adjusted p-value with FDR < 0.05).

To further investigate how expression profiles of novel indole-benzimidazole compounds relate with those obtained from E2 exposure, AA depletion and dioxin treatments, we performed KEGG pathway [69] enrichment analyses using GSEA [70,71]. The numbers of significantly affected genes between exposures to E2 and compound **51** were represented using a Venn diagram and enriched pathways were indicated (Fig. 9; p-value < 0.05 (compound **51** & E2)). According to the comparisons with E2 exposure in MCF-7 cells, the inversely associated signaling pathways included upregulation of TGF- β pathway and downregulation of DNA replication, cell-cycle, mismatch repair, pyrimidine metabolism, cysteine and methionine metabolism and spliceosome pathways by the novel indole-benzimidazole compounds. Mutually upregulated and downregulated pathways were provided in Table A. 7. Interestingly, the downregulation of similar pathways, but this time in the same direction, were observed in the comparisons performed with **51** versus AA (-), whereas dioxin versus **51** revealed involvement of steroid and amino acid related metabolisms, including downregulation of E2 signaling pathway. Furthermore, the term “ferroptosis” was enriched in mutually upregulated pathways for both dioxin and AA (-) and **51** profile. Fisher’s exact tests showed significance (Table A. 7).

3.4.4. Validation of molecular pathways by RT-QPCR in MCF-7 cells

High throughput comparative transcriptomic analysis led to the identification of several pathways and genes whose expressions were altered upon exposure to the novel derivatives as well as E2, one or more SERMs, dioxin or AA depletion. For validation by RT-QPCR, we

Table 5

The top 10 significantly altered genes in compound **51** treated samples. Adjusted (Adj.) p reflects the FDR corrected p-value, calculated with *limma*.

Downregulated				Upregulated			
Gene Symbol	LogFC	p-value	Adj.p value	Gene Symbol	LogFC	p-value	Adj.p value
FAM111B	-3.46	1.38E-07	0.001	SLC7A11	4.5	5.09E-07	0.002
IGFBP5	-2.87	1.21E-06	0.002	FAM129A	3.78	2.84E-08	0.001
GRPR	-2.8	4.62E-06	0.004	ERRF1	3.4	6.66E-08	0.001
TARP	-2.79	7.62E-07	0.002	MT1F	3.35	5.07E-07	0.002
GINS2	-2.62	7.15E-07	0.002	CLGN	3.35	4.34E-07	0.002
CCNE2	-2.52	4.74E-07	0.002	GDF15	3.33	6.56E-08	0.001
DTL	-2.51	5.47E-07	0.002	CYP1A1	3.31	5.57E-08	0.001
MCM10	-2.37	6.26E-07	0.002	SLFN5	2.97	1.83E-07	0.001
UCA1	-2.3	1.71E-06	0.002	DDIT3	2.97	1.11E-06	0.002
IL20	-2.23	8.91E-07	0.002	ANXA3	2.96	1.39E-07	0.001

Table 6

Top 10 ranking compounds that possess transcriptomic similarity with **51** in MCF-7 line. Compounds with either indole or benzimidazole moieties are given with bold characters.

Rank	Score	Name	Description
1	99.98	oxindole-1	VEGFR inhibitor
2	99.98	niguldipine	Calcium channel blocker
3	99.97	AG-592	Tyrosine kinase inhibitor
4	99.96	AG-879	Angiogenesis inhibitor
5	99.96	FCCP	Mitochondrial oxidative phosphorylation uncoupler
6	99.96	ZK-164015	ER antagonist
7	99.96	reserpine	Vesicular monoamine transporter inhibitor
8	99.96	PD-198306	MAP kinase inhibitor
9	99.96	CGK-733	ATR kinase inhibitor
10	99.96	suloctidil	Adrenergic receptor antagonist

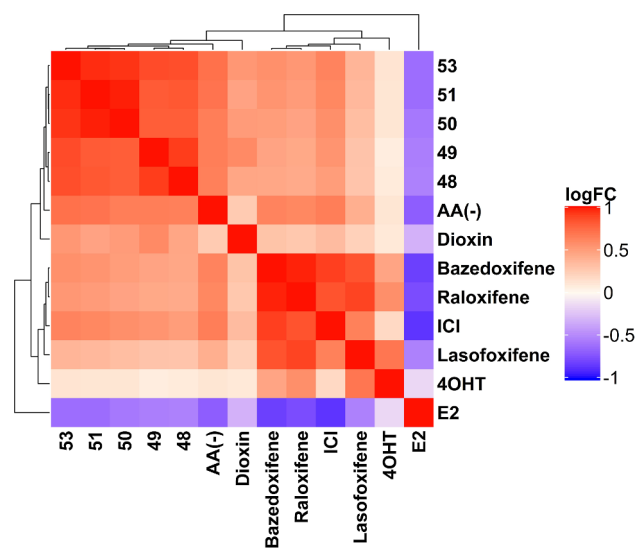


Fig. 8. Clustergram analysis of the pairwise-correlation between generic SERMs and compounds **48**, **49**, **50**, **51** and **53**. The genes were selected with the p-value (< 0.05) and log fold difference (> 1) cut-offs for compound **51**. Ward linkage and Euclidian distance were used for the clustering. Red indicates positive correlation while blue indicates negative correlation in between samples on the heatmap.

identified multiple genes that were modulated by E2, dioxin or AA deprivation and/or involved in cell cycle, integrated stress response, and drug metabolism (Fig. 10).

Our findings first showed that minor structural differences could contribute to detectable changes on the expression of the genes we analyzed (Fig. 10; Table A. 8; Table A. 9). For example, the compounds **49**, **50** and **51** have influenced *CDKN1A* expression remarkably, while

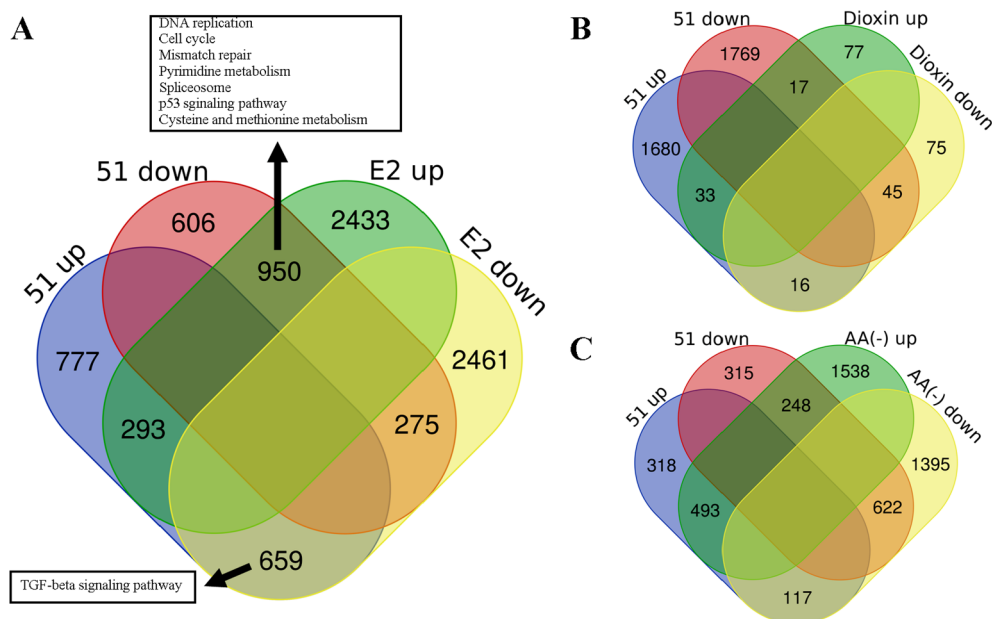


Fig. 9. KEGG pathway enrichment analysis results for Compound 51 and (A) E2, (B) Dioxin and (C) AA (-). Significantly enriched (p -value < 0.05) genes and related pathways that are mutually affected are depicted, especially for E2 comparisons. Fisher's exact p -values are (A) < $2.2e-16$, (B) $4.415e-05$ and (C) < $2.2e-16$. Detailed list of enriched pathways (for A, B and C) and the contingency table for the comparisons are provided in Table A. 7.

the compound **48** (R_1 : -H) was less effective. Moreover, compounds **51** and **53** caused significant decreases in *ANLN* expression and **48** and **50** were additionally more effective in altering the levels of *WDHD1*. Interestingly, *GADD45A* expression was modulated by compounds **48**, **50** and **51** while compound **49** did not lead to overexpression of *GADD45A*. Compound **53** containing 3,4-difluorobenzyl at R_1 position also induced *CDKN1A* and *GADD45A* expression while having reduced expression of cell cycle related genes (at both *ANLN* and *WDHD1*). Further taking GSE35428 and GSE7765 data into account, the exposures to E2 and indole-benzimidazole were found to be inversely associated implicating the derivatives investigated herein as E2 antagonists. In addition to the E2 signaling, *CYP1B1* and *HMOX1* were also upregulated by AhR agonist dioxin while changes in *DDIT3*,

SLC7A11 and *HMOX1* were similarly affected by indole-benzimidazoles and AA depletion which further suggested the involvement of multiple mechanisms in compound responses. Later analyses, where we compared gene expression levels of the primary E2 target genes, *CCND1*, *TFF1* and *PGR*, using different exposure concentrations (20 μ M vs 40 μ M), also presented additional confirmation on the dose-dependent relationship between the derivatives and E2 signaling (Fig. A.6). Here, only *TFF1* gene represented a dose-dependent difference (p -value: 0.0207) whereas *CCND1* and *PGR* did not (p -values: 0.6284 and 0.4252, respectively). Moreover, the microarray and RT-QPCR experiments performed with doses of 20 μ M and 40 μ M respectively, had shown that compounds **50**, **51** and **53** yielded stronger effects on the expression of these genes. However, a 40 μ M exposure to **48** or **49**

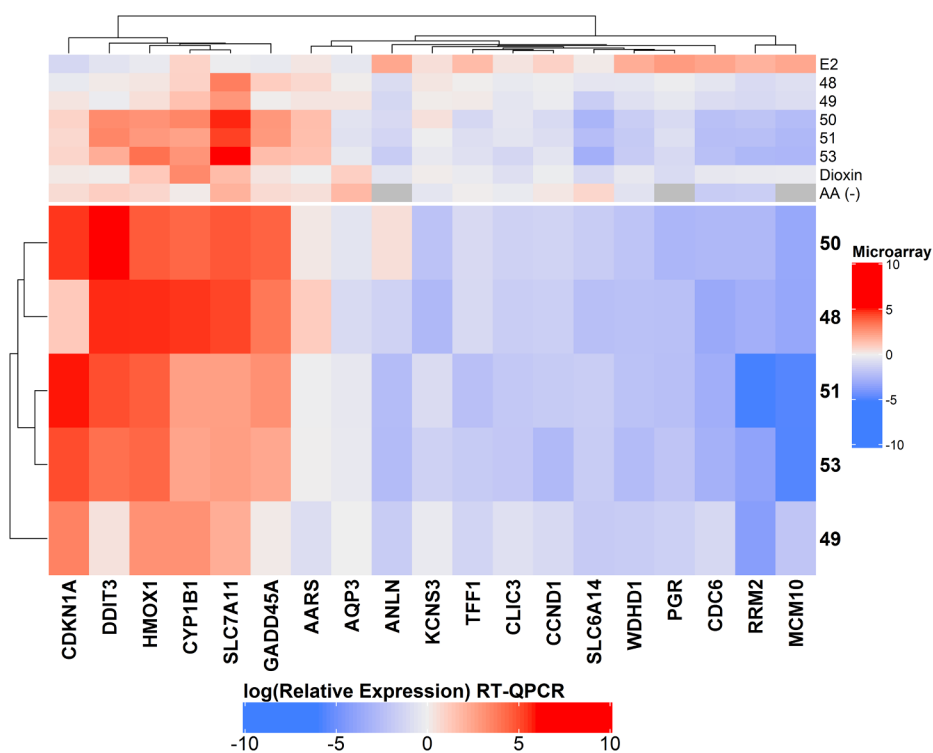


Fig. 10. Validation of selected AhR/dioxin, integrated stress response/AA (-), and E2/SERM modulated genes by RT-QPCR in MCF-7 cells exposed to the compounds **48**, **49**, **50**, **51** and **53** for 24 h at 40 μ M. Relative quantity (RQ) values are depicted in log₂ and color scale (blue-to-red (negative-to-positive)). *TPT1* is used as the house-keeping gene; along the x-axes, the compound names were given. Top annotation values are gathered from three different public datasets and our own microarray data; and log fold change values are represented for the corresponding genes in a color scale (blue-to-red (negative-to-positive)) where gray points represent missing values due to microarray platform used in aminoacid depletion study. Exact log₂ relative quantity values and significance signs can be accessed in Table A. 8 and Table A. 9. (For interpretation of the references to colour in this figure legend, the reader is referred to the web version of this article.)

exhibited similar responses when compared with the other three molecules investigated, suggesting a dose-dependent increase in transcriptional response.

4. Discussion

In the present study, we have synthesized and characterized a set of novel indole-benzimidazoles carrying benzene sulphonyl structures, to assess their cytotoxicity, structural affinity to potential targets (mainly ER), molecular expression profiles and association with the regulators of anticancer pathways. Accordingly, we found most of our compounds significantly reduced the cell viability of ER+ MCF-7 cells, especially at a concentration equaling to 40 μ M. In addition, we have utilized different statistical tools to understand the structure-activity relationships (SARs) better. For that purpose, we have analyzed our data using ANOVA and multivariate techniques such as PCA and hierarchical clustering which proved valuable to make distinctions among the compounds with respect to dose, molecular group, and cell line differences. Regarding the substitutions (Table 1 & Table 2), both R₁ and R₂ groups were found to be important in altering the anticancer effect of the indole-benzimidazole scaffold. However, there was a significant interaction between these two groups of which future studies should take into consideration.

Structurally related R₁ group members (48, 49, 50 and 51) exhibited single position changes yet showed differential anti-proliferative activity on MCF-7 cells. In addition, this group had the lowest average IC₅₀ values when compared with the other molecule series warranting further analyses. Our strategy also involved differential expression profiling of MCF-7 cells exposed to compound 51 exhibiting the lowest growth inhibition at 16 μ M, along with compound 50, followed by stringent transcriptomics comparisons across full series and with an additional related compound 53 from R₁:3,4-difluorobenzyl group, exhibiting even stronger anti-proliferative effects towards E2 responsive cell lines. Future studies should consider extending the above mentioned approach to other compound series and cell lines with differing characteristics to better understand the molecular mechanisms by which novel indole-benzimidazoles exert their effects.

The differences observed in cell viability profiles can be due to multiple factors, such as the dose and/or tissue specificity (breast vs. liver) as well as the cell line's batch, molecular receptor status (e.g., ER and AhR) and pathway activity (e.g., TP53 and AA (-) stress). For example, compound 53, whose microarray-based molecular effects (20 μ M) closely resembling those of compounds 50 and 51 in MCF-7 cells, might lead to a different expression profile in the ER-/TP53 mutant MDA-MB-231 cell line, exhibiting lower sensitivity to 53. On the other hand, a compound which is similarly active in the breast cancer cells based on IC₅₀ values can be more active in another batch or type of cancer cell line, as in the case of compound 51. In conclusion, although our structural models have suggested potential affinity to ER for compounds 51 and 53, a comparative transcriptomics approach further demonstrated that downstream molecular effects of these novel indole-benzimidazoles are likely to be driven via multiple routes/pathways (e.g., AhR), and not just ER. This notion can further explain the observed cell- and dose-dependent differences in anti-cancer activity.

Taking the docking results into account, one possible reason of the higher activity shown by compounds 51 and 53's could be the increased amount of halogen bond (a type of H-bond) interactions. Also, the presence of bromine group may enhance lipophilic characteristic of indole moiety creating a more successful binding pattern. Therefore compound 51 was elected as a possible candidate for future assessment and pharmacokinetic development studies. Unsuccessful ER binding profile obtained for the compound 50 was an unexpected case, considering its similarity to the compounds 51 and 53 based on the gene expression and cytotoxicity results obtained. Although the situation here is suggestive for alternative binding profiles towards ER or other protein targets, such cases demand further re-evaluations, primarily *in*

silico. In addition, glide scores overall yielded positive results, even though observed affinity levels were lesser in the derivatives than the standard compounds, meaning that the derivatives had the tendency to form stable ligand-protein complexes with ER α . Moreover, it was clear that ER α might not be the only binding target of the derivatives, but also some other proteins in inducing cell death. Nevertheless, in this current study, *in silico* findings and literature investigations [72,73] nominate ER α as the most favorable indole-benzimidazole target in comparison to ER β , tubulin and vEGFR.

Aside from docking studies, the expression profiling of compounds 48–51 (R₁:p-fluorobenzyl; R₂:-H, -OCH₃, -Br, -Cl) and 53 (R₁:3,4-difluorobenzyl; R₂:-OCH₃) and comparative transcriptomics with public datasets have significantly increased our understanding of the molecular mechanisms mediating the effects of indole-benzimidazoles in ER + breast cancer cells. The use of comparative transcriptomics and RT-QPCR analyses further validated and supported our findings. Previously, altered expression of cell cycle, DNA replication, endoplasmic reticulum stress and DNA damage response-related processes have been reported in MCF-7 cells when exposed to CTet, an indole-3-carbinol derivative [74,75]. However, herein we, for the first time, show significant and positive associations between the expression profiles of indole-benzimidazoles and those of the selected ER antagonists, AhR agonist dioxin, and AA deprivation. Furthermore, these comparative transcriptomics approaches implicate indole-benzimidazoles in simultaneous modulation of multiple cancer-relevant pathways leading to a strong anticancer behavior in a dose-dependent manner, where the effects were more profound for 50, 51 and 53 at 20 μ M, than the compounds 48 and 49.

STRING analyses have shown that stress mechanisms, aminoacyl-tRNA metabolism and ferroptosis might be involved in these anti-cancer effects. For instance, aminoacyl-tRNA metabolism can be driven by steroids and sex hormones in breast cancer where the ER status of the cancer matters in cell proliferation rate, in return [76–78]. In addition, AA deprivation can affect the charging status of specific tRNA iso-acceptor, underlying interaction between abundant amino acids in the environment which further influences the efficiency of the translation processes [79,80]. The transcriptomic similarity between our derivatives and AA deprivation profiles further supports the involvement of aminoacyl-tRNA biosynthesis pathway where ER modulation can influence this pathway. Interestingly, aminoacyl-tRNA metabolism and AA signaling have regulatory roles also in ferroptosis which can further explain the selected derivatives' anti-cancer responses [81–83].

GSEA results also helped identify the conserved and associated alterations in the molecular/cellular pathways driven by 51 and E2, dioxin or AA (-) exposures. Results pointed to some shared mechanisms among the treatments that have been previously indicated with cancers. Among the associated pathways, TGF- β and cell cycle pathways have been widely studied while pyrimidine metabolism is one of the pathways more recently gained attention in breast cancer therapy [84,85]. Inversely correlated signatures between E2 and AA(-) further underlined the close relationship between amino acid metabolism and ER signaling [86]. Besides that, downregulation of ER signaling was a mutual mechanism between 51 and dioxin exposures further underlying ER modulatory roles for the indole-benzimidazoles and AhR signaling [66,68]. Moreover, aminoacyl and AA-related pathways, as well as ferroptosis, were among the enriched terms across multiple dataset comparisons strongly pinpointing crucial roles in the downstream effects of indole-benzimidazole derivatives.

Additionally, transcriptomic signature of the compound 51 had remarkable similarities with certain LINCS database compounds that were screened in MCF-7 cells. At the top of the most similar compounds was a multitargeting compound oxindole-I, which also carries an indole moiety and constitutes the pharmacophore of the drug sunitinib [87]. Derivatives of this compound have been found to be involved in generation of oxidative stress leading to cell death [88]. In support of that, double-stranded RNA-dependent protein kinase (PKR) that mediates

stress responses can be targeted by an imidazole-oxindole type derivative (C16 compound) also mediating ferroptosis in the end [89]. Additionally, its derivative compound sunitinib shares similar features on cell death with sorafenib, another known ferroptotic agent [90,91]. The presence of oxindole structure can also affect the aryl hydrocarbon receptor which is in a strong relationship with stress pathways, ferroptosis, amino acid metabolism and ER signaling [92–96]. Transcriptomic similarity with dioxin further supports the involvement of this pathway and others in downstream effects of indole-benzimidazole exposure. The second top hit compound, niguldipine, is a calcium channel blocker that can lead to unfolded amino acid stress response and ferroptosis [65,97]. One of the other top hit compounds were FCCP, a mitochondrial oxidative phosphorylation uncoupler and again a ferroptosis inhibitor [98], and ZK-164015, an ER antagonist containing an indole moiety. Moreover, the transcriptional profile of reserpine, another indole carrying structure, which also strongly influences the Nrf2-mediated anti-oxidative stress pathway [99] also has exhibited significant similarity with compound 51. The presence of indole or benzimidazole backbones in multiple ER modulators and tubulin inhibitors strongly supported the notion for the involvement of tubulin related mechanisms in response to indole-benzimidazole derivatives [100–102]. Even though *in silico* docking results revealed low potency of the derivatives in tubulin binding, actual binding and affinity profiles should be further tested via *in situ* experiments.

In this study we have identified several effective novel indole-benzimidazole compound series and found out that some bearing p-fluorobenzyl and alkyl groups on R₁ were active at concentrations lower than 40 μM. In addition, molecular profiling of five related compounds with varying anti-proliferative efficacies enabled us to address the association between levels of anti-proliferation and gene expression modulation. Molecular pathways contributing to drug efficacy included unfolded protein/stress response, cytosolic tRNA aminoacylation, ESR1 signaling and cell cycle. Accordingly the chemical structure of the relatively more active compounds 50, 51 and 53 could be used as templates for future designs.

Among the screened compounds, substitutions on R₂ were restricted to four bases only, and the alterations on R₂ moieties were able to affect the potency of R₁ bearing scaffolds differentially, suggesting that a wider scale of R₂ based substitutions holds potential for improvements in the activity levels. In addition to that, sulfonyl side chain groups were limited with ethyl substitutions only. Therefore, applications of other alkyl moieties as well as aryl groups demand further experiments [103]. In addition, *N*-benzylation of the derivatives could also enhance their activity levels [39].

Moreover, indole aryl sulfonamides are also known to act as aromatase inhibitors in ER+ MCF-7 cell line [103]. Accordingly, our novel compounds carrying these functional groups can exhibit similar activity with steroid based aromatase modulators warranting further study.

5. Conclusions

In conclusion, cellular, structural as well as comparative transcriptomic approaches have enabled us to gather valuable insights into the pharmacological action of the novel derivatives generated in this study. Analyzing the lead compounds in detail we have identified their antiestrogenic effects as well as novel mechanisms involving aminoacyl-tRNA metabolism, AA depletion mediated integrated stress response, ferroptosis and AhR pathway, all of which have not previously been assigned for indole-benzimidazoles. Our study has brought about the possibility that the derivatives can also have the ability to target multiple genes/pathways. Elucidation of the targets requires further study including advanced modeling approaches and functional interventions at the molecular level.

Some important SARs emerging from the present study could also be summarized as follows: indole-benzimidazoles that have either p-

fluorobenzyl or small alkyl groups at their R₁ position in addition to electron-withdrawing groups in R₂ might have relatively more effective anticancer activities. The compound 51 containing p-fluorobenzyl at R₁ position and -Br at R₂ position was one of the prominent compounds against MCF-7 cells as validated by microarray analyses as well as docking studies. Although the limited range of sample size and interaction between side-chain moieties obscure more definitive conclusions, applied statistical approaches underline the nature of R₁ and R₂ groups and their effects on multiple cell lines. Therefore, not only p-fluorobenzyl, but also difluorobenzyl (53), methyl (27) and propyl substitutions (36) on R₁ might warrant future studies where genotypes of the samples and applicable doses should be taken into account.

Binding profiles of the derivatives also supported the notion that there can be multiple targets involved in their cytotoxic action. As we have seen here, the derivatives can play roles as SERMs, tubuline inhibitors, as well as modulators of amino acid metabolism, AhR signaling, and ferroptosis. The relevance of these derivatives as significant antiestrogen molecules demands functional investigations which will clearly provide useful information in the therapy of breast cancer.

Declaration of Competing Interest

The authors declare that they have no known competing financial interests or personal relationships that could have appeared to influence the work reported in this paper.

Acknowledgements

The work was supported by TUBITAK (grant number: 1001 - 213S037).

Appendix A. Supplementary material

Supplementary data to this article can be found online at <https://doi.org/10.1016/j.bioorg.2020.103929>. These data include MOL files and InChIKeys of the most important compounds described in this article.

References

- [1] V.N.R. Gajulapalli, V.L. Malisetty, S.K. Chitta, B. Manavathi, Oestrogen receptor negativity in breast cancer: a cause or consequence? *Biosci. Rep.* 36 (6) (2016).
- [2] I. Paterni, C. Granchi, J.A. Katzenellenbogen, F. Minutolo, Estrogen receptors alpha (ERα) and beta (ERβ): subtype-selective ligands and clinical potential, *Steroids* 90 (2014) 13–29.
- [3] H.-R. Lee, T.-H. Kim, K.-C. Choi, Functions and physiological roles of two types of estrogen receptors, ERα and ERβ, identified by estrogen receptor knockout mouse, *Lab. Anim. Res.* 28 (2) (2012) 71–76.
- [4] M. Madeira, A. Mattar, A.F. Logullo, F.A. Soares, L.H. Gebrim, Estrogen receptor alpha/beta ratio and estrogen receptor beta as predictors of endocrine therapy responsiveness—a randomized neoadjuvant trial comparison between anastrozole and tamoxifen for the treatment of postmenopausal breast cancer, *BMC Cancer* 13 (1) (2013) 425.
- [5] M. Kian Tee, I. Rogatsky, C. Tzagarakis-Foster, A. Cvorov, J. An, R.J. Christy, K.R. Yamamoto, D.C. Leitman, Estradiol and selective estrogen receptor modulators differentially regulate target genes with estrogen receptors α and β, *Mol. Biol. Cell* 15 (3) (2004) 1262–1272.
- [6] J. Russo, I.H. Russo, Toward a physiological approach to breast cancer prevention, *Cancer Epidemiol. Prevent. Biomarkers* 3 (4) (1994) 353–364.
- [7] E.V. Jensen, G. Cheng, C. Palmieri, S. Saji, S. Mäkelä, S. Van Noorden, T. Wahlström, M. Warner, R.C. Coombes, J.-Å. Gustafsson, Estrogen receptors and proliferation markers in primary and recurrent breast cancer, *Proc. Natl. Acad. Sci.* 98 (26) (2001) 15197–15202.
- [8] S. Mann, R. Laucirica, N. Carlson, P.S. Younes, N. Ali, A. Younes, Y. Li, M. Younes, Estrogen receptor beta expression in invasive breast cancer, *Hum. Pathol.* 32 (1) (2001) 113–118.
- [9] E.B.C.T.C. Group, Effects of chemotherapy and hormonal therapy for early breast cancer on recurrence and 15-year survival: an overview of the randomised trials, *Lancet* 365 (9472) (2005) 1687–1717.
- [10] T. Barkhem, B. Carlsson, Y. Nilsson, E. Enmark, J.-Å. Gustafsson, S. Nilsson, Differential response of estrogen receptor α and estrogen receptor β to partial estrogen agonists/antagonists, *Mol. Pharmacol.* 54 (1) (1998) 105–112.
- [11] J. An, C. Tzagarakis-Foster, T.C. Scharschmidt, N. Lomri, D.C. Leitman, Estrogen

- receptor β -selective transcriptional activity and recruitment of coregulators by phytoestrogens, *J. Biol. Chem.* 276 (21) (2001) 17808–17814.
- [12] P.D. Delmas, N.H. Bjarnason, B.H. Mitlak, A.-C. Ravoux, A.S. Shah, W.J. Huster, M. Draper, C. Christiansen, Effects of raloxifene on bone mineral density, serum cholesterol concentrations, and uterine endometrium in postmenopausal women, *N. Engl. J. Med.* 337 (23) (1997) 1641–1647.
- [13] J. Frasar, F. Stossi, J.M. Danes, B. Komm, C.R. Lyttle, B.S. Katzenellenbogen, Selective estrogen receptor modulators: discrimination of agonistic versus antagonistic activities by gene expression profiling in breast cancer cells, *Cancer Res.* 64 (4) (2004) 1522–1533.
- [14] J.S. Lewis-Wambi, H. Kim, R. Curpan, R. Grigg, M.A. Sarker, V.C. Jordan, The selective estrogen receptor modulator bazedoxifene inhibits hormone-independent breast cancer cell growth and down-regulates estrogen receptor α and cyclin D1, *Mol. Pharmacol.* 80 (4) (2011) 610–620.
- [15] S. Martinkovich, D. Shah, S.L. Planey, J.A. Arnott, Selective estrogen receptor modulators: tissue specificity and clinical utility, *Clin. Interv. Aging* 9 (2014) 1437.
- [16] Y.M. Yoo, E.B. Jeung, Melatonin-induced estrogen receptor α -mediated calbindin-D9k expression plays a role in H2O2-mediated cell death in rat pituitary GH3 cells, *J. Pineal Res.* 47 (4) (2009) 301–307.
- [17] F. Payton-Stewart, S.L. Tilghman, L.G. Williams, L.L. Winfield, Benzimidazoles diminish ERE transcriptional activity and cell growth in breast cancer cells, *Biochem. Biophys. Res. Commun.* 450 (4) (2014) 1358–1362.
- [18] N.V. Puranik, P. Srivastava, G. Bhatt, D.J.S.J. Mary, A.M. Limaye, J. Sivaraman, Determination and analysis of agonist and antagonist potential of naturally occurring flavonoids for estrogen receptor (ER α) by various parameters and molecular modelling approach, *Sci. Rep.* 9 (1) (2019) 7450.
- [19] X. Pang, W. Fu, J. Wang, D. Kang, L. Xu, Y. Zhao, A.-L. Liu, G.-H. Du, Identification of estrogen receptor α antagonists from natural products via in vitro and in silico approaches, *Oxid. Med. Cell. Longevity* 2018 (2018).
- [20] K.C. Chang, Y. Wang, P.V. Bodine, S. Nagpal, B.S. Komm, Gene expression profiling studies of three SERMs and their conjugated estrogen combinations in human breast cancer cells: insights into the unique antagonistic effects of bazedoxifene on conjugated estrogens, *J. Steroid Biochem. Mol. Biol.* 118 (1–2) (2010) 117–124.
- [21] E. March-Vila, L. Pinzi, N. Sturm, A. Tinivella, O. Engkvist, H. Chen, G. Rastelli, On the integration of in silico drug design methods for drug repurposing, *Front. Pharmacol.* 8 (2017) 298.
- [22] A.R. El, H.Y. Aboul-Enein, Benzimidazole derivatives as potential anticancer agents, *Mini Rev. Med. Chem.* 13 (3) (2013) 399–407.
- [23] E. Moriarty, M. Carr, S. Bonham, M.P. Carty, F. Aldabbagh, Synthesis and toxicity towards normal and cancer cell lines of benzimidazolequinones containing fused aromatic rings and 2-aromatic ring substituents, *Eur. J. Med. Chem.* 45 (9) (2010) 3762–3769.
- [24] S. Demiryayak, I. Kayagil, L. Yurttas, Microwave supported synthesis of some novel 1, 3-Diarylpiperazine [1, 2-a] benzimidazole derivatives and investigation of their anticancer activities, *Eur. J. Med. Chem.* 46 (1) (2011) 411–416.
- [25] S.M. Sondhi, R. Rani, J. Singh, P. Roy, S. Agrawal, A. Saxena, Solvent free synthesis, anti-inflammatory and anticancer activity evaluation of tricyclic and tetracyclic benzimidazole derivatives, *Bioorg. Med. Chem. Lett.* 20 (7) (2010) 2306–2310.
- [26] I. Kerimov, G. Ayhan-Kilcigil, B. Can-Eke, N. Altanlar, M. İscan, Synthesis, antifungal and antioxidant screening of some novel benzimidazole derivatives, *J. Enzyme Inhib. Med. Chem.* 22 (6) (2007) 696–701.
- [27] M. Rashid, A. Husain, R. Mishra, Synthesis of benzimidazoles bearing oxadiazole nucleus as anticancer agents, *Eur. J. Med. Chem.* 54 (2012) 855–866.
- [28] D. Sharma, B. Narasimhan, P. Kumar, V. Judge, R. Narang, E. De Clercq, J. Balzarini, Synthesis, antimicrobial and antiviral activity of substituted benzimidazoles, *J. Enzyme Inhib. Med. Chem.* 24 (5) (2009) 1161–1168.
- [29] B.V.S. Kumar, S.D. Vaidya, R.V. Kumar, S.B. Bhirud, R.B. Mane, Synthesis and anti-bacterial activity of some novel 2-(6-fluorochroman-2-yl)-1-alkyl/acyl/aryl-1H-benzimidazoles, *Eur. J. Med. Chem.* 41 (5) (2006) 599–604.
- [30] Ö.Ö. Güven, T. Erdoğan, H. Göker, S. Yıldız, Synthesis and antimicrobial activity of some novel phenyl and benzimidazole substituted benzyl ethers, *Bioorg. Med. Chem. Lett.* 17 (8) (2007) 2233–2236.
- [31] E. El-Sawy, F. Bassyouni, S. Abu-Bakr, H. Rady, M. Abdlla, Synthesis and biological activity of some new 1-benzyl and 1-benzoyl-3-heterocyclic indole derivatives, *Acta Pharmaceutica* 60 (1) (2010) 55–71.
- [32] N.I. Ziedan, F. Stefanelli, S. Fogli, A.D. Westwell, Design, synthesis and proapoptotic antitumor properties of indole-based 3, 5-disubstituted oxadiazoles, *Eur. J. Med. Chem.* 45 (10) (2010) 4523–4530.
- [33] N. Misra, R. Luthra, S. Kumar, Enzymology of indole alkaloid biosynthesis in *Catharanthus roseus*, *Indian J. Biochem. Biophys.* 33 (4) (1996) 261–273.
- [34] T. Golob, R. Liebl, E. von Angerer, Sulfamoyloxy-substituted 2-phenylindoles: antiestrogen-based inhibitors of the steroid sulfatase in human breast cancer cells, *Bioorg. Med. Chem.* 10 (12) (2002) 3941–3953.
- [35] R. Mohan, M. Banerjee, A. Ray, T. Manna, L. Wilson, T. Owa, B. Bhattacharyya, D. Panda, Antimitotic sulfonamides inhibit microtubule assembly dynamics and cancer cell proliferation, *Biochemistry* 45 (17) (2006) 5440–5449.
- [36] B.G. Trogden, S.H. Kim, S. Lee, J.A. Katzenellenbogen, Tethered indoles as functionalizable ligands for the estrogen receptor, *Bioorg. Med. Chem. Lett.* 19 (2) (2009) 485–488.
- [37] K. Shah, S. Chhabra, S.K. Shrivastava, P. Mishra, Benzimidazole: a promising pharmacophore, *Med. Chem. Res.* 22 (11) (2013) 5077–5104.
- [38] Y. Bansal, O. Silakari, The therapeutic journey of benzimidazoles: a review, *Bioorg. Med. Chem.* 20 (21) (2012) 6208–6236.
- [39] R. Singla, K.B. Gupta, S. Upadhyay, M. Dhiman, V. Jaitak, Design, synthesis and biological evaluation of novel indole-benzimidazole hybrids targeting estrogen receptor alpha (ER- α), *Eur. J. Med. Chem.* 146 (2018) 206–219.
- [40] A. Adejare, I. Mercier, Z. Ates-Alagoz, Compounds and compositions for treatment of breast cancer, Google Patents, 2018.
- [41] E.-Y. Moon, S.-K. Seong, S.-H. Jung, M. Lee, D.-K. Lee, D.-K. Rhee, S. Pyo, S.-J. Yoon, Antitumor activity of 4-phenyl-1-arylsulfonylimidazolidinone, DW2143, *Cancer Lett.* 140 (1–2) (1999) 177–187.
- [42] Z. Ates-Alagoz, N. Coleman, M. Martin, A. Wan, A. Adejare, Syntheses and in vitro anticancer properties of novel radiosensitizers, *Chem. Biol. Drug Des.* 80 (6) (2012) 853–861.
- [43] H. Goeker, M. Alp, Z. Ates-Alagoz, S. Yıldız, Synthesis and potent antifungal activity against *Candida* species of some novel 1H-benzimidazoles, *J. Heterocycl. Chem.* 46 (5) (2009) 936–948.
- [44] H. Göker, C. Kuş, D.W. Boykin, S. Yıldız, N. Altanlar, Synthesis of some new 2-substituted-phenyl-1H-benzimidazole-5-carbonitriles and their potent activity against *Candida* species, *Bioorg. Med. Chem.* 10 (8) (2002) 2589–2596.
- [45] Z. Ates-Alagoz, C. Kuş, T. Çoban, Synthesis and antioxidant properties of novel benzimidazoles containing substituted indole or 1, 1, 4, 4-tetramethyl-1, 2, 3, 4-tetrahydro-naphthalene fragments, *J. Enzyme Inhib. Med. Chem.* 20 (4) (2005) 325–331.
- [46] N.A. Clark, M. Hafner, M. Kouril, E.H. Williams, J.L. Muhlich, M. Pilarczyk, M. Niepel, P.K. Sorger, M. Medvedovic, GRcalculator: an online tool for calculating and mining dose–response data, *BMC Cancer* 17 (1) (2017) 698.
- [47] D.S. Goodsell, C. Zardecki, L. Di Costanzo, J.M. Duarte, B.P. Hudson, I. Persikova, J. Segura, C. Shao, M. Voigt, J.D. Westbrook, RCSB Protein Data Bank: Enabling biomedical research and drug discovery, *Protein Sci.* 29 (1) (2020) 52–65.
- [48] S. Epik, LLC, New York, NY, 2016; Impact, Schrödinger, LLC, New York, NY, 2016; Prime, Schrödinger, LLC, New York, NY, 2019, Schrödinger Release 2019-3: Protein Preparation Wizard, LLC, New York.
- [49] L. Schrödinger, New York, NY, 2019, Schrödinger Release 2019-3: Maestro.
- [50] L. Schrödinger, New York, NY, 2019, Schrödinger Release 2019-3: LigPrep.
- [51] D.S. Wishart, Y.D. Feunang, A.C. Guo, E.J. Lo, A. Marcu, J.R. Grant, T. Sajed, D. Johnson, C. Li, Z. Sayeeda, DrugBank 5.0: a major update to the DrugBank database for 2018, *Nucleic Acids Res.* 46(D1) (2018) D1074–D1082.
- [52] L. Schrödinger, New York, NY, 2019, Schrödinger Release 2019-3: Glide.
- [53] L. Schrödinger, New York, NY, 2019, Schrödinger Release 2019-3: QikProp.
- [54] L. Gautier, L. Cope, B.M. Bolstad, R.A. Irizarry, affy—analysis of Affymetrix GeneChip data at the probe level, *Bioinformatics* 20 (3) (2004) 307–315.
- [55] M.E. Ritchie, B. Phipson, D. Wu, Y. Hu, C.W. Law, W. Shi, G.K. Smyth, limma powers differential expression analyses for RNA-sequencing and microarray studies, *Nucleic Acids Res.* 43 (7) (2015) e47.
- [56] M. Kanehisa, M. Furumichi, M. Tanabe, Y. Sato, K. Morishima, KEGG: new perspectives on genomes, pathways, diseases and drugs, *Nucleic Acids Res.* 45 (D1) (2016) D353–D361.
- [57] V. Stathias, A. Koletti, D. Vidović, D.J. Cooper, K.M. Jagodnik, R. Terryn, M. Forlin, C. Chung, D. Torre, N. Ayad, Sustainable data and metadata management at the BD2K-LINCS Data Coordination and Integration Center, *Sci. Data* 5 (2018) 180117.
- [58] D. Szklarczyk, A. Franceschini, S. Wyder, K. Forslund, D. Heller, J. Huerta-Cepas, M. Simonovic, A. Roth, A. Santos, K.P. Tsafou, STRING v10: protein–protein interaction networks, integrated over the tree of life, *Nucleic Acids Res.* 43 (D1) (2014) D447–D452.
- [59] V.U.-B.E. Genomics, Calculate and draw custom Venn diagrams. <http://bioinformatics.psb.ugent.be/webtools/Venn/>. (Accessed March 10 2020).
- [60] W.K. Lim, K. Wang, C. Lefebvre, A. Califano, Comparative analysis of microarray normalization procedures: effects on reverse engineering gene networks, *Bioinformatics* 23 (13) (2007) i282–i288.
- [61] Q. Li, N.J. Birkbak, B. Györfy, Z. Szallasi, A.C. Eklund, Jetset: selecting the optimal microarray probe set to represent a gene, *BMC Bioinf.* 12 (1) (2011) 474.
- [62] Z. Gu, R. Eils, M. Schlesner, Complex heatmaps reveal patterns and correlations in multidimensional genomic data, *Bioinformatics* 32 (18) (2016) 2847–2849.
- [63] Z. Ates-Alagoz, Z. Buyukbingol, E. Buyukbingol, Synthesis and antioxidant properties of some indole ethylamine derivatives as melatonin analogs, *Die Pharmazie-Int. J. Pharm. Sci.* 60 (9) (2005) 643–647.
- [64] A.K. Shiau, D. Barstad, P.M. Loria, L. Cheng, P.J. Kushner, D.A. Agard, G.L. Greene, The structural basis of estrogen receptor/coactivator recognition and the antagonism of this interaction by tamoxifen, *Cell* 95 (7) (1998) 927–937.
- [65] M. Niklasson, G. Maddalo, Z. Sramkova, E. Mutlu, S. Wee, P. Sekyrova, L. Schmidt, N. Fritz, I. Dehnisch, G. Kyriatzi, Membrane-polarizing channel blockers induce selective glioma cell death by impairing nutrient transport and unfolded protein/amino acid responses, *Cancer Res.* 77 (7) (2017) 1741–1752.
- [66] P. Gong, Z. Madak-Erdogan, J.A. Flaws, D.J. Shapiro, J.A. Katzenellenbogen, B.S. Katzenellenbogen, Estrogen receptor- α and aryl hydrocarbon receptor involvement in the actions of botanical estrogens in target cells, *Mol. Cell. Endocrinol.* 437 (2016) 190–200.
- [67] E.L. Hsu, D. Yoon, H.H. Choi, F. Wang, R.T. Taylor, N. Chen, R. Zhang, O. Hankinson, A proposed mechanism for the protective effect of dioxin against breast cancer, *Toxicol. Sci.* 98 (2) (2007) 436–444.
- [68] X. Tang, M.M. Keenan, J. Wu, C.-A. Lin, L. Dubois, J.W. Thompson, S.J. Freedland, S.K. Murphy, J.-T. Chi, Comprehensive profiling of amino acid response uncovers unique methionine-deprived response dependent on intact creatine biosynthesis, *PLoS Genet.* 11 (4) (2015).
- [69] A. Subramanian, P. Tamayo, V.K. Mootha, S. Mukherjee, B.L. Ebert, M.A. Gillette, A. Paulovich, S.L. Pomeroy, T.R. Golub, E.S. Lander, Gene set enrichment analysis: a knowledge-based approach for interpreting genome-wide expression profiles,

- Proc. Natl. Acad. Sci. 102 (43) (2005) 15545–15550.
- [70] M. Kanehisa, Enzyme annotation and metabolic reconstruction using KEGG, Protein Function Prediction, Springer, 2017, pp. 135–145.
- [71] V.K. Mootha, C.M. Lindgren, K.-F. Eriksson, A. Subramanian, S. Sihag, J. Lehara, P. Puigserver, E. Carlsson, M. Ridderstråle, E. Laurila, PGC-1 α -responsive genes involved in oxidative phosphorylation are coordinately downregulated in human diabetes, *Nat. Genet.* 34 (3) (2003) 267.
- [72] G.P. Skliris, E. Leygue, P.H. Watson, L.C. Murphy, Estrogen receptor alpha negative breast cancer patients: estrogen receptor beta as a therapeutic target, *J. Steroid Biochem. Mol. Biol.* 109 (1–2) (2008) 1–10.
- [73] H. Hua, H. Zhang, Q. Kong, Y. Jiang, Mechanisms for estrogen receptor expression in human cancer, *Exp. Hematol. Oncol.* 7 (1) (2018) 1–11.
- [74] M. De Santi, L. Galluzzi, S. Lucarini, M.F. Paoletti, A. Fraternali, A. Duranti, C. De Marco, M. Fanelli, N. Zaffaroni, G. Brandi, The indole-3-carbinol cyclic tetrameric derivative CTet inhibits cell proliferation via overexpression of p21/CDKN1A in both estrogen receptor-positive and triple-negative breast cancer cell lines, *Breast Cancer Res.* 13 (2) (2011) R33.
- [75] L. Galluzzi, M. De Santi, R. Crinelli, C. De Marco, N. Zaffaroni, A. Duranti, G. Brandi, M. Magnani, Induction of endoplasmic reticulum stress response by the indole-3-carbinol cyclic tetrameric derivative CTet in human breast cancer cell lines, *PLoS ONE* 7 (8) (2012) e43249.
- [76] S. Honda, P. Lohar, M. Shigematsu, J.P. Palazzo, R. Suzuki, I. Imoto, I. Rigoutsos, Y. Kirino, Sex hormone-dependent tRNA halves enhance cell proliferation in breast and prostate cancers, *Proc. Natl. Acad. Sci.* 112 (29) (2015) E3816–E3825.
- [77] J. Finlay-Schultz, A.E. Gillen, H.M. Brechbuhl, J.J. Ivie, S.B. Matthews, B.M. Jacobsen, D.L. Bentley, P. Kabos, C.A. Sartorius, Breast cancer suppression by progesterone receptors is mediated by their modulation of estrogen receptors and RNA polymerase III, *Cancer Res.* 77 (18) (2017) 4934–4946.
- [78] I. Katsyv, M. Wang, W.M. Song, X. Zhou, Y. Zhao, S. Park, J. Zhu, B. Zhang, H.Y. Irie, EPRS is a critical regulator of cell proliferation and estrogen signaling in ER+ breast cancer, *Oncotarget* 7 (43) (2016) 69592.
- [79] H. Putzer, S. Laalami, Regulation of the expression of aminoacyl-tRNA synthetases and translation factors, *Madame Curie Bioscience Database [Internet]*, Landes Bioscience, 2013.
- [80] K.A. Dittmar, M.A. Sørensen, J. Elf, M. Ehrenberg, T. Pan, Selective charging of tRNA isoacceptors induced by amino-acid starvation, *EMBO Rep.* 6 (2) (2005) 151–157.
- [81] M. Hayano, W. Yang, C. Corn, N. Pagano, B. Stockwell, Loss of cysteinyl-tRNA synthetase (CARS) induces the transsulfuration pathway and inhibits ferroptosis induced by cystine deprivation, *Cell Death Differ.* 23 (2) (2016) 270–278.
- [82] X. Yu, Y.C. Long, Crosstalk between cystine and glutathione is critical for the regulation of amino acid signaling pathways and ferroptosis, *Sci. Rep.* 6 (1) (2016) 1–11.
- [83] M. Gao, P. Monian, N. Quadri, R. Ramasamy, X. Jiang, Glutaminolysis and transferrin regulate ferroptosis, *Mol. Cell* 59 (2) (2015) 298–308.
- [84] K.K. Brown, J.B. Spinelli, J.M. Asara, A. Toker, Adaptive reprogramming of de novo pyrimidine synthesis is a metabolic vulnerability in triple-negative breast cancer, *Cancer Discov.* 7 (4) (2017) 391–399.
- [85] E. Villa, E.S. Ali, U. Sahu, I. Ben-Sahra, Cancer cells tune the signaling pathways to empower de novo synthesis of nucleotides, *Cancers* 11 (5) (2019) 688.
- [86] E. Kulkoyluoglu-Cotul, A. Arca, Z. Madak-Erdogan, Crosstalk between estrogen signaling and breast cancer metabolism, *Trends Endocrinol. Metab.* 30 (1) (2019) 25–38.
- [87] G.S. Papaetis, K.N. Syrigos, Sunitinib, *BioDrugs* 23 (6) (2009) 377–389.
- [88] Y. Hirata, C. Yamada, Y. Ito, S. Yamamoto, H. Nagase, K. Oh-hashii, K. Kiuchi, H. Suzuki, M. Sawada, K. Furuta, Novel oxindole derivatives prevent oxidative stress-induced cell death in mouse hippocampal HT22 cells, *Neuropharmacology* 135 (2018) 242–252.
- [89] Y. Hirata, T. Iwasaki, Y. Makimura, S. Okajima, K. Oh-hashii, H. Takemori, Inhibition of double-stranded RNA-dependent protein kinase prevents oxytosis and ferroptosis in mouse hippocampal HT22 cells, *Toxicology* 418 (2019) 1–10.
- [90] M. Santoni, C. Amantini, M.B. Morelli, V. Farfariello, M. Nabissi, S. Liberati, L. Bonfili, M. Mozzicafreddo, A.M. Eleuteri, L. Burattini, Different effects of sunitinib, sorafenib, and pazopanib on inducing cancer cell death: The role of autophagy, *Am. Soc. Clin. Oncol.* (2013).
- [91] S.J. Dixon, D.N. Patel, M. Welsch, R. Skouta, E.D. Lee, M. Hayano, A.G. Thomas, C.E. Gleason, N.P. Tatonetti, B.S. Slusher, Pharmacological inhibition of cystine–glutamate exchange induces endoplasmic reticulum stress and ferroptosis, *Elife* 3 (2014) e02523.
- [92] T.D. Hubbard, I.A. Murray, W.H. Bisson, T.S. Lahoti, K. Gowda, S.G. Amin, A.D. Patterson, G.H. Perdew, Adaptation of the human aryl hydrocarbon receptor to sense microbiota-derived indoles, *Sci. Rep.* 5 (1) (2015) 1–13.
- [93] E. Zgheib, A. Limonciel, X. Jiang, A. Wilmes, S. Wink, B. Van De Water, A. Kopp-Schneider, F.Y. Bois, P. Jennings, Investigation of Nrf2, AhR and ATF4 activation in toxicogenomic databases, *Front. Genet.* 9 (2018) 429.
- [94] Y. Cheng, U.-H. Jin, C.D. Allred, A. Jayaraman, R.S. Chapkin, S. Safe, Aryl hydrocarbon receptor activity of tryptophan metabolites in young adult mouse colonocytes, *Drug Metab. Dispos.* 43 (10) (2015) 1536–1543.
- [95] J.K. Tomblin, S. Arthur, D.A. Primerano, A.R. Chaudhry, J. Fan, J. Denvir, T.B. Salisbury, Aryl hydrocarbon receptor (AHR) regulation of L-Type Amino Acid Transporter 1 (LAT-1) expression in MCF-7 and MDA-MB-231 breast cancer cells, *Biochem. Pharmacol.* 106 (2016) 94–103.
- [96] P. Tarnow, T. Tralau, A. Luch, Chemical activation of estrogen and aryl hydrocarbon receptor signaling pathways and their interaction in toxicology and metabolism, *Expert Opin. Drug Metab. Toxicol.* 15 (3) (2019) 219–229.
- [97] P. Maher, K. van Leyen, P.N. Dey, B. Honrath, A. Dolga, A. Methner, The role of Ca²⁺ in cell death caused by oxidative glutamate toxicity and ferroptosis, *Cell Calcium* 70 (2018) 47–55.
- [98] J. Lewerenz, G. Ates, A. Methner, M. Conrad, P. Maher, Oxytosis/ferroptosis—(Re-) emerging roles for oxidative stress-dependent non-apoptotic cell death in diseases of the central nervous system, *Front. Neurosci.* 12 (2018) 214.
- [99] B. Hong, Z. Su, C. Zhang, Y. Yang, Y. Guo, W. Li, A.-N.T. Kong, Reserpine inhibit the JB6 P+ cell transformation through epigenetic reactivation of Nrf2-mediated anti-oxidative stress pathway, *AAPS J.* 18 (3) (2016) 659–669.
- [100] A. Brancale, R. Silvestri, Indole, a core nucleus for potent inhibitors of tubulin polymerization, *Med. Res. Rev.* 27 (2) (2007) 209–238.
- [101] F.C. Torres, M. Eugenia Garcia-Rubino, C. Lozano-Lopez, D.F. Kawano, V.L. Eifler-Lima, G.L. von Poser, J.M. Campos, Imidazoles and benzimidazoles as tubulin-modulators for anti-cancer therapy, *Curr. Med. Chem.* 22 (11) (2015) 1312–1323.
- [102] Y.-T. Wang, Y.-J. Qin, N. Yang, Y.-L. Zhang, C.-H. Liu, H.-L. Zhu, Synthesis, biological evaluation, and molecular docking studies of novel 1-benzene acyl-2-(1-methylindol-3-yl)-benzimidazole derivatives as potential tubulin polymerization inhibitors, *Eur. J. Med. Chem.* 99 (2015) 125–137.
- [103] M. Fantacuzzi, B. De Filippis, M. Gallorini, A. Ammazalorso, L. Giampietro, C. Maccallini, Z. Aturki, E. Donati, R.S. Ibrahim, E. Shawky, Synthesis, biological evaluation, and docking study of indole aryl sulfonamides as aromatase inhibitors, *Eur. J. Med. Chem.* 185 (2020) 111815.